A Model of Sinoatrial Node Cell Regulation by the Autonomic Nervous System

by

Danilo Šćepanović

M.S.E. Biomedical Engineering
The Johns Hopkins University, 2005

B.S. Biomedical Engineering
The Johns Hopkins University, 2004

SUBMITTED TO THE HARVARD-MIT DIVISION OF HEALTH SCIENCES AND TECHNOLOGY
IN PARTIAL FULFILLMENT OF THE REQUIREMENTS FOR THE DEGREE OF

DOCTOR OF PHILOSOPHY
IN ELECTRICAL ENGINEERING AND BIOMEDICAL ENGINEERING
AT THE
MASSACHUSETTS INSTITUTE OF TECHNOLOGY

September 2011

Author: _____
Danilo Šćepanović
Harvard-MIT Division of Health Sciences and Technology
July 29, 2011

Certified by: _____
Richard J. Cohen
Whitaker Professor in Biomedical Engineering
Thesis Supervisor

Accepted by: _____
Ram Sasisekharan
PhD/Director, Harvard-MIT Division of Health Sciences and Technology
Edward Hood Taplin Professor of Health Sciences & Technology and Biological Engineering

A Model of Sinoatrial Node Cell Regulation by the Autonomic Nervous System

by

Danilo Šćepanović

Submitted to the Harvard-MIT Division of Health Sciences and Technology on
July 29, 2011, in partial fulfillment of the requirements for the degree of
Doctor of Philosophy in Electrical Engineering and Biomedical Engineering

ABSTRACT

The primary function of the heart is to pump blood at a sufficient rate to ensure perfusion of all the organs. This vital task is achieved in large part by controlling the rate of cardiac contractions, which are initiated by cells in the sinoatrial node, the "pacemaker" of the heart. The oscillation rate of these spontaneously active cells is tightly regulated by the sympathetic and parasympathetic branches of the autonomic nervous system.

Our understanding of sinoatrial node cell function has been greatly advanced by experimental and modeling efforts that quantitatively describe the numerous ionic currents responsible for the cell's spontaneous depolarization and generation of the action potential. Several models have also explored the effect of sympathetic and parasympathetic activity on specific ion channels and have reproduced the classic slowing and acceleration phenomena. However, a complete model of this interaction does not exist: current models lack the ability to simulate simultaneous sympathetic and parasympathetic activation or to reproduce heart rate dynamics in response to time-varying autonomic inputs.

We addressed this need by constructing a bottom-up model of sinoatrial node cell regulation by the autonomic nervous system, with a focus on reproducing the full range of heart rates observed under simultaneous sympathetic and parasympathetic nerve stimulation, as well as the dynamic heart rate response to steps in sympathetic or parasympathetic stimulation rate.

In constructing our model, we consolidate a large body of experimental data in a consistent mathematical framework. The model comprises 57 nonlinear coupled ordinary differential equations based on first-principles and the current mechanistic understanding of the component reactions, fits well all the experimental data used to build the model, and reproduces high-level features of the system that were not explicitly fit when building the model. The detailed nature of the model also allows numerous conclusions to be drawn about the mechanisms of heart rate control. A better understanding of these mechanisms in health and disease may enable the development of better diagnostics for cardiovascular disease and more targeted drug design. We also identified a number of limitations in the present model that can be refined through further experimental and numerical efforts.

Thesis Supervisor: Richard J. Cohen
Title: Whitaker Professor in Biomedical Engineering

ACKNOWLEDGEMENT

This thesis is the culmination of the professional and personal development I enjoyed while a graduate student in the Harvard-MIT Division of Health Sciences and Technology. I have many individuals and organizations to thank for enabling and supporting my growth during these six years.

Professionally, I was fortunate to have been surrounded and coached by inspirational mentors in both the lab and the classroom. First, I would like to thank Dr. Cohen for the incredible intellectual freedom he granted me, which I think few graduate students are exposed to. He introduced me to an interesting problem when I first entered the lab, and was supportive along every step of the way despite the numerous twists, turns, and tangential explorations I pursued while chasing my evolving interests. He has been an excellent advisor, offering pointed technical suggestions whenever I needed an extra push forward, but also a compassionate friend who would tell me to slow down, relax, and enjoy the really important things in life. Thanks also to all the Cohen Lab members: Tatsuya Arai, Wener Lv, Kichang Lee, Maya Barley, Tamara Rosbury, Grace Xiao, Candy Weaver and Amy Donovan.

I would also like to thank my committee members, Dr. Mark and Dr. Verghese, for setting the highest standards and encouraging me to achieve them. They administered my research qualifying exam at an early point in my graduate career, and asked many insightful questions about various assumptions I was unknowingly making. They taught me to focus on the details and take nothing for granted: the comprehensive analysis of experimental methods and modeling assumptions that fills many of the pages in this thesis is a direct result of the value system that Dr. Mark and Dr. Verghese instilled in me.

I consider myself very lucky to have been a student in HST and to have had the in-depth exposure to both medicine and engineering offered by this unique program. I have interacted with many inspirational professors: Dr. Gehrke, Dr. Mitchell, Dr. Freeman, Dr. Jaakkola and Dr. Rohrs, and wish to thank them for being masters of their craft and motivating me to strive for the same. I would also like to thank all the friendly and knowledgeable HST staff that I had the pleasure of interacting with: Cathy Modica, Patty Cunningham, Laurie Ward, Lora Maurer, Traci Anderson, and Julie Greenberg.

I was also very fortunate to have been funded by the Department of Energy Computational Science Graduate Fellowship (grant DE-FG02-97ER25308). This organization contributed greatly to my professional development through networking opportunities with other fellows and a three-month practicum at Sandia National Lab, not to mention four years of generous financial support. I would like to thank select staff at the Krell Institute who administered this award: James Corones, Mary-Ann Leung, Jeana Gingery, and Michelle King.

Finally, I received tremendous personal support from my friends and family. My wife Tina nurtured both my body and mind: cooking gourmet lunches and dinners and bringing them to lab so I wouldn't eat the same Kendall Food Court meal every day, as well as stepping through the mechanisms of my model and checking my equations when I needed a second opinion or an extra brain. My son Kesten, a recent addition to our family, has also been a great joy and has given me a large part of the energy needed to complete this thesis. I would like to thank my parents Bojana and Ranko for always supporting and encouraging me, and my brother Obrad for blazing a path through graduate school at MIT and showing me the ropes when I began my journey. I would also like to thank the numerous friends I met while in school, and with whom I made many memories. In particular, I would like to mention Yibo Ling, without whom I probably would not have passed the technical qualifying exam, Sourav Dey, who excited me about math and electrical engineering, Ben Larman, who taught me to box, cook steak, and appreciate bioinformatics, Jack Milwid, who taught me that steel is real, Nick Castro, who showed me that man can be made of steel, Cathal Kearney, who proved that being a grad student and being social are not mutually exclusive, and Uri Laserson, who made me laugh, and almost convinced me to switch to Python.

Table of Contents

Glossary:

This glossary contains abbreviations used throughout the text. For a list of parameter values, see Table 22.

AC	adenylate cyclase
ACh	acetylcholine
AChE	acetylcholinesterase
ANS	autonomic nervous system
AP	action potential
bpm	beats per minute
BS	Blood stream (compartment for neurotransmitter diffusion)
ECM	extracellular matrix
EJS	extrajunctional space
GAP	GTPase activating protein
G_I	Inhibitory G-protein
GPCR	G-protein coupled receptor (β-adrenergic and M2 muscarinic receptors)
G_S	Stimulatory G-protein
HH	Hodgkin and Huxley
HR	heart rate
HRV	heart rate variability
I_{bCa}	Ca^{2+} dependent background current
I_{bNa}	Na^{+} dependent background current
$I_{Ca,L}$	L-type Ca^{2+} current
$I_{Ca,T}$	T-type Ca^{2+} current
I_f	Hyperpolarization-activated "funny" current
$I_{K,ACh}$	Acetylcholine-activated K^{+} current
I_{Kr}	Rapidly activating delayed rectifier K^{+} current
I_{Ks}	Slowly activating delayed rectifier K^{+} current
I_{NaK}	Na^{+}-K^{+} pump current
I_{NCX}	Na^{+}-Ca^{2+} exchanger current
Iso	isoproterenol (β adrenergic agonist)
I_{st}	Sustained non-selective current
I_{sus}	Sustained 4-aminopyridine-sensitive current
I_{to}	Transient outward 4-aminopyridine-sensitive current
MDP	Maximum diastolic potential (measured from 0, larger value means more negative)
NE	norepinephrine
NJ	neuroeffector junction
NT	neurotransmitter
PDE	phosphodiesterase
PKA	phosphokinase A
RGS	Regulator of G-protein signaling
SAN	sinoatrial node

SANC	sinoatrial node cell
U	Enzyme activity unit: μmol substrate catalyzed/min/active site, at 25°C unless specified
β-AR	β-adrenergic receptor

1 INTRODUCTION

This thesis is concerned with the regulation of heart rate (HR) by the autonomic nervous system (ANS). The *importance* of HR regulation is easy to grasp: it is one of the major mechanisms by which the cardiovascular system ensures sufficient blood flow, which in turn is necessary for an organism's continued survival. On the other hand, the *mechanisms* involved in this process are very complicated: we have a fairly good qualitative understanding of the molecular signals, but a comprehensive quantitative model does not yet exist.

A quantitative description of the mechanisms of autonomic nervous system regulation of HR has implications for both basic-science and application development. Viewed through the lens of a scientist, a quantitative model of this complicated system summarizes our collective understanding of the chemical and biological processes at play. Due to the number of components and the level of detail required to build a quantitative model, this is not an easy task. For example, G-proteins and phosphokinase A are both involved in the signal transduction cascade from autonomic nervous system activity to HR (more detail on this below). However the G-protein scientific literature is vast and separate from the equally broad and specific body of work describing phosphokinase A. To delve into the depths of each subject area and extract the necessary information requires mastering the specific terminology adopted by each field, understanding the pertinent chemical reaction mechanisms, and often re-analyzing historic experimental data. However, summarizing this knowledge in a unified mathematical model leads not only to a better understanding of each component system, but also the nature of their interaction. Equally as important, when a quantitative model built upon the current understanding of the system falls short of reproducing documented phenomena, the model becomes a useful tool for identifying areas that we do not understand and which can be refined through further experimentation.

From the standpoint of a biomedical engineer who aspires to use an understanding of biology to design new diagnostics or therapies, a quantitative model similarly allows him to understand the problem and focus in on the possible solutions. A model of HR control by the autonomic nervous system is particularly useful because heart disease is the leading cause of death in the US (191) and worldwide (2), and changes in autonomic control of HR occur early in the onset of disease (119). Furthermore, cardiac autonomic changes are not restricted to heart disease and have also been observed in a number of health conditions and lifestyle choices (hypertension (172, 268), diabetes (226, 239, 243, 268), obesity (150, 268), schizophrenia (12), gastroesophageal reflux disease (204), physical exercise (45, 302, 335), mental strain (337), diet (235), and others (303)). A quantitative model of HR regulation by the autonomic nervous system allows a researcher to identify the biological changes that lead to specific disease manifestations

and develop targeted diagnostics based on statistical properties of the heart rate signal, or on biomarkers for the process of interest. For example, the algorithms for estimating heart rate variability (HRV), although mostly based on a simple quantitative description of the autonomic nervous system (the parasympathetic system changes HR quickly whereas sympathetic changes are slow), have been useful for diagnosing disease and tracking its progression. Examples include: screening for diabetic neuropathy (173) and heart failure (366), assessing the degree of sleep apnea (267), predicting orthostatic intolerance (258), and others (10). A more detailed model would enable improvements in such estimation algorithms. In addition, a very detailed model of the type presented in this thesis also allows more targeted design of therapies in the form of specific receptor, enzyme, or ion channel inhibitors/stimulators.

In this thesis, we specify the numerical details of HR regulation by the autonomic nervous system. We show that the model reproduces low-level (specific chemical reactions that are sub-components of the complete system) and high-level (HR changes due to ANS stimulation) experimental data.

1.1 Model overview

To help orient the reader with regard to the general anatomy, see Figure 1. Our focus is at the level of the sinoatrial node cell and sympathetic and parasympathetic nerve varicosities shown on the right. We can think of this system in three parts: 1) extracellular signals, 2) intracellular signals, and 3) the effect of the ANS signal cascade on the sinoatrial node cell (see Figure 2, Figure 3, and Figure 4, respectively).

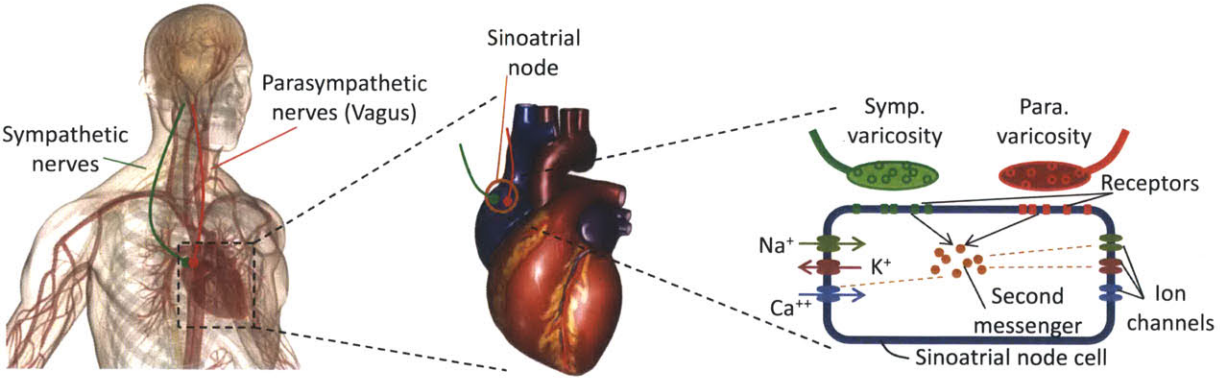

Figure 1. High-level hierarchical view of HR control by the ANS. The color scheme green = sympathetic/stimulatory and red = parasympathetic/inhibitory is maintained wherever possible. Brain/heart illustration from (116), heart image from (159).

The extracellular side of the system concerns neurotransmitter and receptor dynamics. As shown in Figure 2, sympathetic nerve varicosities store and release the sympathetic neurotransmitter

which synthesizes the ubiquitous second messenger cAMP. cAMP exists in equilibrium between the generating process of adenylate cyclase and its destruction by phosphodiesterase. cAMP also activates phosphokinase A. The second messengers regulated by these processes (inhibitory G-protein βγ subunit, cAMP and PKA) modify the properties of ion channels and pumps in the sinoatrial node cell, and thereby affect the cell's beating rate.

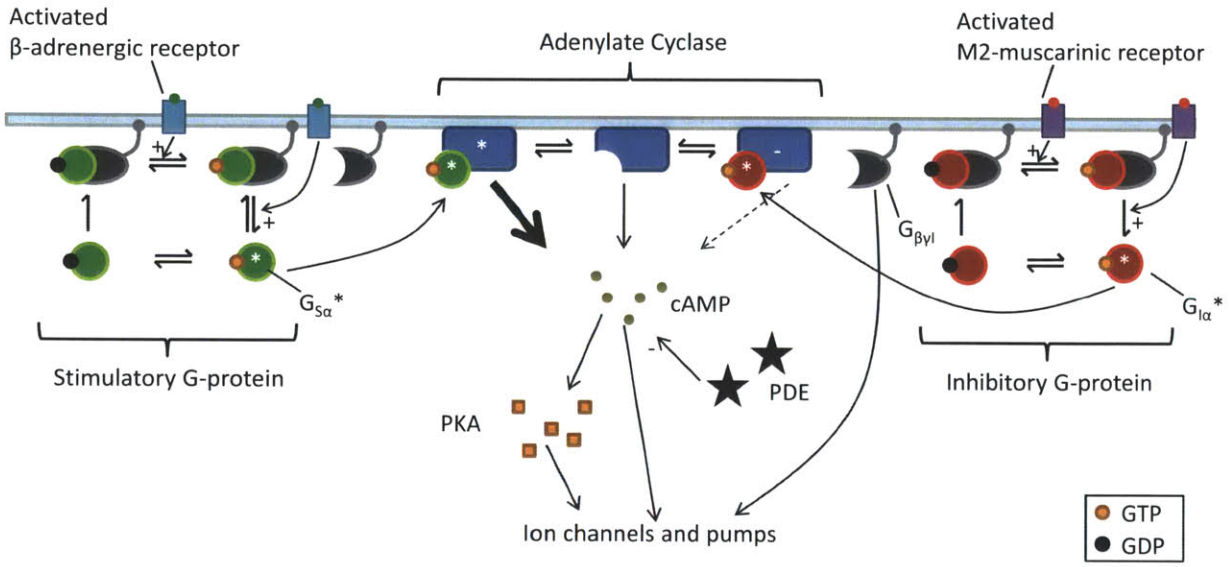

Figure 3. Intracellular components of autonomic nervous system-sinoatrial node cell interaction. *: activated form, -: inhibited form, $G_{S\alpha}$*: activated stimulatory G-protein α subunit, $G_{I\alpha}$*: activated inhibitory G-protein α subunit, $G_{\beta\gamma I}$: free inhibitory G-protein βγ subunit, cAMP: cyclic adenosine monophosphate, PDE: phosphodiesterase, PKA: phosphokinase A.

Finally, a summary of the entire system with a focus on the intrinsic components of the sinoatrial node cell are shown in Figure 4. This figure illustrates the complexity of the sinoatrial node cell: the membrane contains a plurality of ion channels, exchangers, and pumps; the intracellular space is divided into three compartments: the cytosol, submembrane space, and sarcoplasmic reticulum (SR), which communicate through ionic fluxes due to diffusion, active transport, and gated channels. These features define the basal activity of the sinoatrial node cell in the absence of autonomic nervous system stimulation. The major components under autonomic control are also shown in the figure, with the signaling cascade flowing as: neurotransmitter release → receptor activation → G-protein activation → modulation of adenylate cyclase cAMP synthesis rate → establishment of a cAMP equilibrium between synthesis by adenylate cyclase and destruction by phosphodiesterase → activation of phosphokinase A. All three second messengers (G-protein, cAMP, PKA) modulate ion channel and pump properties, and thus control heart rate. This figure summarizes most of the components in our model; some elements were left out for the sake of clarity, but are described in full detail in the body of the thesis.

norepinephrine (NE). Norepinephrine interacts with β-adrenergic receptors within the neuroeffector junction (NJ) and in the extrajunctional space (EJS), and is cleared by three mechanisms: diffusive transport, reuptake into the nerve varicosity, and absorption into the sinoatrial node cell. An analogous process occurs on the parasympathetic side: parasympathetic varicosities release the neurotransmitter acetylcholine (ACh), which binds M2 muscarinic receptors on the cell membrane. Acetylcholine is cleared by two processes: diffusive transport, and hydrolysis by the membrane-bound enzyme acetylcholinesterase. Both neurotransmitters are synthesized in their respective nerves.

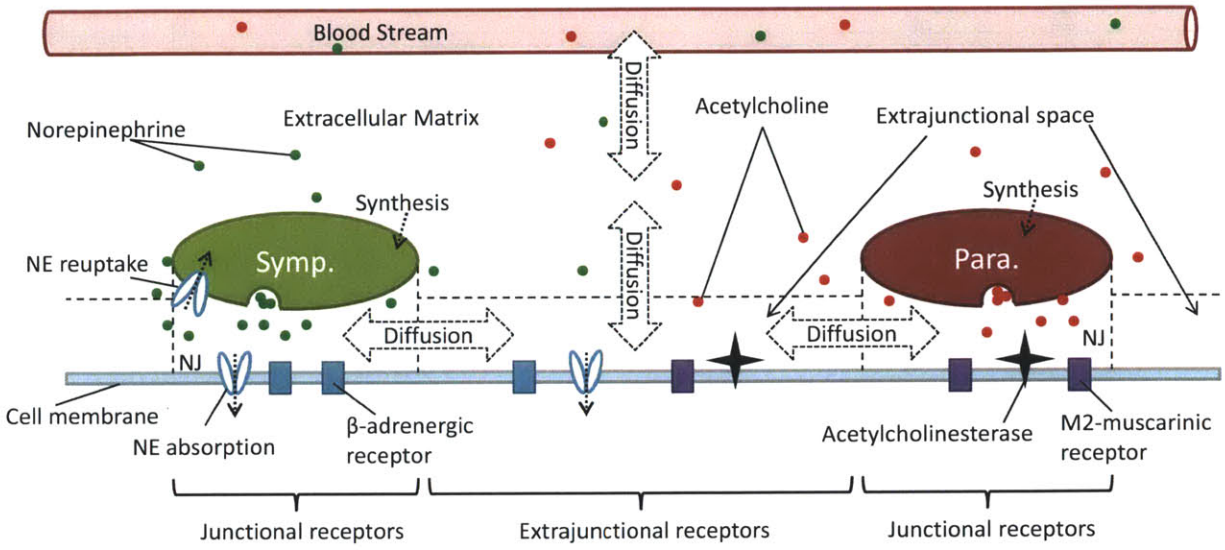

Figure 2: Extracellular components of autonomic nervous system-sinoatrial node cell interaction. NE: norepinephrine, NJ: neuroeffector junction, Symp.: sympathetic varicosity, Para.: parasympathetic varicosity.

The extracellular signals from the sympathetic and parasympathetic nerves are transduced across the cell membrane by the β-adrenergic and M2 muscarinic receptors, respectively. The intracellular processes are shown in Figure 3. We model five major intracellular players:

1) G-proteins
2) Adenylate cyclase (AC)
3) cAMP
4) Phosphodiesterase (PDE)
5) Phosphokinase A (PKA)

β-adrenergic and M2 muscarinic receptors are activated by binding their respective neurotransmitters, and once activated, they catalyze the subsequent activation of stimulatory or inhibitory G-proteins, respectively. The activated G-protein α subunits bind and modulate the activity of adenylate cyclase,

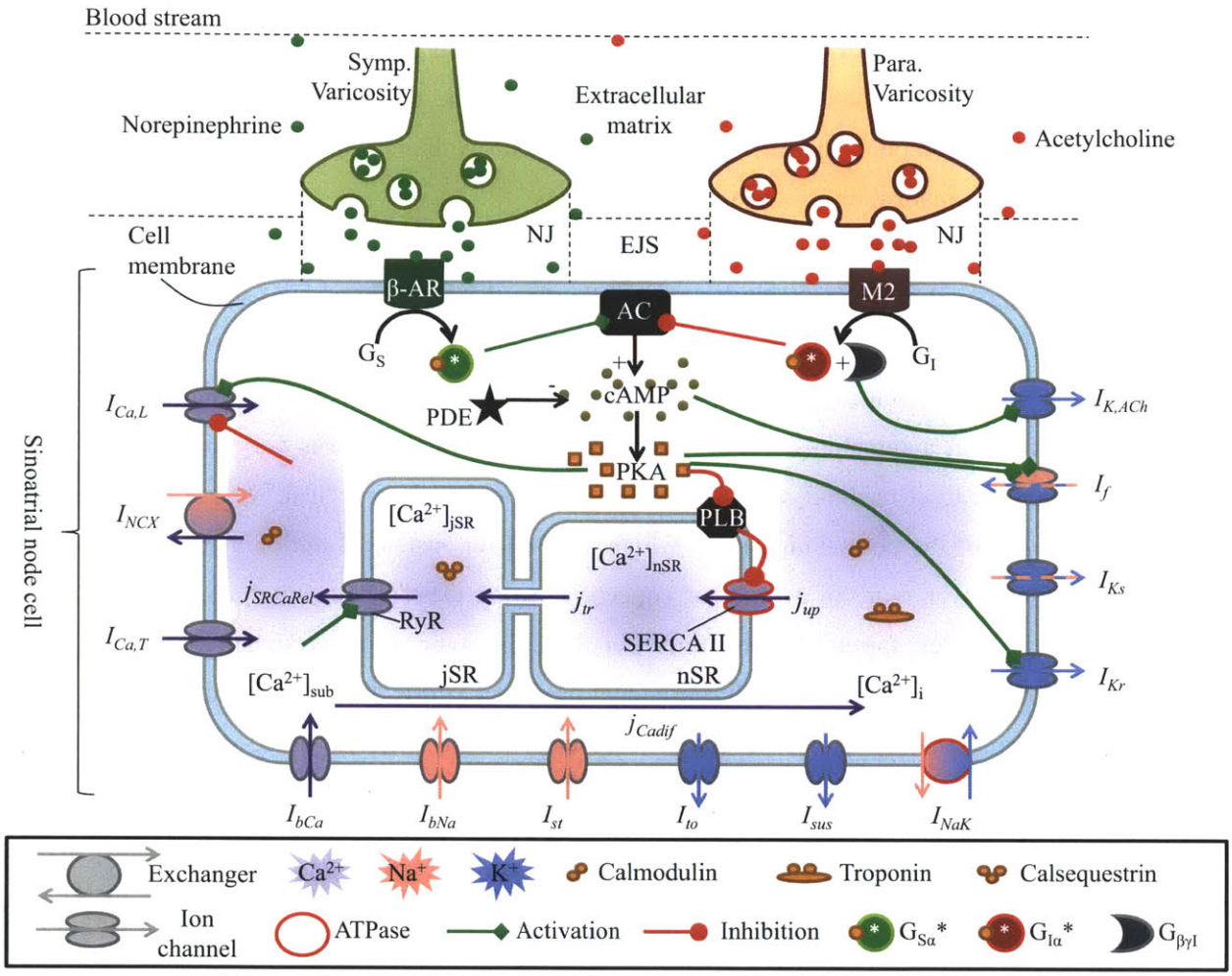

Figure 4. Full illustration of sinoatrial node cell model components, with a summary of autonomic nervous system interaction. NJ: neuroeffector junction, EJS: extrajunctional space, β-AR: β-adrenergic receptor, M2: M2 muscarinic receptor, AC: adenylate cyclase, G_S: stimulatory G protein (not activated), $G_{S\alpha}$*: activated stimulatory G-protein α subunit, G_I: inhibitory G protein (not activated), $G_{I\alpha}$*: activated inhibitory G-protein α subunit, $G_{\beta\gamma I}$: free inhibitory G-protein βγ subunit, PDE: phosphodiesterase, PKA: phosphokinase A, PLB: phospholamban, $I_{Ca,L}$: L-type Ca^{2+} current, I_{NCX}: Na^+/Ca^{2+} exchanger current, $I_{Ca,T}$: T-type Ca^{2+} current, I_{bCa}: background Ca^{2+} current, I_{bNa}: background Na^+ current, I_{st}: sustained inward current, I_{to}: 4-aminopyridine sensitive transient outward current, I_{sus}: 4-aminopyridine sensitive sustained current, I_{NaK}: Na^+/K^+ exchanger current, I_{Kr}: rapidly activating delayed rectifier K^+ current, I_{Ks}: slowly activating delayed rectifier K^+ current, I_f: hyperpolarization-activated "funny" current, $I_{K,ACh}$: acetylcholine-activated K^+ current, $[Ca^{2+}]_{sub}$: Ca^{2+} concentration in the subspace, $[Ca^{2+}]_i$: Ca^{2+} concentration in the cytosol, jSR: junctional sarcoplasmic reticulum, nSR: network sarcoplasmic reticulum, j_{up}: Ca^{2+} uptake flux, j_{tr}: Ca^{2+} transfer from nSR to jSR, $j_{SRCaRel}$: Ca^{2+} flux out of jSR, j_{Cadif}: Ca^{2+} flux due to diffusion, RyR: ryanodine receptor, SERCAII: sarcoplasmic reticulum Ca^{2+} pump, $[Ca^{2+}]_{jSR}$: Ca^{2+} concentration in the jSR, $[Ca^{2+}]_{nSR}$: Ca^{2+} concentration in the nSR.

1.2 Background on sinoatrial node cell models

This thesis is a natural outgrowth of the advancements in numerical modeling of excitable cells. In this section, we provide a brief historical overview to help place the current work in context. We also introduce the three recent models that serve as the basis for our work and against which we compare our model in terms of mathematical definition and performance.

The field of excitable cell modeling took the stage following the groundbreaking work of Hodgkin and Huxley (HH) in 1952 (151). This first quantitative model of action potential (AP) generation in the squid giant axon, soon inspired scientists to turn their attention to the spontaneously active cells of the heart. The first model of heart automaticity developed by Noble in 1960 (253), was very similar to the HH model: it contained the three original currents (sodium I_{Na}, potassium I_K, and "leak" I_L, see Figure 5) with a slight modification of the potassium current which allowed for sustained, periodic AP generation. In retrospect, this model was more of a proof of concept showing that "pacemaking" could be simulated using the Hodgkin-Huxley formalism; the finer detail of the ionic currents actually responsible for automaticity and AP shape evolved through subsequent modeling efforts that were based on experimental measurements of individual currents in mammalian (usually rabbit) sinoatrial node cells (SANCs). For more detailed reviews on SANC models see Wilders et al. (360) and the more recent (359), as well as the excellent review of major ionic currents responsible for SANC automaticity by Mangoni and Nargeot (231).

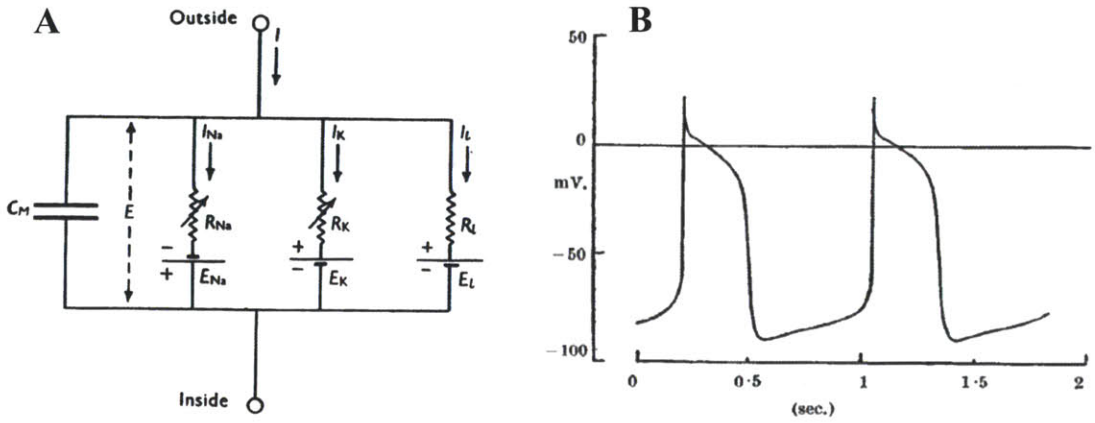

Figure 5 A. Original illustration of the squid giant axon model by Hodgkin and Huxley showing the two time-varying currents I_{Na} and I_K, and the passive "leak" current I_L (figure from (151)). I: total transmembrane current, CM: membrane electric capacitance, E: transmembrane potential, R_{Na}, R_K and R_L: resistance of sodium, potassium and leak channels, E_{Na}, E_K, and E_L: electrochemical driving force of sodium, potassium and leak current B. Simulated transmembrane membrane potential from the Noble model showing sustained, periodic oscillations (figure from (253)).

We bring attention to three models in particular, which serve as the inspiration and foundation for the further development described in this thesis:

- "Dokos Model" – developed by Dokos et al. in 1996 (96)
- "Demir Model" – developed by Demir et al. in 1999 (81)
- "Maltsev Model" – developed by Maltsev and Lakatta in 2010 (227)

A schematic comparison of these three models against the "complete" model presented in this thesis is shown in Figure 6. The specific virtues and limitations of each model are discussed below.

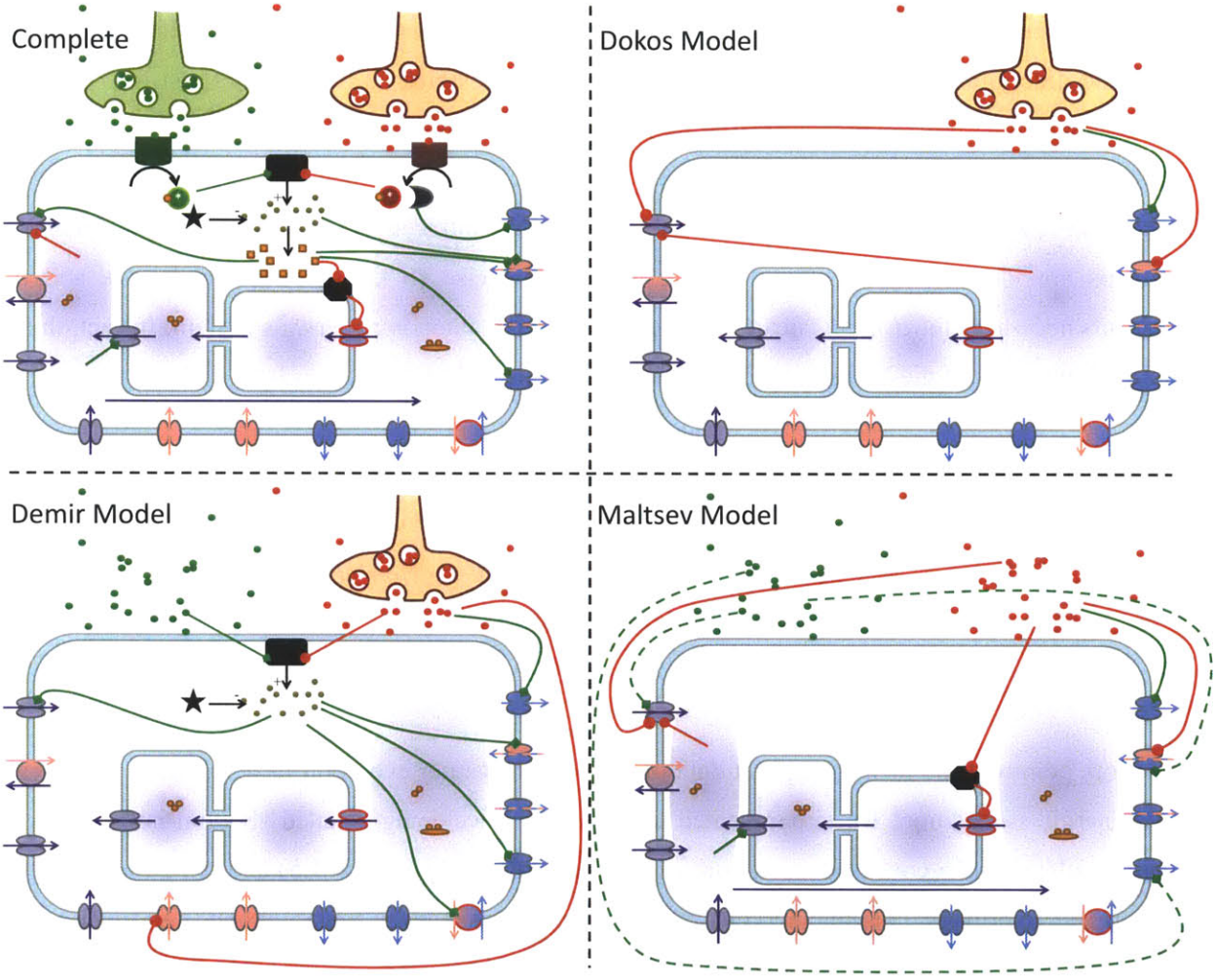

Figure 6. Comparison of the complete model presented in this thesis versus the Dokos (96), Demir (81), and Maltsev (227) models. See Figure 4 for a labeled version of the full system. Unique aspects of each model are discussed in the text.

The Maltsev model is the most complete SANC model to date. It features:

- Mathematical descriptions of almost all ionic currents that have been identified in the SANC (231).
- Subcellular compartmentalization and Ca^{2+} buffering developed by Kurata et al. (198).
- Spontaneous Ca^{2+} release. The existence and importance for pacemaking of this "Ca^{2+} clock" were recently elucidated (199, 200, 229, 338, 340-344).
- A simple implementation of some of the functional changes that occur in response to adrenergic and cholinergic stimulation. As shown in Figure 6, the Maltsev model does not include explicit descriptions of neurotransmitter release from the autonomic nerves, receptor activation, or any of the second messengers. Rather, acetylcholine concentration acts directly on specific ion channels. The description of sympathetic control is even more abstract, and is only defined for "maximal adrenergic stimulation." Because of this limited description, we show it with dashed lines in Figure 6.

We chose this model as the baseline cell model: note that the intracellular compartments, ion channels, and pumps are identical in the complete and Maltsev models. To this baseline model we add the components necessary for *dynamic* heart rate regulation by the autonomic nervous system. In fact, this is one of the limitations of the Maltsev model pointed out by the authors:

> *"Our present model does not describe the kinetics of the evolution of the responses to β-AR [β-adrenergic receptor] and ChR [Cholinergic receptor] stimulation. Additional experimental data that define the transient state kinetics of cAMP, PKA and CaMKII signaling in spontaneously firing SANCs are required for systems modeling of biochemistry kinetics to simulate the transitions." – Maltsev and Lakatta 2010 (227)*

The authors point out the lack of explicit data on second messenger evolution in response to adrenergic and cholinergic stimulation; we circumvented this issue by developing detailed "bottom-up" models of the major molecular players based on in-vitro experimental data (see Section 1.5) and tying these into the Maltsev model to bridge autonomic nervous system activity to changes in sinoatrial node cell function.

The Dokos model is unique in its detailed description of acetylcholine release from the parasympathetic nerves. However, no sympathetic effects are modeled, and the baseline sinoatrial node cell model is incomplete (lacks submembrane compartment, spontaneous Ca^{2+} release from the sarcoplasmic reticulum, and Ca^{2+} buffering; see Figure 6). Also, the downstream treatment of acetylcholine-mediated effects is similar to that in the Maltsev model: acetylcholine directly modifies ion channel properties (see Figure 6).

This framework is incorrect because it is known that NTs bind receptors on the cell surface and initiate a second messenger cascade, which in turn interacts with the ion channels and influences their activity (see Figure 4). The consequences of this model choice are 1) the dynamic response to ACh is assumed to be rate-limited at the point of ACh release and not anywhere downstream, which is a questionable assumption given the complexity of the downstream processes and 2) this model does not provide a venue for adrenergic/cholinergic interaction, which occurs (in large part) postsynaptically, through opposing influences on cAMP generation. Despite these limitations in the description of the mechanisms, the model successfully reproduces a number of experimentally observed phenomena. Its treatment of vagal release of acetylcholine was also a major influence in how we described neurotransmitter release in our complete model (for example, the idea of explicitly modeling the extrajunctional space originated in the Dokos model).

The Demir model features the most detailed description of intracellular second messengers, and includes responses to the adrenergic agonist isoproterenol (Iso) (see Figure 6). Its more explicit nature is this model's main virtue: for example, the second messenger cAMP is explicitly modeled, and it modulates ion channel properties. This allows the model to reproduce the individual effects of adrenergic (bath applied) and cholinergic (bath applied and neural) stimulation, as well as some interaction between these two stimuli when applied simultaneously. Its major shortcomings however, are the arbitrary form of some of the functions: for example, the description of phosphodiesterase activity is based entirely on a single data point (the baseline concentration of cAMP), and is reasonable but arbitrary outside the baseline range. Also, since the model only includes bath application of Iso, it cannot simulate responses to *dynamic* adrenergic stimulation.

Taken together, these three models identified the important membrane and intracellular players and thereby set the stage for developing a truly unified molecular-level model of autonomic nervous system control of heart rate. In this thesis we take the next step, by describing explicit relationships between molecules that are known to interact with each other. We provide a thorough model framework based on the current understanding of the signaling cascade from sympathetic and parasympathetic nerve activity to the final end effectors (ion channels and Ca^{2+} clock). To determine model parameters, we use available data from a variety of sources and rather than disregarding values that seem disparate, we consider the actual experimental methods used to obtain at the measurements and explain the inconsistencies mechanistically in an attempt to use the most accurate parameter values.

1.3 Aims

General aim:

- Build a sinoatrial node cell model capable of reproducing dynamic heart rate changes in response to simultaneous sympathetic and parasympathetic stimulation.

Specific aims:

1) Build a model of sinoatrial node cell regulation by the autonomic nervous system which is mechanistically motivated and can accurately reproduce both steady-state and dynamic experimental data. The components of the model are:
    a. Neurotransmitter release from sympathetic and parasympathetic nerves and neurotransmitter clearance mechanisms
    b. Binding of neurotransmitter to β-adrenergic and M2 muscarinic receptors
    c. Intrinsic and receptor-mediated activation of stimulatory and inhibitory G-proteins
    d. Activation/inhibition of adenylate cyclase by activated G-proteins
    e. cAMP hydrolysis by phosphodiesterase
    f. Activation of phosphokinase A by cAMP
    g. Changes in ion channel and pump function due to second messengers
2) Use the model to understand the critical steps along the signaling cascade and to explore the mechanisms underlying high-level phenomena that have been observed experimentally
    a. Identify the molecular origin of the disparity between sympathetically- and parasympathetically-mediated changes in heart rate
    b. Identify major ionic currents responsible for sinoatrial node cell beating rate
    c. Reproduce impulse response functions describing the effects of sympathetic and parasympathetic nerve stimulation on heart rate
3) Identify model components that require further refinement or experimental study

1.4 Summary of accomplishments

This thesis is very lengthy and dense, and the major contributions of the work are distributed over a number of chapters. To help guide the reader, we provide a summary here.

1) We provide a full mathematical specification of all the components shown in Figure 4
    a. The 57 state variables (Table 21) are described by a system of coupled nonlinear ordinary differential equations (section 9.5.2)
    b. The majority of model parameters (Table 22) are rigorously derived from experimental data from numerous sources. Experimental values are organized in tables (Table 1-Table 6, Table 8, Table 9, Table 17, Table 20)
    c. The neurotransmitter release model can be used independently to calculate average neurotransmitter concentration as a function of sympathetic or parasympathetic nerve stimulation frequency (Figure 26). This allows comparison of data collected under nerve stimulation versus bath application of known neurotransmitter concentration.
2) The biological origin of the slow rate of sympathetically mediated changes in heart rate occurs at the level of the β-adrenergic receptors (Figure 24), whereas M2-muscarinic rate is limited downstream, by second messenger kinetics
3) Our model fits all of the steady-state "training data" used to build it, including heart rate responses to simultaneous sympathetic and parasympathetic nerve stimulation (Figure 105)
4) Our model reproduces behaviors that were not explicitly fit when building the model ("test data")
    a. Sympathetic and parasympathetic impulse response functions (Figure 113)
    b. Phase response curves (sensitivity to stimulus time over the course of an action potential) for parasympathetic stimulation (Figure 111)
5) Our model produces more accurate action potential shapes and eliminates a major limitation of the Maltsev model wherein heart rates below 100 bpm could not be reliably simulated (Figure 97, Figure 102)
6) We show that ion channel kinetics can be a subtle but powerful determinant of sinoatrial node cell beating rate, and that the effect of classic "pacemaker currents" is not as potent as previously believed (Figure 107)
7) We describe a feasible hypothesis to explain quantitative differences between experimental data collected on isolated sinoatrial node cells versus whole sinoatrial node tissue (Figure 89, Figure 105k)

1.5 Thesis organization

This thesis describes a very complicated biological system in great detail. Experimental data from numerous sources are gathered and the merits of specific experimental protocols are discussed to determine the most suitable values. All assumptions are explicitly stated, and in many cases, the validity of the assumptions is discussed at length. This thesis is therefore a valuable record of all the experimental data we considered and the thought process involved in building the model. It will also be a useful guide for future work on the model, which can re-examine the more questionable assumptions or experimental values. On the other hand, it is very dense and hard to follow on a first read.

This is a necessary compromise; to present a large amount of information, one must choose between *length* and *focus*. A work that re-introduces the same important concept multiple times gently reminds the reader of the topic and allows him to keep going forward. This approach has the drawback of *length*. Given the amount of information in this thesis, and the detailed nature of some of the concepts, we reasoned that the extra length would be prohibitive. We chose instead to use specific language ("jargon") and describe concepts only on a first presentation for the sake of succinctness. This format demands great *focus* from the reader, to note and remember particular definitions on a first read. However, for a reader who is familiar with the concepts, this format should not be overly taxing and should allow a faster conveyance of ideas.

We separate the thesis into chapters that describe components of the signal transduction cascade (see Figure 7). To highlight the important concepts and results of each chapter, a high-level summary is provided at the beginning of the chapter. The remainder of each chapter reads like a mini-review that gives the pertinent background information, presents the new material, and discusses the proposed model in the context of the experimental data or previous published models. The content of each chapter is:

Chapter 2: Neurotransmitter Release from Autonomic Nerves. Describes the geometry of the SANC and nerve varicosities; release, diffusion, hydrolysis, uptake, and clearance of NT; and the abundance and kinetics of β-AR and M2 muscarinic receptors.

Chapter 3: G-Proteins (EC 3.6.5.1) and Adenylate Cyclase (EC 4.6.1.1). Describes the intrinsic properties of stimulatory and inhibitory G-proteins, their activation by β-AR and M2 muscarinic receptors, and their influence on AC.

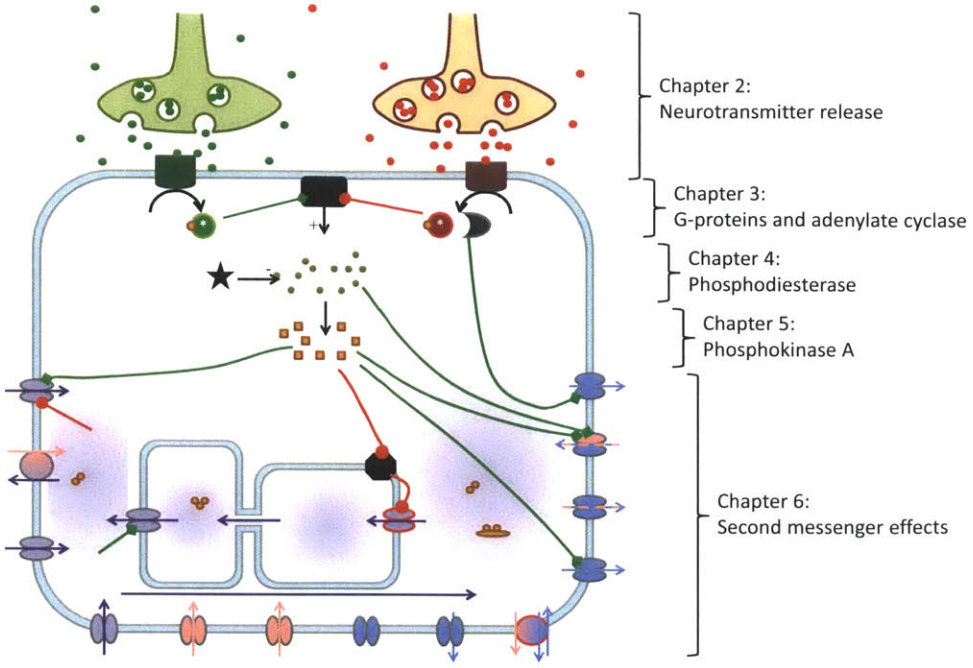

Figure 7 Thesis chapter organization in terms of the signal transduction cascade.

Chapter 4: Phosphodiesterase (EC 3.1.4). Describes the function of PDE, its modulation by various regulators, and specifies a detailed and a reduced model pertaining to cAMP regulation in the SANC.

Chapter 5: Phosphokinase-A (EC 2.7.11.11). Describes the structure and cellular roles of PKA, and its activation by cAMP in a minimal model.

Chapter 6: Modification of Ion Channels and Calcium-Cycling Machinery by Second Messengers. Combines the components from Chapters 2-5 with the Maltsev model; uses experimental data on the effects of ACh, NE, and nerve stimulation to find best-fit parameters for the direct effects of second messengers on ion channels and Ca^{2+} clock (most of the fitting/optimization is described in this chapter). Compares the ANS-mediated changes in the new model against the Maltsev, Dokos, and Demir models.

Chapter 7: Model Properties. Describes high-level features of the model and compares performance against published results from other modeling studies or experiments.

Chapter 8: Conclusion and Future Work. Summarizes the model and the conclusions that it enables us to draw about the physiological system. Proposes future work to

address the model's major limitations and potential other uses of the model for answering interesting questions.

Chapter 9: Appendix. Provides full model specification and more detail on model construction.

2 NEUROTRANSMITTER RELEASE FROM AUTONOMIC NERVES

2.1 Overview

This chapter describes the processes involved in norepinephrine and acetylcholine storage and release from sympathetic and parasympathetic nerve varicosities, respectively, their clearance from the extracellular spaces and their interaction (binding/unbinding) with β-adrenergic and M2 muscarinic receptors. This part of the system is highlighted in Figure 8.

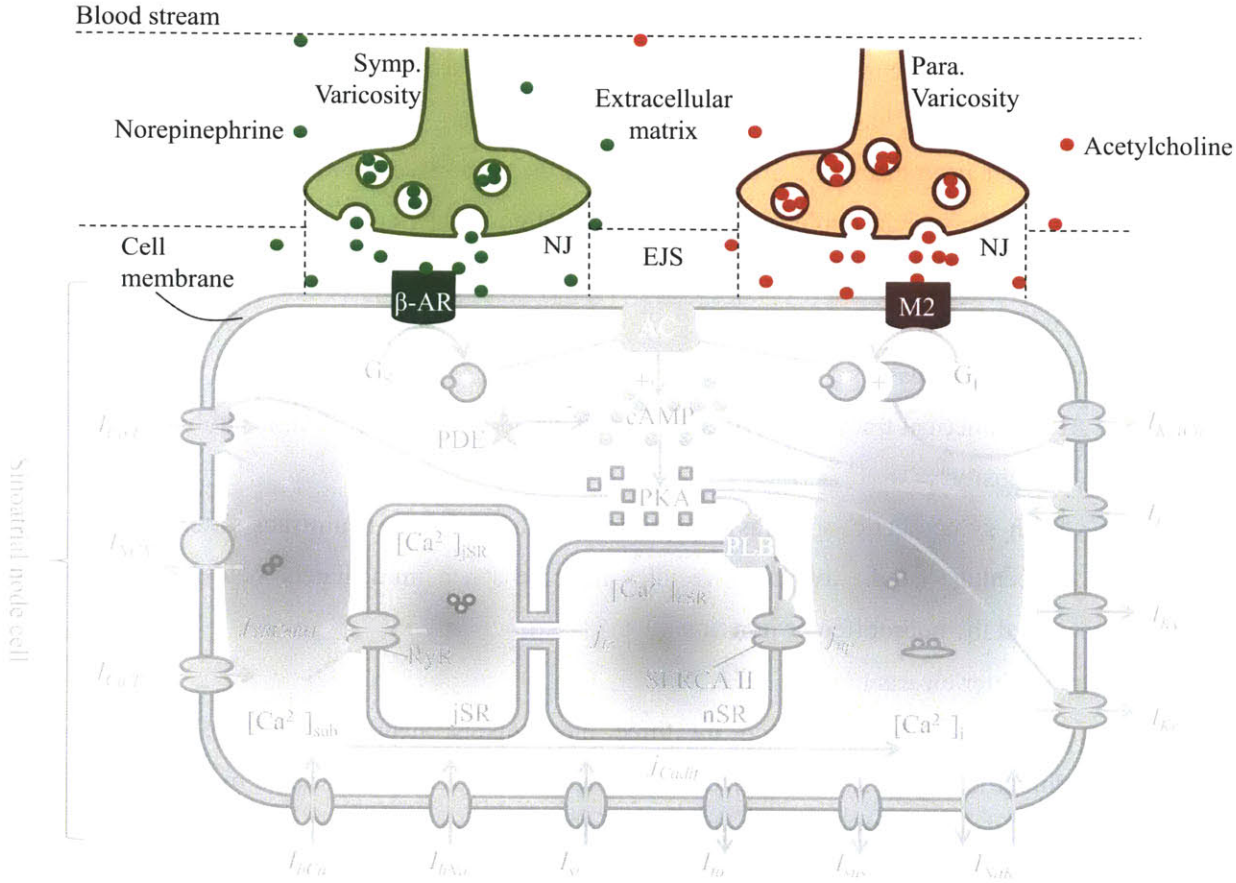

Figure 8. High level illustration of neurotransmitter release in the context of the entire model originally shown in Figure 4 (see original figure for key).

Anatomy

- Our model focuses on the local interaction between sympathetic and parasympathetic nerve varicosities and a single sinoatrial node cell
- The autonomic nervous system anatomy is complicated, with many opportunities for sympathetic-parasympathetic interaction prior to the termination at the sinoatrial node

- The sinoatrial node is a collection of heterogeneous cells with dissimilar properties; we attempt to describe the function of the entire mode using the specific properties of a single cell

Model features

- Neurotransmitter storage
    - ACh and NE are stored in hundreds of vesicles inside on the order of ten adrenergic and cholinergic varicosities per sinoatrial node cell
    - Vesicle and varicosity dimensions are based on microanatomical measurements
    - Amount of NE and ACh in each vesicle are based on experimental measurements
    - The blood stream is modeled as a separate compartment with a fixed neurotransmitter concentration, based on experimental measurements
    - Both neurotransmitters are synthesized in the respective nerves, at rates high enough to preclude vesicle depletion for stimulation frequencies at or below 7 Hz (experimental observation). Synthesis equations are based on current understanding of pertinent mechanisms.
- Neurotransmitter release
    - For numerical tractability, we model a single adrenergic and a single cholinergic "lumped varicosity"
    - Each sympathetic or parasympathetic stimulus releases neurotransmitter from a small percentage of the available vesicles into the space immediately below the varicosity, called the neuroeffector junction
- Neurotransmitter clearance
    - Norepinephrine is cleared by three mechanisms: neuronal reuptake, absorption by sinoatrial node cells, and diffusive transport and eventual clearance by the blood stream (see Figure 9). The model reproduces experimentally measured clearance ratios.
        - **Neuronal reuptake** occurs through a high affinity norepinephrine transporter, modeled using standard Michaelis-Menten kinetics, measured norepinephrine affinity, and necessary abundance (maximal uptake rate) needed to produce clearance of 86% of released norepinephrine by reuptake (experimental value).
        - **Cell absorption** occurs through a low affinity transporter, modeled using standard Michaelis-Menten kinetics, measured affinity, and necessary abundance (maximal absorption rate) to produce clearance of 5% of released norepinephrine by this route (experimental value).
        - **Diffusion** is modeled using rate constants theoretically/numerically deduced from microanatomical measurements of adrenergic varicosity-sinoatrial node cell

geometry and experimentally measured norepinephrine diffusivity in the appropriate media. Overall diffusion into the bloodstream reproduces the measured clearance of 9% of released norepinephrine by this route.

- Acetylcholine is cleared by two mechanisms: hydrolysis by sinoatrial node cell membrane-bound acetylcholinesterase and diffusive transport similar to that for norepinephrine (see Figure 9)
  - **Hydrolysis** is modeled using acetylcholinesterase properties: Michaelis-Menten kinetics, acetylcholine affinity, hydrolytic turnover rate, and enzyme abundance are all derived from measured values. Overall hydrolysis rate matches experimental measurements.
  - **Diffusion** is modeled using the same framework as for norepinephrine, with rate constants derived from the actual cholinergic varicosity-sinoatrial node cell geometry and measured diffusivities.

- Interaction with receptors
  - Acetylcholine and norepinephrine bind M2 muscarinic and β-adrenergic receptors, respectively.
  - The abundances and spatial distribution of both receptors are based on experimental measurements
  - The kinetics of the binding/unbinding reactions are based on measured affinities and dissociation rates

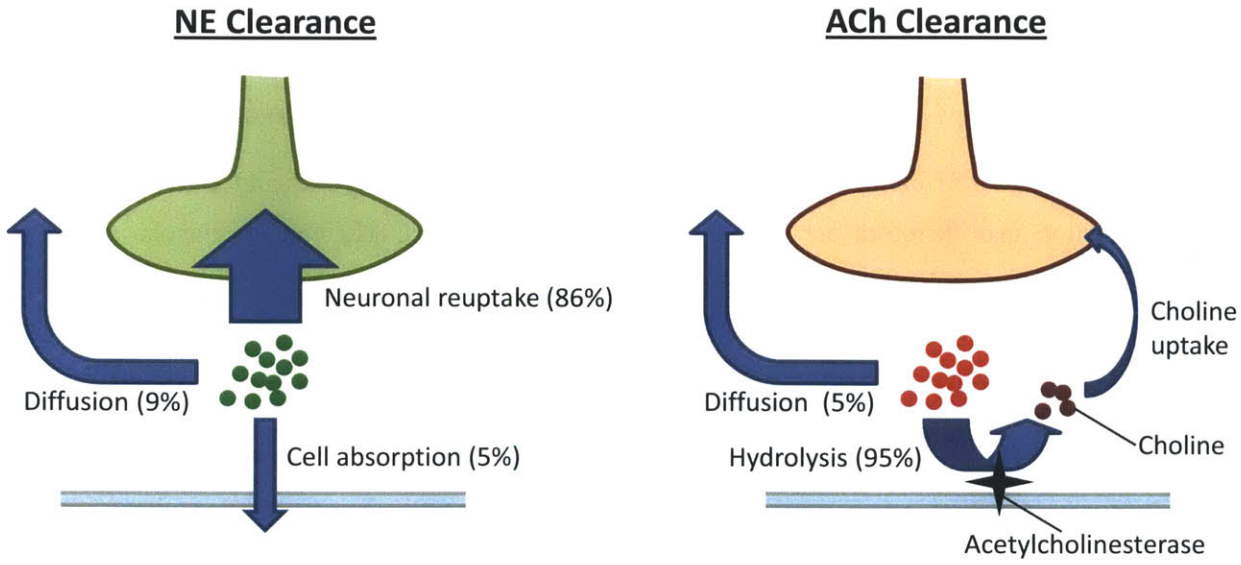

Figure 9. Modes of norepinephrine (NE) and acetylcholine (ACh) clearance. Left: norepinephrine is cleared by neuronal reuptake, diffusion to the blood stream, and cell absorption, with the indicated ratios. Right: acetylcholine is cleared by acetylcholinesterase-mediated hydrolysis and diffusion to the blood stream with the indicated ratios.

Results:

- The rate disparity between sympathetic and parasympathetic effects on heart rate begins at the level of the β-adrenergic and M2-muscarinic receptors: β-adrenergic receptors respond slowly to norepinephrine release, requiring ~20 seconds to reach 95% of steady-state value. M2-muscarinic receptors only require < 1s to reach 95% of steady-state value (see Figure 24).
- Acetylcholine hydrolysis by acetylcholinesterase has a large effect on the *rate* at which acetylcholine is removed following cessation of stimulation. The *rate* of norepinephrine removal following cessation of stimulation is not greatly affected by neuronal reuptake. The *overall receptor activation* by neurotransmitter binding is greatly increased by blockage of acetylcholine hydrolysis and norepinephrine reuptake (for respective receptors). See Figure 25.
- The relationship between the rate of sympathetic or parasympathetic nerve stimulation and the equivalent amount of neurotransmitter released is quantified using a power law (see Figure 26)
- The extracellular matrix can act as a buffer: if an experiment is done on non-isolated cells (with the extracellular matrix intact), and neurotransmitter concentration is maintained in the cell bathing solution, the actual "effective" neurotransmitter concentration at the cell membrane will be about 1.5 orders of magnitude less due to the local clearance mechanisms (neuronal reuptake for norepinephrine, hydrolysis for acetylcholine), see Figure 27. This has implications for properly interpreting experimental data based on preparation.
- A direct pathway of parasympathetically-mediated inhibition of β-adrenergic receptor activation is described (necessary to reproduce heart rate data)

2.2 Introduction

2.2.1 Anatomy: from the brain to the sinoatrial node, via the autonomic nervous system

The sinoatrial node (SAN) of the heart is populated by spontaneously depolarizing cells that initiate cardiac contraction and therefore act as the pacemaker of the heart. The rate of depolarization is modulated by the sympathetic and parasympathetic branches of the autonomic nervous system. Sympathetic and parasympathetic signals travel from the brainstem to the heart through the sympathetic and vagus nerves, respectively. These nerves do not synapse directly on the cells in the SAN, but rather, they first interact with intracardiac ganglia (reviews: (197, 219)).

The existence of intracardiac *parasympathetic* ganglia is generally accepted, and has been visualized with cholinesterase staining (284), see Figure 10. Intracardiac parasympathetic ganglia spread across a significant portion of the base of the heart and postganglionic parasympathetic neurons project primarily

to the sinoatrial and atrioventricular nodes, with minimal innervation of the atrial and ventricular myocardium (review: (219)).

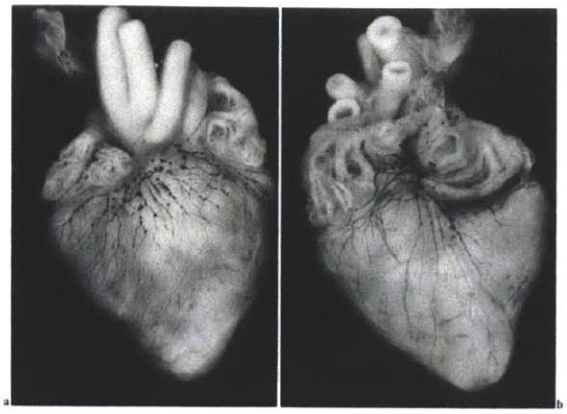

Fig. 2 a and b. Heart of a 13 days old chick embryo. Gomori staining. Epi-illumination. × 10. a ventral aspect; b dorsal aspect

Figure 10 Chick heart stained for cholinesterase activity, indicating the distribution of intracardiac parasympathetic ganglia. Figure taken from (284).

It is unclear whether intracardiac *sympathetic* ganglia exist however, as there are data that both support (241) and refute (252) their existence. It is known however that sympathetic fibers innervate a more diffuse area of the myocardium, including not only the sinoatrial node, but also the working myocardium of the atria and ventricles (review: (324)). In birds, it has been shown that sympathetic fibers contribute to the intracardiac parasympathetic ganglia (324), so even if there are no adrenergic ganglion cells in the heart, the sympathetic nerves may still be a part of the intracardiac ganglion network.

The role of the intracardiac ganglia is also an evolving concept. Previously, the ganglia were thought of as distribution points for parasympathetic nerves (127, 197), but more recently, the idea of a highly interconnected and sophisticated intracardiac ganglion network, or "heart brain" has gained prominence (9, 197, 277, 278). Thus, the intracardiac ganglia may, and likely do, provide a venue for sympathetic-parasympathetic interactions. Furthermore, some sympathetic fibers from the stellate ganglion join the vagus nerve and travel to the heart in close physical contact (171, 324). The proximity of these axons opens doors for mutual excitation of these two, usually opposing, branches.

Finally, the end effector cells (SANCs) are not homogeneous. It is known that cells in the SA node differ with respect to ionic current densities and innervation (32, 94, 368). It has also been observed that the leading pacemaker site shifts with autonomic stimulation (153, 261, 328, 352). Because the cell that depolarizes the fastest initiates cardiac contraction, we include the effects of heterogeneity by modeling a

cell with the weakest parasympathetic innervation, and the strongest sympathetic innervation. This is manifested through tight adrenergic neuroeffector junctions (NJs) and wide cholinergic NJs (more detail on this in section 2.3.1).

There are many opportunities for interaction between the two branches of the ANS, and presynaptic mechanisms of accentuated antagonism and reciprocal excitation have been proposed (review: (210)). Also, following the idea of cotransmission, wherein a neuron releases more than a single type of NT, it is possible that sympathetic and parasympathetic fibers can independently produce a variety of effects (for a review, see Burnstock 2009 (47)). We appreciate that such interactions may exist, but focus our efforts by assuming that the major molecular players are ACh and NE, and that they are released independently of each other. Under these assumptions, we construct a model where downstream interactions (through cAMP production) are responsible for reproducing the majority of observed behaviors. This approach worked well for moderate vagal stimulation; however, to reproduce HR effects at high rates of vagal stimulation, we found it necessary to include a mechanism of direct inhibition of sympathetic activity as suggested by Levy (210) and Loffelholz and Pappano (219), described in section 2.5.10.

Our model focuses on the sympathetic and parasympathetic neuroeffector junctions, where we assume that stimulation of the nerve causes a release of neurotransmitter into the neuroeffector junction, which in turn exerts changes on sinoatrial node cell activity.

2.2.2 Previous models of neurotransmitter release

Several models of neurotransmitter release, diffusion and hydrolysis have been published. They range from the highly theoretical development by Purves (276), to more empirical/experimental approaches used by Warner and Cox (349), Celler (56), Dexter et al. (86), and Dokos et al. (96). Here we provide a succinct, high-level overview; for a detailed evaluation of each model, see Appendix section 9.3.

The Purves equation has been used in a number of models including those by Pott and Pusch (275), Osterrieder et al.(265), and Demir et al. (81). The appeal of the Purves formulation is that it has a closed form:

$$C(x,t) = \frac{M}{8(\pi Dt)^{1.5}} e^{-k_h t - \frac{x^2}{4Dt}} \quad (1)$$

Where C is the concentration of the molecule at time t and radial distance x away from the source, M is the number of moles of ACh released at time 0, D is the diffusion coefficient, and k_h is the rate of

hydrolysis. The equation was obtained by solving diffusion equations under various assumptions in order to calculate the time course of neurotransmitter concentration following its release from a pipette some distance away from the cell of interest (276). This approach is mathematically rigorous and suitable for explaining in-vitro data, but is not well suited for the in-vivo system (see 2.5.2 for Discussion).

In our model, we use the compartmental approach similar to (56, 86, 96, 349). The advantages of this framework are 1) we can use actual measurements/anatomy to define the geometry of each compartment, 2) the reactions within each compartment are relatively simple 3) the rate constants for each reaction have been measured and are fairly well characterized, and 4) similar frameworks can be used for ACh and NE although they are cleared from the system in different ways. The main disadvantage is that the solution is not closed-form, but rather involves the numerical integration of a system of differential equations. This is not a major drawback however, since the SANC model is already implemented in this fashion.

2.3 Model Development

2.3.1 Geometry

The physical configuration of a SANC and the pertinent compartments for neurotransmitter diffusion are schematized in Figure 11. The dimensions of model components are based on the detailed study of guinea pig SAN anatomy by Choate et al. (65), modified to reflect rabbit data whenever available. The guinea pig SAN is about 6-8 cells thick and is bordered on either side by a 15-20 μm thick layer of connective tissue and epithelial cells (65). Light micrographs of rabbit and guinea pig SAN show that the former is about twice as thick (262). This difference is likely due to a larger cell diameter of rabbit SANCs rather than a greater number of cells: in their model of the rabbit SANC, Kurata et al. (198) used a cylindrical cell with a diameter of 8 μm and a length of 70 μm, whereas Choate et al. observed cells with 4-5 μm diameters and lengths up to 27 μm in the guinea pig (65). Given this apparent species difference, and that the present model is an extension of the Maltsev model (227), which in turn was built upon the Kurata model, we use the larger cell. The cell volume and surface area are calculated assuming that the cells are attached end-to-end, 8 cells thick, with 20 μm of extracellular matrix (ECM) on either side. The ECM is a compartment for diffusion of neurotransmitter released from a single cell, so the pertinent ECM volume is divided by the number of cells that influence that compartment (4 cells). A complete list of parameter values can be found in Table 22.

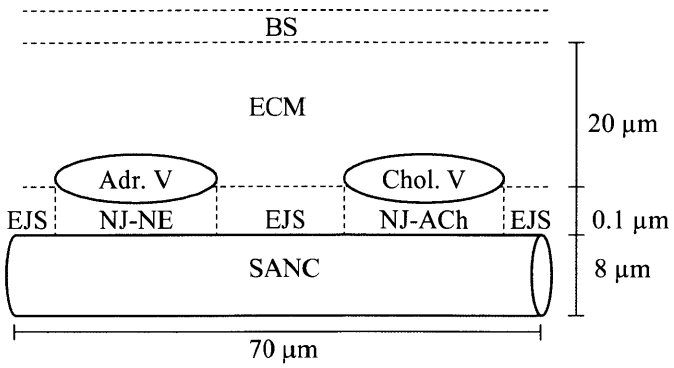

Figure 11 Neurotransmitter diffusion compartments: BS: blood stream, ECM: extracellular matrix, Adr. V: adrenergic varicosity, Chol. V: cholinergic varicosity, EJS: extrajunctional space, NJ-NE: adrenergic neuroeffector junction, NJ-ACh: cholinergic neuroeffector junction, SANC: sinoatrial node cell. Upon release from the adrenergic and cholinergic varicosities, neurotransmitter fills the neuroeffector junctions, diffuses into the EJS and ECM, and is cleared from the system once it reaches the blood stream.

Adrenergic and cholinergic varicosity dimensions and their location relative to SANCs were thoroughly characterized by Choate et al. (65) as summarized in Figure 12. We model varicosities as oblate spheroids (a reasonable representation, see Fig 2 in (65)) with major and minor axis dimensions shown in Figure 12 that reproduce the measured varicosity volume and surface area.

Choate et al. estimate that 0.2% of SANC membrane area is involved in close apposition with adrenergic and cholinergic varicosities. Using the measured average areas of close apposition per varicosity and the fraction of adrenergic and cholinergic varicosities that make close appositions (0.75 cholinergic, 0.25 adrenergic), we calculate that there are about 13.5 cholinergic and 4.5 adrenergic varicosities per SANC (non-integer numbers are acceptable, as some varicosities were noted to make contacts with 2 or even 3 cells (65)).

Cholinergic and adrenergic varicosities contain hundreds of spherical, membrane-bound vesicles filled with neurotransmitter (65). Upon depolarization of the varicosity by an excitatory spike traveling down the nerve fiber, Ca^{2+} influx at the varicosity causes one or more vesicles to fuse with the cell membrane and release their contents into the neuroeffector junction. Typically, each excitatory spike arriving at the varicosity causes the release of a fixed amount of neurotransmitter, a "quantum". For a review of autonomic signal transmission, see Burnstock 2009 (47).

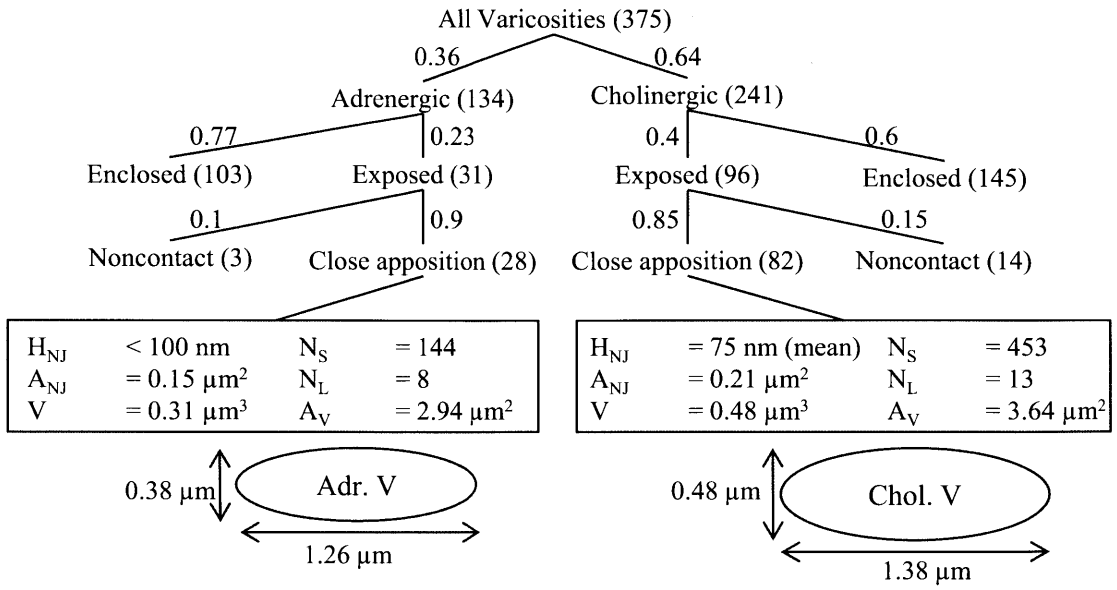

H_{NJ} – height of neuroeffector junction; A_{NJ} – area of close apposition in NJ; V – varicosity volume; N_S – number of small vesicles (40-50nm diameter); N_L – number of large vesicles (80nm diameter); A_V – varicosity surface area

Figure 12 Summary of adrenergic and cholinergic varicosities in guinea pig sinoatrial node, from (65). The major and minor axis diameters of the varicosities illustrated at the bottom were chosen in order to fit the measured surface area and varicosity volumes in a least squares sense: for an oblate spheroid with major axis radius a and minor axis radius b, the volume is $V_{OS}=4/3\pi a^2 b$ and the surface area is $A_{OS}=2\pi(a^2+b^2/\sin(ae)\log(1+\sin(ae)/\cos(ae))$, $ae=\arccos(b/a)$. The values of a and b were chosen to minimize the root sum squared error between calculated and measured volume and surface area using `fminsearch` in Matlab.

Following the information in Figure 12, and the observation that large vesicles are rarely found in the area of the varicosity closest to the neuroeffector junction and therefore do not participate in fusion with the varicosity membrane (65), we model the typical cholinergic and adrenergic varicosities as containing a maximum of 450 and 150 vesicles, respectively.

The neurotransmitter contents of a single vesicle define the size of a quantum. For cholinergic vesicles, the number of ACh molecules per vesicle has been measured in various tissues and varies with tissue type. Whittaker estimates an ACh concentration of at least 200 mM (356) in vesicles from mammalian brain, which equates to 4,020-7,800 molecules per small vesicle (dimensions as in Figure 12) and matches the 6,000 ACh molecules/vesicle mentioned in a recent review (355). In a model of cholinergic synapses of the chick ciliary ganglion a value of 5,000 ACh molecules per vesicle was assumed (68); the same value was also used in a previous model of the mammalian neuromuscular junction (15). On the other hand, values as low as 1,600 ACh molecules /vesicle in sympathetic ganglia (295) to 58,000-246,000 ACh/vesicle in the specialized electromotor synaptic vesicles in *Torpedo marmorata* (electric ray) (354, 355). Functionally, the size of a quantum is estimated to be from a few hundred (124) to 50,000 (97, 184,

232) ACh molecules. It has also been noted however, that a quantum interacts with an area of membrane that presents as many ACh receptors and AChE binding sites as there are ACh molecules (19, 232). In our model of the cholinergic neuroeffector junction, we estimate ~3500 binding sites (M2 receptors and AChE combined, details below), so a cholinergic quantum of 5,000 ACh molecules matches not only the measured size of ACh quanta and vesicle contents, but also satisfies this idea of ligand-receptor correspondence.

Quantal size has also been measured for adrenergic vesicles. In bovine adrenal medullary cells, the NE concentration in vesicles is measured to be 360 mM (273), which equates to about 7,200-14,000 molecules per small vesicle. This estimate is in line with measurements in the sympathetic adrenergic varicosities in rat vas deferens (15,000 NE/vesicle (78)). In sympathetic nerves of the rabbit pulmonary artery, a quantum is estimated to be about 2,000 molecules of NE (24). This value is smaller than the contents of a single vesicle, an inconsistency that the authors explain by proposing two hypotheses: either one vesicle is only released every 7 or 8 pulses (which would be the case if the number of vesicles is nearly depleted), or there is partial release from a vesicle (the explanation favored by the authors based on reports by Burnstock (48, 49)). We model an adrenergic quantum as 20,000 molecules of NE. This figure is in agreement with the measured vesicular contents cited above, as well as with the total NE content of rabbit SAN tissue: 2.04-3.58 μg/g wet tissue (8, 320), which converts to $25\text{-}45\times10^6$ NE molecules per SANC using cell dimensions in our model (see Appendix section 9.2 for unit conversions). At 20,000 molecules /vesicle, and using the total number of vesicles per varicosity, and total number of adrenergic varicosities per SANC in our model, we obtain a similar value of 65×10^6 NE molecules. This quantal size also allows us to reproduce the observation that sympathetic nerve stimulation at 10 Hz produces a maximal adrenergic effect and 10% liganded β-ARs (162).

Neurotransmitter is released into the neuroeffector junction, the compartment between a varicosity and the cell membrane (see Figure 11). In our model, the volume of this compartment is determined by the neuroeffector junction height (distance from the varicosity to the SANC membrane). All varicosities that make close contacts have a neuroeffector junction height of less than 100 nm, with cholinergic varicosities tending to be closer (average height of 75 nm) than adrenergic (minimum height 90 nm) (65). To capture the phenomenon of pacemaker shift (153, 261, 328, 352) wherein the leading pacemaker site changes position based on sympathetic and parasympathetic drive, we choose to model a cell with the weakest cholinergic innervation and the strongest adrenergic innervation. This idea is motivated by the fact that the SA node contains a heterogeneous population of cells, and the cell which depolarizes the fastest is the one that initiates the heart beat (153, 368). Thus, we model the cholinergic neuroeffector

junction height as 100 nm (the largest height that still provided close apposition), and the adrenergic as 90 nm (an estimate of the smallest height). However, as Toda and Shimamoto observed (328), pacemaker shift was more prominent in response to bath application of NE rather than sympathetic nerve stimulation, therefore in the physiological system, this phenomenon may not be significant. The neuroeffector junction height allows us to compute the adrenergic and cholinergic neuroeffector junction volumes by numerically integrating the space between the oblate spheroid varicosity and the cylindrical SANC, values shown in Table 22.

Neurotransmitter quickly diffuses to fill the entire area beneath a varicosity, and more slowly expands into the surrounding space (see section 2.3.2). For this reason, we consider the neuroeffector junction to have a footprint equal to the entire area beneath a varicosity rather than the measured area of close contact. Thus, although the contact area accounts for only 0.2% of total cell surface area (65), the combined neuroeffector junction area is about 1.5% of total cell surface area. Following the nomenclature of Dokos et al. (96) in their formulation of ACh release, we refer to the space outside the neuroeffector junction as the extrajunctional space (EJS). The EJS occupies 98.5% of the cell surface area and has a height of 100 nm based on microscope images of the guinea pig sinoatrial node (65), which we assume is similar in rabbit.

To simplify the model, we consider an aggregate cholinergic and adrenergic varicosity and neuroeffector junction. Thus, rather than having 13.5 individual cholinergic varicosities, we model only one, where the total number of vesicles is 13.5×450=6075, and the neuroeffector junction volume is similarly multiplied by the number of varicosities to yield the total cholinergic neuroeffector junction volume. When simulating vesicle release, we require an integer number of vesicles to be released from each varicosity, thus release is always a multiple of 13.5. Adrenergic varicosities are treated similarly, containing 4.5×150=675 vesicles and releasing multiples of 4.5 vesicles with each stimulus.

2.3.2 Neurotransmitter release and diffusion

We model neurotransmitter release using the same release rate constant $k_r = 0.01$ used in the Dokos model (96). This constant implies that 1% of the vesicles release their neurotransmitter contents into the neuroeffector junction in response to each stimulus. The quantal nature of this process is captured in implementation by not allowing fractions of a vesicle to be released at a time. The functional implication is that vesicle depletion causes the sporadic release of full quanta, rather than a smoother "analog" decrease in released neurotransmitter.

Upon vesicle fusion with the varicosity membrane, neurotransmitter diffuses throughout the neuroeffector junction, EJS, ECM, and is eventually cleared by the bloodstream. For computational simplicity and compatibility with the Maltsev SANC model, we model diffusion between compartments using rate constants to describe the transport between each pair of adjacent compartments (as was done by Dokos et al. (96)). These rate constants were obtained through molecular Monte-Carlo simulations using measured diffusivities of ACh and NE and the 3-dimensional geometry of each compartment. The diffusivity of ACh and NE measured in a variety of media are summarized in Table 1. The diffusion coefficient of ACh in solution is similar to that in the synaptic cleft, and is on the range 5.38-7.75 $\times 10^{-6}$ cm^2/s (93, 99, 201, 290). The diffusion coefficient for NE in solution was measured as 7.0 $\times 10^{-6}$ cm^2/s (118). Since ACh and NE are of similar molecular weight and both are positively charged (283, 301), we conclude that the diffusivity of ACh and NE in the neuroeffector junction and EJS is 7 $\times 10^{-6}$ cm^2/s.

Table 1 Measured diffusion coefficients for ACh and NE.

Source	Molecule [g/mol]	Medium	Temperature (°C)	*D* measured ($\times 10^{-6}$ cm^2/s)	*D* at 37°C ($\times 10^{-6}$ cm^2/s)
Sattarahmady et al. 2010 (290)	ACh [146]	Solution	22	4.74	6.38
Land 1984 (201)		Lizard NJ	22	4	5.38
Dionne 1976 (93)		Solution	25	6.11	7.75
Krnjević and Mitchell 1960 (196)		Rat diaphragm Agar gel	20 20	1.4 9.8	2.0 13.7
Eccles and Jaeger 1958 (99)		Synaptic cleft	37	7.6	7.6
Rice et al. 1985 (283)	NE [169]	Rat brain	37	0.77	0.77
Gerhardt and Adams 1982 (118)		Solution	25	5.5	7.0
Bevan and Torok 1970 (25)		Rabbit aorta media	37	0.729	0.729

Krnjević and Mitchell noted a Q_{10} of about 1.2 (2% per degree); this value was used to correct measured values to 37°C (196). See section 9.1 for a note on temperature corrections.

The diffusion of ACh through connective tissue is about 7 times less than in gel (196). Similarly, the diffusion of NE through connective tissue is about 9 times less than in solution (25, 283). This large difference is postulated to be due to electrostatic interactions between these positively charged molecules and areas of negative charge in the extracellular matrix (ECM) (25, 283). Thus, we estimate the diffusion coefficient of ACh and NE through ECM to be 0.8×10^{-6} cm^2/s.

To determine the appropriate rate constants for the diffusive transport between compartments, we used the numerical approach detailed below. We considered the three intersections: neuroeffector junction to EJS, EJS to ECM, and ECM to BS (refer to Figure 11 for illustration). We looked to molecular Monte-Carlo simulations because of the ease with which they can be implemented, and the unlimited flexibility they provide with regard to specifying the problem geometry. Before launching into the details, we provide a brief summary: owing to the proximity of the varicosity and the cell, diffusion through the neuroeffector junction is rapid. Our simulations indicate that all of the released molecules make contact with the cell membrane within 50 μs of release, a result in line with a more detailed finite element simulation of ACh diffusion in the neuromuscular junction showing that the time to peak postsynaptic detection is on the order of tens of μs (313). Since the fastest processes within the SANC occur on the timescale of milliseconds, we assume that diffusion within the neuroeffector junction is instantaneous for both ACh and NE. The diffusion rate constant between the neuroeffector junction and EJS compartments is rapid with a rate on the order of 10,000 /s, whereas the diffusion rate constant from the EJS to the ECM is slower at 20 /s, and clearance from the ECM slower still at 0.4/s due to the thickness of and lower diffusivity within the ECM.

▪ Diffusion out of the neuroeffector junction:

Assuming the concentration of neurotransmitter within the neuroeffector junction is homogeneous, we ran three sets of simulations to compute the best diffusion rate out of the neuroeffector junction:

1) Idealized 2D system – to verify molecular Monte-Carlo simulation versus analytic 2D solution
2) Idealized 3D system – to verify correspondence of simulation and numerical approximation
3) Actual 3D system – to obtain the best approximate solution given actual model geometry

Each simulation was run with two sets of initial conditions: a) point source in the space immediately below the varicosity, centered on the varicosity in the xy plane, and b) uniform distribution of particles across the underside of the varicosity. These two conditions were used to obtain the slowest (a) and "average" (b) diffusion out of the varicosity since vesicles can in theory be released at any point on the underside of the varicosity. These geometries and initial conditions are shown in Figure 13.

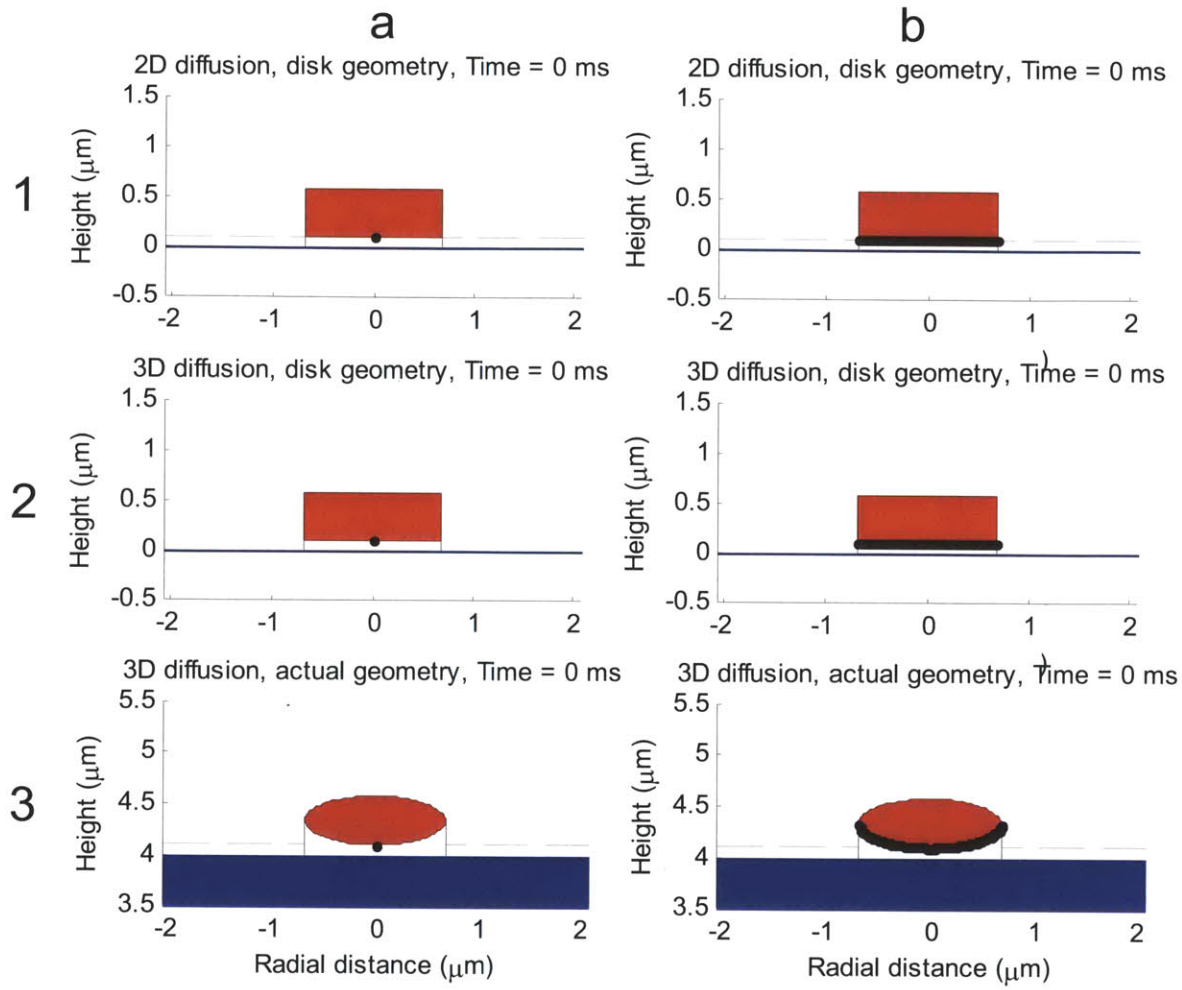

Figure 13 Illustration of three diffusion models and two initial conditions. Left column: point source initial condition, where a quantum (5000) of molecules are located at x=0, y=0, and immediately below the bottom edge of the varicosity. Right column: uniformly distributed initial condition, where a quantum of particles is uniformly distributed over the bottom of the varicosity. Model 1: the cell is a plane at 0 elevation (solid line in figures) and diffusion is restricted to the plane of the neuroeffector junction (shown with horizontal dashed line). The varicosity is a cylinder whose cross-section is shown. Model 2: geometry identical to model 1, but diffusion in the z direction is not restricted for z>0. Models 1 and 2 use a single diffusion constant (appropriate for the neuroeffector junction) for all regions of space. Model 3: cell is a cylinder with center at z=0 and radius 4 μm. The varicosity is an oblate spheroid with dimensions appropriate for the type of varicosity (see Figure 12). Diffusion is allowed in all dimensions but diffusing molecules cannot enter the space occupied by the cell or the varicosity. Diffusion constants for the neuroeffector junction, EJS, and ECM regions were used as appropriate.

Simulations were run for 1 ms, and the concentration of molecules within the neuroeffector junction was tracked on this interval. Physical contact of molecules with the cell surface in the neuroeffector junction was also tracked in order to assess how quickly molecules diffused from the varicosity to the cell membrane (Figure 14). For an illustration of the various systems at 50 μs, see Figure 15.

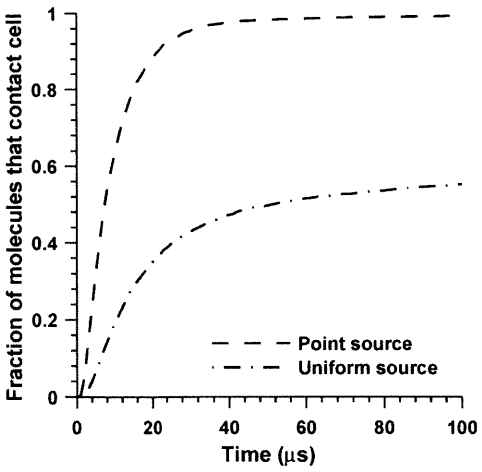

Figure 14 Diffusion of molecules from the varicosity to the cell membrane is very rapid. The cumulative fraction of molecules that make at least one contact with the cell surface in the NJ is plotted as a function of time (3D diffusion, actual geometry). Top line: point source initial condition, bottom line: uniform initial condition. In the first case, all of the molecules contact the cell membrane before escaping the neuroeffector junction; in the second case, about 50% of the molecules contact the cell membrane while the remainder escapes into the EJS without contacting the cell.

The average concentration in the cholinergic neuroeffector junction as a function of time is shown in Figure 16 (adrenergic neuroeffector junction simulations look similar and are omitted for succinctness). The first panel contains the results of the 2D system, where the analytic concentration gradient for M moles of matter with diffusion coefficient D deposited at the origin and allowed to diffuse radially (r is the radial distance from the origin) within a plane of height h is given by:

$$C(r,t) = \frac{M}{h4\pi tD} e^{-\frac{r^2}{4Dt}}$$

If the neuroeffector junction is modeled as a disk with radius R, we obtain the average concentration by integrating this profile:

$$\begin{aligned} \bar{C}(t) &= \frac{1}{\pi R^2 h} \int_0^R \frac{M}{h4\pi tD} e^{-\frac{r^2}{4Dt}} 2\pi rh\, dr \\ &= \frac{M}{\pi R^2 h}\left(1 - e^{-\frac{R^2}{4Dt}}\right) \end{aligned} \tag{2}$$

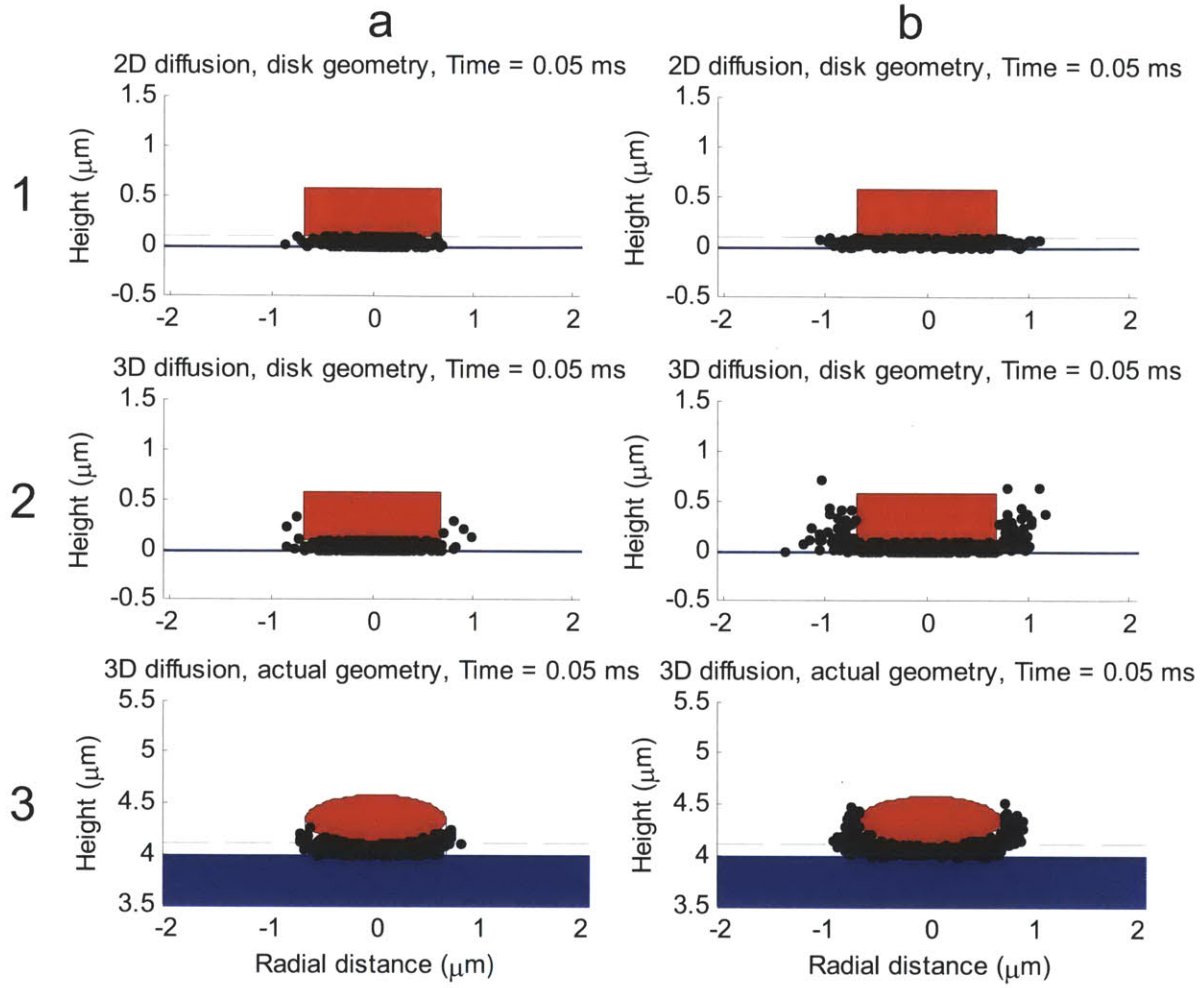

Figure 15 Simulations at 50 μs showing that molecules diffuse across the neuroeffector junction space very quickly, and illustrating the diffusive behavior of the three models. Same figure layout as Figure 13.

The analytic solution shown in Figure 16 is Equation (2) evaluated for M=5000/6×10^{23} mol, R=0.69 μm, h=0.1 μm, and D=7x10^{-6} cm^2/s, with units appropriately converted to give final concentration in mM. Note that the analytic solution is almost perfectly replicated by the 2D Monte-Carlo simulation, validating the implementation. The implementation is identical in all three simulations; the only aspect that differs is the particular geometry, as explained above. Each panel contains three curves: simulation results with the point and uniform initial condition, and an approximate solution.

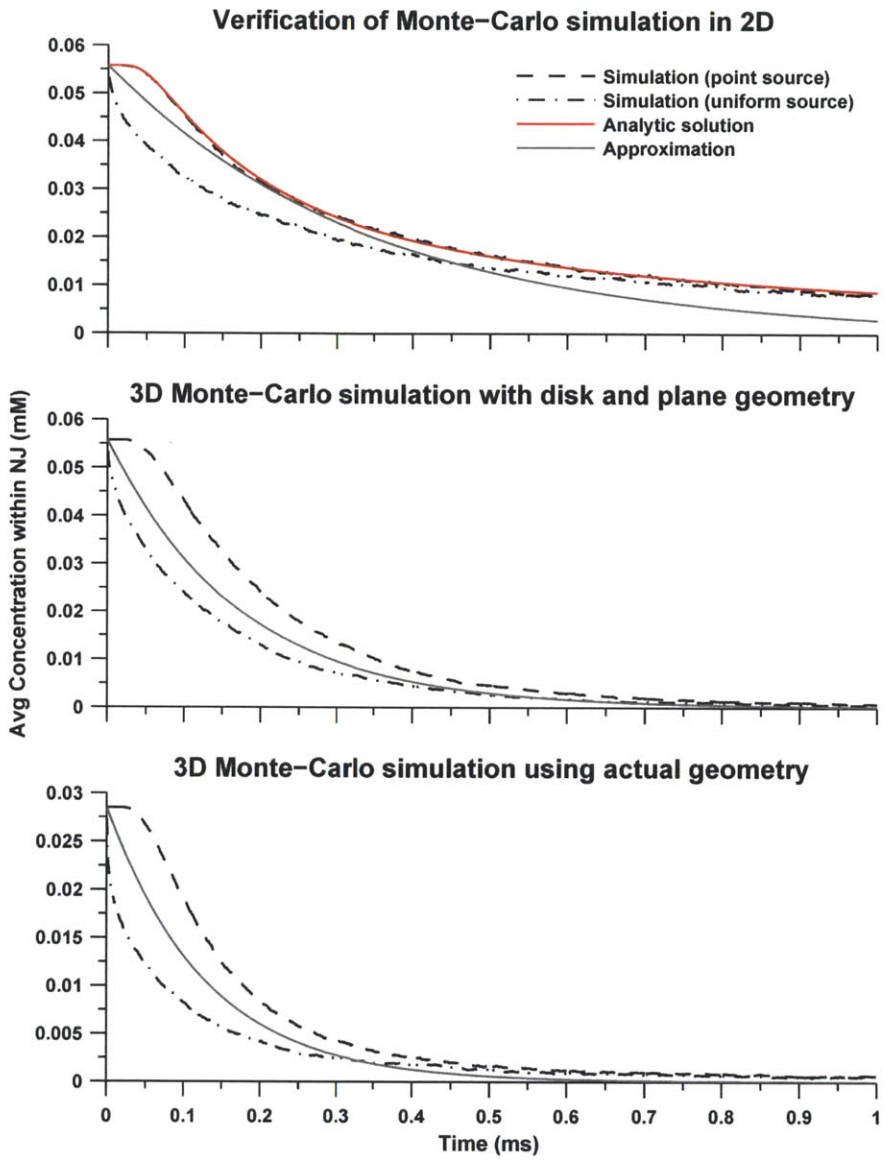

Figure 16 Concentration in neuroeffector junction as a function of time for the six Monte-Carlo simulations as well as an explicit analytic solution in two dimensions and numerical approximations for all three models. Dimensions of the cholinergic varicosity are used in these figures. Legend in top plot refers to all three plots.

The approximate solution for each scenario was obtained as follows. The concentration within the neuroeffector junction is assumed to be homogeneous and the spatial gradient is assumed to be established instantaneously. In two dimensions, the steady state concentration gradient surrounding a disk of radius R with concentration C falls as $1/r$; scaling this relationship in order to obtain a concentration of C at distance R yields the equation $C(r)=CR/r$. Given this concentration profile, we can calculate the flux J through the sides of the disk (flux leaving the neuroeffector junction is positive):

$$J = -D\frac{dC}{dr}\bigg|_{r=R} = \frac{D}{R}C$$

Since J has units of mol/time/area, we multiply by the surface area through which the diffusion happens (for this idealized geometry the neuroeffector junction is a cylinder with open surface area $2\pi Rh$) and divide by the volume of the neuroeffector junction ($\pi R^2 h$) to obtain the rate of change in mol/time (negative sign appears again because flux leaving the neuroeffector junction is positive):

$$\frac{dC}{dt} = -J\frac{A}{V} = -\frac{D}{R}C\frac{2\pi Rh}{\pi R^2 h} = -\frac{2D}{R^2}C$$

Using the values of R=0.69 μm and D=7x10^{-6} cm^2/s, and correcting units appropriately, we obtain the rate constant r=2,940/s, implying that the concentration in the neuroeffector junction as a function of time can be approximated as $C(t)=C_0e^{-rt}$. This approximation is plotted in the top panel of Figure 16. In three dimensions (still using idealized geometry), the spatial gradient outside the disk is $C(r)=CR^2/r^2$, which gives

$$\frac{dC}{dt} = -\frac{4D}{R^2}C$$

and yields the approximate rate constant of r=5,880/s, which is plotted in the middle panel of Figure 16. Finally, using the actual geometry and numerically integrated values for the surface area through which the flux flows (the actual area was scaled by a factor of 0.7 to calculate an "effective diffusive area") and for the volume of the neuroeffector junction, we obtain estimated rate constants of $k_{dNJ,NE}$=8,800/s for the adrenergic neuroeffector junction and $k_{dNJ,ACh}$=7,800/s for the cholinergic varicosities (the cholinergic rate is plotted in the third panel of Figure 16).

To test model sensitivity to the neuroeffector junction diffusion rate, we ran the neurotransmitter release simulation with rates that are 50% faster and 50% slower (these simulations use our full neurotransmitter release model with receptor binding and various clearance mechanisms detailed below). The results are shown in Figure 17. The M2 muscarinic receptor occupancy was virtually unaffected by the change. The slower neuroeffector junction diffusion rate seemed to favor more β-adrenergic receptor activation, however adjusting the reuptake rate to reproduce the desired NE clearance fractions (86% reuptaken, 9% diffused, 5% absorbed, see section 2.3.6) made the receptor occupancy unaffected by neuroeffector junction diffusion rate. For the model, we use the baseline diffusive transport rate constants of $k_{dNJ,NE}$=8,800/s for the adrenergic and $k_{dNJ,ACh}$=7,800/s for the cholinergic varicosities.

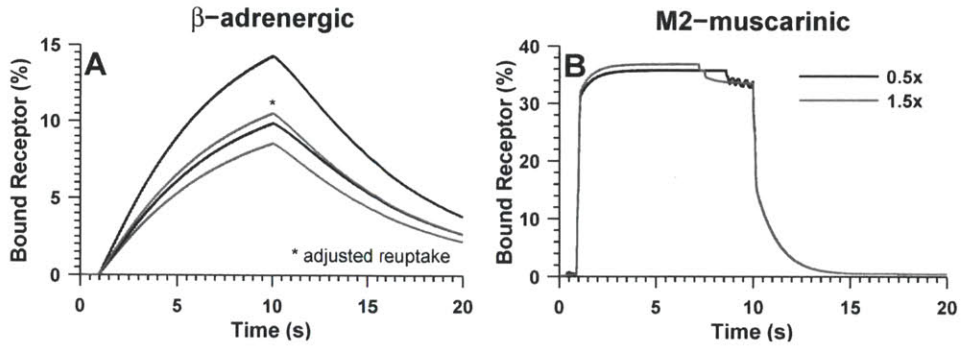

Figure 17. Model sensitivity to neuroeffector junction diffusion rate constants. A. β-adrenergic receptor occupancy is plotted as a function of time for 10 Hz sympathetic stimulation from 1 to 10 seconds. Black and gray lines were obtained using slow and fast $k_{dNJ,NE}$ as indicated in legend in B. *: maximum reuptake rate constant (v_{maxn}×9 for slow and v_{maxn}/1.9 for fast $k_{dNJ,NE}$) was adjusted to maintain ~86% NE reuptake despite change in $k_{dNJ,NE}$. B. M2 muscarinic receptor occupancy as a function of time for 10 Hz vagal stimulation at two scalings of baseline $k_{dNE,ACh}$ as indicated in legend. Due to fast M2 muscarinic receptor kinetics, receptor occupancy fluctuates between 10-90% for each neurotransmitter release; for clarity, we show a smoothed version using a centered 0.2s-wide rectangular window.

▪ Diffusion out of EJS and ECM:

The EJS is a 100 nm thick shell surrounding the SANC. We assume that diffusion within this shell happens very quickly so that the entire EJS can be considered as a single compartment with no local concentration gradients. This assumption is reasonable given the fast diffusion rate constants between the neuroeffector junction and extrajunctional space (above), and the assumption that a number of varicosities are uniformly distributed over the sinoatrial node cell membrane. We do however test this assumption (that neurotransmitter instantly diffuses throughout the extrajunctional space) to see the effect on the diffusive rate constant between the extrajunctional space and ECM.

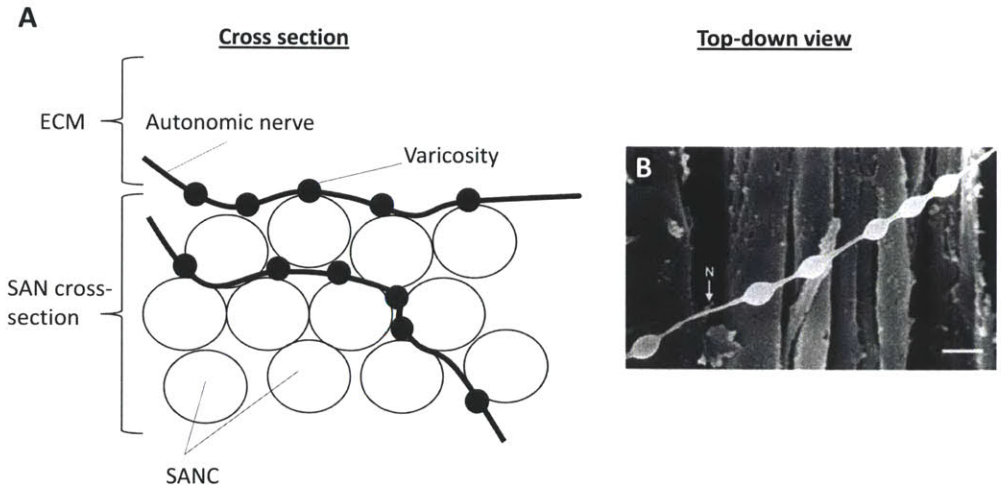

Figure 18. Innervation of sinoatrial node. A. Cross section showing two autonomic nerves running through the tissue. ECM: extracellular matrix, SAN: sinoatrial node. B. Figure from (46) showing an autonomic nerve (white) running along the surface of smooth muscle in rat intestine (darker vertical cells).

To estimate the rates of concentration change for the EJS and ECM, we constructed a molecular Monte-Carlo simulation of a cross section of cell, EJS and ECM as shown in Figure 19. We ran simulations with two initial conditions:

Initial condition 1: Molecules distributed evenly across the whole EJS: using the assumption of rapid diffusion throughout the EJS and uniform coverage by autonomic varicosities. Such uniform coverage is expected if autonomic nerves run through the sinoatrial node tissue as shown in Figure 18A.

Initial condition 2: Molecules distributed evenly through only the top half of the EJS: relaxed assumption of rapid diffusion throughout the EJS and assuming instead that the autonomic varicosities primarily run along the epicardial side of the sinoatrial node (as in Figure 18B) and the released neurotransmitter stays more localized to the site of release.

Only the top half of the EJS can directly communicate with the ECM. The top surface of the ECM is in contact with the bloodstream, and this boundary was modeled as an absorber under the assumption that the bloodstream irreversibly washes away the neurotransmitter. As shown in Figure 20, the number of molecules within the EJS initially decays very rapidly (rate constant >1000/s, virtually instant), followed by a slower rate constant which is 30/s for initial condition 1 and ~20/s for initial condition 2. The rate constant of decay of the concentration from the ECM is the same regardless of initial condition, and is 0.3-0.4/s, as shown in Figure 20. This rate constant is also supported by an analytic approximation (similar to what was done for the neuroeffector junction), wherein we assume that the spatial concentration gradient within the ECM rapidly reaches steady state. Since the neurotransmitter originates at the SANC and exits into the bloodstream, these two sides of the ECM can be thought of as having a fixed concentration thereby giving a linear concentration within the ECM at steady state (a linear profile was indeed seen in the Monte-Carlo simulation). A mean ECM concentration of C implies that the flux out of the ECM (x is the distance away from the cell, through the ECM) is

$$J = -D\left.\frac{dC}{dx}\right|_{x=h_{ECM}} = \frac{2D}{h_{ECM}}C$$

where h_{ECM} is the height of the ECM. As above, we multiply by the diffusive area and divide by the volume of the ECM to obtain the rate of change of concentration in the ECM:

$$\frac{dC}{dt} = -J\frac{A}{V} = -\frac{2D}{h_{ECM}}C\frac{A}{Ah_{ECM}} = -\frac{2D}{h_{ECM}^2}C$$

which evaluates to a rate constant of 0.4/s using D=0.8×10^{-6} cm^2/s, h_{ECM}=20 μm. This value is close to that observed in the Monte-Carlo simulations (see Figure 20), so it is the value we adopt for the model.

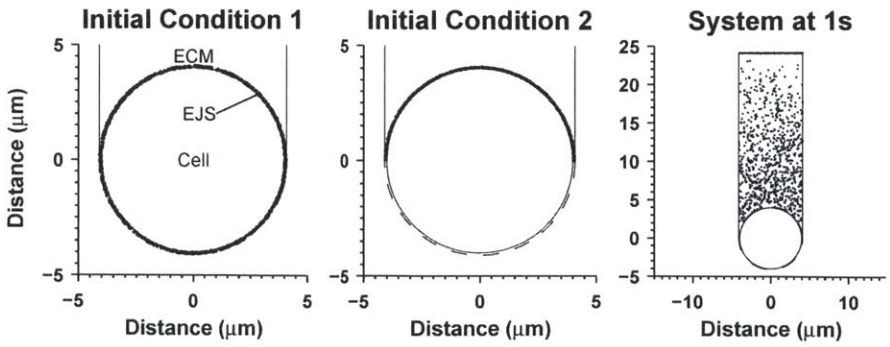

Figure 19 Illustration of physical setup for molecular Monte-Carlo simulation of diffusion out of the EJS. Initial condition 1: Cell: sinoatrial node cell cross section with radius 4 μm. EJS: extrajunctional space, ECM: extracellular matrix immediately above cell. Initial condition 2: Molecules are initially distributed only in the top half of the EJS. System at 1s: sample molecule distribution at 1s for initial condition 1; 2 was similar. The molecules stuck at the top have been captured by the bloodstream.

Given the large difference between the fast and slow time constants for the EJS, we ran the neurotransmitter release model with two rate constants: 20/s and 1000/s. As shown in Figure 21, although the rate constants differ by 2 orders of magnitude, the amount of bound receptor is not affected to that degree (neurotransmitter concentrations in both compartments followed similar trends, not shown), implying that the model is fairly insensitive to this parameter. Because adrenergic and cholinergic varicosities may be located at any depth in the tissue (Figure 18A, and ref (65), although the majority are on the epicardial side (262)), we adopt the slower time constant k_{dEJS}=20/s.

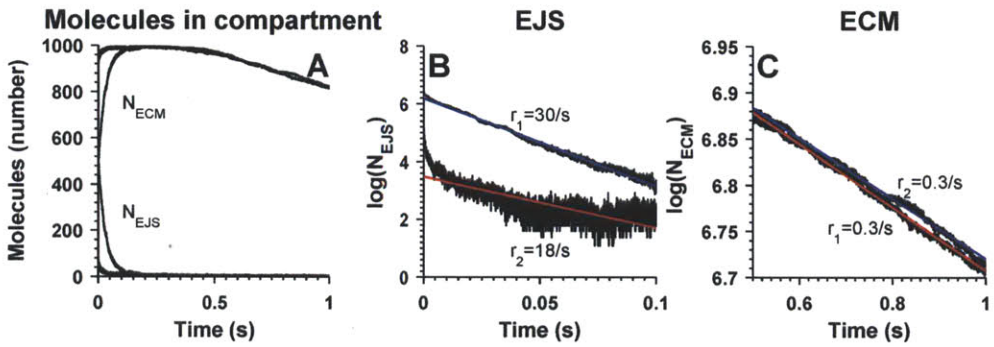

Figure 20 Time course of Monte-Carlo simulation in extrajunctional space and extracellular matrix. A. N_{ECM}: number of molecules in the extracellular matrix with time, N_{EJS}: number of molecules in the extrajunctional space with time. Slower lines are from initial condition 1 and the faster lines are from initial condition 2. B. Black lines: number of molecules in the extrajunctional space is plotted on a logarithmic y-axis for the first 0.1 seconds of the simulation in A. Colored lines: linear fits to logarithmic data, slopes as indicated on the figure (r_1: initial condition 1, r_2: initial condition 2). C. Black lines: number of molecules in the extracellular matrix for last 0.5 seconds of simulation, logarithmic y axis. Colored lines: linear fits to the data, slopes as indicated. Both initial conditions yielded the same decay rate.

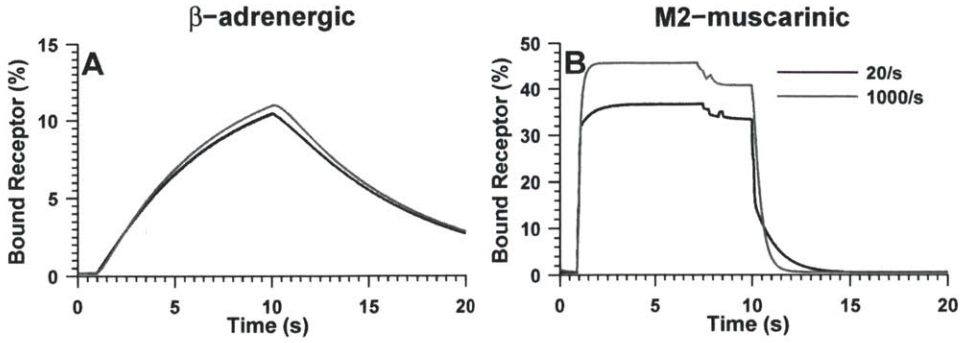

Figure 21. Slow (20/s) versus fast (1000/s) rate constants for EJS-ECM diffusion produce a small difference in receptor binding NE or ACh. A. β-adrenergic receptor occupancy as a function of time for 10 Hz sympathetic stimulation between 1 and 10 s. Black and gray lines are for k_{dEJS} values as indicated in the legend in B. B. M2 muscarinic receptor occupancy for 10 Hz vagal stimulation between 1 and 10 s. Due to fast M2 muscarinic receptor kinetics, receptor occupancy fluctuates between 10-90% for each neurotransmitter release; for visual clarity, we show a smoothed version using a centered 0.2s-wide rectangular window. The orders of magnitude difference in diffusion out of the EJS produces <5% difference in β-adrenergic receptor occupancy and ~25% difference in M2 muscarinic receptor occupancy. The slow diffusion rate constant favors lower β-AR and M2 muscarinic occupancy (by allowing more time for the membrane-localized clearance mechanisms of NE reuptake/absorption and ACh hydrolysis by AChE).

Our model includes a blood stream (BS) compartment into which the NTs ACh and NE eventually diffuse. The BS also contains a baseline concentration of these NTs which diffuses into the system and may affect HR (thus, we have the capability to model changes in HR due to intravenously applied neurotransmitter; this feature was not used in the present study, where the focus was on in-vivo activity).

ACh in plasma has been measured to range from 0.2 nM (goat) to 15 nM (swine), with 3.1 nM being the concentration in human (117, 185). For our rabbit model, we assume the intermediate value of $[ACh]_{BS}$ = 3 nM, and that this value is constant.

The plasma concentration of NE is subject to more variability, since plasma concentration is determined by "spillover" from sympathetic nerves and sympathetic stimulation of the adrenal glands (see section 2.3.6). Thus, for high sympathetic tone, the NE content in the blood stream may be significantly higher than baseline. For example, for humans in the supine position, plasma NE has been measured on the range 1.3-1.6 nM (21, 79, 83, 107, 109). In the standing position (higher sympathetic tone), this concentration roughly doubles to 2.8-3.1 nM (21, 83), and higher levels of activity such as exercise may significantly increase the plasma NE concentration. The plasma NE concentration has also been measured in rabbits, at around 2.6-2.9 nM (133). For our model, we follow the example of Warner and Cox 1962 and assume that the concentration in blood is constant (349). We assume a value near that measured for rabbits at baseline, $[NE]_{BS}$ = 3 nM.

2.3.3 M2 muscarinic receptor binding/activation by ACh

The M2 muscarinic receptor is the major ACh receptor in mammalian hearts (137, 156, 157). Measurements of M2 muscarinic receptor density in cardiac tissue are summarized in Table 2. Unfortunately, we were unable to find data for rabbits, and the human vs. canine data imply inter-species or tissue-specific variability. It is interesting to note that the high receptor density in dogs may explain the pronounced respiratory sinus arrhythmia (RSA) seen in these mammals (182), since RSA comes about from an inhibition of parasympathetic outflow during inspiration (183) and the M2 muscarinic receptor density effectively sets the gain of the system in transducing parasympathetic variation to changes in HR. During inspiration, HR in dogs increases by about 58% relative to the HR during exhalation (estimated from data in (182)), whereas in humans this increase is around 12-25% depending on respiration rate (100). For comparison, rats experience RSA of about 6% (30). We were unable to find any RSA measurements on rabbits, so we assume moderate RSA on the order of humans and rats, and therefore conclude that the average M2 muscarinic receptor density in rabbit atrium is about 8 receptors/μm^2. In terms of variability across tissue type, the M2 muscarinic receptor density of the SA node has been measured to be ~5 times that of the atrium (17), so we set the average M2 muscarinic receptor density in rabbit SA node to 40 receptors/μm^2. We convert this average receptor density to neuroeffector junction- and EJS-specific densities that give a 45 times greater density in the neuroeffector junction. The large difference is thought to exist because local receptor concentration is proportional to local neurotransmitter concentration. This hypothesis is supported by data in the neuromuscular junction and autonomic neuroeffector junction showing that receptor density is highest near the site of neurotransmitter release (232), that receptor clusters migrate over time to follow the displacement of autonomic varicosities (47), and that muscarinic M2 receptor density matches the density of innervation (16, 19, 135). As an estimate of local concentration differences, we compare the volumes of the neuroeffector junction versus the EJS to obtain the value of 45-fold greater receptor density in the cholinergic neuroeffector junction than the EJS (in the frog neuromuscular junction, this ratio is 500 (232)). The result of this scaling is that roughly 34% of the M2 receptors are confined to the neuroeffector junction despite the small fraction of SANC surface area dedicated to the neuroeffector junction. This figure is supported by measurements of acetylcholinesterase (AChE), which is also present in the cell membrane and aggregates in the neuroeffector junction such that 45% of total AChE activity occurs there (134, 286). Due to the fast diffusion within the neuroeffector junction and EJS, the concentration of M2 receptors in these compartments is computed using the volume of each compartment (rather than confining them to the 2-dimensional membrane) to arrive at the total receptor concentrations in Table 22.

Table 2 Measured M2 Muscarinic and β-adrenergic receptor density in various mammals.

Source	Receptor	Anatomy	Measured Density (fmol/mg protein)	Calculated density (receptors/μm^2)
Dunlap et al. 2003 (98)	M2	Canine SAN	250	17.5
	M2	Canine RAA	300	21.0
Brodde et al. 1998 (43)	M2	Human RA <20 YO	130	9.1
	M2	Human RA 20-50 YO	110	7.7
Giessler et al. 1999 (119)	M2	Human RA	115	8.1
	β-Adr	Human RA	70	4.9
Bristow et al. 1992 (42)	β-Adr	Human LV	87.7	6.1
	β-Adr	Human RV	102.1	7.1
Muntz et al. 1988 (248)	β-Adr	Rat V	--	25
Bristow et al. 1986 (40)	β-Adr	Human LV	88	6.2
Fowler et al. 1986 (115)	β-Adr	Failing Human RV	--	1.9[†]
Karliner et al. 1985 (174)	β-Adr	Rat V[*], no serum	--	2.48
		Rat V[*], in serum	--	6.96
Bristow et al. 1984 (39)	β-Adr	Human LV	62.1	4.3
McKean 1988 (234)	β-Adr	Guinea pig RV	154.6	10.8
	β-Adr	Muskrat RV	99.8	7.0
Zola et al. 1988 (373)	β-Adr	Rabbit LV	119	8.3

See section 9.2 for details on unit conversion. [*] rat ventricle cells cultured in serum-free or serum containing solution. [†] 1732 fmol receptor/gram wet weight, converted using 1 g/mL, see section 9.2 for source of this value.

Detailed data on M2 receptor kinetics could not be found, so the binding and dissociation rates are formulated based on the average dwell time of ACh in a receptor and estimates of affinity and Hill coefficient. Katz and Miledi estimate the average dwell time as ~1 ms at 23 °C (184), which yields a dissociation rate constant of $k_{off,M}$ of 2,100 /s (temperature corrected to 37 °C). Following the example of Demir et al. (81), we deduce the Michaelis-Menten coefficient K_{MM} from the dose-response relationship curve for ACh-activated potassium current ($I_{K,ACh}$) measured by DiFrancesco et al. (88) and Inomata et al. (160). $I_{K,ACh}$ can be used as a surrogate for ACh-receptor binding because this current is stimulated directly by the G-protein βγ subunit which in turn is activated by the M2 muscarinic receptor (358). The Hill coefficient n_M was set to 0.7 to reflect the existence of high and low affinity receptors. A Hill

coefficient less than unity was also needed in order to replicate the wide dynamic range of ACh modulation (see Chapter 6). These parameters set the binding rate to:

$$k_{on,M} = \left(\frac{[ACh]}{K_{MM}} \right)^{n_M} k_{off,M}$$

We use the actual binding and dissociation rate coefficients rather than steady-state occupancy functions because the amount of ACh released into the neuroeffector junction is on the same order as the number of M2 receptors. This means that binding causes significant neurotransmitter depletion in the physiological system, so the usual assumption of constant ligand concentration used to arrive at steady-state occupancies is invalid.

2.3.4 ACh hydrolysis by acetylcholinesterase

Acetylcholinesterase (EC 3.1.1.7) is a membrane-bound enzyme that rapidly breaks down ACh. This reaction involves three steps, binding, hydrolysis and unbinding (286):

$$E + ACh \underset{k_{-1}}{\overset{k_1}{\rightleftharpoons}} E \bullet ACh \xrightarrow{k_2} E \bullet Ch \xrightarrow{k_3} E + Ch$$

where E is the enzyme (AChE), and Ch is choline. Under the common enzyme kinetics assumption of rapid equilibrium, we can encapsulate the intermediate states and model the rate of hydrolysis as

$$E + ACh \xrightarrow{r_H(ACh,E)} E + Ch$$

where the rate of hydrolysis $r_H(ACh,E)$ is a function of ACh concentration and AChE density expressed in standard Michaelis-Menten form:

$$\begin{aligned} r_H(ACh,E) &= k_{cat,AChE} E \frac{[ACh]}{[ACh] + K_{app,AChE}} \\ &= v_{\max,AChE} \frac{[ACh]}{[ACh] + K_{app,AChE}} \end{aligned}$$

Where $k_{cat,AChE}$ is the turnover number (ACh molecules hydrolyzed per second per active site) $K_{app,AChE}$ is the apparent Michaelis-Menten constant, E is the number of AChE active sites, and v_{max} is the maximal hydrolysis rate (ACh molecules hydrolyzed per second).

$K_{app,AChE}$ has been measured in human erythrocytes and electric eel (106, 287, 312, 361). For human erythrocyte, the range is 45-200 μM (106, 169, 312) and 100 μM for electric eel (287, 361); we use the intermediate value of $K_{app,AChE}$=100 μM.

$k_{cat,AChE}$ has also been measured in human erythrocyte and electric eel. At 25 °C electric eel AChE has a turnover number of 12,300-16,000/s (287, 361), and human erythrocyte AChE is about half as fast at 6,700/s (125). For our estimate of rabbit AChE, we choose a value close to that reported for human erythrocytes since both are mammals and the electric organ of the electric eel is highly specialized and may contain an equally specialized AChE. Furthermore, a k_{cat} of 7000/s at 25 °C was used in a model by Szegletes et al. (312). After temperature correction to 37 °C, $k_{cat,AChE}$ = 13,000/s.

AChE is plentiful in SAN and its activity is often used to identify the pacemaker anatomically (175). Since AChE density overlaps the density of M2 muscarinic receptors (135), we again make the argument that AChE density varies with local ACh concentration, in other words, that it is proportional to M2 muscarinic receptor density. Using a proportionality factor of unity gives an AChE density of ~1200 AChE sites/μm^2 in the neuroeffector junction, which is close to that measured in the frog neuromuscular junction (2000-2600 sites/μm^2, (232)). The AChE density in the EJS is smaller, at 27 /μm^2. To check the absolute value of these figures, we convert the AChE density to catalytic units per mg protein (0.46 U/mg, for conversions see section 9.2). This value agrees well with the total AChE rate measured in the rat diaphragm at 37°C (0.48-0.6 U/mg protein, (134)), with 40% of the activity localized to the neuromuscular junction. In our model, about 35% of the AChE is located within the neuroeffector junction and since the neuroeffector junction sees a higher ACh concentration than the EJS, these figures agree closely. Furthermore, the overall AChE hydrolysis rate we observe using our model is close to that measured in a number of systems (see discussion in section 2.5.2) produces ACh profiles similar to those generated by the Dokos model (data not shown), and reproduces the shift in ACh-activated potassium current ($I_{K,ACh}$) in response to AChE inhibition ((264), see Figure 89). The value of kcat,AChE and the AChE densities described above are multiplied and scaled by the area of the neuroeffector junction and the extrajunctional space to yield the maximal velocities of ACh hydrolysis by AChE in these two compartments: $v_{maxNJ,AChE}$=525 amol/s and $v_{maxEJS,AChE}$=1014 amol/s.

2.3.5 *β-adrenergic receptor binding/activation by NE*

Cardiac myocytes contain β_1-adrenergic and β_2-adrenergic receptors, with β_1 being about 3 times as plentiful as β_2 (42, 307). Evidence regarding the role of β_1 and/or β_2 receptors in the regulation of cAMP is inconsistent: studies show the involvement of both β_1 and β_2 (41, 139), only β_1 (155, 372), and only β_2 (345). A recent study showed that both β_1 and β_2 adrenergic receptors effect increases in cAMP, but these changes are physically segregated within the cell: β_2-induced cAMP remains near the cell membrane whereas β_1 creates a more far-reaching signal (251). There is also evidence that β_2 receptors may activate both the stimulatory and inhibitory G-proteins whereas β_1 acts only through the stimulatory pathway (71). Since their functional differences are unclear, we consider only the total β-adrenergic receptor population.

Data on the β-adrenergic receptor density in a number of species are presented in Table 2. From these numbers we estimate that the β-adrenergic receptor density in rabbit atrium is about 6 receptors/μm^2. Similar to the M2 muscarinic receptor case, the β-adrenergic receptor density of SA node is about 3 times that of the right atrium (17), giving an average β-adrenergic receptor density in rabbit SA node of 20 receptors/μm^2. Using the same reasoning as for the M2 muscarinic receptor, we compute the ratio of ~200 for β adrenergic receptors in the neuroeffector junction to that in the EJS. This computation results in about 39% of the total β adrenergic receptor population being confined to the neuroeffector junction, a figure similar to that for the cholinergic case.

β-adrenergic receptor kinetics are defined in the same way as for the M2 muscarinic receptors. The half-binding ligand concentration $K_{M\beta}$ has been measured in various ways, and a wide range of values have been reported depending on the cellular origin of the receptor and the specific ligand. Interestingly, norepinephrine (NE) is not the most commonly used β-adrenergic agonist in these studies (experimental compounds include DHA (51), ICYP (115), Iso (142, 245, 309), CGP 12177 (80), iodohydroxybenzylpindolol (224), epinephrine (306)), however some studies reported data from which NE binding kinetics could be deduced (6, 51, 136, 205-207, 223), and are summarized in Table 3. An explanation for the widely varying $K_{M\beta}$ values is that β adrenergic receptors exist in a high-affinity and a low-affinity state, with the difference in affinities being roughly 10-fold (307). The NE-β adrenergic receptor affinity is set to $K_{M\beta}$ of 1.5 μM with a Hill coefficient n_β of 0.7, and the overall rate is dictated by a $k_{off,\beta}$ of 0.15 /s at 37 °C. The dissociation rate is significantly slower than that of the M2 muscarinic receptor, however it is on the right order of magnitude when compared to the rate measured for the more potent (205, 345) β-adrenergic agonist Iso ($k_{off,Iso}$= 0.067/s in human polymorphonuclear lymphocytes (245)).

Table 3 β-adrenergic receptor kinetic data for binding NE.

Source	Cell Type	Temperature (°C)	K_D (μM)	k_{on} (/(mM s))	k_{off} (/s)
Stiles et al. 1983 (308)	Human LV	--	0.95	--	--
Bylund and Snyder 1976 (51)	Rat brain	--	0.8	--	--
Harden 1976 (136)	Rat V	--	2.5-25	--	--
Lefkowitz 1975 (205)	Canine V	--	3-8	--	--
Alexander et al. 1975 (6)	Canine V	--	10	--	--
Lefkowitz and Haber 1971 (206)	Canine V	37	0.8	150[a]	0.12[b]
Maguire 1974 (223)	Rat glioma	37	--	77[c]	--
Lefkowitz et al. 1972 (207)	Canine V	37	4.3	58-96[d]	0.25-0.4[b]

[a] -50% binding is reached by ~15 minutes in 5nM [NE], [b] -Calculated from K_D reported in paper and k_{on} calculated here, [c] -50% binding happens in ~30 minutes in 5nM [NE]; however maximal rate of cAMP production is seen within <5 seconds of 50 nM or 10 μM NE application., [d] -Complete binding happens in ~2 hours at 5nM [NE], assuming that this is 3-5 time constants yields the calculated k_{on} range.

2.3.6 NE clearance through reuptake and absorption

In addition to diffusive transport and clearance by the bloodstream, NE is removed through reuptake by the sympathetic nerve varicosities and absorption by end-effector cells (for review, see (102)). NE is rapidly reuptaken by a NE transporter (NET) in sympathetic nerve terminals (102, 161). This rate is believed to be fast enough to clear the volume immediately surrounding sympathetic varicosities on the order of milliseconds, the entire extracellular space of the heart in 10 seconds (161). The NET is a high-affinity transporter, with a measured K_M of 0.27 μM and a maximal uptake rate v_{max} of 1.18 nmol/min per gram of heart tissue in rat heart (161).

$$k_n = v_{maxn} \frac{[NE]}{[NE] + K_M}$$

NE is also absorbed by tissues, although significantly less NE is removed through this route compared to neuronal reuptake (161). NE absorption is a low-affinity, but high rate process, with a measured K_M of 252 μM and a maximal rate v_{max} of 100 nmol/min per gram of heart tissue in rat heart (163).

We set the affinities to their measured values (K_{Dn}=0.27μM for neuronal reuptake, K_{Da}=252μM for absorption), and chose maximal rates of neuronal reuptake and effector cell absorption to reproduce measurements of the fraction of NE removed by each mechanism. In humans, spillover of NE from the heart into the circulation is 11 ng/min, and NE clearance by the heart (presumably through absorption and subsequent metabolism) is 22 mL/min, which equates to 6 ng/min (109). In rats, the rate of NE reuptake is 9.7 times the spillover rate, which yields 107 ng/min (104). Using these values, we conclude that of all the NE released from sympathetic varicosities, 86% is reuptaken by the nerve, 9% spills over into the circulation, and 5% is absorbed and metabolized by the myocardial cells, figures which are in agreement with the general scheme presented by Eisenhofer (102) and the observation that less than 10% of the released NE is spilled over into plasma (103). The maximal rate of neuronal reuptake is $v_{max,n}$=18.7 amol/s and only occurs in the neuroeffector junction. Cellular absorption is divided into neuroeffector junction and EJS rates: $v_{max,NJ,a}$=0.374 amol/s, $v_{max,EJS,a}$=115.566 amol/s. The total absorption rate was set to satisfy clearance rates, and neuroeffector junction vs. EJS fractions were calculated assuming uniform absorption across the cell membrane and the ratio of cell surface area dedicated to adrenergic neuroeffector junction versus EJS. These values reproduce the observed clearance ratios, and are valid on a range of sympathetic stimulation frequencies (see Figure 22).

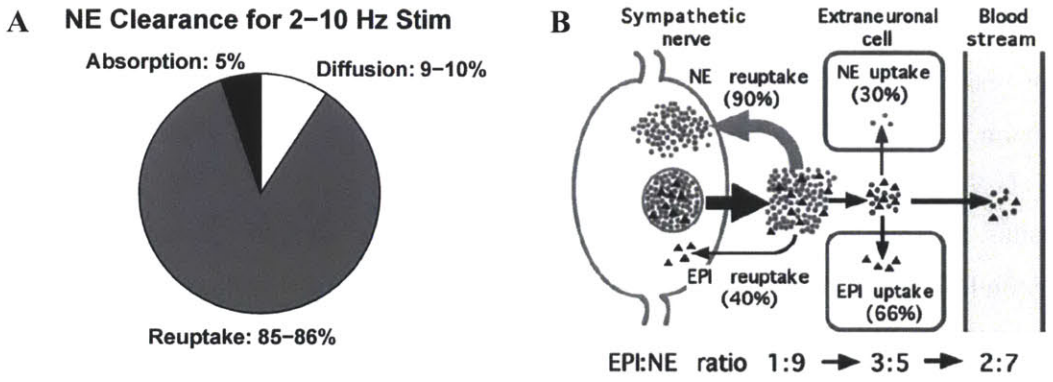

Figure 22 Our model reproduces NE clearance ratios observed experimentally. A. Percent of sympathetically-released NE absorbed, diffused into the bloodstream, or reuptaken by the varicosity. The range of values is for sympathetic stimulation frequencies 2-10 Hz. B. Illustration taken from a review by Eisenhofer (102), showing the flow and relative absorption of NE. In this figure, 90% of NE is reuptaken, 3% is absorbed by cells, and 7% diffuses into the blood stream; the numbers we used are based on particular measurements so they are slightly different. To compute the percentages in A, we simulated 60 seconds of sympathetic stimulation at 2, 4, 6, and 10 Hz. This duration is long enough to allow the system to come to steady state. The total amount of NE absorbed, reuptaken, and diffused was computed in the space of time between the last two stimuli, and the results are expressed as percentages of the sum total.

2.3.7 *Neurotransmitter synthesis*

Both ACh and NE are synthesized in the nerves from which they are secreted ((218) for ACh, (162) for NE).

The synthesis of ACh is catalyzed by the enzyme choline acetyltransferase, which assists the reaction of choline and acetyl-CoA (218). Choline (Ch) is taken up from the extracellular space (218), and acetyl is obtained from the surrounding tissue (334). As pointed out by Loffelholz, the [Ch] in the blood stream (~5-15 μM in various mammals (140, 218, 291)) is an order of magnitude greater than the half-maximal concentration for high affinity Ch uptake (which is on the range 0.5-2 μM) and therefore ensures sufficient ACh synthesis to prevent depletion under physiological conditions (167, 218). However, even when the Ch source is removed by isolating the heart, the [ACh] store cannot be exhausted by physiological vagal stimulation. This has been demonstrated in isolated chicken, rabbit, cat, and guinea pig hearts, which maintained a steady-state ACh release at 29 -58% of the initial value during 20 minutes of 20 Hz stimulation (87, 218). In this setting, the primary source of Ch is from the hydrolysis of released ACh as well as from metabolism of choline-containing compounds (phospholipids, glycerophosphocholine, phosphorylated choline) in the tissue (218). In our model, these aspects are described as follows: we include two sources of Ch for ACh synthesis – a "constant" source from the blood stream/tissue, and a vagal stimulation-dependent source from the hydrolysis of ACh. Thus, the number of vesicles in the varicosity is recharged by both a constant rate process that works to maintain the maximum number of vesicles (with time constant τ_{ACh}), as well as at a rate proportional to ACh hydrolysis (k_{hNJ} and $U_{EJS}\times k_{hEJS}$). Each varicosity releases an integer number of vesicles with the arrival of each stimulus, as indicated by the last term in equation (3). In the last term, I_{stim} is a stimulatory impulse which is infinitesimal in time, but integrates to 1 around the time of the stimulus t_s (Dirac delta function at t_s). In implementation, this is realized by running the numerical ODE integrator (`ode15s` in Matlab) between sets of stimulation times, and adjusting the initial condition according to how many varicosities are released at each stimulus as described in the last term of equation (3). For descriptions of the other variables in this equation, see Table 22.

$$\frac{dN_{v,ACh}}{dt} = \overbrace{\frac{N_{vMax,ACh} - N_{vACh}}{\tau_{ACh}}}^{\text{from constant store}} + \overbrace{\frac{k_{hNJ}\left[ACh\right]_{NJ} V_{NJ,ACh} 6\times10^5}{Q_{ACh}}}^{\text{all ACh hydrolyzed in NJ is absorbed}} + \overbrace{U_{EJS}\frac{k_{hEJS}\left[ACh\right]_{EJS} V_{EJS} 6\times10^5}{Q_{ACh}}}^{\text{a portion of ACh hydrolyzed in EJS is absorbed}} \underbrace{-\left\lfloor \frac{N_{vACh}k_r}{N_{var,ACh}} \right\rfloor N_{var,ACh} I_{stim}}_{\text{integer number of vesicles released per varicosity per stimulus}} \quad (3)$$

We assume that all of the Ch created in the neuroeffector junction is uptaken due to its proximity to the varicosity, and we use measurements from the frog neuromuscular junction to determine the value of the time constant τ_{ACh} and the uptaken fraction of Ch produced in the EJS U_{EJS}. In the frog neuromuscular junction, it has been observed that 6 minutes of 10 Hz stimulation caused end plate potentials to drop to 21% of initial value in intact preparations, 10% in preparations with blocked AChE, and 2% in preparations with blocked high-affinity active transport (194). Our model can reproduce these values if τ_{ACh}=100s, and U_{EJS}=0.3 (see Figure 23). Due to differences between the neuromuscular junction and the cardiac neuroeffector junction, these measurements are not necessarily appropriate for our model. Using the parameter values from above, 20 Hz vagal stimulation causes steady state release that is ~10% of maximum, which contrasts the 29-58% seen in perfused hearts (87, 218). Furthermore, these parameter values also cause decreases in ACh released during 1-minute stimulation at 7Hz; but this is not evident in the data of Brack et al. in perfused rabbit heart (33). To correct these discrepancies we found it necessary to decrease τ_{ACh} to 5s, and increase U_{EJS} to 0.5.

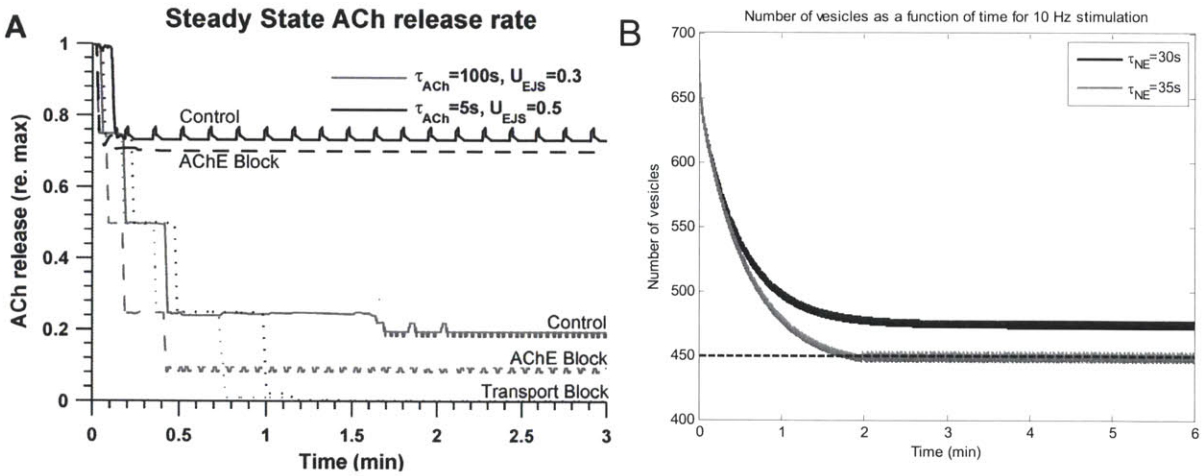

Figure 23 A. τ_{ACh} and U_{EJS} values were chosen to allow 7 Hz stimulation for 1 minute without a drop in ACh release (black lines). Here we also show the replication of an experiment where ACh release was monitored for the control system, for a system with inhibition of AChE (and therefore, no uptake of Ch from hydrolysis), and with blockage of Ch transport from the bloodstream ($\tau_{ACh}=\infty$). The gray lines show the model reproduction of the results of this experiment (see text for details). B. τ_{NE} was chosen to allow stimulation at 10 Hz without depletion. We show the NE release as a function of time for τ_{NE}=30s and τ_{NE}=35s to illustrate that depletion does not occur with the faster time constant but does occur if the time constant is slowed.

NE is synthesized in sympathetic nerve varicosities (105) in the following reaction (162):

L-tyrosine → L-DOPA → dopamine → L-norepinephrine

Following synthesis, NE is stored in release vesicles through a dynamic process that allows NE to leak out into the cytoplasm (where the majority of NE metabolism occurs) and is replaced back into the vesicles through active pumping (105).

Since reuptake of NE from the synaptic cleft reclaims the majority of the neurotransmitter, and since most sympathetic nerve activity happens at slow rates (typically ~1-2 Hz, rarely exceeding 10 Hz (162)), it is unlikely that vesicles become depleted. In a recent review, Eisenhofer points out that even if NE release increases 10-fold due to exercise, the rate of NE synthesis only needs to increase 3.2 times due to the "gearing down" afforded by the high rate of reuptake (105). Finally, Warner and Cox successfully used a constant neurotransmitter supply in their model of HR control in the dog (349). For these reasons, we model the number of NE vesicles as:

$$\frac{dN_{v,NE}}{dt} = \overbrace{\frac{N_{vMax,NE} - N_{v,NE}}{\tau_{NE}}}^{\text{synthesis from blood stream}} + \overbrace{\frac{k_n [NE]_{NJ} V_{NJ,NE} 6\times10^5}{Q_{NE}}}^{\text{reuptake from NJ}} \overbrace{-\left\lfloor \frac{N_{v,NE} k_r}{N_{var,NE}} \right\rfloor N_{var,NE} I_{stim}}^{\text{integer number of vesicles released per varicosity per stimulus}}$$

where τ_{NE} is set to a value small enough (τ_{NE}=30s) to ensure no depletion at 10 Hz (see Figure 23).

2.3.8 Direct inhibition of β-AR activation by ACh

Levy (210) discusses the possibilities for "mutual inhibition" and "mutual excitation" of the two branches of the ANS. We constructed our model by first assuming that there were no direct effects of one branch on the other; however, when we attempted to reproduce HR data collected by Brack et al. (33), we noticed that our model produced higher HRs than measured for high vagal stimulation rates (7 Hz) and moderate to high sympathetic stimulation rates (2-10 Hz). Thus, we include a path of direct β-AR inhibition at these high vagal rates. A perusal of the literature did not provide a clear mechanism for this interaction; both presynaptic (ACh inhibits the amount of NE released from adrenergic varicosities) and postsynaptic (regulatory machinery activated by M2 receptors deactivates β-AR) mechanisms seem plausible. Given the complexity of intracellular processes, we model this interaction postsynaptically by introducing a variable X as a surrogate for vagal activity/M2 activation. This variable is essentially a delayed version of the activated M2-muscarinic receptor concentration inside the cell ($M2^*$). It was necessary to introduce the τ_X=3 s time constant in order to smooth out the pulsatile nature of M2 activation (see Figure 25). The inactivating effect of X on β^* (the activated β-AR concentration inside the cell) is modeled using a standard Hill equation, with parameters chosen to reproduce the HR data of Brack et al. (33)

$$M2^* = \left([AChM]_{NJ} V_{NJ,ACh} + [AChM]_{EJS} V_{EJS} \right) / V_{cyto}$$

$$\frac{dX}{dt} = \frac{M2^* - X}{\tau_X}$$

$$\beta^* = \left([NE\beta]_{NJ} V_{NJ,NE} + [NE\beta]_{EJS} V_{EJS} \right) / V_{cyto} \times \left(1 - I_{M^*,max} \frac{X^{nM^*}}{X^{nM^*} + K_{M^*}^{nM^*}} \right)$$

2.4 Results

The complete equations describing the phenomena of neurotransmitter release, diffusion, clearance, and receptor binding can be found in the Appendix, section 9.5. Here, we summarize model performance.

As the function of neurotransmitter release is to transduce activity in sympathetic and vagus nerves to activation of β-AR and M2 muscarinic receptors, we show the steady state receptor activation and time to maximum activation as a function of nerve stimulation frequency in Figure 24. Regarding receptor occupancy (panel A), three differences between sympathetic and vagal stimulation can be appreciated: 1) neurotransmitter depletion is more pronounced in the sympathetic branch, 2) the disparity between receptor activation in the neuroeffector junction and EJS is greater for sympathetic stimulation, and 3) the maximal percent of receptors that can be activated with nerve stimulation is greater for M2 receptors.

The SS values reflect neurotransmitter depletion from the varicosity, whereas the peak values show the maximum attainable occupancy for a particular stimulation frequency, assuming that the varicosities contain the maximum number of vesicles at the start of stimulation. The depletion effect is drastic for sympathetic stimulation, with receptor occupancy reaching a maximum of ~15% activation at 10 Hz stimulation and not increasing beyond that. This occurs because each adrenergic varicosity contains a maximum of 150 vesicles, and k_r=0.01 means that 1% of available vesicles are released with each stimulus. Once the number of vesicles is depleted to below 100, no vesicles are released despite increasing stimulation rates (quantal release does not allow for fractions of a vesicle). In this regime, the rate of NE release is limited by the rate of synthesis which is a constant, rather than the rate of stimulation, so the receptor occupancy function is also a constant. A depletion effect is also present for vagal stimulation, causing a widening gap between steady-state and peak receptor activation for stimulation frequencies beyond 7 Hz. The M2 SS curve drops in a stepwise manner because quantal release permits only integer-valued numbers of vesicles to be released with each stimulus. Since each varicosity contains 450 vesicles, and 1% are released for each stimulus, this allows the release of 4 (for f <10 Hz), 3 (for 10 Hz<f<30Hz), 2 (for 30 Hz<f<100 Hz), or 1 (for f>100 Hz) vesicle with each stimulus, resulting in the stair-step appearance of the M2 SS curve.

For M2 receptors, the neuroeffector junction/EJS occupancy is only slightly different from the total; however β-AR occupancy in the EJS is significantly greater than that in the neuroeffector junction. This difference arises due to the high rate of NE reuptake by sympathetic nerve varicosities from the adrenergic neuroeffector junction, which is absent from the EJS. The hydrolysis of ACh by AChE on the other hand, affects both the neuroeffector junction and EJS more equally.

The maximum β-AR occupancy does not exceed 30% with increasing rates of stimulation, but M2 muscarinic receptors approach 100% occupancy. This phenomenon arises for two reasons: the smaller number of vesicles present in the adrenergic varicosities which results in lower maximal neurotransmitter release despite high stimulation frequency, and the high rate of NE clearance by the reuptake process compared to the relatively sluggish rate of NE-(β-AR) binding, which results in NE being removed from the neuroeffector junction before having sufficient time to bind the receptors.

More information on the kinetics of β-AR and M2 muscarinic receptor activation is provided in Figure 24B and Figure 25. M2 receptors activate very quickly: the first stimulus always resulted in greater than half-maximal receptor activation, and 0.95 of peak value is reached within ~1 second over the physiologic range of stimulations (< 10Hz). β-AR are significantly slower, with half-times of about 4s, and requiring 10-20s to reach 0.95 of peak value on the physiologic range of stimulations.

Sample time courses of β-AR and M2 muscarinic activation by 6 Hz stimulation are shown in Figure 25. The difference in responsiveness of these two receptors to nerve stimulation is apparent, and is manifested in two ways. Not only is the approach to peak value faster for the M2 muscarinic receptor (panel A), but the response to each individual stimulus elicits a rapid binding (to ~80% of total receptors) followed by a fast decay (to ~15%) before the following stimulus (panel B). This phenomenon does not occur with the β-AR, which undergoes a more monotonic rise in total binding. Deactivation kinetics also differ, wherein the M2 muscarinic receptor undergoes a rapid (12/s) decay from 27% to 15%, followed by a slower (0.86/s) decay toward baseline value (panel C). The β-AR on the other hand, follows an approximately single-exponential decay with a slow rate (0.14/s).

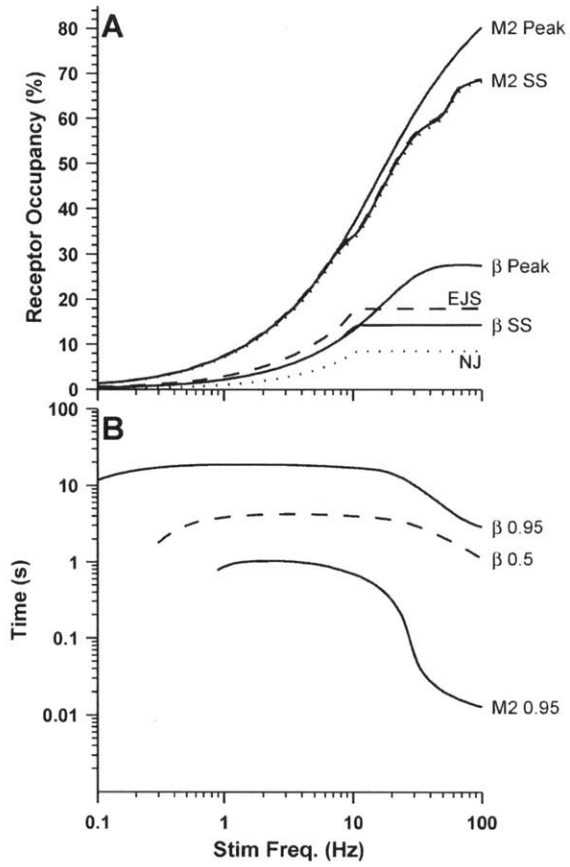

Figure 24. Receptor sensitivity and rate of activation (model simulation). A. The solid lines show the percent of total receptors occupied/bound by neurotransmitter. Each family of receptor shows two curves, a steady-state (SS) and peak, as labeled. The occupancies for the neuroeffector junction and EJS receptor populations are also shown individually by dotted and dashed lines as indicated in the figure. B. The rates of activation from a baseline level of ~0 to the peak values indicated in A. did not follow an exponential rise, so we show the time required to reach 0.5 and 0.95 of peak value. Missing values indicate frequencies where the first stimulus surpassed either the 0.5 or 0.95 point.

To better understand the effect of ACh hydrolysis and NE reuptake and absorption, simulations were run using the system state at the end of stimulation as the initial condition, and setting the various clearance rates to 0. The effect of eliminating AChE hydrolysis is drastic, eliminating the rapid decay phase, and slowing the slow decay by a factor of 5 (from 0.86/s to 0.17/s). The rapid decay phase is actually replaced by a temporary increase in receptor activation (see Figure 25C), because the ACh liberated from bound receptors (the last stimulation peak) is made available for re-binding receptors rather than being hydrolyzed. The second effect of AChE blockade is that the baseline receptor occupancy due to the BS concentration of ACh increases to the expected $0.003^{0.7}/(0.003^{0.7}+0.3^{0.7})=3.8\%$ (this is simply the Hill equation describing M2 muscarinic receptor occupancy evaluated at ACh_{BS}=3 nM [ACh]). The effects of eliminating NE reuptake and/or absorption are not as drastic: the effect on rate of clearance is virtually unaffected by the absence of absorption, and only decreases from by 21% when reuptake is eliminated.

The combined effect of reuptake and absorption blockade is a slowing of the deactivation rate by 36%. The biggest effect of these clearance pathways is on the baseline β-AR occupancy, which also rises to the expected $0.003^{0.7}/(0.003^{0.7}+1.5^{0.7})=1.3\%$ in the absence of both reuptake and absorption. The reason that the M2 deactivation rate is more strongly affected by elimination of hydrolysis is also due to the rapid kinetics of M2 muscarinic receptors: binding/unbinding of these receptors is rapid enough that receptor occupancy is in equilibrium with the local ACh concentration, so the rate of ACh removal is the limiting process. For β-AR however, the rate limiting process is not the local NE concentration, but rather the binding/unbinding rates, so its rate of deactivation is not affected nearly as strongly by blockage of reuptake and absorption. As we pointed out though, the maximal receptor occupancy would be affected by elimination of these clearance pathways for both M2 muscarinic receptors and β-AR (running the same simulation with AChE rate set to 0 resulted in average M2 occupancy of 80% during stimulation and setting reuptake and absorption rates to 0 resulted in 40% peak β-AR activation, data not shown).

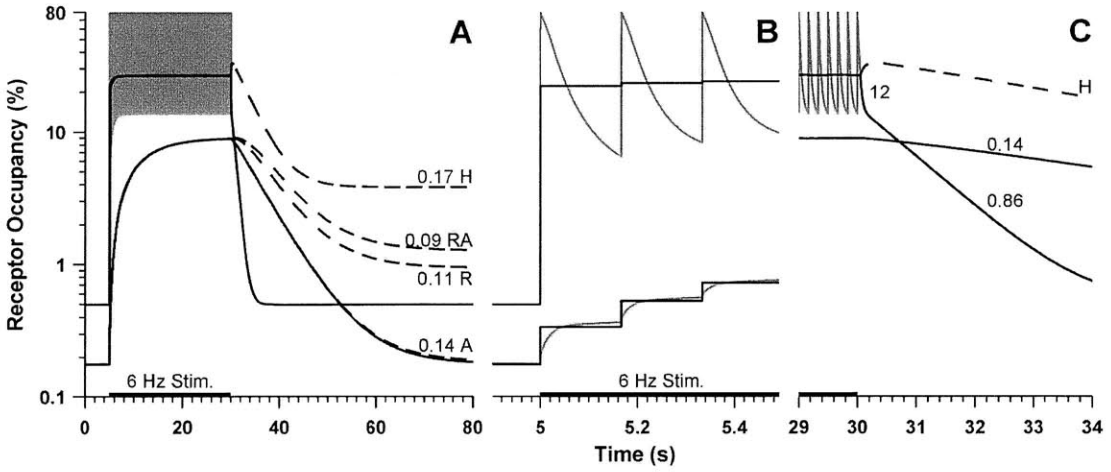

Figure 25 Sample time courses of β-AR and M2 muscarinic receptor activation and deactivation (model simulation, note logarithmic axis for receptor occupancy). Gray lines show actual percentage of total receptors bound to neurotransmitter for 6 Hz stimulation as indicated. Solid black lines show average receptor occupancy between adjacent stimuli. Dashed lines show alternate simulations, where ACh hydrolysis (H), NE reuptake (R), NE absorption (A), and NE reuptake and absorption (RA) were blocked after cessation of stimulation, to study the clearance processes. The numbers indicate the decay rate constant (/s) for each intervention. Rate constants were calculated by fitting the linear part (on log scale) of the decay curves. All panels share the same y-axis. A. Full simulation, showing receptor activation from 5 to 30 seconds, and subsequent deactivation due to unbinding and neurotransmitter clearance. B. Enlarged view of the activation process. C. Enlarged view of the deactivation process and deactivation rates for the baseline simulations.

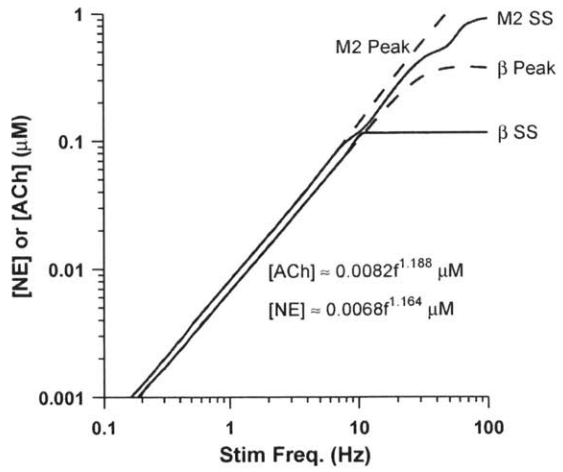

Figure 26. Relationship between stimulation frequency and the neurotransmitter concentration (in the neuroeffector junction and EJS) necessary to produce an equivalent total receptor activation (model simulation). Solid lines show the equivalent neurotransmitter concentration for matching steady-state receptor occupancy and dashed lines show neurotransmitter concentrations required for peak receptor occupancy. For frequencies where neurotransmitter depletion was not encountered (<7 Hz), the relationship is well described by a power law, as indicated in the figure, where f is the stimulation frequency in Hz.

For the range of physiological stimulation frequencies, the neurotransmitter concentration required to elicit an equivalent activated receptor fraction is related to stimulation frequency by a power law (Figure 26). For frequencies beyond 7 Hz, the peak attainable M2 muscarinic occupancy continues to obey the power law, whereas peak β-AR, and the SS occupancy of both receptors drops off from this relationship due to the depletion phenomena discussed above. In this figure, the equivalent neurotransmitter concentration is assumed to be present in the local environment of the receptors (neuroeffector junction and EJS), which appears possible in isolated SANC preparations (see the discussion in section 6.3). If the various neurotransmitter clearance mechanisms present in-vivo are not eliminated by thorough isolation of cells (as in experiments done on tissue slices), and neurotransmitter concentration is fixed at some distance from the cell membrane, a drastic shift in apparent affinity is observed. Figure 27 illustrates this effect: the expected affinities are observed for M2 muscarinic and β-AR for neurotransmitter concentrations in the neuroeffector junction/EJS, but both are shifted to the right by a factor of roughly 20 when neurotransmitter concentration is maintained in the BS. This occurs because the ECM acts as a diffusion barrier, allowing clearance processes at the cell membrane (ACh hydrolysis, NE reuptake and absorption) to decrease the local neurotransmitter concentration. The M2 curve is shifted to the right without a significant change in slope because AChE is a relatively low-affinity process, with an apparent affinity of 100 μM. The same is true for the effect of only NE absorption on β-AR (affinity 252 μM). However, since the majority of NE is cleared by reuptake, and this process is fairly high-affinity (0.27 μM), it saturates around 10 μM NE and that is why we see the steepening in the β-AR curve for high BS NE concentrations.

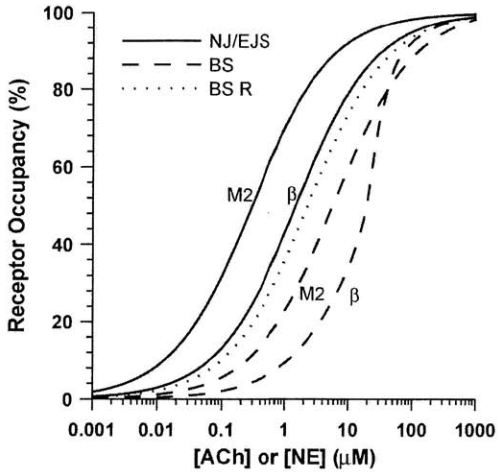

Figure 27. Clearance processes (hydrolysis, reuptake, absorption) reduce the effectiveness of neurotransmitter concentration in the BS (model simulation). Solid lines show the receptor occupancy when neurotransmitter concentration in the neuroeffector junction and EJS is set to the indicated values. Dashed lines show the occupancy for neurotransmitter concentrations in the BS. The dotted line shows the β-AR occupancy for neurotransmitter applied in the BS but with reuptake rate set to 0.

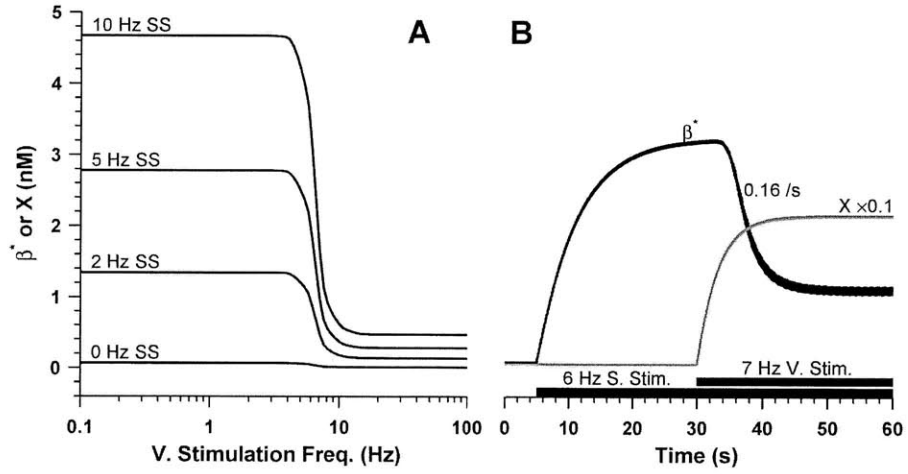

Figure 28. Direct inhibition of β-adrenergic activity by the cholinergic system occurs sharply and maximally reduces effective β^* to 10% of uninhibited value (model simulation). A. Steady state β^* for the indicated values of sympathetic stimulation (SS) and simultaneous vagal (V) stimulation as shown on the x axis. B. Sample time course of β^* activation and inhibition for dual sympathetic and vagal stimulation as shown by the bars at the bottom of the figure. The rate of β^* inhibition indicated next to the curve was computed by a linear fit to the log of the data between 35.5 and 37.5s. The value of X is also shown, multiplied by 0.1 in order to be visible using the y-scale in A. The pulsatile nature of the neural stimulation contributes to the thickness of the lines, similar to but less drastic than Figure 25.

The direct-inhibitory effect of high vagal stimulation rates is shown in Figure 28. Panel A shows the sharp onset of inhibition around 5 Hz vagal stimulation, and reaches maximum inhibition by 15 Hz. The inhibition is multiplicative, reducing the effective β^* concentration by a maximum of 90%, independent of

the sympathetic stimulation frequency. Panel B shows the time course of β^* activation and inactivation, showing the same activation dynamics as discussed for β-adrenergic receptors in Figure 24 and Figure 25. The X-mediated inactivation lags by about 4 seconds, which is the time required for X to approach its steady-state value. Due to the sharpness of the inhibition curve, virtually no effect is seen for X<15nM, but beyond this point inhibition becomes apparent and proceeds with a rate similar to that of β^* activation.

2.5 Discussion

We constructed a detailed model of neurotransmitter release from vagus and sympathetic nerve varicosities to describe the transduction of neural impulses originating in the brain to changes in β-AR and M2 muscarinic receptor activation on rabbit SANCs. Our model combines elements from the Dokos (96) and Demir (81) models of ACh release, and includes a number of novel elements. We focus this discussion on a comparison of these two models; a more general discussion of past ACh release and diffusion models can be found in Appendix section 9.3.

2.5.1 ACh model compartments and receptor populations

The full diagram of our ACh release model is shown in Figure 29. It features six compartments: the number of cholinergic vesicles ($N_{v,ACh}$), ACh concentrations in the neuroeffector junction, EJS, and ECM ($[ACh]_{NJ}$, $[ACh]_{EJS}$, and $[ACh]_{ECM}$), and bound M2 muscarinic receptors in the neuroeffector junction and EJS ($[AChM]_{NJ}$ and $[AChM]_{EJS}$). What it shares in common with the Dokos model are three compartments: the main vesicle store, ACh concentration in the neuroeffector junction, and ACh concentration in the EJS, where the latter two compartments communicate through diffusion and ACh is released from the main store into the neuroeffector junction. The Dokos model does not explicitly model the activation of M2 muscarinic receptors by ACh, and it does not include any M2 muscarinic receptors in the EJS. The Demir model on the other hand, includes two populations of receptors: what they term "junctional" and "extrajunctional" receptors, which directly activate different ion channels following the example of Edwards et al. (101). These two populations were included to reproduce the differences in SANC responses to bath application of ACh vs. neuronal release, as recorded by Campbell et al. (53) in the guinea pig. Our model is similar in that M2 muscarinic receptors exist in both the neuroeffector junction and EJS, but we model these two populations as activating the same second messenger cascade through G-proteins (see Chapter 3). We chose this approach because it is known that M2-muscarinic receptors are localized in the sympathetic neuroeffector junction, and the kinetic mechanisms of M2-muscarinic receptor activation and interaction with inhibitory G-proteins have been experimentally described. This approach does not require us to postulate the existence of some other "junctional" receptor type with undocumented properties, as was done by Demir et al. (81). Furthermore, we were able to

reproduce the experimental data concerning the modulation of ion channel properties by ACh (both vagally-released and bath-applied) using our model (see Chapter 6), without the need for an additional junctional receptor type. On the other hand, the Demir model assumption of different intracellular effects of junctional vs. extrajunctional receptors may be justified from the point of view of subcellular compartmentalization (see section 6.7). Thus, perhaps both groups of receptors are M2 muscarinic and they activate the same type of inhibitory G-proteins, but because they are tethered to different locations in the cell membrane, they may hold sway over different populations of ion channels. Modeling such interactions explicitly would require more experimental data to describe the areas/volumes of influence, the mechanisms by which second messengers are localized, and the physical distribution of ion channel types on the cell membrane. Finally, we also include the ECM and BS compartments (included in neither the Dokos or Demir models), which is not only anatomically justified, but limits the rate of ACh clearance through diffusion to a reasonable value (see below) and provides an explanation for the apparent ACh affinity difference observed in isolated cells vs. whole tissue (see Figure 27 and section 2.5.4).

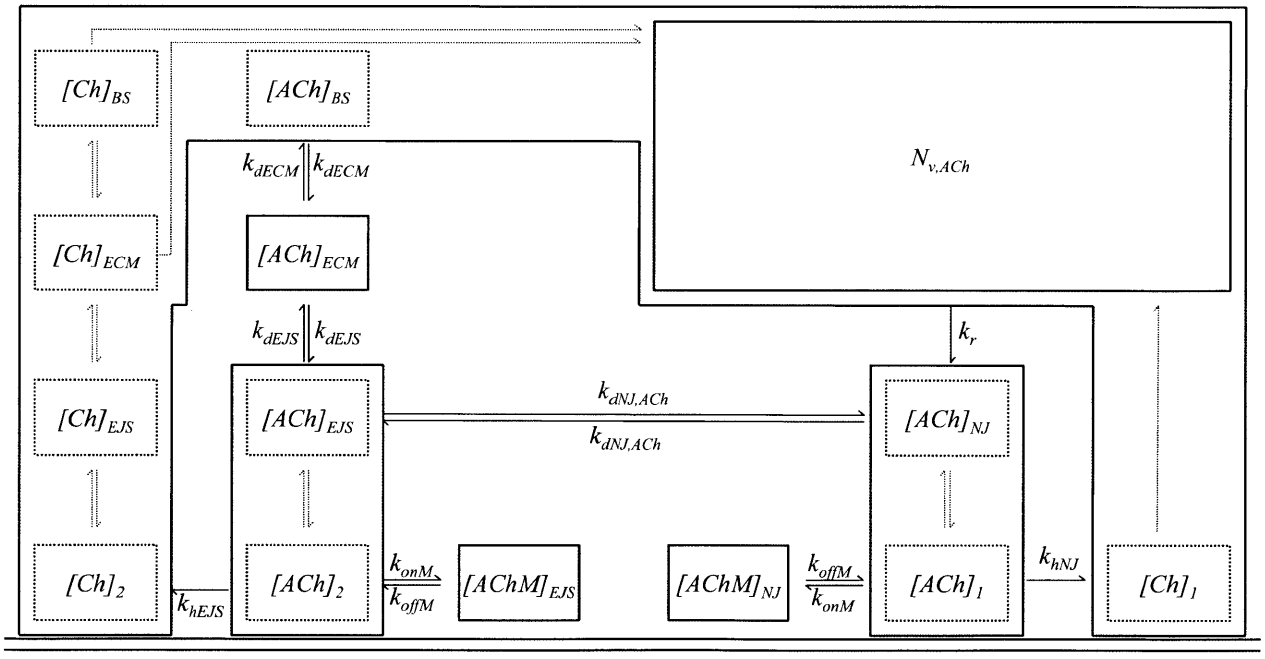

Figure 29. Reaction diagram for ACh release, diffusion, clearance, binding, and synthesis. Solid lines delineate compartments that are explicitly modeled, dashed lines show compartments that have been lumped together either because diffusion between them is instantaneous ($[ACh]_{NJ}$ and $[ACh]_1$, $[ACh]_{EJS}$ and $[ACh]_2$) or because it is not necessary to model them explicitly (all $[Ch]$; $[ACh]_{BS}$ exists as a parameter but does not change with time). The six compartments are described by six differential equations, see section 9.5.2; for a key of abbreviations see Table 22.

2.5.2 *ACh diffusion and hydrolysis*

Our model is similar to the Dokos model in that diffusion across the neuroeffector junction is assumed to be instantaneous; an assumption that we justified with molecular Monte-Carlo simulations and experimentally-measured physical parameters. A similar method was applied to calculate the diffusion coefficients between the neuroeffector junction and EJS, EJS and ECM, and ECM and BS compartments, which yielded reasonable M2 muscarinic receptor activation and ACh clearance profiles (see Figure 25). We modeled ACh hydrolysis based on the experimental characterization of AChE affinity, maximal catalytic rate, and density. While the Demir and Dokos models both included hydrolysis terms, their models were more arbitrary: Dokos chose a hydrolysis rate of 14/s in order to produce desired ACh profiles, and Demir assumed a rate of 50/s, which appeared as a parameter in the Purves equation for ACh diffusion. Several models (81, 265, 275) use the Purves equation (276) to account for diffusion of ACh across the neuroeffector junction, but it is not an appropriate model for the in-vivo system. This equation (equation (1)) assumes that diffusion happens in an infinite sphere surrounding the point source (usually the tip of a pipette), with hydrolysis occurring in the diffusive medium (276). For the models of Osterrieder et al. (265) and Pott and Pusch (275), where ACh was released onto target cells from a micropipette some 30-100 microns away, it is important to account for diffusion, because using the values of Osterrieder et al. with D=8 $\times 10^{-6}$cm^2/s, x=100 $\times 10^{-4}$cm, and k_H=5/s , the concentration at the specified distance takes about 650 ms to reach its peak (265). A similar value is obtained for the time to peak using the parameters from Pott and Pusch (275). Demir et al. used a much smaller distance of 75 nm (81), which is more appropriate for the width of the neuroeffector junction. However, their assumed diffusion constant (D=5.1469 $\times 10^{-11}$cm^2/s) is *five orders of magnitude* smaller than the measured value (see Table 1). Thus, the reason that ACh diffusion was not instantaneous in these models is that either the distance from source to cell is much farther or the assumed diffusion coefficient is too small. Furthermore, the assumption of the Purves model that diffusion happens in an infinite sphere would tend to overestimate the delay in the neuroeffector junction, which is more like two parallel plates with diffusion only occurring in a single dimension from one plate to the other, rather than in all radial directions from the source.

As support for our bottom-up approach, we point out that the M2-muscarinic receptor deactivation process occurred at two rates with AChE intact: 12/s and 0.87/s (Figure 25C). With AChE inhibition, a single rate of 0.17/s was observed and is credited to the rate of diffusion into the BS. This value is in line with the experimentally measured rate of ACh "washout" in perfused chick heart (0.069/s (214)). Furthermore, these figures imply that ACh hydrolysis occurs at two rates, a fast rate close to 12/s that is

similar to the 14/s used by Dokos et al (96), and 0.7/s, which is close to the values experimentally measured or assumed in a number of models (see "Hydrolysis" column in Table 20).

2.5.3 ACh synthesis

Our model of ACh synthesis is based on the current mechanistic understanding of this process, where ACh is synthesized in the nerve varicosities from Ch that enters the nerve after being created by hydrolysis of ACh or from the surrounding tissue (ECM) and BS. The Dokos model is similar in that all of the ACh hydrolyzed in the neuroeffector junction re-enters the varicosity, and there is a second source of ACh from the BS. The Demir model on the other hand, includes ACh depletion (see equation 13 in (81)), but does not specify any mechanism of synthesis. The downside of this specification is that long stimulus trains lose potency very quickly, and indeed, the data shown by Demir et al. usually uses 6- or 9-pulse stimulus trains. Since our aim was to model in-vivo parasympathetic activity with sustained ACh release, mechanisms of ACh synthesis are crucial. Our model shows reasonable ACh depletion as a function of stimulation rate and synthesis, supported by experimental data (Figure 23, Figure 24).

2.5.4 ACh-M2 affinity

Neither the Dokos nor Demir model includes explicit M2 muscarinic receptor activation. We model M2 activation by ACh using a standard Hill equation, with an experimentally measured affinity (K_{MM}), and a Hill coefficient n_M needed to reproduce downstream data. We use the value K_{MM}=0.3 μM, based on the half-activation concentration of $I_{K,ACh}$ measured by DiFrancesco et al. (88). As pointed out by the authors, this value is similar to that measured in another isolated cell preparation by Breitwieser and Szabo (0.16 μM) but much lower than that measured in whole SA node tissue by Osterrieder et al. (1.7 μM) (38, 88, 264). We suspect that Osterrieder et al. observed a lower affinity because of they used tissue slices rather than isolated cells. As we show in Figure 27, the effect of neurotransmitter applied in the BS compartment of our model yields lower apparent affinities for both receptors; since whole SAN tissue would likely have some components of the ECM intact, it is likely that the local ACh concentration at the cell membrane was lower than Osterrieder et al. expected due to the activity of AChE. In further support of this argument is data from the same study, where the $I_{K,ACh}$ affinity for ACh was measured in the presence of the AChE inhibitor neostigmine (see Figure 30). This data yielded a half-activation value in line with the observations in isolated cells (88, 160, 264). This issue is discussed further in our $I_{K,ACh}$ activation model (section 6.3). On the other hand, Lazareno and Birdsall mention a much lower K_D of 1 nM for ACh with M2 muscarinic receptors (see bottom of right column, page 363 in (203)). This extremely high affinity would have caused receptor saturation for ACh concentrations in the high μM range, and would not have allowed us to reproduce the measured ACh effects on $I_{K,ACh}$, $I_{Ca,L}$, I_f and P_{up} (see Chapter 6).

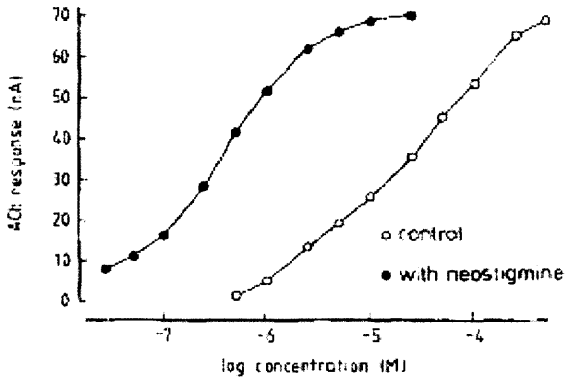

Figure 30 AChE inhibitor neostigmine shifts the apparent activation curve for $I_{K,ACh}$ to the left in experiments done on whole SAN tissue. X axis shows the log [ACh], and the y axis shows the peak $I_{K,ACh}$ current elicited during voltage clamp to -40 mV. Figure taken from Fig 1 in (264).

2.5.5 NE model compartments and receptor populations

Our NE release model is shown in Figure 31. It features six compartments, just like the ACh model: the number of adrenergic vesicles ($N_{v,NE}$), NE concentrations in the neuroeffector junction, EJS, and ECM ($[NE]_{NJ}$, $[NE]_{EJS}$, and $[NE]_{ECM}$), and bound β-AR in the neuroeffector junction and EJS ($[NE\beta]_{NJ}$ and $[NE\beta]_{EJS}$). It is difficult to compare his model with those of Dokos and Demir because they did not include neural release of NE. In fact, Dokos did not model adrenergic effects at all, and Demir only modeled bath application of the adrenergic agonist Iso. In effect, the Demir model includes a single compartment with a constant Iso concentration; it interacts with the cell by affecting cAMP production, which in turn affects ion channel properties. Our model, on the other hand, includes the compartments that have been observed in micro-anatomical studies, and the interaction of neurotransmitter between compartments is based on the same first principles and physical measurements used for the ACh model. This illustrates the main advantage of the "bottom-up" modeling approach we undertook. While the functional effects of ACh and NE on the SANC are very different, going down to the molecular level allowed us to build a general framework (diffusion-connected compartments) of simple reactions (binding, diffusion, active transport, hydrolysis) that is the same for both. Furthermore, we were able to use experimental data on the kinetics of these simple reactions and were rewarded by observing the expected high-level phenomena.

As detailed as our model is, some details were not included. On the topic of different receptor populations, we model junctional and extrajunctional β-AR, and although the current model does not differentiate the two in terms of intracellular effects, it leaves the doors open for future refinement as data on receptor/channel/second messenger localization becomes available. We also did not differentiate

between β_1 and β_2 receptors for reasons mentioned in section 2.3.5. These two simplifications of our model may prove to be important, since new data is emphasizing more and more the importance of subcellular compartmentalization on signal transduction (see section 6.7).

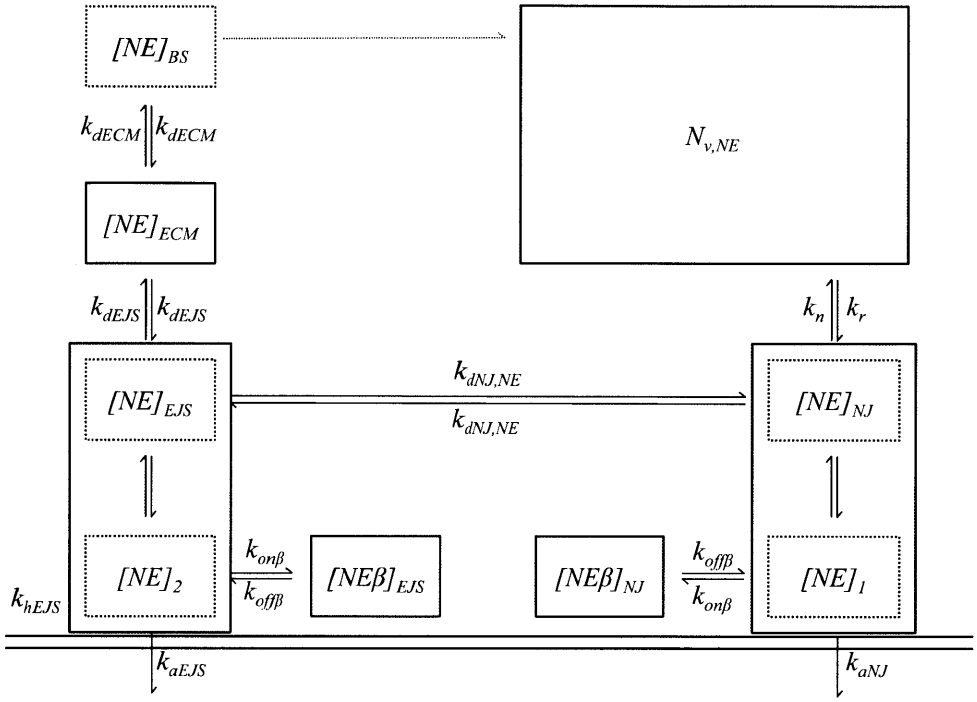

Figure 31. Reaction diagram for NE release, diffusion, clearance, binding, and synthesis. Solid lines delineate compartments that are explicitly modeled, dashed lines show compartments that have been lumped together either because diffusion between them is instantaneous ($[NE]_{NJ}$ and $[NE]_1$, $[NE]_{EJS}$ and $[NE]_2$) or because they are assumed to be constant with time ($[NE]_{BS}$). The six compartments are described by six differential equations, see section 9.5.2; for a key of abbreviations see Table 22.

2.5.6 NE diffusion and clearance

Since the Demir model simulated bath applications of Iso, no dynamic processes were included. We followed the same approach as for ACh: calculating diffusion coefficients based on diffusivities and compartment geometry, and using a mechanistic model for NE clearance through neural reuptake, cell absorption and diffusion. We chose the maximal rates of NE reuptake and absorption in order to replicate the experimentally observed clearance ratios (Figure 22). The maximal reuptake rate we chose (v_{maxn}=18.5 amol/s/cell) can be converted to a rate of 1.12×10^7 molecules/s/cell, whereas the measured rate of 1.180 nmol/min/g tissue (161) converts to 4.15×10^4 molecules/s/cell (for conversions, see section 9.2). Similarly, the maximal cellular absorption rate in our model is equivalent to 6.96×10^7 molecules/s/cell, whereas the measured rate of 100 nmol/min/gram tissue (163) converts to 3.52×10^6 molecules/s/cell. In both cases, we use faster reuptake and absorption rates than measured. This could be due to species

differences between rabbit and rat (measurements were in rat), experimental error, or perhaps our diffusion rate for NE is too fast. Since the diffusion rate was calculated rigorously and matches data fairly well, and since the reuptake rate we used is 1000 times faster than the measured value, while the absorption rate is only 10 times faster, we do not think that the discrepancy is due to an incorrect diffusion rate. We mention this issue for completeness and conclude that further experimental data would be needed to better quantify these NE clearance mechanisms.

2.5.7 NE synthesis

Our NE replenishment model describes two processes: reuptake of NE from the neuroeffector junction, and synthesis of NE from L-tyrosine (not explicitly modeled) in the BS. We chose the simplest synthesis model, wherein the varicosity attempts to maintain the maximal level of NE-filled vesicles. This process is described with a time constant that was set to a value small enough to allow stimulation without depletion in the physiologic range (<10 Hz) (162). It is unclear whether NE depletion is a physiologic process that needs to be accounted for however, since the model of dog HR by Warner and Cox successfully reproduced experimental data using a fixed NE store (349).

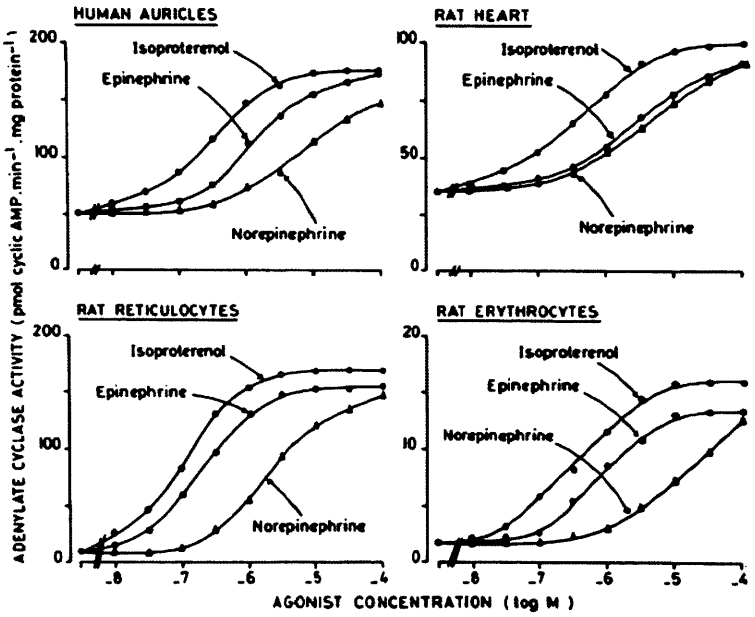

Figure 32. Iso is a more potent β-adrenergic activator than NE. Figure taken from Waelbroeck et al. (345). The y-axis shows the rate of AC activity as a measure of β-AR activation, since AC is activated by β-AR-activated stimulatory G-proteins (for detail, see section 3.3).

2.5.8 *NE-β-AR affinity*

While the Demir model does not include explicit β-AR binding, they use a term with an affinity for Iso of 0.14 μM in their cAMP specification (81). Since Iso binds β-AR with higher affinity than NE (about a factor of 10-100, see Figure 32), this value is in fairly good agreement with the 1.5 μM affinity for NE that we use. The Hill coefficient we use is not unity however, which implies cooperative binding. Since β-ARs only have a single site for ligand binding, this reaction should in theory have a Hill coefficient of 1. Non-unity Hill coefficients are often used in modeling as an empirical tool rather than to imply a specific mechanism, and it is in this spirit that we use it. As we pointed out, β-ARs can exist in low- and high-affinity states (307), so we use the Hill coefficient to represent the sum of these two affinities, which has the effect of decreasing the total slope of activation.

2.5.9 *M2, AChE, and β-AR dynamics*

We assume that the abundances of M2-muscarinic receptors, AChE, and β-AR do not change with time. This is in line with the Dokos model and Demir model. However, it is not true, as AChE has been shown to change with half times of 12 hours -3 days (195) M2 muscarinic receptors desensitize by being removed from the cell membrane (333), and β-AR are known to desensitize due to phosphorylation with half times on the order of 10 minutes (31). Because these half-times are rather long compared to reasonable stimulation protocols of the neurotransmitter release model, we assume that receptor and enzyme concentrations are constant. Furthermore, this data further supports our use of non-unity Hill coefficients for M2 and β-AR binding, as desensitization processes would cause shifts in affinity or total rate with time.

2.5.10 *Direct inhibition of β-adrenergic activity by vagal stimulation*

Neither the Dokos nor Demir models include direct inhibition of β-AR effectiveness. We found this interaction necessary only under high vagal stimulation rates and non-zero sympathetic stimulation. In contrast, Dokos et al. did not model sympathetic effects, and Demir et al. did not study the effect of simultaneous β-adrenergic and cholinergic stimulation. Thus, these studies did not model this cholinergic-β-adrenergic interaction because it was outside their modeling aims. As we briefly mentioned in the description of X, we only added this term when it became necessary to reproduce HR data. Although Levy (210) proposes various opportunities for presynaptic interaction that would result in modified NE release due to vagal activity, we model the interaction as an intracellular process. This approach seemed more reasonable because it does not force us to commit to a particular mechanistic explanation: the reduction in β^* could be the result of reduced NE release, reduced β-AR abundance, reduced β-AR affinity for NE, reduced β-AR affinity for G-protein, reduced catalytic rate of β-AR for activating G-

protein, or any combination of the above. Many of these changes may be mediated by intracellular modifications of β-ARs such as phosphorylation, which most likely cause conformational changes in the protein, and may lead to the functional changes mentioned above. The fact that our model indicates the necessity for direct cholinergic-adrenergic interaction, and the mechanistic uncertainty surrounding this issue both point to the need for further experimentation and better understanding of this phenomenon.

2.6 Conclusion

We created a novel model of neurotransmitter release and M2-muscarinic and β-AR activation in the rabbit SANC based on the current mechanistic understanding and experimental kinetic data. The model reproduces macro-phenomena such as the fast activation of M2 muscarinic receptors, and the slow activation of β-AR. ACh diffusion and hydrolysis rates reproduce experimental values, as do the rates of NE neural reuptake, absorption, and diffusion. It is also interesting to note that the ACh hydrolysis is responsible for both reduced M2 receptor activation and fast rate of deactivation following cessation of stimulation, while NE clearance mechanisms also decrease the peak β-AR activation but only slightly affect the rate of deactivation. Furthermore, the rate limiting step in sympathetic modulation of HR appears to be receptor activation, because the observed time constants for β-AR activation are on par with HR changes elicited by sympathetic nerve stimulation. This is not the case for M2 muscarinic receptors, which have an almost instantaneous activation, so the rate limiting steps for parasympathetic HR modulation actually emerge intracellularly, through the more sluggish second messenger cascade. We also proposed a plausible inhibitory effect of cholinergic activity on β-ARs, which is supported by experimental observations, and allowed us to reproduce experimental HR data over the full range of physiological vagal and sympathetic stimulation (Figure 105 g,j,k).

No model is complete without a list of limitations. In our case, the limitations stem from uncertainty in the experimental measurements of rate constants and other physical parameters, and simplifying assumptions (diffusion being modeled as a single rate constant, that junctional and extrajunctional receptors are identical, quantal release). We also assume that cell membrane-localized receptors are static, in the sense that their numbers or affinities do not evolve with time. However, the explicit nature of our model framework allows relatively easy changes to these assumptions as more experimental data becomes available.

In all, our neurotransmitter release model was rigorously developed and compares favorably with existing models, setting the stage for quantifying the intracellular processes that ultimately affect SANC properties and HR.

3 G-PROTEINS (EC 3.6.5.1) AND ADENYLATE CYCLASE (EC 4.6.1.1)

3.1 Overview

This chapter describes the intrinsic GTP turnover cycle of G-proteins, the facilitation of this process by activated (ligand-bound) β-adrenergic and M2 muscarinic receptors, the properties of adenylate cyclase, and the nature of the interaction between activated G-proteins and adenylate cyclase as highlighted in Figure 33.

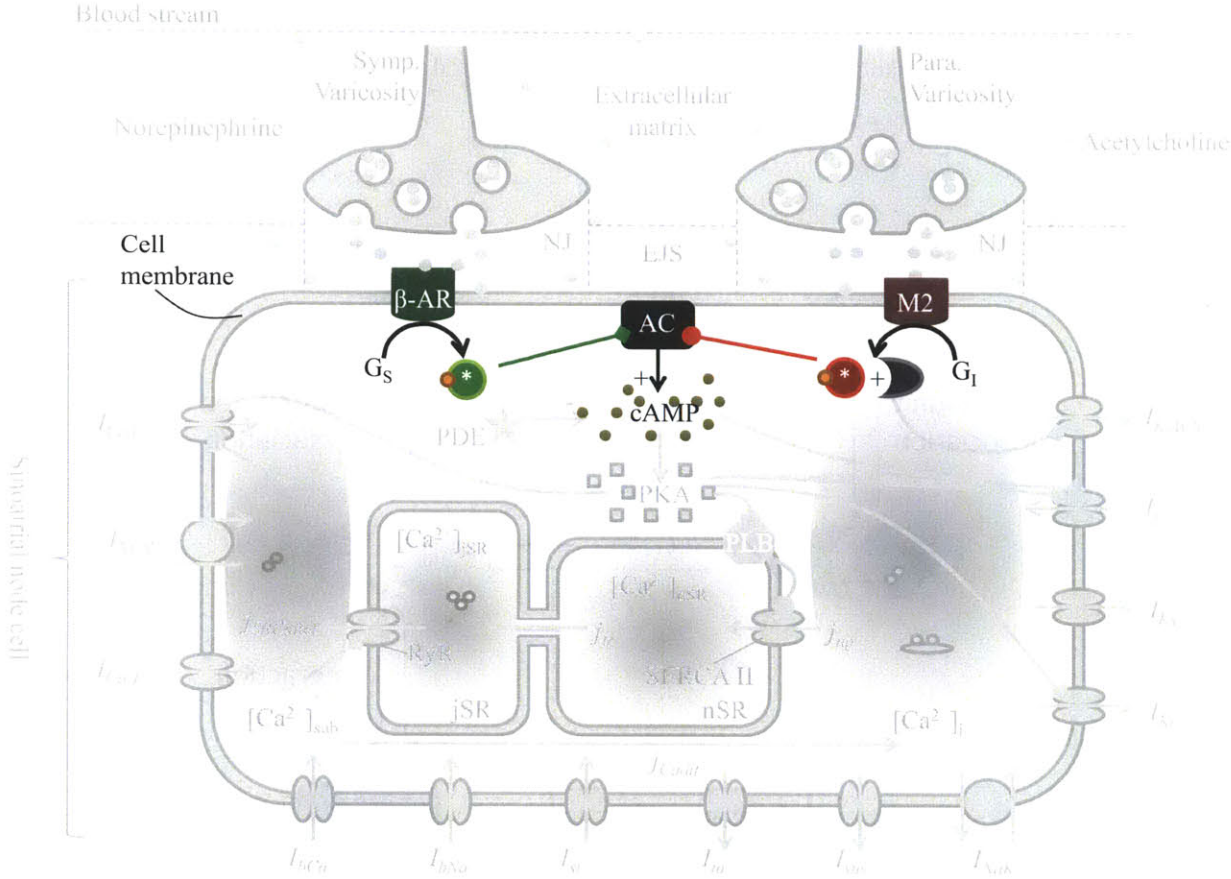

Figure 33. High level illustration of G-protein activation and modulation of adenylate cyclase in the context of the entire model originally shown in Figure 4 (see original figure for key).

G-proteins

- G-proteins are heterotrimers, consisting of α, β , and γ subunits
- The stimulatory (G_S) and inhibitory (G_I) G-proteins differ in α subunit only
- Stimulatory and inhibitory G-proteins have a similar activation mechanism: the α subunit is activated when it binds GTP and dissociates from the βγ subunits (which stay bound). Activated α and free βγ subunits serve as second messengers inside the cell. The α subunit has an intrinsic catalytic ability, hydrolyzing GTP to GDP and inactivating itself. The activation steps are

catalyzed by liganded β-adrenergic (for stimulatory G-proteins) and M2 muscarinic (for inhibitory G-proteins) receptors. See Figure 34.

- The rate coefficients for each component reaction are derived through detailed re-analysis and reproduction of historic G-protein data/experiments, summarized in Figure 65.
- Both G-protein models reproduce the measured steady-state GTP turnover rates at baseline and with adrenergic or cholinergic stimulation (see Figure 66). G-protein abundances are based on experimentally measured values
- The activation of G-proteins by activated β-adrenergic and M2 muscarinic receptors is modeled using standard Michaelis-Menten kinetics, and measured receptor-G-protein affinities and maximal catalytic velocities.

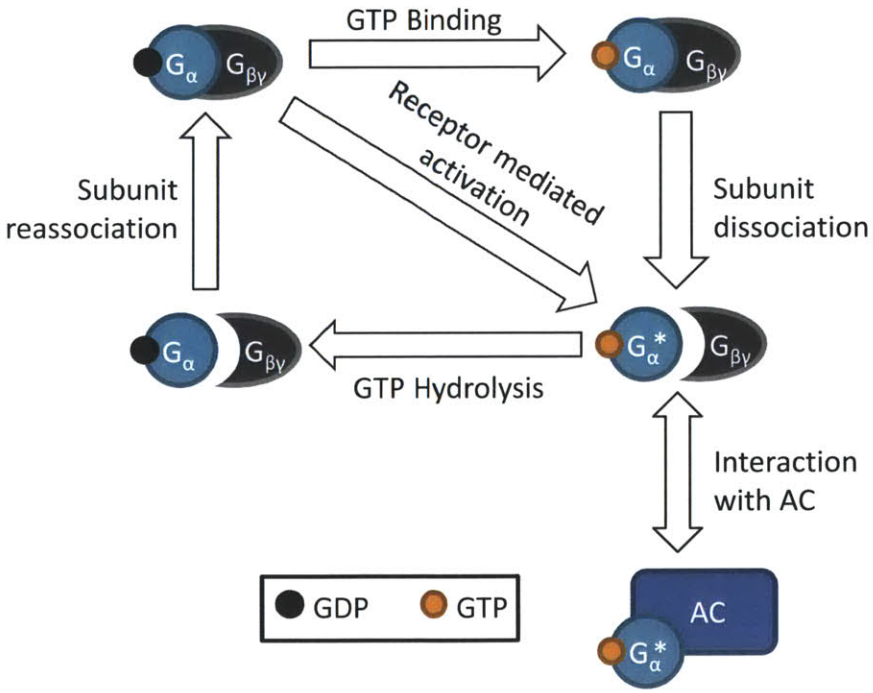

Figure 34. The G-protein activation-inactivation cycle. G_α*: activated α subunit, must be dissociated from βγ and bound to GTP in order to be activated. The other three –protein states are inactive and do not interact with adenylate cyclase (AC). Activated β-adrenergic or M2 muscarinic receptors catalyze the GTP-binding and subunit dissociation steps.

Adenylate Cyclase

- Adenylate cyclase synthesizes the second messenger cAMP
- The abundance of adenylate cyclase, and its baseline, stimulated, and inhibited rates of cAMP production are based on experimental measurements
- Adenylate cyclase activity is modulated by competitive binding of activated stimulatory or inhibitory G-proteins

Results

- G-protein activation is not rate-limiting for either sympathetic or parasympathetic effects (see Figure 67 compared to receptor activation in Figure 24)
- Modulation of adenylate cyclase rate through binding with activated G-proteins is the main venue for sympathetic-parasympathetic interactions (see Figure 69)

3.2 Introduction

G-proteins link the activation of β-AR and M2 muscarinic receptors on the cell's surface to the generation of intracellular second messengers. Because their main role is to activate G-proteins, the M2 muscarinic and β-AR of the heart belong to the family of G-protein coupled receptors (GPCRs). For a review of GPCR structure and function, consult Gilman 1987 and Taylor 1990 (323). Here, we present a brief summary.

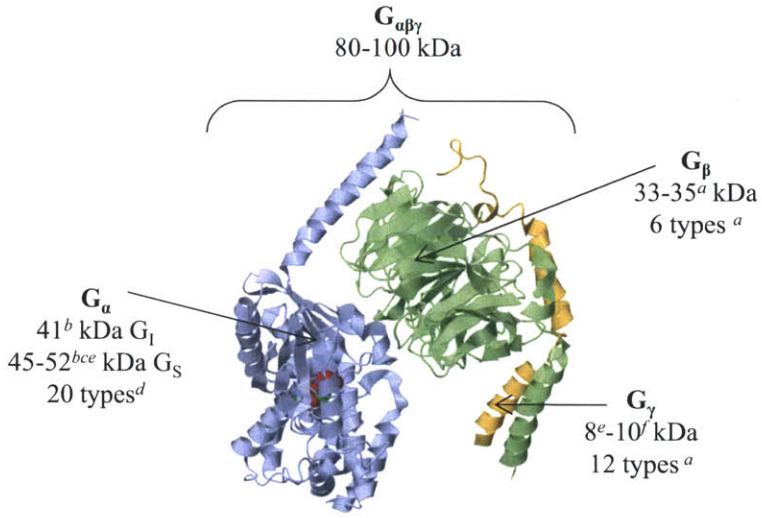

Figure 35 G-protein structure and atomic weights of its subunits. G-proteins are heterotrimeric, consisting of three distinct subunits: α, β, and γ. In the early literature, before these names were adopted, the subunits were referred to by their molecular weight. It is now understood that the G_α subunit is the business-end of this protein, as it binds the guanine-nucleotide GTP, hydrolyzes it to GDP, and the type of α subunit specifies its end-effector and ultimate role. Binding of GTP causes the dissociation of the G_α from the βγ subunits, and both parts effect changes within the cell. The βγ subunit is tethered to the cell membrane, while the dissociated G_α subunits are free to diffuse throughout the cytoplasm. References: *a* (66), *b* (257), *c* (122), *d* (315), *e* (36), *f* (29). Image from Wall 1995 (346) and Jena Library of Biological Images (PDB 1gg2).

Three major components exist in the GPCR signal transduction cascade: the receptor, G-protein (see Figure 35), and end effector. Each of these components exists in a basal (low activity) form as well as an activated form (denoted by * in figures). In Figure 36, we diagram the process of G-protein activation: A GPCR (A) is activated when it binds ligand (B), in this case, ACh or NE. The activated GPCR catalyzes the activation of the G-protein, by facilitating its release of GDP and binding to GTP (C). The activated G-protein α subunit then dissociates from the GPCR and the membrane-tethered $G_{\beta\gamma}$ subunit (D) and can

bind the end effector. Figure 36 A-D illustrate the activation of the stimulatory G-protein (G_S) by β-adrenergic receptors. M2 muscarinic receptors follow a similar G-protein activation mechanism, however they are linked to an inhibitory G-protein (G_I) (E). It is also of note that while the GPCR is activated (D and E), it can catalyze GDP-GTP exchange for a number of GDP•$G_{S\alpha\beta\gamma}$ (6-8 per active receptor (35)).

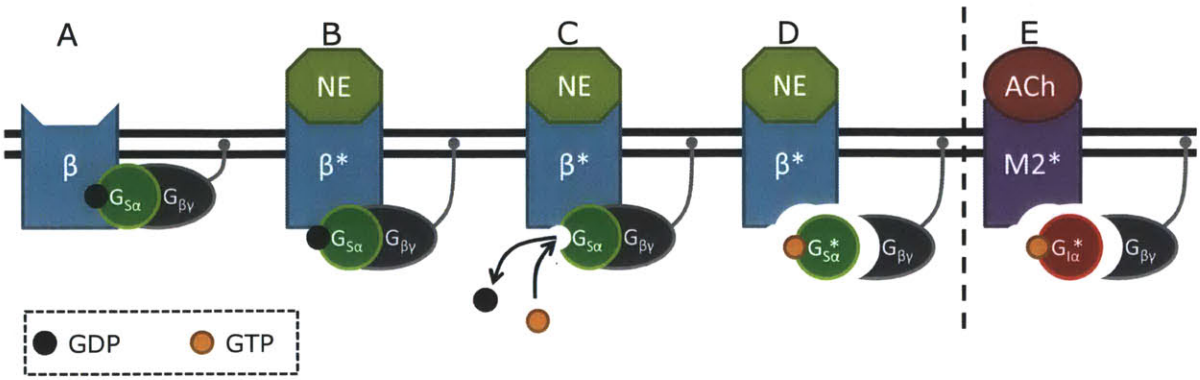

Figure 36 Activation of stimulatory $G_{S\alpha}$ and inhibitory $G_{I\alpha}$ G-proteins by β-adrenergic and M2 muscarinic receptors, respectively. See text for description of steps A-E.

Activated G-proteins regulate AC. For a detailed review of AC function and regulation, see Patel et al. 2001 and Iyengar 1993 (164, 269). Briefly, ten isoforms of mammalian AC have been identified: membrane-localized AC I-AC IX and one soluble form (for reviews see (164, 269)). The major isoforms in cardiac tissue are AC V and VI (164, 269), and AC serves a critical function in SANC as over-expression of AC VI was recently shown to confer pacemaking ability to ventricular cells (288). All AC subtypes catalyze the conversion of ATP to cAMP, but some differences in regulation by the G proteins exist. For this reason we limit our discussion to AC V and AC VI, to which we refer simply as AC.

Modulation of the catalytic rate of AC by activated G proteins is illustrated in Figure 37. In its basal state, AC catalyzes the production of cAMP from ATP (A). Binding of activated $G_{S\alpha}$* stimulates cAMP production by stabilizing the AC dimer (B), while binding of activated $G_{I\alpha}$* destabilizes the dimer and virtually abolishes its activity (C) (164, 269). There is also evidence that the βγ subunits can directly stimulate or inhibit some AC subtypes (67, 178, 315), however for AC V and AC VI only an indirect effect is believed to occur through sequestration of $G_{S\alpha}$ (D) ((256, 282), reviews: (164, 269, 310)).

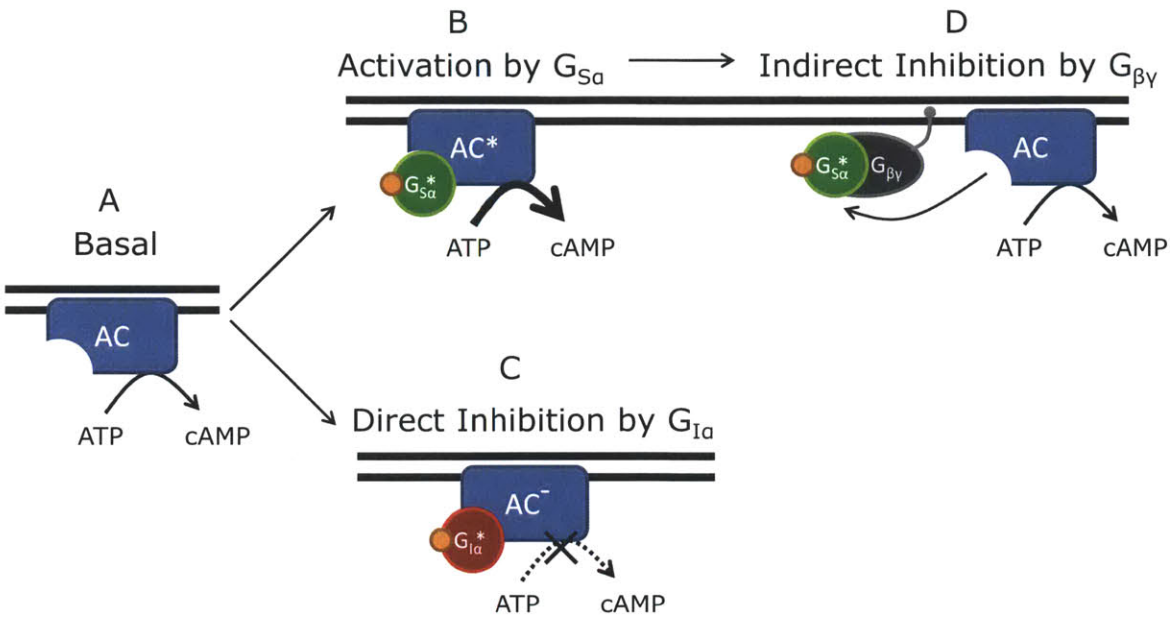

Figure 37 The baseline catalytic rate of AC (A) is increased by $G_{S\alpha}$ (B) and reduced by $G_{I\alpha}$ (C), through direct binding with a regulatory site. Two distinct sites exist, one for $G_{I\alpha}$ and another for $G_{S\alpha}$; since binding by either induces conformational changes that may alter the unoccupied binding site (269), we conclude that only one G-protein can bind at a time. Activation of $G_{\alpha I}$ also increases available $G_{\beta\gamma}$ which indirectly "inhibits" AC by competing for $G_{S\alpha}$ (D). Some experimental results have been interpreted to mean that $G_{\beta\gamma}$ can also directly inhibit or activate AC; we assume that this direct action of $G_{\beta\gamma}$ does not occur, and rather that the effects of $G_{\beta\gamma}$ on AC activity are through buffering G_S or G_I as espoused by Gilman (122).

G-proteins have an intrinsic control to limit the duration of their signal, as shown in Figure 38. The G_α subunits of both stimulatory and inhibitory proteins are GTPases, which hydrolyze GTP to GDP, releasing P_i and inactivating themselves (B). The inactivated G-protein has a reduced affinity for AC, and therefore unbinds and is reunited with a $G_{\beta\gamma}$ subunit (C).

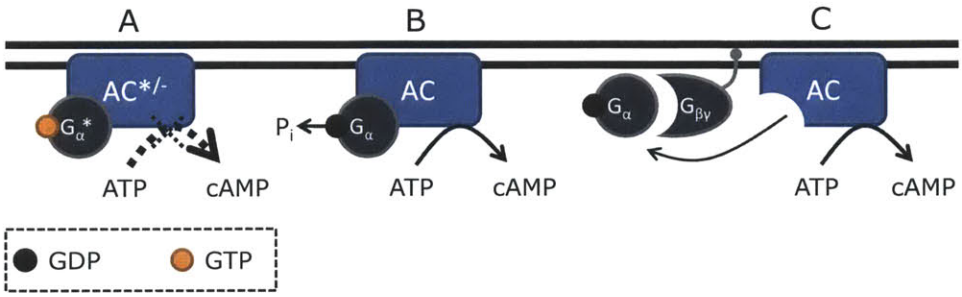

Figure 38 Regulation of AC activity by activated G_α subunits (A) of both G_S and G_I terminates when the G_α hydrolyzes the bound GTP (B), thereby decreasing its affinity for AC and increasing its affinity for $G_{\beta\gamma}$ (C).

In the following sections, we quantify the intrinsic GTP turnover cycle of stimulatory and inhibitory G-proteins, their activation by β-AR and M2 muscarinic receptors, and their interaction with AC.

Unfortunately, the G-protein literature does not report explicitly the rate constants needed to describe the intrinsic GTP turnover of G proteins. We derive these rate constants by re-analysis of the pertinent experimental data. In most cases, the data we analyzed were digitized from figures in published papers so we include the original figure and the digitized versions to show that digitization was done properly.

3.3 The Stimulatory G-protein G_S

In this section we detail the intrinsic function of G_S; we leave the activation of G_S through interaction with β-AR for section 3.5. First, we consider the abundance of stimulatory G-protein in mammalian cells. A number of measurements are listed in Table 4, from which we conclude a reasonable value for G-protein abundance of 2×10^6 molecules, which for the sake of all the reactions, we consider dissolved in the entire cytoplasmic volume of the SANC to yield a total concentration G_{ST}=2 μM. Although the βγ subunits are tethered to the cell membrane, this assumption is justified by the fast rate of diffusion estimated to occur within the SANC (see section 9.4).

Table 4 Abundance of G-protein in mammalian and insect cell membranes.

Source	System	Measured amount (pmol/mg membrane protein)	Number per cell
Neubig et al. 1985	Human platelet G_I	25.8	$3.1\text{x}10^6$
Mosser et al. 2002	Insect Sf9 G_I	50*	$6.0\text{x}10^6$
Bokoch et al. 1984	Rabbit liver G_I	42†	$5.0\text{x}10^6$
	Rabbit liver G_S	17.5‡	$2.1\text{x}10^6$
Ransnas et al. 1992	Mouse S49 G_S	19.3	$2.3\text{x}10^6$

* from a maximum amount of $GTP_\gamma S$ binding to membranes of 50 pmol/mg protein. † reported value is 300 nmol G_I per 7,082 mg protein. ‡ purification of G_I yielded 1.05 mg (5% recovery of original amount) and G_S yielded 0.347mg (4% recovery). Assuming comparable molecular weight of G_I and G_S, the ratio of the original abundances is (1.05/0.05)/(0.347/0.04)=2.4, we used this ratio to calculate pmol G_S from the reported value for G_I.

The kinetics of stimulatory G-protein were probed by Northup et al. in 1982-1983 (255-257). Below, we reproduce the model and summarize pertinent experiments for determining the rate constants.

The stimulatory G-protein has the following characteristics:

1. $G_{S\alpha}$ is activated by binding GTP and dissociation from $G_{\beta\gamma}$ (255-257)
    a. Dissociation is promoted by binding of GTP or F^- and Al^{3+} (256, 257)
    b. $G_{S\alpha}$ is deactivated by GTP hydrolysis or binding $G_{\beta\gamma}$ (256)
2. $G_{S\alpha}$ contains a single GTP binding site (255)

a. Under physiologic [Mg^{2+}], GTP binding to dissociated $G_{S\alpha}$ is irreversible ((255) Fig 4)
b. GTP binding activates $G_{S\alpha}$ by promoting dissociation from βγ subunits and increasing affinity for effector (AC)

3. GTP is in rapid equilibrium with $G_{S\alpha}$, followed by a rate-limiting $G_{S\alpha}$-$G_{\beta\gamma}$ dissociation step (255)

The G_S activation model presented by Northup et al. (256) is reproduced below. We consider free, GDP-bound $G_{S\alpha}$ to be inactivated in the sense that its affinity for AC is very low. This idea is supported by the observation that GTP binding produces a conformational change in the $G_{S\alpha}$ effector-binding site and that this conformational change increases affinity (70, 300). This model is consistent with the data and models presented by both Northup et al. (256) and Brandt and Ross (36). We go into the details of each reaction (A-F) below.

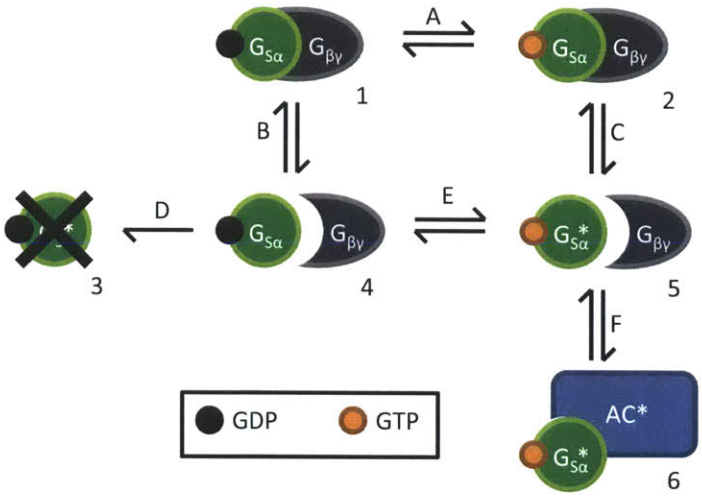

Figure 39 Overall state diagram for activation of stimulatory G protein and subsequent activation of AC. States are numbered 1-6 and reactions are specified by letters A-F.

3.3.1 A. Guanine nucleotide exchange/hydrolysis, $G_{S\alpha\beta\gamma}$

Reaction A is a reduction of the full model that includes an intermediate state where $G_{S\alpha\beta\gamma}$ is not bound to nucleotide (similar to Fig. 9 in (35)):

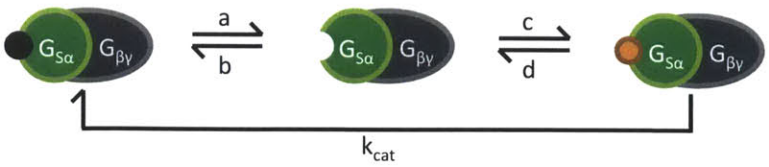

Figure 40 Diagram for reaction A in Figure 39, showing the intermediate state.

The simplest reaction to consider is the binding of GTP, described by rate constants c and d. This reaction is considered to be in rapid equilibrium (c+d is large) (35, 255), with a dissociation constant K_d=0.1μM (35). This value is smaller than what was measured by Northup et al. (1.3μM) (255); we choose the smaller value because Northup et al. conducted experiments in solution and mention that the affinities they observed were an order of magnitude less than what is seen in plasma membranes. Brandt and Ross (35) used phospholipid vesicles to simulate the presence of a plasma membrane, and they report the value of 0.1μM. Another simplifying circumstance is that the physiological plasma concentration of GTP in cells (~25-100μM) (38, 281) is significantly higher than the measured dissociation constant for GTP. Thus, the reaction is essentially *irreversible* and *rapid*, allowing us to ignore the intermediate state and yielding the A reaction illustrated in Figure 39.

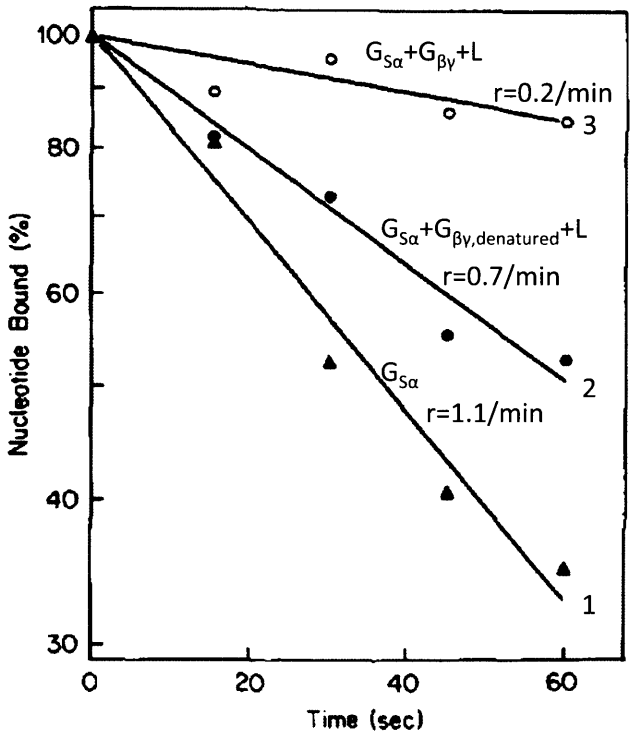

Figure 41 Rate of GDP dissociation in the presence or absence of $G_{\beta\gamma}$, taken from (36). $G_{S\alpha}$ was pretreated with [α-^{32}P]GTP, which quickly hydrolyzes to [α-^{32}P]GDP; the figure shows the amount of bound ^{32}P under three conditions: 1 contained isolated $G_{S\alpha}$ and a very low concentration of the detergent Lubrol; 2 contained isolated $G_{S\alpha}$ as well as buffer with heat-denatured $G_{\beta\gamma}$ and a high concentration of Lubrol; 3 contained isolated $G_{S\alpha}$ and buffer with active $G_{\beta\gamma}$ and a high concentration of Lubrol. The dissociations proceeded with rates indicated on the figure. From lines 1 and 2, the presence of a higher Lubrol concentration seems to decrease the GDP dissociation rate by ~40%.

The leftmost reaction, described by rates a and b concerns the dissociation of GDP. This has classically been considered the rate limiting step in the activation of G-protein and in the full-cycle hydrolysis of

GTP (see Introduction in (35) for a summary, (122) for review). The dissociation rate of GDP is reported by Brandt and Ross to be 1.3-1.7/min at 30 °C (Fig 6 in (36)) but other data in the same paper show fast and slow dissociation rates of 0.7-1.1 /min and 0.1-0.2 /min, respectively (Figs 5 and 7 in (36), the latter is reproduced in Figure 41). The authors' interpretation of the data may have been confounded by their hypothesis that GTP association (rather than GDP dissociation) is the rate limiting step, and they note that this rate limiting step proceeds at 0.43/min at 30°C (36). This is on the same order as the GDP dissociation rate measured for G_I (0.3/min at 22-24°C (38)) and G_O (0.03-0.3 /min at 20°C (146-148)). It is also similar to the 0.2/min GDP dissociation rate in the presence of $G_{\beta\gamma}$ shown in Figure 41. We conclude that a is approximately 0.4/min, to match not only the apparent GDP dissociation rate, but also the overall GTP hydrolysis rate in which this is the rate limiting step (see Table 6). A further simplification can be made because the intermediate is rapidly converted to the GTP bound form: as soon as a GDP is released, a GTP takes its place virtually irreversibly. Therefore the rate of GDP binding is very low, and b can be ignored. The only remaining way that $G_{S\alpha\beta\gamma}GDP$ can be created is through hydrolysis of GTP, which happens with rate k_{cat}=10/min (see Table 5). The overall reaction A is:

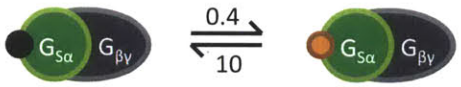

Figure 42 Reduced form of Figure 40, showing rate constants in units of /min. Simplifying circumstances are the rapid equilibrium and abundance of GTP, which make both dissociation of GDP and binding of GTP essentially irreversible.

The equality of the models presented in Figure 40 and Figure 42 was tested by assuming that [GTP] = [GDP] = 50 μM. The [GTP] value falls within the measured range (38, 281) and the [GDP] is actually a 'worst case' assumption because a high [GDP] would shift the reaction to the left and most stringently tests the idea that the dissociation of GDP is irreversible. The K_d for GTP is 0.1μM, and for GDP it is 0.3μM (using the value of 3 μM reported in (255), and decreasing an order of magnitude to compensate for the lack of plasma membrane as was done for GTP). Since K_d= a/b for GDP, and a=1 /min, then b=3.3/min/μM GDP. At 50 μM, this rate is b=167/min. Doing similarly for GTP, where K_d=d/c, we see that c=10d /min/μM GTP, so at 50 μM, this is c=500d/min. The value of d has not been measured, but is expected to be large to satisfy rapid equilibrium. Even if we assume a relatively low value of d=10/min, the models of Figure 40 and Figure 42 produce very similar results, as shown in Figure 43:

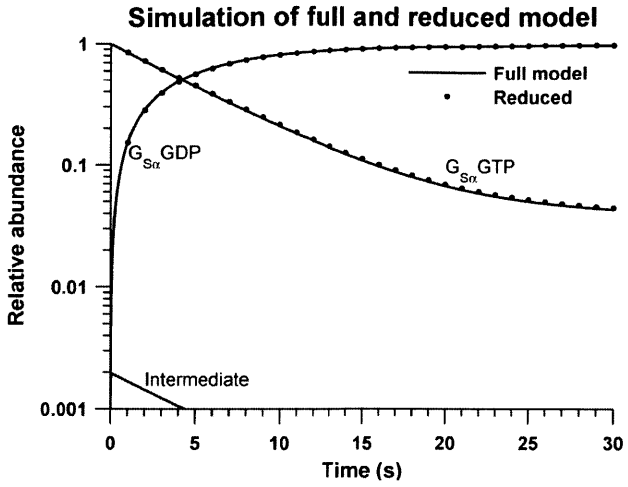

Figure 43 Comparison of full and reduced model for reaction A. Parameters described above were used, with solid lines representing the solutions to the full model and points showing the reduced model. The initial condition on the system was that all of the G protein was bound to GTP, lines as labeled. At its maximal value, the intermediate state accounted for less than 0.2% of total G protein abundance.

Table 5 Measured values of k_{cat} for G_S and G_I, temperature corrected using a Q_{10} of 1.7. k_{cat} is the rate constant for the catalysis of GTP to GDP as shown in Figure 40.

Source	System	Temperature (°C)	Measured value (/min)	Value at 37°C (/min)
Cassel et al. 1977 (54)	Turkey G_S*	37	15	15
Brandt and Ross 1985 (36)	Rabbit G_S	30	8.3	12
Brandt and Ross 1986 (35)	Rabbit G_S	30	4	6
Graziano et al. 1989 (128)	Rabbit G_S	20	3.2-4.5	8-11
Linder et al. 1990 (213)	Recombinant Rat olfactory G_I	20	1.8-2.7†	4-7
Kleuss et al. 1994 (189)	Recombinant Rat olfactory G_I	20	3.4	8

* The study was done before the role of G-proteins in AC activation was known, so G protein type was not specified. The reported rate is the rate of GTP hydrolysis, which the authors presumed to be due to GTPase activity of AC. † values obtained using solution with the detergent Lubrol PX which decreases the catalytic rate of G-proteins (35, 36).

Table 6 Measured values of k_h for G_S and G_I, temperature corrected using a Q_{10} of 1.7. k_h describes the hydrolysis rate of GTP, thus it includes the full cycle of GTP→GDP catalysis and the rate-limiting step of GDP release.

Study	System	Temperature	Measured value (/min)	Value at 37°C (/min)
Sevilla et al. 1976 (292)	Turkey G_S	37	0.7	0.7
Brandt et al. 1983 (34)	Rabbit G_S	30	1-1.5*	1.4-2.2*
Cerione et al. 1984 (58)	Human G_S	30	0.3	0.4
Brandt and Ross 1985 (36)	Rabbit G_S	30	0.2-0.41†	0.3-0.6
Graziano et al. 1989 (128)	Recombinant Rabbit G_S	20	0.13-0.34	0.3-0.8
Sunyer et al. 1984 (311)	Human G_I	32.5	0.01‡	0.01‡
Milligan et al. 1985 (240)	Bovine G_I	37	0.3	0.3
Katada et al. 1986 (181)	Rat brain G_I	30	0.16-.34	0.2-0.5
Linder et al. 1990 (213)	Recombinant Rat olfactory G_I	30	.03-.1‡	0.04-0.1‡
Kleuss et al. 1994 (189)	Recombinant Rat olfactory G_I	30	0.026	0.04
Gilman 1987 (122)	G_S, G_I, G_O	30-37	0.3	0.3-0.4

* maximum observed k_h with Iso-stimulated β-adrenergic receptors. Cerione et al. 1984 also report a turnover number of 2/min with high activated β-adrenergic receptor concentrations. † Brandt and Ross also report k_h values >1.5/min, but at extremely high Mg^{2+} concentrations (>100 mM (34), compared to physiological Mg^{2+} of 2.5 mM (198)). ‡ values obtained using solution with the detergent Lubrol PX which decreases the catalytic rate of G-proteins (35).

3.3.2 B. G-protein dissociation (GDP)

Reaction B describes the dissociation of the $G_{S\alpha}$ and $G_{\beta\gamma}$ subunits, while $G_{S\alpha}$ is bound to GDP. While the dissociation reaction happens in a single step, reassociation most likely occurs through an intermediate state illustrated in Figure 44.

To obtain the function for e and the rate constant f, we consult binding studies reported by Northup et al. (256, 257). In these experiments, Al^{3+} and F^- were used to activate $G_{S\alpha}$ (dissociate it from $G_{\beta\gamma}$) and various concentrations of free G_β subunit were added while observing the rate of inactivation of $G_{S\alpha}$. At this time, the γ subunit had not yet been identified, so its presence was not specified. Judging by the molecular

weight of the β subunit reported in the study however, it seems like no γ was present. We therefore assume that the γ subunit only marginally affects the interaction between $G_{S\alpha}$ and G_{β}.

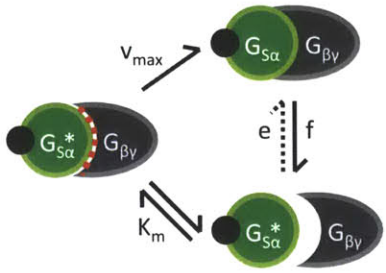

Figure 44 Schematic of reaction B, including an intermediate state (left) the presence of which is supported by data. The implicit association rate (e) is illustrated because we reduce the transition through the intermediate state to a function of $[G_{\beta\gamma}]$ and treat this as the concentration-dependent rate e. Dissociation rate (f) is also included for completeness, although it turns out to be negligible.

Figure 45A shows the time course of Al^{3+} and F^- activated $G_{S\alpha}$ subunit activity (measured as the rate of production of cAMP by AC) in the absence (top line) or presence of 1μg/mL (30 nM) of G_{β} subunit. The rate constants (slopes) of the two reactions are 0.01/min and 0.8 /min, and these rates equal the rate of $G_{S\alpha}$ deactivation through thermal denaturation or unbinding of AlF_4^- and through binding G_{β}, respectively. Figure 45B shows that the deactivation of $G_{S\alpha}$ follows Michaelis-Menten kinetics:

$$V(\beta) = v_{max}\frac{[\beta]}{[\beta]+K_m} \tag{4}$$

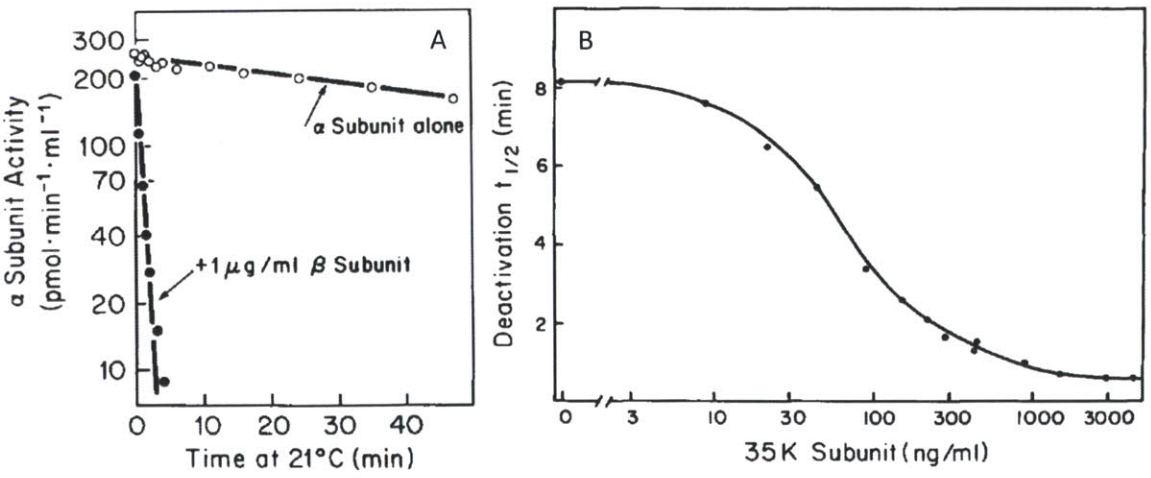

Figure 45 Binding experiment of $G_{S\alpha}$ and G_{β} subunits. Figure A is from (256) and B is from (257). The 35K subunit refers to the G_{β} subunit. A was performed at 21°C, B was at 20°C.

Figure 46 summarizes the process for obtaining the constants v_{max} and K_m from the data in Figure 45.

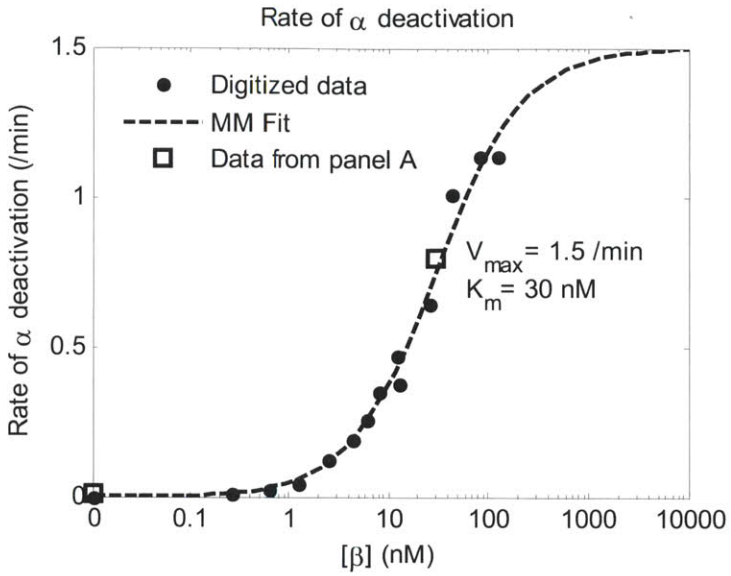

Figure 46 Michaelis-Menten fit to the data digitized from Figure 45B. The data are plotted with $[G_\beta]$ on the x axis (converted using molar weight 35 kDa) and deactivation rate (not half-time as in Figure 45; converted as $r=log(2)/t_{half}$) on the y axis. The deactivation rate was shifted down by 0.08/min to be 0 at the origin in order to cancel the rate of $G_{S\alpha}$ denaturation in the absence of G_β. The constants for the inactivation rate in Eq (4) were obtained by fitting the data in a least squares sense (`lsqcurvefit` in Matlab).

Considering all the data presented above, we conclude that rate e is a function of free $G_{\beta\gamma}$ concentration as quantified by equation (4) with parameters shown in Figure 46 for 20°C. Using a Q_{10} of 1.7 to convert v_{max} to 37°C yields

$$V(\beta) = 3.7\frac{[\beta]}{[\beta]+30nM} \tag{5}$$

Since the deactivation reaction appears to go to completion (see Figure 45A), rate f is assumed to be insignificant when compared to e. Therefore, the overall reaction is:

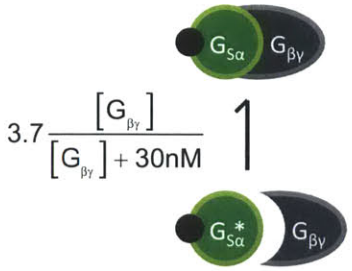

Figure 47 Complete reaction diagram for reaction B, showing the actual association rate as a function of $[G_{\beta\gamma}]$.

3.3.3 C. G-protein dissociation (GTP)

Reaction C is similar to B, except that $G_{S\alpha}$ is bound to GTP. GTP has a stabilizing effect on $G_{S\alpha}$ so the balance of this reaction is shifted toward the dissociated state (256). The simplified diagram for this reaction is shown in Figure 48.

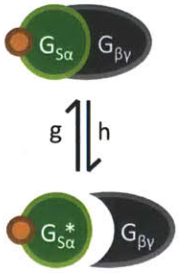

Figure 48 Schematic of reaction C, with explicit association (g) and dissociation (h) rates.

To quantify this reaction, we refer to experimental data from Northup et al. (256), reproduced in Figure 49. Since $GTP_\gamma S$ is non-hydrolyzable, the $G_{S\alpha}$•$GTP_\gamma S$ subunits are very stable and show no deactivation over 200 minutes. Addition of 20 μg/mL (0.6 μM) of free G_β subunits induces a slow deactivation of $G_{S\alpha}$.

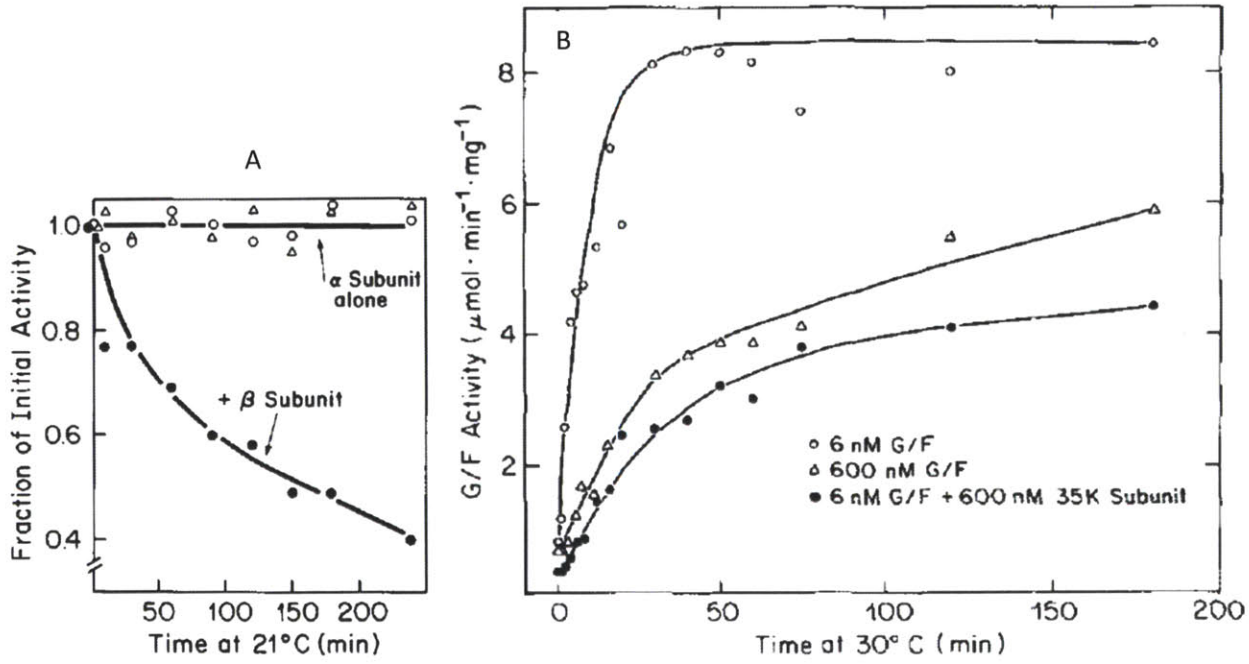

Figure 49 Deactivation of $G_{S\alpha}$•$GTP_\gamma S$ by free G_β subunit. A is from (256); the top line shows relative cAMP production rate for the system with $G_{S\alpha}$ activated by $GTP_\gamma S$ in the absence of G_β, and the bottom line shows the deactivation process with 20 μg/mL of G_β, at 21°C. B is from (255); the data shows cAMP production rate as a function of time for the indicated combinations of G-protein (G/F) and free G_β subunit (35K Subunit). Experiments done at 30°C.

The binding/dissociation reaction between G_β and $G_{S\alpha}$•$GTP_\gamma S$ as schematized in Figure 48 can be fit by the equation

$$\alpha(t) = s + (1-s)e^{-rt} \tag{6}$$

$$r = g + h; \quad s = h/(g+h) \tag{7}$$

which describes a first-order reaction with rate r that reaches a steady state value s. The data and fit of equation (6) are shown in Figure 50.

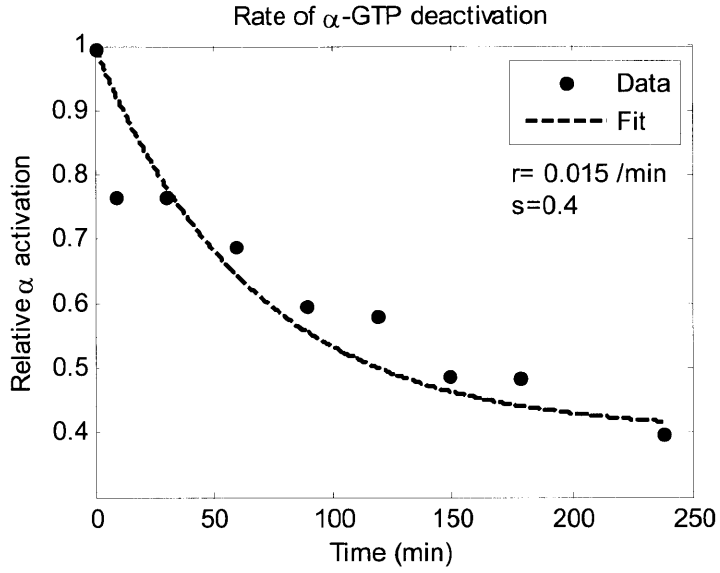

Figure 50 Exponential decay fit to the binding reaction between G_β and $G_{S\alpha}$•$GTP_\gamma S$ ('data' were digitized from Figure 49A). The parameters for equation (6) were obtained by a least-squares fit to the data, using `lsqcurvefit` in Matlab.

The data in Figure 50 give h(600 nM)= 0.006 /min and g(600 nM)=0.009 /min at 21°C, which converts to h(600 nM)=0.014/min and g(600 nM)=0.02/min at 37°C. The data in Figure 49B confirm this estimate at 600 nM G_β and add another data point for 6 nM G_β, allowing us to establish a trend. Figure 51 shows the digitized data from Figure 49B and the parameters of the exponential fits. From these data, we see that the two experiments with ~600 nM G_β have a rate of 0.03/min at 30°C, which is 0.04/min at 37°C, and agrees with the sum of h(600 nM)+g(600 nM) = 0.034/min obtained from Figure 50. Assuming that 6 nM G_β is a low enough concentration that $G_{S\alpha}$ is almost completely dissociated, Figure 51 implies h(6 nM)=0.14/min and g(6 nM)≈0/min at 30°C, or h(6nM)=0.20/min and g(6nM)≈ 0 at 37°C. This information is summarized in Table 7.

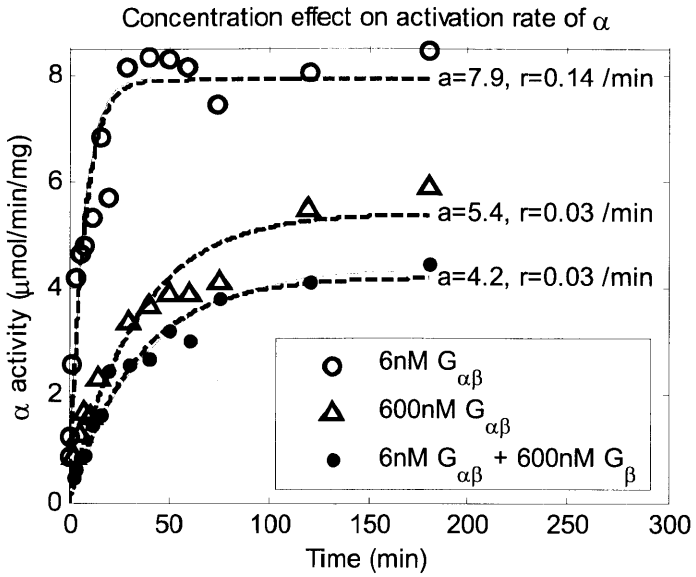

Figure 51 Inhibitory effect of G_β subunit on the rate of activation of $G_{S\alpha}$ by $GTP_\gamma S$. Data from Figure 49B were digitized (symbols) and fit with exponential functions of the form $a(1-e^{-rt})$ (dashed lines). Least squares fit parameters are shown on the figure. The red lines show model reproductions of the two conditions with 6 nM $G_{\alpha\beta}$ and 0 nM (top) or 600 nM (bottom) additional G_β. We did not reproduce the middle curve because this experiment involved the 100-fold dilution of the solution before measurement of G_α activity which could have introduced an error due to imprecision in the dilution procedure as well as promoting dissociation of G_α from G_β due to the lowered concentration.

It is expected that the association rate (g) increases with increasing G_β concentration, and this is most likely due to an intermediate state in the $G_{S\alpha}$-G_β binding process as shown for reaction B. As Northup et al. point out, and as we quantify in Table 7, the β subunit has an inhibitory effect on the rate of $G_{S\alpha}$ activation (h) (255). This observation cannot be explained simply through the increase in g, because the overall rate of activation or inactivation is actually r=g+h. As we see from the values in Table 7, h *decreases* with increasing β subunit concentration. The overall behavior of this system can be explained by a number of models, but the simplest one is diagrammed in Figure 52. Enough proof does not exist to insist that this is indeed the molecular mechanism, but it does serve the purpose of providing a mathematical form for the rate functions g and h.

Table 7 Association and dissociation rate constants as a function of G_β concentration, at 37°C.

$[G_\beta]$ nM	h (/min)	g (/min)
6	0.19	~0
600	0.014	0.02

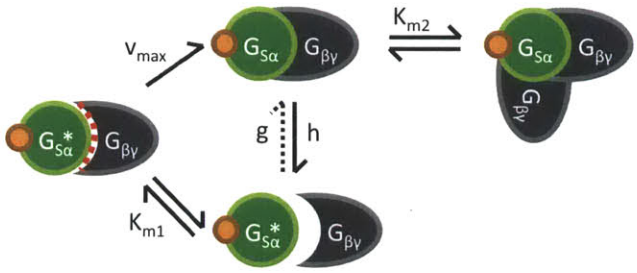

Figure 52 Potential mechanism for explaining the dependence of rates g and h on $G_{\beta\gamma}$ concentration. The increase in g with increasing $G_{\beta\gamma}$ is explained by the existence of an intermediate state, similar to the reaction in Figure 44. The decrease in h with increasing $G_{\beta\gamma}$ can be explained by an alternate state, were an extra $G_{\beta\gamma}$ unit stabilizes the $G_{S\alpha\beta\gamma}$•GTP complex. This reaction is presumed to be in rapid equilibrium with Michaelis-Menten coefficient K_{m2}. Because of the stabilizing effect of the second $G_{\beta\gamma}$ subunit, this state does not dissociate with an appreciable rate and therefore limits the amount of $G_{S\alpha\beta\gamma}$•GTP available to dissociate with rate h.

The mechanism for activation and deactivation of $G_{S\alpha}$ shown in Figure 52 is summarized by the two functions for g and h shown in Figure 53.

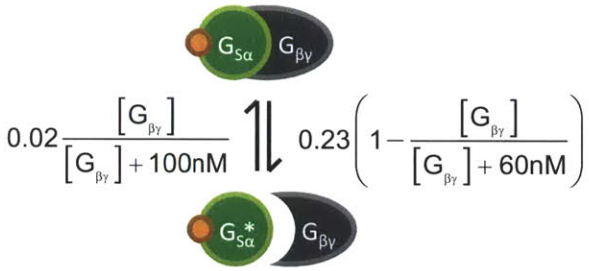

Figure 53 Reaction C with first-order rate functions based on the data in Figure 49, scaled to 37°C. This model (adjusted for temperature to 30°C) was used to generate the red lines in Figure 51.

To reproduce the data in Figure 51, we numerically integrated the following differential equation, obtained from the reaction in Figure 53:

$$\frac{d\alpha^*}{dt} = 0.23T\left(1-\frac{\alpha^*+\beta_{extra}}{\alpha^*+\beta_{extra}+60}\right)\left(\alpha_T-\alpha^*\right)-0.02T\frac{\alpha^*+\beta_{extra}}{\alpha^*+\beta_{extra}+100}\alpha^*$$

Where T=1.7$^{-7/10}$ is the temperature correction to reduce the rate to 30°C, α^* is the concentration of activated $G_{S\alpha}$ subunit (0 nM initial condition), α_T=6 is the total concentration of $G_{S\alpha}$ (nM), and β_{extra}=0 or 600 is the concentration of additional G_{β} subunit (nM).

The activation and deactivation rates as functions of $[G_{\beta\gamma}]$ are shown in Figure 54.

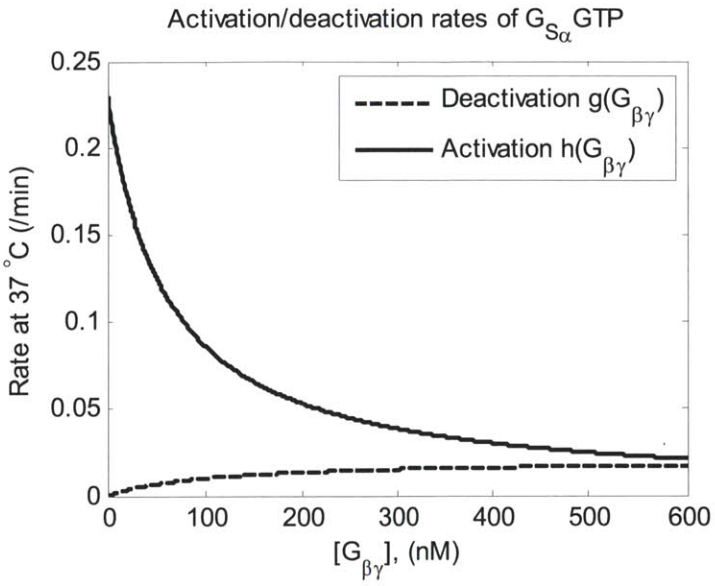

Figure 54 Free $G_{\beta\gamma}$ subunits decrease the activation rate and increase the deactivation rate of $G_{S\alpha}$▪GTP.

3.3.4 D. Thermal inactivation of $G_{S\alpha}$

Activated $G_{S\alpha}$ undergoes thermal denaturation with a rate of ~0.01-0.08/min, estimated from the data in Figure 45. Given this very low rate, and assuming that total $G_{S\alpha}$ abundance is actively regulated by the cell, we choose to exclude this reaction.

Similarly, Northup et al. report a half-time of 4 hours at 21°C for thermal inactivation of dissociated $G_{S\alpha}$▪$GTP_{\gamma}S$ (state 5 in Figure 39) in the absence of Mg^{2+} (256). This converts to a rate of 0.007/min at 37°C. For reasons discussed above, we also do not include this reaction.

3.3.5 E. Guanine nucleotide exchange/hydrolysis, dissociated $G_{S\alpha}$

Reaction E is similar to reaction A discussed above, with the only difference being that these reactions concern the dissociated form of $G_{S\alpha}$. Following the same reasoning as in reaction A, the two pertinent rates are the rate of GDP dissociation (i) and the rate of GTP hydrolysis (j):

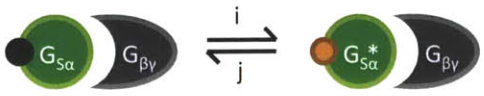

Figure 55 Guanine nucleotide exchange (i) and GTP hydrolysis (j) reactions for free and AC-bound $G_{S\alpha}$.

Rate i can be obtained from Figure 41, which shows that the GDP dissociation rate for isolated $G_{S\alpha}$ is approximately 1.1 /min at 30 °C (1.6 /min at 37 °C). Furthermore, the GDP dissociation rate for isolated

$G_{S\alpha}$ is about 4 times faster than the rate for $G_{S\alpha\beta\gamma}$ (comparing lines 2 and 3 in Figure 41; also stated in the text of (36)). Given the rate of 0.4/min we calculated for GDP dissociation from $G_{S\alpha\beta\gamma}$, we conclude that rate i is 1.6 /min. We assume that $\beta\gamma$ subunit does not affect the catalytic ability of $G_{S\alpha}$, so the catalytic rate (j) of activated $G_{S\alpha}$ is 10 /min (Table 5).

We model the activation of AC by $G_{S\alpha}$* as an instantaneous process (see section 3.6) meaning that a fraction of $G_{S\alpha}$* is bound to AC* at any time. We do not include an explicit model of guanine nucleotide exchange and hydrolysis for $G_{S\alpha}$ bound to AC, which is equivalent to assuming that binding of AC does not affect these processes. Brandt and Ross showed that interaction with AC does not stimulate the GTPase activity of $G_{S\alpha}$ (34), and they hypothesized that this interaction may decelerate the GTPase rate in order to prolong AC activation but were unable to present experimental data to this end (36). Furthermore, Cassel et al. (54) computed the decay of AC activity due to GTP hydrolysis to be 15/min at 37 °C, which is close to the assumed GTP hydrolysis rate in this model. Thus, we conclude that the GTP hydrolysis rate of AC-bound $G_{S\alpha}$ is 10 /min. We assume that AC does not bind dissociated $G_{S\alpha}$-GDP, so we do not need to consider how the rate of nucleotide exchange is affected by AC.

3.3.6 F. $G_{S\alpha}$–AC binding kinetics

The affinity of $G_{S\alpha}$* for AC was chosen to replicate data describing the cAMP synthesis rate and concentration as a function of Iso and ACh in Chapter 6. For completeness, here we report data of direct measurements of $G_{S\alpha}$ affinity for AC, and point out the inconsistency in the reported values.

Northup et al. report that activated $G_{S\alpha}GTP\gamma S$ is in rapid equilibrium with AC, with dissociation constant K_D=3 pM (256). The authors contrast this value with the significantly higher K_D observed in cyc$^-$ membranes (240 pM), but conclude that the lower value is more representative of the actual interaction between pure AC and activated $G_{S\alpha}$ (256). Interestingly, the K_D obtained by calculating the slope of the Hofstee plot of the data from Northup et al. (reproduced in Figure 56A) is 0.3 pM, not 3 pM as the body of the paper states. This prompted us to digitize and re-plot the given data with bound GTPγS concentration on the x axis (Figure 56B, see caption for procedure). Fitting this rescaled data gave higher dissociation constants, of 14-19 pM, as indicated in the figure. In this analysis, it is reasonable to equate bound $GTP_\gamma S$ concentration to activated $G_{S\alpha}$ concentration because the binding of non-hydrolyzable GTP analogs to $G_{S\alpha}$ is irreversible (255), and at these low concentrations, the dissociation reaction is essentially irreversible as well (see Figure 53). Therefore, bound $GTP_\gamma S$ is equivalent to dissociated/activated $G_{S\alpha}$.

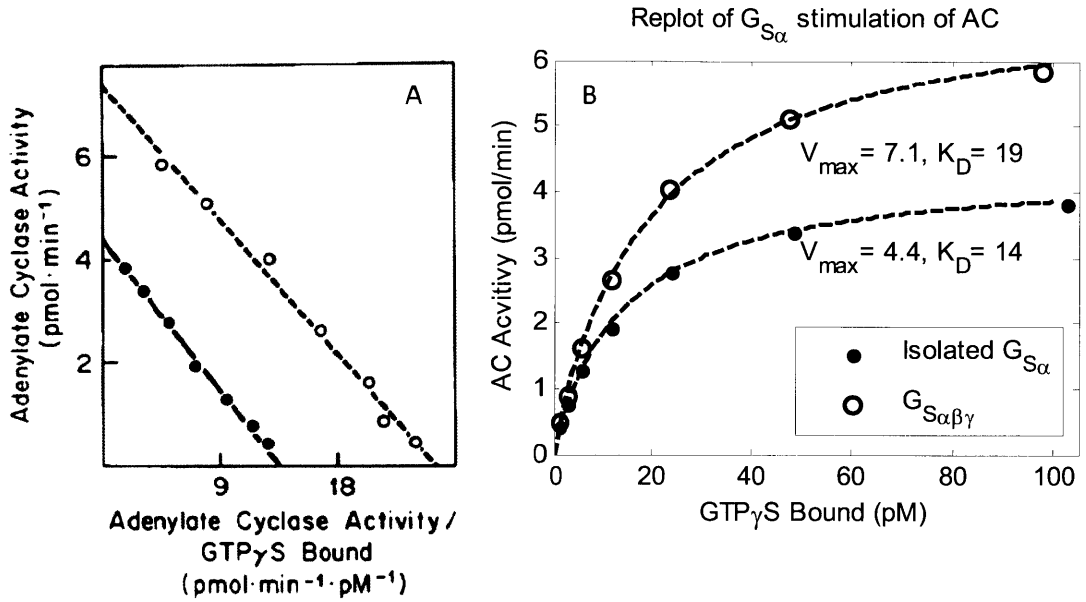

Figure 56 Original (A) and re-plot (B) of the data from (256) used for determining AC-$G_{S\alpha}$ dissociation constant K_D. The re-plot uses the same y-axis values, but the x axis was processed to yield bound GTPγS concentration by dividing the x values from (A) by the y values from (A) and then scaling these concentrations by a constant in order to reproduce the reported range of 1.5-97pM $GTP_\gamma S$ bound (from original figure caption). These scaling constants were ~40 and ~70. The data were fit with standard Michaelis-Menten functions with the parameters shown in B.

For a summary figure showing all the rates calculated above, see Figure 65.

3.4 The Inhibitory G-protein G_I

As with G_S, here we discuss the intrinsic properties of G_I and leave activation of G_I by M2 muscarinic receptors for section 3.5. The abundance of G_I is shown in Table 4. From these data, we conclude that there are 10×10^6 G_I molecules per rabbit SANC. The value we chose for G_S matches that found in rabbit liver and mouse S49 lymphoma cells, however we choose a G_I value higher than that measured in human platelet and rabbit liver cells in order to achieve a high G_I:G_S abundance ratio of 5. We assume that a high abundance ratio is likely present in SANC cells (compared to the cells in Table 4) because strong cholinergic stimulation can abolish spontaneous depolarization and the overabundance of G_I is considered to make the indirect G_S inhibition pathway more powerful. As with G_S, We assume that G_I is dissolved in the entire SANC cytoplasmic volume, giving a total concentration of G_{IT}=10 μM.

The kinetics of inhibitory G-protein were studied by Katada et al., Bokoch et al., and Sunyer et al. in 1984 (29, 177, 178, 180, 311). The mechanisms of isolated G_I protein activation are very similar to what was discussed for G_S, and are summarized below. It helps remove some confusion if we point out that the initial studies (177, 178) were misinterpreted because they were conducted in membranes containing both

G_S and G_I, and the combined effect of these two proteins was ascribed to the activity of G_I only. The later study however (180), was conducted in cyc$^-$ mutant cells that lack fully-functional G_S, and the independent effect of G_I was clearly understood.

The inhibitory G-protein has the following characteristics:

1. $G_{I\alpha}$ is activated by binding GTP and dissociation from $G_{\beta\gamma}$ (177, 178, 180)
    a. Dissociation is promoted by binding of GTP or F^- and Al^{3+} (177, 178, 180)
    b. $G_{I\alpha}$ is deactivated by GTP hydrolysis or binding $G_{\beta\gamma}$ (178)
2. $G_{I\alpha}$ contains a single GTP binding site (28, 29, 177)
    a. Under physiologic [Mg^{2+}], GTP binding to dissociated $G_{I\alpha}$ is irreversible (29, 180)
    b. GTP binding activates $G_{I\alpha}$ by promoting dissociation from $\beta\gamma$ subunits and increasing affinity for effector (AC) (177, 178, 180)
3. GTP is in rapid equilibrium with $G_{I\alpha}$, followed by a rate-limiting $G_{I\alpha}$-$G_{\beta\gamma}$ dissociation step (178)

The fact that the mechanism of G_I activation is identical to that of G_S, we reproduce below the G_S activation framework, with the difference that activated G_I inhibits (rather than activates) AC. Note that the $G_{\beta\gamma}$ subunit is identical to that used in the G_S figures; this is so because the $\beta\gamma$ subunits of G_I and G_S are identical both functionally and in terms of amino acid composition (178). The interchangeability of $\beta\gamma$ subunits is the mechanism of G_S/G_I interaction, and the main culprit in the difficulty with interpreting experimental results from systems that contain both forms of the G-protein (177, 180).

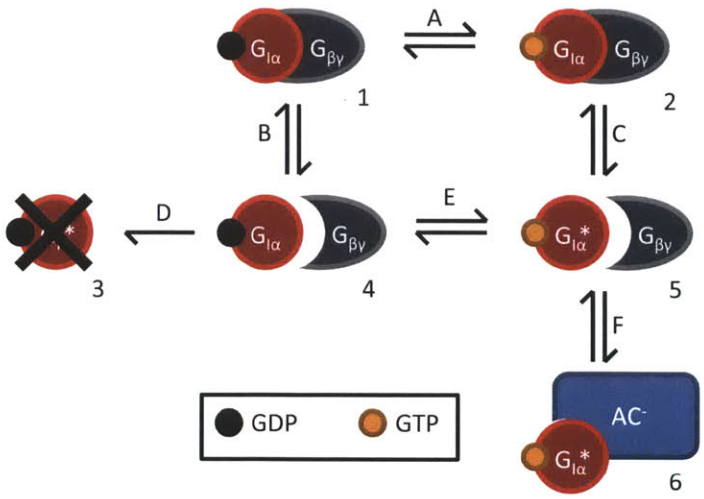

Figure 57 Overall state diagram for activation of inhibitory G protein and subsequent inhibition of AC.

3.4.1 *A. Guanine nucleotide exchange/hydrolysis, $G_{I\alpha\beta\gamma}$*

The generally accepted mechanism of guanine nucleotide exchange in G_I is the same as that for G_S: GDP dissociation is rate-limiting, followed by fast and irreversible binding of GTP (29, 178, 189, 213). This model of slow dissociation followed by fast binding is supported by experimental data showing that the rate of $GTP_\gamma S$ binding is insensitive to $GTP_\gamma S$ concentration (Fig 8 in (29)). The irreversibility of GTP binding at physiologic GTP concentration is supported by the high affinity of G_I for GTP, with a K_D of 25 nM (29) to 40nM (311). Also, experiments in the presence of Mg^{2+} show irreversible binding of $GTP_\gamma S$ to G_I ((29) Fig 9).

Similar to $G_{S\alpha}$, $G_{I\alpha}$ hydrolyzes GTP with an intrinsic catalytic rate k_{cat} (see Table 5) that is higher than the rate of GDP dissociation, thus GDP dissociation limits the full-cycle GTP hydrolysis rate (189, 213) (see Table 6). These properties imply that the rate of GDP dissociation, GTP binding, and overall GTP hydrolysis are equal, and that the only mechanism for generating $G_{I\alpha}$-GDP is through hydrolysis of bound GTP.

The measured values for the rate limiting step (GDP dissociation) differ by an order of magnitude depending on the particular G-protein source or experimental conditions. On the low end are GDP dissociation values on the order of 0.04 /min at 37 °C (29, 189, 213, 311), and on the high end are values on the order 0.1-0.4 /min at 37 °C (29, 178, 181, 240). It is interesting to note that Bokoch et al. show an order of magnitude different $GTP_\gamma S$ binding rates in the same paper (Fig 8 shows an initial rate of ~0.1/min whereas Fig 10 shows ~0.01/min) using the same G_I protein (from rabbit liver), under similar G_I, Mg^{2+} and $GTP_\gamma S$ concentrations but different buffers (Tris-HCl vs. sodium Hepes, respectively) and Na^+ concentrations (0 vs. 100 mM, respectively) (29). Milligan and Klee state that Na^+ can either accelerate or retard GTPase activity, depending on the source of G_I (240). On the other hand, Katada et al. report $GTP_\gamma S$ binding rates of ~0.05/min and ~0.1-0.4 /min at 30 °C using the same buffer solutions (Tris-HCl with 100mM Na^+) but G_I protein from different sources (rabbit liver (177) vs. rat brain (181)). The reported GTP catalytic rate k_{cat} is more consistent however, with values 4-8/min at 37 °C (189, 213) (see Table 5).

Given this information, we adopt the faster GDP dissociation/GTP binding/ GTP hydrolysis rate constant of 0.4/min. We choose this higher value for two reasons: 1) an excess or dearth of a number of substances can alter enzyme function, so it is likely that various *in vitro* experiments may have been conducted in a suboptimal chemical environment and therefore give an underestimate of the enzyme's native, in-vivo performance. 2) The rate of 0.4 /min is the same as that measured for GDP dissociation from $G_{S\alpha}$, and

despite dissimilar actions on the end effector, it is reasonable to assume that the guanine nucleotide binding site in this protein family is highly conserved and therefore exhibits similar kinetics. Similar arguments apply to choosing the catalytic rate k_{cat} of 10/min, which is close to the rates explicitly measured for $G_{I\alpha}$ (Table 5).

3.4.2 B. G-protein dissociation (GDP)

Unfortunately, we were unable to find data of the form shown in Figure 45 for G_I. The only data we found that could be used to quantify this reaction is shown in Figure 58. The denaturation of $G_{I\alpha}$ can be modeled by the reaction shown in Figure 59. In this scheme, free $G_{I\alpha}$ denatures with rate a, and is stabilized through interaction with other $G_{I\alpha}$ subunits or components in the buffer with rate b and binds $G_{\beta\gamma}$ subunits with rate c (rate c is a function of $G_{\beta\gamma}$ concentration). The portion of non-denatured $G_{I\alpha}$ subunit at time *t* is:

$$\alpha_{active}(t) = \frac{b+c}{a+b+c} + \frac{a}{a+b+c} e^{-(a+b+c)t} \tag{8}$$

Since the 'control' reaction in Figure 58A was done in the absence of βγ subunits (c=0), we can use it to calculate rates a and b; this result is shown in Figure 61A, with the calculated rates a and b displayed on the figure.

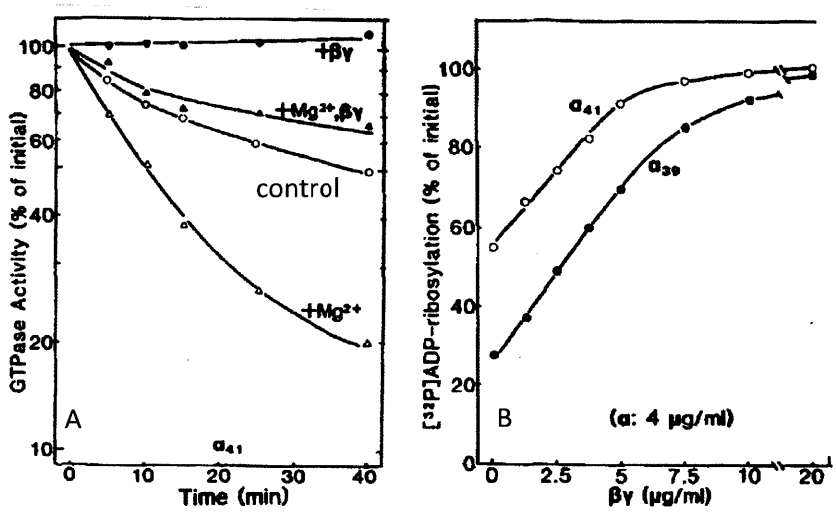

Figure 58 Rate of $G_{I\alpha}$ denaturation in the absence of βγ subunits at 30 °C. A is from Fig 15a and B is from Fig 16a in (181). In A, isolated α_{41} subunits were monitored for GTPase activity in Mg^{2+}-free buffer (control), and combinations of added βγ subunits and Mg^{2+} as indicated. The decline in GTPase activity is ascribed to thermal denaturation of $G_{I\alpha}$. In B, isolated α_{41} and α_{39} were evaluated for ADP-ribosylation as a measure of intact (non-denatured) protein. Isolated α subunits were incubated with βγ subunits of various concentrations, and ADP-ribosylation was evaluated at 60 minutes. We use the data for α_{41} subunit because its mass (41 kDa) is closest to that measured for G_I; the α_{39} subunit is hypothesized to be a different type of G-protein, G_O (181).

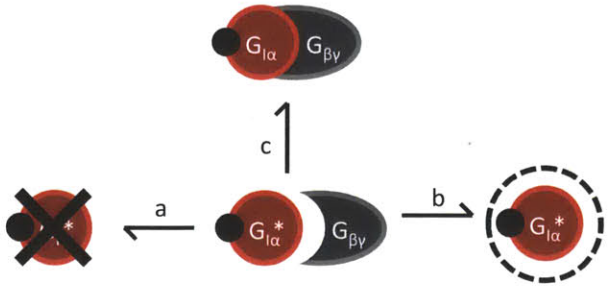

Figure 59 $G_{I\alpha}$ denaturation and binding of βγ. An extra state (right) is added to represent aggregated or otherwise stabilized $G_{I\alpha}$ which is not prone to denaturation. We do not include a dissociation rate because it is very slow, as can be seen from the top line in Figure 58A showing that in the presence of βγ subunits, $G_{I\alpha}$ does not denature at all over 40 minutes.

After obtaining rates a and b from Figure 58A, we use Figure 58B to determine the function for rate c as a concentration of βγ subunit. Equation (8) still applies for this data since we are using the same model, but we can further simplify it by noting that the only time-dependent term is $e^{-(a+b+c)t}$, which for a=b=0.04/min and t=60 min (the data in Figure 58B were collected at 60 min) is less than 0.01 which is negligible. Ignoring the time-dependent term allows us to solve equation (8) for c at each βγ concentration given in Figure 58B:

$$c(\beta\gamma) = \frac{\alpha_{active}(a+b) - b}{1 - \alpha_{active}} \tag{9}$$

The rates c calculated according to equation (9) are well fit by a 3-parameter logistic function (for data and fit see Figure 60):

$$c(\beta\gamma) = \frac{15}{1 + e^{-([\beta\gamma]-276)/40}} \tag{10}$$

where βγ concentration is in nM.

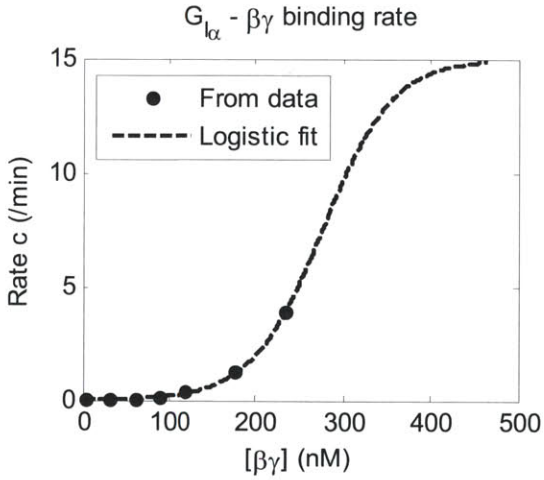

Figure 60 Rate c calculated from data of Figure 58B and equation (9), as well as the logistic function fit of equation (10).

Using this form for rate c, and rates a and b as calculated previously allows us to reproduce the data from Figure 58B, as shown in Figure 61B.

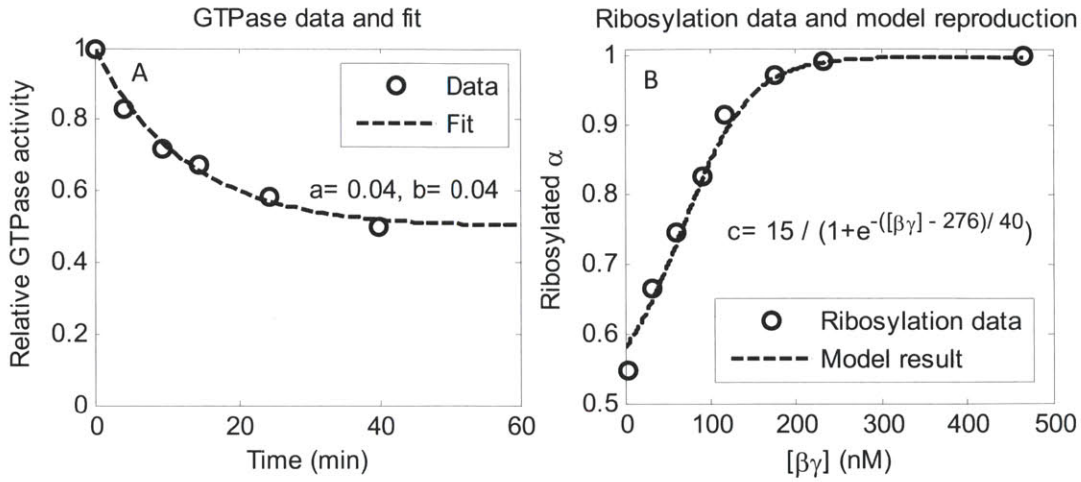

Figure 61 Data digitized from Figure 58 and fit with model of Figure 59. Both of these figures contain data at 30 °C.

Correcting the function in equation (10) to 37 °C gives the model for $G_{I\alpha}$ association with $G_{\beta\gamma}$ in :

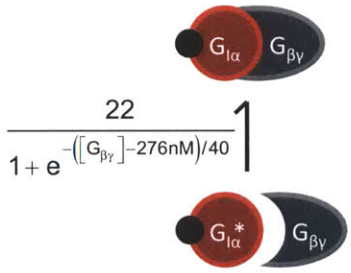

Figure 62 Summary of reaction B showing $G_{\beta\gamma}$-dependent reassociation rate for GDP-bound $G_{I\alpha}$ and $G_{\beta\gamma}$ at 37 °C. The dissociation rate is negligible.

Notes on this rate: the data we used to calculate the association rate were obtained in the absence of Mg^{2+} and guanine nucleotides. Mg^{2+} has been shown to promote subunit dissociation (29), so the association rate calculated above may be an overestimate (cells have a nonzero Mg^{2+} concentration). Guanine nucleotides tend to stabilize free $G_{I\alpha}$ (181), and this increased stability may imply a lower affinity for $G_{\beta\gamma}$, so the above function may be an overestimate of $G_{\beta\gamma}$ affinity. Together, these two observations imply that the above association rate may need to be scaled down and shifted to the right; we did not find this change necessary to fit the available data.

3.4.3 C. G-protein dissociation (GTP)

We are unable to find any data that would allow us to quantify reaction C. Thus, we adopt a minimal model, where the dissociation occurs at a constant rate and association rate is negligible. This rate does not alter the baseline GTP turnover rate, but does affect the baseline AC rate. We set this rate to 1 /min.

3.4.4 D. Thermal inactivation of $G_{I\alpha}$

Here we discuss the denaturation of the three possible $G_{I\alpha}$ configurations: unliganded $G_{I\alpha}$, $G_{I\alpha}$-GTP, and $G_{I\alpha}$-GDP. In the absence of βγ subunits, unliganded $G_{I\alpha}$ subunits appear to denature with rate 0.04 /min (α_{41} subunit in (181) Fig 15A, reproduced in Figure 58A), but due to the high affinity for GTP, the amount of unliganded $G_{I\alpha}$ is expected to be negligible. Katada et al. (181) show that GTP has a stabilizing effect on $G_{I\alpha}$ and effectively prevent its denaturation at GTP concentrations above 10 μM, a condition that is met in the GTP-rich SANC. Since GTP protects $G_{I\alpha}$ from denaturation, it is not unreasonable to assume that GDP also confers some degree of stability so the denaturation rate for GDP-bound $G_{I\alpha}$ is expected to be lower than 0.04 /min. $G_{\beta\gamma}$ subunits also confer significant stability to $G_{I\alpha}$ (181), and their presence in the physiological environment therefore limits the loss of $G_{I\alpha}$ to heat denaturation.

Finally, we also assume that the cell actively synthesizes $G_{I\alpha}$ at a rate sufficient to maintain total abundance, so we choose not to include this reaction, as we did for G_S.

3.4.5 E. Guanine nucleotide exchange/hydrolysis, dissociated $G_{I\alpha}$

The rate of GTP hydrolysis was measured for free $G_{I\alpha}$ subunits as well as $G_{I\alpha}$ in the presence of $G_{\beta\gamma}$, and the data are reproduced in Figure 63. This figure shows a Lineweaver-Burk plot of GTP hydrolysis rate as a function of GTP concentration for two $G_{I\alpha}$ proteins α_{41} and α_{39} (the subscript indicates the molecular weight). Since α_{41} was shown to be an inhibitor of AC activity whereas α_{39} was not (181), we look to the α_{41} data and see that the GTP hydrolysis rate for the free unit is 1/3 as fast as the $G_{\beta\gamma}$ bound unit. Converting these rates from 30 °C to 37 °C gives rates of approximately 0.1 /min for free $G_{I\alpha}$ and 0.4 /min for $G_{\beta\gamma}$-bound $G_{I\alpha}$. The latter agrees with the GDP dissociation rate in reaction A, so we adopt the slower 0.1 /min rate for the GDP dissociation rate for reaction E. It is interesting to note that $G_{S\alpha}$ releases GDP more readily when it is activated, whereas $G_{I\alpha}$ releases GDP faster when bound by $G_{\beta\gamma}$. This observation has also been made by Bokoch et al. (29), noting that the βγ subunit "promotes dissociation of nucleotide" from the $G_{I\alpha}$ subunit. The greater affinity of free $G_{I\alpha}$ for GDP may explain the greater stability of $G_{I\alpha}$ to thermal denaturation (29) and provides a mechanism for prolonging the activated state of G_S, but limiting the duration of the inhibiting effects of G_I.

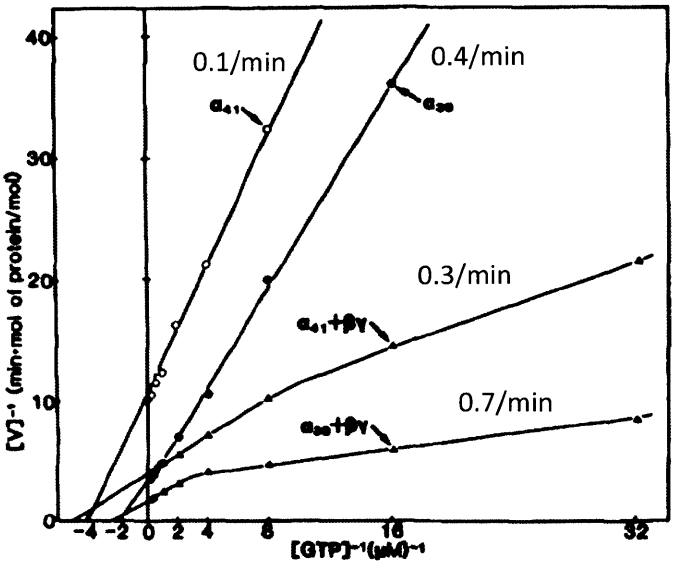

Figure 63 Effect of βγ subunits on GTP hydrolysis rate of $G_{I\alpha}$ subunits at 30 °C, taken from (181). For the $G_{I\alpha}$ types tested, the GTP hydrolysis rate (set by the rate limiting GDP dissociation) is 2-3 times faster in the presence of βγ than for isolated $G_{I\alpha}$. The maximal hydrolysis velocities (inverse of y-intercept) are shown for each condition. GTP dissociation coefficients (inverse of negative x-intercept) are 0.2-0.8 μM.

As for G_S, we assume that the catalytic rate of GTP hydrolysis remains unaltered by being in solution or bound to AC, so k_{cat}=10/min.

3.4.6 F. $G_{I\alpha}$ –AC binding kinetics

The affinity of $G_{I\alpha}$* for AC was chosen to fit data on cAMP synthesis rate and concentration as a function of Iso and ACh in Chapter 6. As we did for GS, here we report some direct measurements of $G_{I\alpha}$*-AC affinity.

We assume that activated $G_{I\alpha}$ binds AC rapidly, like $G_{S\alpha}$. This view is supported by experiments showing that the time course of $GTP_\gamma S$ binding to G_I is directly proportional to the inhibition of AC activity without a delay (Fig 3 in (177)). Katada et al. (178) state that G_I binds AC with a lower apparent affinity than does G_S, and the experimental data shown in Figure 64 allow the calculation of K_D=60-90 nM for the $G_{I\alpha}$-AC reaction. These values are indeed higher than the K_D for $G_{S\alpha}$-AC reported by the same group, which was in the picomolar range (256). We assume that the affinity of $G_{I\alpha}$-GDP for AC is very low so we do not consider binding of these molecules.

The overall model with all the rates for G_I activation is shown in Figure 65.

3.5 Activation by GPCRs

3.5.1 Mechanism of GPCR-G-protein interaction

The kinetics of G-protein interaction with GPCRs has been modeled in two ways. The collision coupling model of Tolkovsky and Levitzki (329) assumes that G-protein and GPCRs freely diffuse through the membrane, and that an instantaneous collision (or finite-duration encounter (305)) between an activated GPCR and a G-protein activates the G protein. The other class of models are standard enzyme models with a rapid binding/unbinding of G-protein and GPCR, followed by an irreversible activation of G-protein (244). These two types of models have different kinetic mechanisms, but share the feature of rapid equilibrium, where the rate of G-protein activation instantly changes as a function of activated GPCR population. Estimates for encounter frequency are on the order of 100-350/min (225, 305), so compared to the slower downstream rates of G_α activation (on the order of 1/min), the assumption of rapid G-protein-GPCR equilibrium is justified.

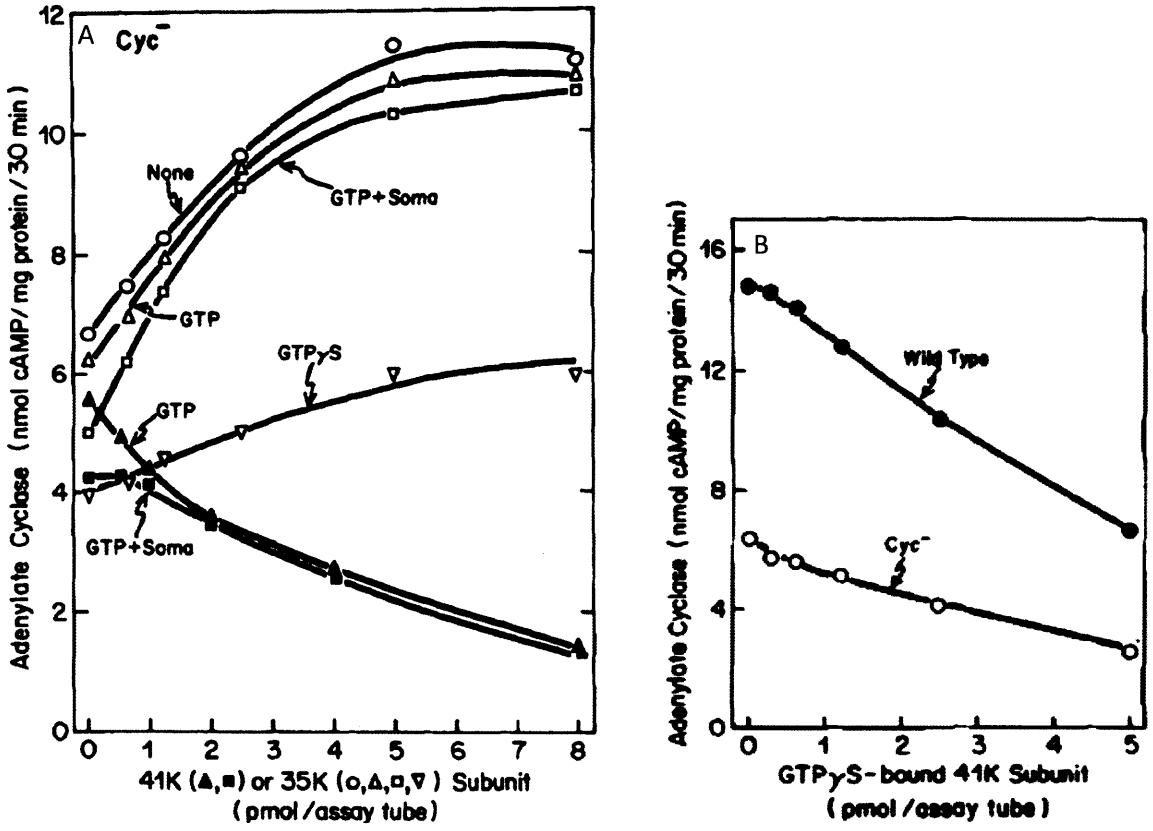

Figure 64 Effect of $G_{I\alpha}$ and $G_{\beta\gamma}$ subunits on AC modulation; both figures taken from (178). X axis is in pmol/assay tube, assay tubes contained 50μL of buffer and membrane. A shows that half-inactivation of AC occurs at ~3 pmol/assay tube (solid symbols ▲; disregard empty symbols since they represent βγ subunit). B shows half-inactivation occurring ~4.5 pmol/assay tube for both wild-type and cyc- cells. Dividing by assay tube volume gives the concentrations as 60 and 90 nM, respectively.

Since $G_{\beta\gamma}$ is necessary for interaction with GPCRs (114), we do not model the binding of free G_α with GPCR. Also, since both guanine nucleotide exchange and G protein subunit dissociation are facilitated by interaction with a liganded GPCR ((34, 35), for review see (122)), we bypass the 'intermediate' state (state 2 in both Figure 39 and Figure 57) and introduce a direct GPCR mediated rate from state 1 to state 5 (see Figure 65). Due to the rapid equilibrium between GPCRs and G-proteins discussed above, the GPCR-mediated rates of G-protein activation can reasonably be modeled using instantaneous functions of G-protein concentration. In fact, GPCRs are known to catalyze the activation of a number of G proteins while themselves activated by hormone (122). We use the standard enzyme kinetics form (equation (11)) where the maximal rate V_{max} is related to the amount of liganded β-adrenergic (β^*) or M2 muscarinic receptor ($M2^*$) and $G_{\alpha\beta\gamma}$ is treated as substrate with the specified dissociation constants. Note that in the R_β equation, we also include a second term for activation of G_S by unliganded β-AR. This term has a lower $v_{max,\beta 0}$ and a higher K_{GS0}, and was necessary in order to raise the baseline $G_{S\alpha}$* concentration and allow the reproduction of data showing AC to be about 50% activated at steady state (see fig 4b in (320)) while still allowing full activation by NE stimulation and full inactivation by ACh stimulation.

$$
\begin{aligned}
R_\beta &= \left[\beta^*\right] v_{max,\beta} \frac{\left[G_{S\alpha\beta\gamma} GDP\right]}{\left[G_{S\alpha\beta\gamma} GDP\right] + K_{GS}} + \left(\beta_T - \left[\beta^*\right]\right) v_{max,\beta 0} \frac{\left[G_{S\alpha\beta\gamma} GDP\right]}{\left[G_{S\alpha\beta\gamma} GDP\right] + K_{GS0}} \\
R_M &= \left[M2^*\right] v_{max,M} \frac{\left[G_{I\alpha\beta\gamma} GDP\right]}{\left[G_{I\alpha\beta\gamma} GDP\right] + K_{GI}}
\end{aligned}
\tag{11}
$$

3.5.2 Parameters for GPCR-G-protein interaction

We could not locate references that explicitly report the parameters for the model in equation (11), so we convert published measurements related to the quantities of interest. From the model and experimental measurements done in mouse S49 cells by Stickle and Barber (305), where the encounter frequency was f_E=100/min and an average encounter duration of 0.2 seconds, we calculate that K_{GS} is 3[G_S] where [G_S] is the baseline concentration of G_S in the cell:

$$
K_{GS} = \frac{k_{off}}{k_{on}} = \frac{k_{off}\left[G_S\right]}{k_{on}\left[G_S\right]} = \frac{k_{off}\left[G_S\right]}{f_E} = \frac{1/0.2}{100/60}\left[G_S\right] = 3\left[G_S\right]
$$

We assume that [G_S] is not significantly depleted by binding, a valid assumption given that the G_S abundance is two orders of magnitude greater than the abundance of β-AR (our estimate of G_S abundance is $2\text{x}10^6$ /cell, and β-AR abundance is ~$3.5\text{x}10^4$ /cell).

To obtain a similar estimate for G_I, we look to experiments done on insect Sf9 cells by Mosser et al. (244), which show that addition of ACh increases the portion of M2-G_I binding from 0.07 to 0.26. These values imply K_{GI} is 13[G_I] for unliganded M2 muscarinic receptors and 3[G_I] for ACh-bound M2 muscarinic receptors by the following formula, where P is the portion of receptors bound for a given [G_I]:

$$P = \frac{[G_I]}{[G_I] + K_{GI}} \Rightarrow K_{GI} = \frac{1-P}{P}[G_I]$$

In purely theoretical models, values on the range 1-30 ×[G] have been assumed/computed (225, 259). Thus, we regard the estimates of 3[G] for liganded GPCRs and 13[G] for unliganded GPCRs reasonable, giving K_{GS}=6 μM, K_{GS0}=26 μM, and K_{GI}=30μM.

It is estimated that a liganded β adrenergic receptor can catalyze the activation of ~10 G_S proteins over the course of a few seconds (122). Setting $v_{max,\beta}$=10/s gives an overall GTP turnover by G_S of 2.1/min (turnover is calculated as mol GTP hydrolyzed per mol of G_S per minute). This value is in line with the measurements made by Brandt et al. (34), who measured GTP turnover of 1-1.5 /min for Iso-stimulated vesicles (containing β-adrenergic receptors) at 30°C. Correcting these rates to 37 °C, we obtain GTP turnover of 1.4-2.2/min. Setting $v_{max,M2}$=10/s gives a maximally M2-stimulated GTP turnover of 1.3/min for G_I, which is approximately 3× the baseline value of 0.4/min, and 1.4× the total baseline GTP turnover of 0.9/min. These values are in accordance with data (130, 149, 177, 178). The effect of hormone on platelet membranes (Fig 6 in (177)) and S49 cells (Fig 1b in (178)) increased the activation of G_I by a factor of 3. The M2-muscarinic receptor agonist carbachol increased GTP hydrolysis rate by a factor of 2 in reconstituted phospholipid vesicles (Fig 3 in (130)), and by a factor of 1.7 in porcine atrial membranes (Fig 2 in (149)).

The rate $v_{max,\beta 0}$=1.54/s was chosen in order to generate a high enough $G_{S\alpha}$GTP concentration at baseline to allow for an AC rate of about 50% of maximum, as shown by Taniguchi et al. (see Fig 4b in (320)).

3.6 AC and its modulation by G_S and G_I

AC catalyzes the conversion of ATP to cAMP (reviews: (164, 269)). From studies of purified AC (Table 8), the basal turnover number is on the order of 1/s, and it increases roughly 10-100 fold upon activation (85, 292, 353). AC activated by forskolin or $G_{S\alpha}$ yields turnover numbers on the range from 5-91/s, with AC I and II being on the lower end with rates 5-18/s (316, 322, 364), and AC V and VI (the isoforms of interest to us) on the higher end with rates 54-91/s (85, 271). We adopt the baseline rate v_{AC}=1/s and $G_{S\alpha}$GTP-stimulated rate v_{AC*}=100/s. Experiments on the inhibition of AC rate by activated $G_{I\alpha}$ show 12-50% inhibition: Fig 6 in (178) shows 12% inhibition, Fig 1 in (240) shows 25% maximal AC inhibition

by G_I, Figs 1 and 2 in (178) and Fig 4 inset in (180) show ~50% inhibition. We set the $G_{I\alpha}$GTP-bound AC rate to v_{AC^-}=0.5/s, noting that the absolute value is not critical since the major inhibitory effect is obtained by competing AC away from G_S. We treat these three AC rates as constants, which is appropriate under the assumption that the substrate ([ATP] ≈ 9-11 mM in perfused rat heart, converted from 4-5 μmol/g wet tissue (187, 260), see section 9.2 for conversion) concentration in the cell is actively maintained and therefore does not fluctuate significantly with time.

Table 8 Basal and activated turnover rates (mol cAMP/mol AC/s) of purified AC.

Source	AC type	Temp. (°C)	Reported value (μmol/min/mg)	Turnover (/s)*	Turnover at 37°C (/s)
Takai et al. 1974 (314)	*Brevibacterium liquefaciens*	33	30	23	28
Sevilla et al. 1976 (292)	Turkey erythrocyte	37	--	2† 15-20	2† 15-20
Pfeuffer et al. 1985 (271)	Rabbit myocardium	30	15	37.5	54
Smigel 1986 (297)	Bovine brain	30	10	20	29
Tang et al. 1991 (316)	I	30	5	9.2	13
Taussig et al 1993 (322)	I II	30	7 2	12.4 3.5	18 5
Yan et al. 1996 (364)	$IC_1 + IIC_2$	30	--	8.2	12
Dessauer et al. 1997 (85)	IIC_2+VC_1	30	0.6† 63	0.6† 63	0.9† 91

* Conversion from μmol/min/mg was converted to mol cAMP produced/mol AC/second (turnover) by dividing the reported values by the molecular weight of AC provided in the paper. The following weights were used: Takai et al. (46 kDa), Pfeuffer et al.(150 kDa), Smigel (120 kDa), Tang et al.(110 kDa), Taussig et al.(106 kDa), Dessauer et al.(60 kDa, since activity is reported per mg of one of the AC subunits which we assume is half the weight of the whole protein).

† basal activity, in the absence of activating substances like $G_{S\alpha}$ or Forskolin, all other rates are activated

Experiments done on crude membranes (Table 9) allow us to estimate the basal and maximally activated rates of cAMP generation per cell. These measurements are made in different tissues in a number of species, but the cAMP production rates per cell are fairly consistent. Basal rates are on the order of 10,000 cAMP molecules/s/cell whereas maximal rates are 10-100 times higher, in agreement with observations on purified AC ((85, 177, 353) (shows 30× increase due to G_S)). We assume a total AC abundance of 6,000 per cell (AC_T=6.25 nM), which gives baseline and maximal cAMP synthesis rates in line with the data in Table 9.

Because AC can bind either $G_{S\alpha}$ or $G_{I\alpha}$ at a time (see Figure 37 caption), the two reactions are competitive. We use a simple, phenomenological model based on competitive binding of G_S and G_I parameterized by and apparent dissociation constants K_{SAC} and K_{IAC} and Hill Coefficients n_{SAC} and n_{IAC}. This gives the concise form for AC, AC* and AC$^-$, which are weighted by their respective cAMP velocities to produce the overall velocity $v_{AC,Total}$:

$$AC^* = AC_T \frac{[G_{S\alpha}GTP]^{n_{SAC}}}{[G_{S\alpha}GTP]^{n_{SAC}} + K_{SAC}^{n_{SAC}}\left(1 + \frac{[G_{I\alpha}GTP]^{n_{IAC}}}{K_{IAC}^{n_{IAC}}}\right)}$$

$$AC^- = AC_T \frac{[G_{I\alpha}GTP]^{n_{IAC}}}{[G_{I\alpha}GTP]^{n_{IAC}} + K_{IAC}^{n_{IAC}}\left(1 + \frac{[G_{S\alpha}GTP]^{n_{SAC}}}{K_{SAC}^{n_{SAC}}}\right)}$$

$$AC = AC_T - AC^* - AC^-$$

$$v_{AC,Total} = v_{AC^*}[AC^*] + v_{AC}[AC] + v_{AC^-}[AC^-]$$

Table 9 Basal and maximal rates of cAMP production in mammalian cells

Source	Cell type	Temp (°C)	Reported value (pmol/min /mg)	cAMP rate (x10^5 molecules /s/cell)*	cAMP rate at 37°C (x10^5 molecules /s/cell)
Lefkowitz and Levey 1972b (208)	Cat LV	37	60† 160	1.2† 3.2	1.2† 3.2
Sevilla et al. 1976 (292)	Turkey erythrocyte	37	1,200	24	24
Spiegel et al. 1976 (299)	Turkey erythrocyte	37	292	5.8	5.8
Waelbroeck et al. 1983 (345)	Human adult LV Human fetus LV Human R auricle Human R auricle Rat LV Rat LV	37	225 350 50† 175 35† 100	4.5 7 1† 3.5 0.7† 2	4.5 7 1† 3.5 0.7† 2
Fowler et al. 1986 (115)	Human LV Human LV Human RV Human RV	30	8.5-14.1† 136-224‡ 5.7-10.9† 97.8-162‡	0.17-0.3† 2.7-4.5‡ 0.11-0.2† 2.0-3.2‡	0.2-0.4† 3.9-6.5‡ 0.2-0.3† 2.9-4.6‡
Bristow et al. 1989 (41)	Human LV	30	43	8.6	12.4

* cAMP rate calculated by multiplying pmol/min/mg membrane protein values by mg of membrane protein in the model cell (see section 9.2 for conversion constants) and converting minutes to seconds and moles to number of molecules. † basal rate, in the absence of β-adrenergic agonists or AC activators like forskolin. ‡ rates in presence of Iso and forskolin; Iso alone only stimulated 15-16% of this amount of cAMP production

The parameters for the binding reaction were chosen in order to reproduce AC rate and cAMP concentration data in response to adrenergic and cholinergic stimulation (see Chapter 6). This procedure provided the values K_{SAC}=45.9 nM, n_{SAC}=1, K_{IAC}=213.9 nM, n_{IAC}=1.74. The Hill coefficients are close to unity, which is expected for binding of single molecules. The affinities agree with the qualitative observation that G_S binding is higher affinity than G_I (178). Quantitatively, our K_{SAC} value is higher than the reported values (3-240 pM, see section 3.3.6), while our K_{IAC} value is reasonably close to the values we estimated from experimental data (60-90 nM, see section 3.4.6).

The overall model for G-protein activation and modulation of AC is shown in Figure 65; the full list of instantaneous and differential equations is in section 9.5.2.

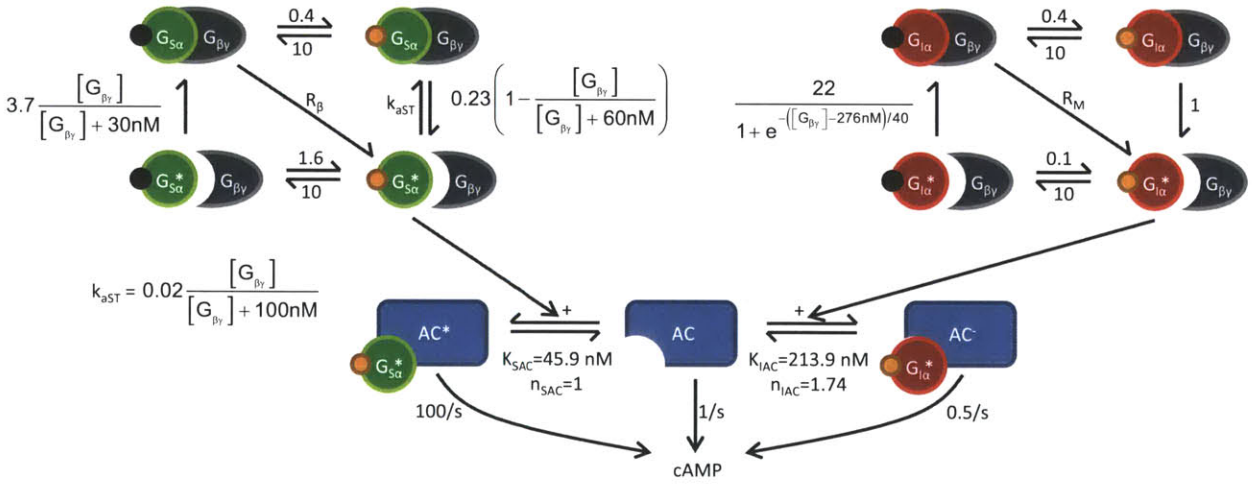

Figure 65 Entire G protein – AC model. The rate functions and constants shown were deduced from detailed in-vitro experimental data. In the final model implementation, all G-protein rates were scaled by a constant factor in order to match higher-level kinetic data. See section 6.7 for details.

3.7 Results

We showed some results in sections 3.3 and 3.4 in the form of reproductions of experimental data by isolated reactions in our G_S and G_I models. In this section, we show the characteristics of the G_S, G_I and AC system when coupled with the neurotransmitter release model of Chapter 2.

Figure 66 shows snapshots of the G_S, G_I, and AC system at steady state, at 0.1 μM ACh, baseline, and 0.1 μM NE. The baseline system is in the absence of ACh or NE perturbations; the concentrations are not 0 however, due to the nonzero concentrations in the BS. The fixed ACh and NE concentrations were chosen to correspond to ~10 Hz stimulation, as the maximal physiological effect. In all three situations, the bulk of G-protein resides in the heterotrimeric, GDP-bound state ($G_{\alpha\beta\gamma}GDP$). Upon activation by ACh, the percentage of activated G_I increases from near 0% to 4%, causing the G_I-mediated GTP turnover to almost double from 0.4 to 0.7/min. ACh causes a negligible change in the GTP turnover rate of G_S and activated amount of G_S (a very slight deactivation due to the increased concentration of βγ subunits causes the $G_{S\alpha\beta\gamma}GDP$ state to increase by a fraction of a percent). The effect of ACh on AC rate is large however, causing a shift from 41% activated at baseline to only 17% with ACh, and a matching 2.3-fold decrease in cAMP synthesis rate. Adrenergic stimulation tells the opposite story, with a significant rise in activated G_S, from 2% at baseline to 6%, and a similar near-doubling of G_S-mediated GTP hydrolysis rate that we saw with G_I and ACh. The relatively high baseline AC rate increased 1.6-fold in response to the 1.7-fold increase in the percent activated AC^*. The most striking feature of these data is the high sensitivity of the system, where only small fractions of total G_S and G_I (< 10%) need to be activated for maximal adrenergic and cholinergic effects. These results are supported by experimental measurements indicating 90-97% of G_S in the GDP-bound states (36), and baseline and stimulated GTP turnover rates on the order of 0.4 /min and 1 /min (Table 6, (34, 130, 149, 177, 178). A difference between the activation response of G_S and G_I is that G_I activation results in increased $G_{I\alpha}GTP$ with the other states remaining virtually unchanged, whereas activation of G_S greatly increases both dissociated states: $G_{S\alpha}GTP$ and $G_{S\alpha}GDP$.

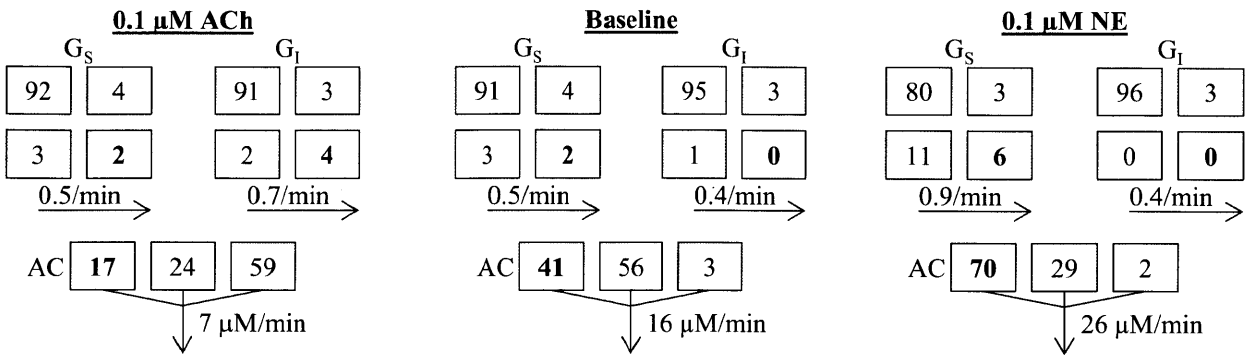

Figure 66. The percent of G_S and G_I found in GDP/GTP/βγ- bound forms match experimental observations; small changes in activated G-protein abundance lead to large changes in AC activation. State diagrams are shown for three conditions: 0.1 μM ACh, baseline (minor effect of BS concentrations of NE and ACh), and 0.1 μM NE. Each condition shows the same diagram, where each box shows the distribution of a species (G_S, G_I, and AC) in terms of percentages. The boxes are arranged in a geometric pattern similar to Figure 65: for the G-proteins, the top left is $G_{\alpha\beta\gamma}GDP$, top right is $G_{\alpha\beta\gamma}GTP$, bottom left is $G_\alpha GDP$, and bottom right is the activated form $G_\alpha GTP$; for AC, the left box is activated AC^*, the middle is AC, and the right is inhibited AC^-. The percent of each species that is in the activated form is shown in bold. The horizontal arrows beneath the G-protein boxes show the GTP turnover due to G_S and G_I, respectively. The arrow beneath AC shows the overall AC rate, $v_{AC,Total}$.

The concentration of activated G_S and G_I as a function of nerve stimulation frequency are shown in Figure 67A. Nerve stimulation causes peak $G_{I\alpha}GTP$ concentration to rise from 0.05 μM to over 0.8 μM, and while the steady-state concentration manifests the same depletion phenomena as M2-muscarinic receptor activation, the difference between steady-state and peak is not great. $G_{S\alpha}GTP$ increases from a baseline value of 0.035 μM to a modest 0.18 μM peak and 0.12 μM steady-state concentration. The lower $G_{S\alpha}GTP$ concentrations, despite greater fractional activation (see Figure 66), are a result of the 5-fold greater G_I abundance in the rabbit SANC. We also see the drastic effect of NE depletion on the difference between the peak and SS values, as we saw with β-AR activation. The kinetics of G_S and G_I activation are shown in Figure 67B. G_S activation is about an order of magnitude slower than G_I, with G_I taking a fraction of a second to reach half of its peak value and virtually reaching the peak within one second, while G_S requires about 5 seconds to climb half-way and about 20 seconds to reach the peak. These rates are similar to those of the M2-muscarinic and β-AR activations we showed in Figure 24.

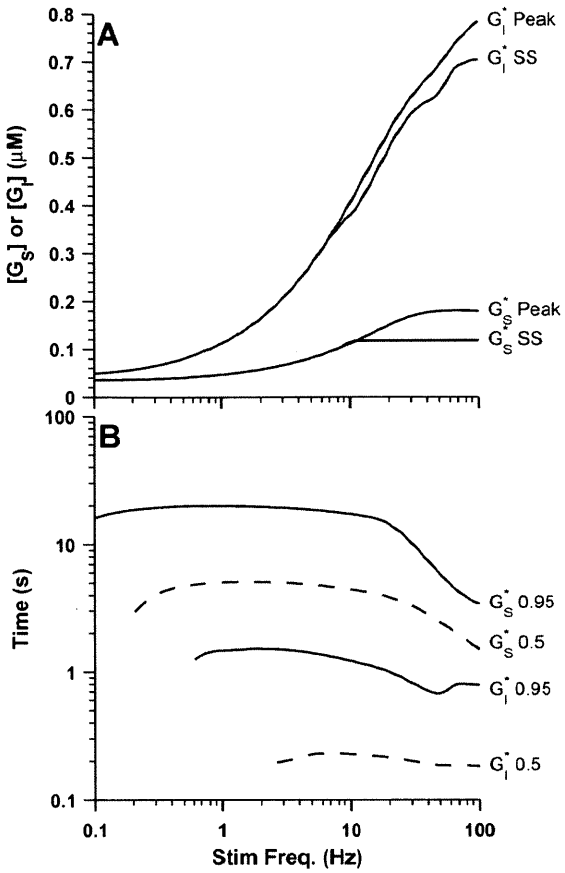

Figure 67. G_S and G_I sensitivity and rate of activation (model simulation). A. Steady-state (SS) and peak concentrations of G_S and G_I are shown as functions of sympathetic and vagal stimulation frequency, respectively. B. The rates of activation from a baseline level (>0 μM for both G_S and G_I) to the peak values indicated in A. did not follow an exponential rise, so we show the time required to reach 0.5 and 0.95 of peak value. Missing values indicate frequencies where the first stimulus surpassed either the 0.5 or 0.95 point.

Despite our faithful reproduction of the G_S-deactivating effect of βγ subunits (Figure 51), the effect is very small for our in-vivo model, as seen in Figure 68. With increasing ACh, $G_{I\alpha}GTP$ concentration rises more than one order of magnitude and liberates the same amount of βγ subunits, but these free βγ subunits only cause a minimal decrease in $G_{S\alpha}GTP$ from 0.033 to 0.031 μM. This is an unexpected result given the potency of βγ subunits in deactivating $G_{S\alpha}GTP$ in-vitro (255, 256); but it is an important observation, as it implies that the direct pathway of AC inhibition is more important than the indirect (Figure 37). On the other end of this spectrum, increasing NE concentration causes a similar order of magnitude increase in $G_{S\alpha}GTP$ concentration, but there is no inhibitory effect on $G_{I\alpha}GTP$.

The effects of G-protein activations on AC is summarized in Figure 69. Starting at the baseline AC rate in the middle of the figure, addition of ACh in the absence of sympathetic stimulation (SS=0 Hz) causes a sigmoidal decline in $v_{AC,Total}$ to a minimum value of about 2 μM/min. Concurrent sympathetic stimulation

(SS=2, 5, 10 Hz) increases the AC rate, but only at low cAMP concentrations. Note that for ACh>0.1 μM, all the SS lines fuse into one, showing the ineffectiveness of sympathetic stimulation at high ACh concentrations. This effect arises due to the direct inhibition pathway described in section 2.3.8 and Figure 28. Looking at the NE-stimulated side of Figure 69, we see the expected sigmoidal increase in $v_{AC,Total}$ in the absence of concurrent vagal stimulation (VS=0 Hz). The effect of vagal stimulation at 2 and 5 Hz is simply to shift the curve down, as the AC available to bind $G_{S\alpha}GTP$ is competed away by $G_{I\alpha}GTP$. At the high vagal stimulation rate of 7 Hz, we again start to see the effect of direct cholinergic inhibition on β-adrenergic activation, as the curve is not only shifted down more drastically, but it is also shifted to the right such that the physiologically-achievable NE concentration range (up to 0.1 μM) results in minimal activation of AC.

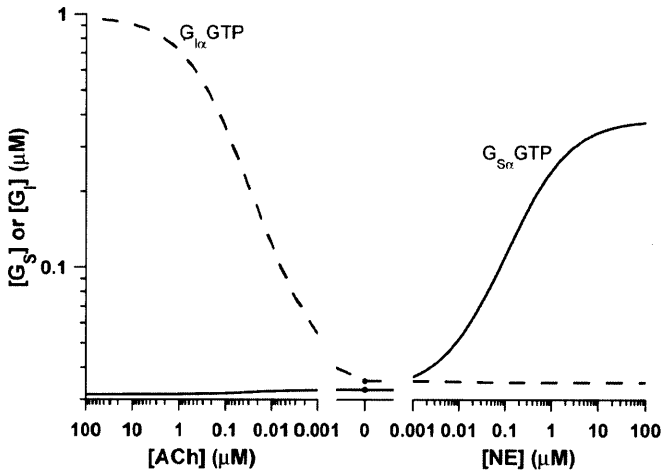

Figure 68. Cholinergic activation results in a $G_{I\alpha}GTP$-dominated cellular environment, while adrenergic activation causes $G_{S\alpha}GTP$ dominance; the in-vivo effect of βγ inhibition of $G_{S\alpha}GTP$ is small (model simulation). Note that the ACh scale is reversed, so the left side of the plot shows the maximal cholinergic effect, the middle shows 'baseline' (both neurotransmitter concentrations at 0) and the right side shows the maximal adrenergic effect. The solid line and dashed line are G_S and G_I as labeled. Neurotransmitter concentrations were clamped in the neuroeffector junction and EJS (no effect of reuptake / absorption / hydrolysis).

3.8 Discussion

We constructed models of G_S and G_I activation from the basic reactions of guanine nucleotide exchange (both intrinsic and GPCR-mediated), hydrolysis, and dissociation. Our model of AC activation and inhibition is similarly based on a simple competitive binding with activated $G_{S\alpha}$ and $G_{I\alpha}$. In building these models, we made what we consider to be the most reasonable assumptions; below, we summarize some of the possibly contentious points.

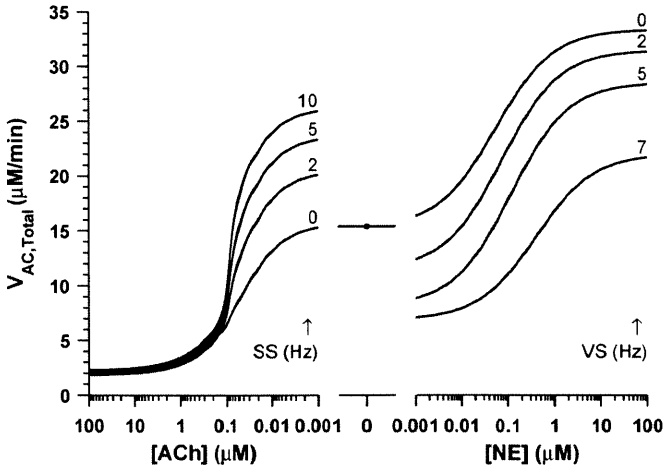

Figure 69. AC rate is modulated by both sympathetic and parasympathetic activity (model simulation). Note the reverse ACh scale; showing maximal cholinergic effect on the left and maximal adrenergic effect on the right. In the ACh regime, four sets of simulations were done, with simultaneous sympathetic stimulation (SS) at 0, 2, 5, and 10 Hz as labeled. In the NE regime, simultaneous vagal stimulation (VS) frequencies are similarly indicated. The baseline panel shows the AC rate in the absence of neurotransmitter. neurotransmitter concentrations were clamped in the neuroeffector junction and EJS (no effect of reuptake / absorption / hydrolysis).

We model $G_\alpha GTP$ as entering the cytoplasm following its dissociation from $\beta\gamma$. This issue has been debated: Taylor (323) argued that it is unlikely because the resulting dilution would lower the effectiveness of the activated subunits in interacting with membrane-bound proteins like AC. On the other hand, a number of studies support the mechanism diagrammed in Figure 36, with a membrane-tethered $\beta\gamma$ and freely-diffusible G_α (27, 122, 281, 282). Our model produces activated G_I and G_S concentrations in the 0.1-1 μM range (Figure 67, Figure 68), and AC-binding affinities in the nM range, close to what was experimentally observed (178, 256). However, we found it necessary to speed-up all our G-protein reactions by a factor of 20 (see section 6.7 for details) in order to reproduce the half-time of $\beta\gamma$-mediated activation of the $I_{K,ACh}$ channel. We argue that this speed-up represents the localization of G-proteins to specific cellular domains (166, 250), or interaction with regulators of G-protein signaling (RGS) or GTPase activating proteins (GAPs) which can speed up GTP hydrolysis rates by a factor of 50 (23, 327). In future refinement of this model, it would be prudent to revisit the assumption of G-protein dilution in the entire cytoplasmic volume, since reducing the volume in which reactions occur would result in faster rates and may provide a mechanistic explanation for the 20-fold speedup we currently use.

For dissociation of either $G_{S\alpha}$ or $G_{I\alpha}$ from $G_{\beta\gamma}$, a concentration of at least 1 μM Mg^{2+} is necessary (180, 256, 281). We do not model the dependence of G-protein subunit dissociation on Mg^{2+} because according to the SANC model of Kurata et al., physiologic Mg^{2+} concentration is 2.5 mM (198). Experimentally, the

effect of Mg^{2+} and GTP is sometimes simulated by Al^{3+} and F^-, which can mimic the γ-phosphate of GTP and cause G_α activation (122, 300).

In the G-protein literature, the activation of G-proteins by GTP and dissociation from βγ is not explicitly described in terms of these two processes: is GTP necessary and sufficient to activate G_α, regardless of whether βγ is attached or dissociated? Or, is GTP binding necessary, but only as a mechanism for dissociating the α and βγ subunits? In our model, we consider only the *GTP-bound and dissociated* G_α subunit as "activated". This decision is supported by a review that summarizes the structure of G_α and $G_{\beta\gamma}$ subunits and points out that the same residues of G_α are responsible for binding effector and $G_{\beta\gamma}$ (70). Thus, $G_{\alpha\beta\gamma}$GTP cannot interact with AC since the βγ is in the way. When G_α binds GTP, these residues undergo a conformational change and become less suitable for binding βγ, and more suitable for interacting with AC (300). This is why we also consider G_αGDP as inactive; although this conformation does not have the physical barrier or βγ; it also lacks the high enough affinity to bind AC. If we removed this assumption (that both GTP and dissociation are necessary) from our model, the inhibitory activity of GI would not be greatly affected because ACh causes a much greater activation of $G_{I\alpha}$GTP than any other potentially active state (see Figure 66). On the other hand, if $G_{S\alpha}$GDP were considered an active species; the effect of NE would be much greater than it currently is, owing to the significant increase in not only $G_{S\alpha}$GTP, but also $G_{S\alpha}$GDP (see Figure 66). We did not find the adrenergic activation of AC to be problematic in reproducing experimental data on SANC modulation by NE and Iso, so we are fairly confident that our decision on this issue is correct.

For determining the rates of GTP hydrolysis by G_S and G_I, we presented measurements from a number of studies in Table 5 and Table 6. The k_h value we chose (~0.4 /min) is close to what is generally accepted (122). The k_{cat} measurements show a bit of variance though: the G_S measurements were made using rabbit proteins (35, 36, 128), and tend to have larger values than the G_I measurements, which coincidentally were made using rat protein (189) or recombinant G-protein from cDNA of unspecified origin (213). In our model of the rabbit SANC, we use a single k_{cat} value of 10 /min for both G_S and G_I based on the reported values for rabbit G_S. A single catalytic rate is generally considered sufficient to summarize this property across G-protein subtypes (122). A much higher rate was reported by Breitwieser and Szabo, who estimate k_{cat}=135/min in bullfrog cardiac myocytes (38). These authors obtained this estimate through observation of $I_{K,ACh}$ and argue that hydrolysis rates in vivo are larger than in solubilized systems. We concluded that this value is questionable because it was obtained using hydrolysis-resistant GTP analogues and nanomolar concentrations of ACh to derive a linear relationship between ACh concentration and $I_{K,ACh}$ activation rate, and then extrapolated this relationship to 160 nM ACh, at which

concentration the rates of hydrolysis and $I_{K,ACh}$ activation are equal. The authors also mention that under control conditions, nanomolar ACh concentrations failed to activate $I_{K,ACh}$, and activation only occurred after the addition of non-hydrolyzable GTP. Because of the multiple system perturbations, the use of non-hydrolyzable GTP analogues to estimate GTP hydrolysis rate, and the linear extrapolation, we find this data questionable. However; the authors do bring up a valid point by questioning the applicability of *in-vitro* G-protein kinetics to *in-vivo* systems. For example, it has been noted that $G_{S\alpha}$* bound to AC hydrolyzes GTP more rapidly than free $G_{S\alpha}$*, implying that interaction with AC and other GAPs may happen *in-vivo* but would not be observed *in-vitro* if the appropriate components are not explicitly included (see (269) for a review).Most of our G-protein kinetic constants were derived from *in-vitro* experiments, so it is possible that the natural system behaves more rapidly (this also partly validates the 20× speedup we had to apply to the G-protein kinetics).

We modeled modulation of AC by G_S and G_I. There is also evidence showing that both cardiac AC isoforms are inhibited by adenosine, PKA, and Ca^{2+} (164, 179, 269). We do not include these effects because their mechanisms are not as well-understood as those of G-protein interaction, and because they did not seem necessary in order to reproduce high-level SANC data.

GPCRs desensitize when exposed to ligand for an extended period (see Chapter 2 in (37)). Three processes have been identified: 1) GPCRs can be phosphorylated, and as a result, their affinity for the G-protein decreases. In an elegant negative feedback mechanism, $G_{\beta\gamma}$ subunits have been implicated in stimulating GPCR kinases and contributing to GPCR phosphorylation (170, 190) 2) GPCRs are removed from the external membrane and sequestered within the cell; however the effect of sequestration on GPCR activity is unclear as there has been recent evidence that even sequestered β-adrenergic receptors can continue to stimulate/inhibit their end effectors (see (165) for review, (52, 110, 247)). 3) The number of potentially active GPCRs is reduced either by destruction of sequestered receptors or transcriptional downregulation. We do not include these processes in our model because they happen on longer timescales (phosphorylation and sequestration on the order of minutes, downregulation on the order of hours (see Chapter 2 in (37)) and the mechanisms and effects are not fully understood. However, we mention these processes here as a potential limitation of the model and as an issue to be addressed when it is better understood.

It has also been shown that although β-adrenergic receptors typically cause a *stimulatory* effect, high ligand concentrations cause activation of *inhibitory* G-proteins in cardiac myocytes (217). This is thought to be a protective mechanism to guard against catecholamine overstimulation, and it seems to be

modulated by the β-adrenergic receptor phosphorylation mechanism mentioned above and takes on the order of 3 minutes before any effect is seen (217). Because of this long delay, and since we are modeling a physiological system where catecholamine overstimulation should not be an issue, we do not include this mechanism in our model.

The completed model, with all the assumptions mentioned above, produces G_S and G_I activation profiles and rates very similar to those of the M2 muscarinic and β-AR. We had anticipated that the "indirect inhibition" of AC, through removal of activated $G_{S\alpha}GTP$ by high concentrations of free βγ would be a powerful effect and a possible mechanism of direct cholinergic inactivation of the adrenergic system. Our model did not show this to be the case, as the effect of ACh on reducing GSαGTP concentration was minimal (see Figure 68).

The major cholinergic/adrenergic interaction occurs through the opposite effects of these two branches on the overall AC rate. As seen in Figure 69, independent ACh or NE decrease or increase AC rate in a sigmoidal manner, similar to the model used by Demir et al. (81), with the main difference being that our model explicitly includes the activation of G-proteins, and that all the rate constants and affinities are supported by experimental data. Furthermore, we show that concurrent stimulation of adrenergic and cholinergic branches likewise produces reasonable effects: sympathetic stimulation can stimulate AC rate despite inhibition by ACh (but only at low ACh concentrations), and vagal stimulation can inhibit AC despite activation by adrenergic agonists. The powerful effect of direct cholinergic inhibition of the adrenergic system is also seen, since sympathetic stimulation has almost no effect on AC rate for ACh concentrations >0.1 μM.

3.9 Conclusion

We developed a G-protein and AC model by studying in detail the major reactions that define these molecules. The stimulatory and inhibitory G-proteins are characterized by GTP-binding, dissociation, and GTP hydrolysis, where the first two reactions are catalyzed by interaction with liganded GPCRs (M2-muscarinic receptors and β-ARs). The activation of GPCRs through the release of neurotransmitter by the sympathetic and parasympathetic nerve varicosities speeds the activation of respective G-proteins, which interact with AC and either stimulate or inhibit its rate. AC generates cAMP, which is an important second messenger in the cell, and modulates many cellular functions.

Our model was constructed in a bottom-up manner in order to utilize all of the available experimental data. This approach generated reaction rates that are more than just model parameters: the parameters in

our model all have specific meanings because they represent actual reactions. This is different from other high-level models where parameters are sometimes arbitrarily placed in order to reproduce a desired behavior, and a large uncertainty surrounds their actual value and meaning. Due to the explicit nature of our model, new experimental data can more easily be incorporated to improve the accuracy of any one reaction, or to replace entire mechanisms if necessary. It also lets us make some basic-science conclusions: for example, illustrating the importance of subcellular compartmentalization, or the ineffectiveness of $\beta\gamma$-mediated inhibition of $G_{s\alpha}GTP$.

Despite being very thorough, our model contains a number of limitations arising from the simplifying assumptions we made. The biggest limitation of our model is that we did not include compartmentalization of G-proteins, GPCRs, and AC. More data on this topic is becoming available however, and we suspect that future models that incorporate second messenger localization will have much better performance and will shed new light on the real molecular mechanisms driving the processes within the cell. Another limitation of our model is that we did not consider interactions with regulatory proteins like RGS and GAPs, and this likely contributed to the need for a 'speedup factor' of undetermined molecular origin. Finally, we did not include the long-term processes of receptor desensitization, or the co-stimulation of both the stimulatory and inhibitory G-proteins by the same GPCR family.

Despite all these potential limitations, the model in its current state produces reasonable G_S and G_I activation dynamics and cAMP synthesis rates. It also shows the relative effectiveness of simultaneous adrenergic and cholinergic stimulation, and sets the stage for computing downstream second messenger activation and ion channel modifications that ultimately result in changes in HR.

4 PHOSPHODIESTERASE (EC 3.1.4)

4.1 Overview

This chapter describes the hydrolysis of cAMP by the enzyme phosphodiesterase. We provide two models: 1) a full model with two distinct phosphodiesterase types and explicit modulation of hydrolysis rate by Ca^{2+}-calmodulin and cGMP, 2) a reduced model that is described by a single equation and provides the overall cAMP hydrolysis rate appropriate for the specific chemical environment of the sinoatrial node cell.

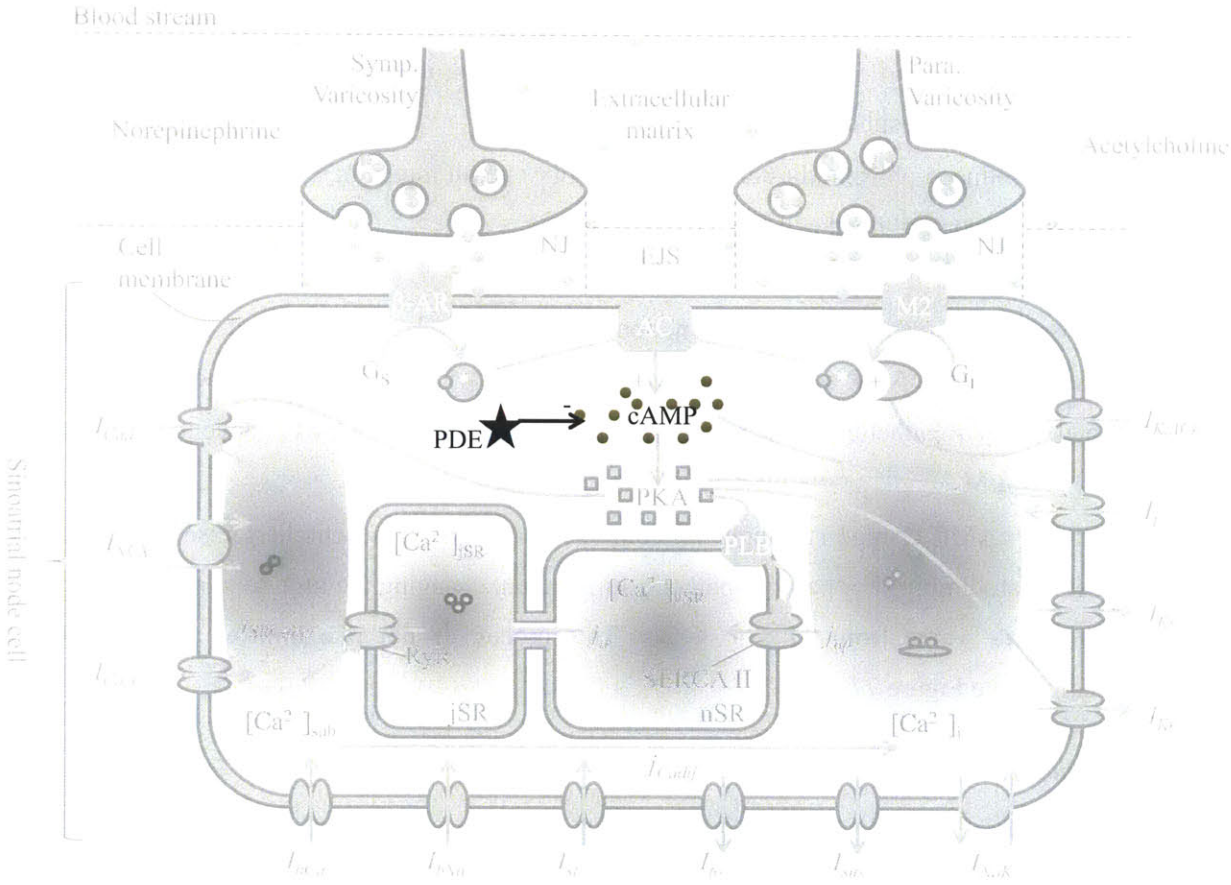

Figure 70. High level illustration of phosphodiesterase (PDE)-mediated hydrolysis of cAMP in the context of the entire model originally shown in Figure 4 (see original figure for key).

Full Model

- Sinoatrial node cells contain two phosphodiesterase types: PDE1 and PDE3, both of which exist in soluble or membrane-localized forms
- PDE1 is activated by Ca^{2+}-calmodulin and cGMP, and it hydrolyzes both cGMP and cAMP (see Figure 72)

- PDE3 hydrolyzes only cAMP; cGMP competitively inhibits this activity (see Figure 72)
- The PDE subtype distributions between cytosolic and membrane-localized fractions, affinities, and catalytic rates are from experimental measurements and the proposed mechanisms are based on the structure of the protein and reproduce experimental data

Reduced model

- The overall cAMP hydrolysis rate by the full model was evaluated at extremes of Ca^{2+}-calmodulin and cGMP concentration encountered by a sinoatrial node cell and this relationship is well-described by a Hill function
- The reduced model is similar to the phosphodiesterase model used by Demir et al. (81), but more rigorously derived and with more accurate absolute hydrolysis rate which agrees well with another published phosphodiesterase model
- We use the reduced phosphodiesterase model in our overall model of autonomic nervous system regulation of sinoatrial node cell function

Results

- The phosphodiesterase model in conjunction with the adenylate cyclase and G-protein models produces a baseline cAMP concentration of 3 μM, in line with experimental values
- Maximal parasympathetic and sympathetic stimulation produce cAMP concentrations on the range 0.3-10 μM
- The rate of cAMP change (through the combined activity of phosphodiesterase and adenylate cyclase) is rate limiting for parasympathetic stimulation, changing the time required to reach 95% of steady-state value from ~1 s to 4-5 s. This process is not rate limiting for sympathetic stimulation. See Figure 77

4.2 Introduction

cAMP is hydrolyzed by enzymes called phosphodiesterases (PDEs). For recent reviews of PDE types, function, and regulation, see (72, 263); here we provide a high-level summary and focus on the characteristics pertinent to our rabbit SANC model. PDEs are classified based on properties of their catalytic domains (class I, II, III), with all mammalian PDEs belonging to class I. This class houses 11 families (PDE1-PDE11), and each family has multiple variants generated through a variety of promoters and alternate splicing. The PDE families differ in cyclic nucleotide selectivity (cAMP or cGMP), regulatory effects (stimulation/inhibition by cAMP/cGMP, phosphorylation, etc.), and localization on the species, organ, and intracellular levels. The effects of PDEs are broad, through downstream effects of cAMP regulation, but also through direct interaction with receptors, ion channels, and various other intracellular proteins (see Fig. 4 in (72)). It has also been recently shown that PDEs act in specific

compartments of cardiac myocytes, and that this localization has important implications for their function (for review, see (176)). We recognize that insufficient data exists to formulate a complete PDE model so we focus on the main features: cAMP and cGMP hydrolysis and regulation by cGMP and Ca^{2+}-calmodulin (Ca-CaM). This approach follows the example of Demir et al. (81), where an even simpler model featuring only hydrolysis of cAMP was used with success. In our model, as in the Demir model, the main purpose of PDEs is to allow for a steady-state cyclic nucleotide concentration despite ongoing synthesis by AC and negligible membrane permeability to cAMP (285, 363).

PDEs contain two important structural domains: a single catalytic site which can bind cAMP and cGMP with varying affinities, and regulatory sites that bind Ca^{2+}-calmodulin (Ca-CaM) or cGMP, or serve as phosphorylation targets for kinases (for a review see (72)). The presence of a single catalytic site that can bind either cyclic nucleotide implies that cAMP and cGMP may competitively inhibit the other's hydrolysis depending on their relative affinities for the catalytic site. This indeed seems to be the case, as measurement shows good agreement between K_I and K_M (317). Binding of regulatory entities may alter the selectivity of the catalytic site or the maximal catalytic rate (62).

PDEs have a profound effect on cardiac contractility, so the bulk of investigation has focused on the effects of PDE inhibitors in ventricular cells (for review see (263)). These studies indicate that PDE3 is the major family found in mammalian cardiac myocytes, it exists in membrane-bound and soluble forms (the membrane bound form is mainly confined to sarcoplasmic reticulum, SR), and the majority of cAMP hydrolysis happens in the cytosol (263). PDE3 hydrolyzes both cAMP and cGMP, has a high affinity for cAMP (K_M<1μM in rabbit, <0.3μM in human) and has a maximal hydrolysis rate for cAMP that is 5-10 times higher than for cGMP, and is inhibited by cGMP with a K_I <1μM (263). In addition to PDE3, rabbit ventricular myocytes have been found to contain PDE1 and PDE2, and human ventricular myocytes contain PDE1-4 (263, 317). From PDE inhibitor studies on rabbit ventricular myocytes, Shahid and Nicholson conclude that under physiological conditions, cAMP levels are controlled mainly by PDE1 and PDE3, while cGMP is regulated by PDE1 and PDE2 (293).

A number studies in rabbit SA node cells were also conducted (317-320, 328, 342, 352, 363). These studies support the general observations from cardiac myocytes but also illustrate that PDE1 and PDE3 are the main families responsible for cAMP and cGMP hydrolysis in the rabbit SANC. Figure 71 shows the cAMP and cGMP hydrolysis rates in the supernatant fraction (soluble proteins) of rabbit SAN homogenate in various fractions of a protein separation column at low (0.4 μM) and high (100 μM, inset) substrate concentrations (317). The peaks of hydrolytic activity (labeled FI-FIII) indicate distinct PDE

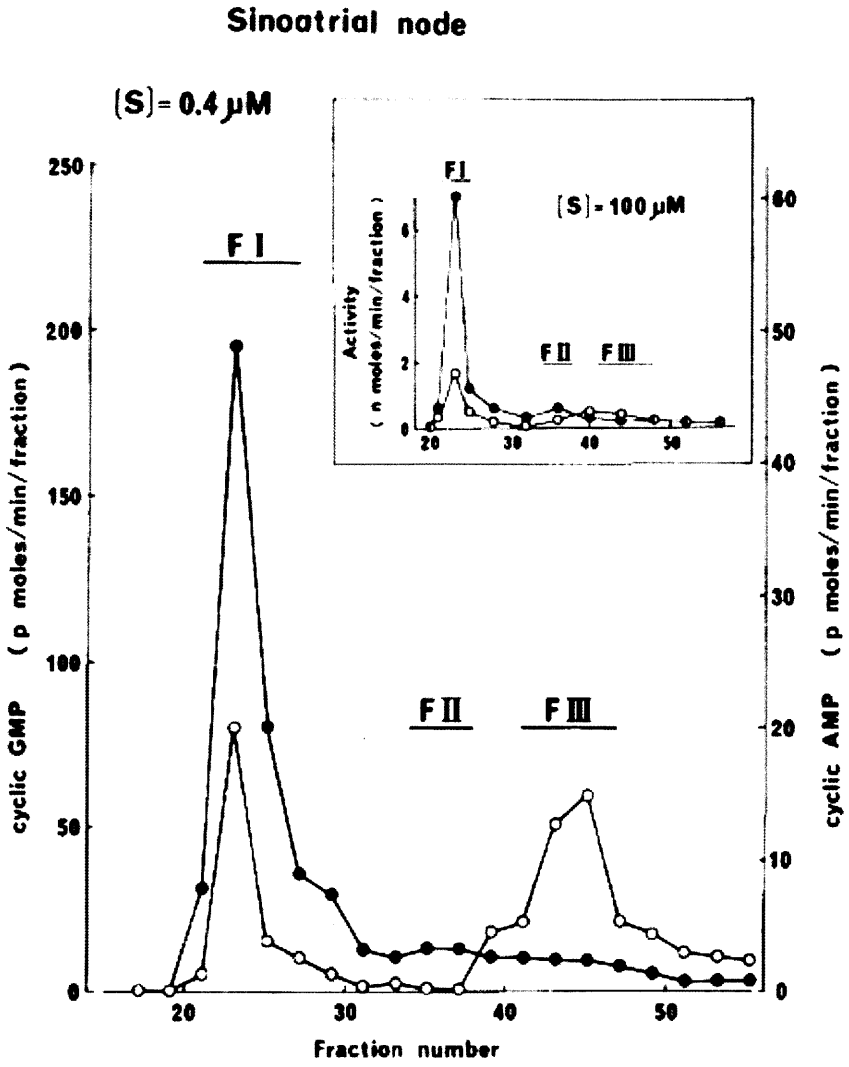

Figure 71 The dominant cAMP and cGMP hydrolyzing PDE families in cytosol are fractions FI and FIII; these fractions correspond to PDE1 and PDE3, respectively. Figure from (317), cGMP (•) hydrolysis and cAMP hydrolysis (○) are indicated as a function of elution fraction. At low substrate concentrations (main figure), cAMP hydrolysis is split between PDE1 and PDE3 (twice as much hydrolysis by PDE3 as PDE1, judging by areas under peaks), whereas PDE1 dominates at high concentrations (inset). cGMP is hydrolyzed by PDE1 only, at both low and high substrate concentrations. PDE2 was shown to hydrolyze cGMP 4× faster in the presence of saturating amounts of Ca-CaM, but even as such, its contribution is less than that of PDE1. Direct information is not available for the dominant families in the sarcolemmal fractions, but cyclic nucleotide specificity and total hydrolysis rates (317), as well as the presence of a transmembrane domain in PDE3 (see Fig 1 in (72)) imply that PDE3 is localized to the sarcolemma.

families, and the numbering convention is in line with that used in ventricular myocyte experiments (FI corresponds to PDE1, FII to PDE2, etc.) (77, 293). Furthermore, the defining characteristics of each PDE family (PDE1 is Ca-CaM stimulated, PDE3 is cGMP inhibited (263, 293)) match with those seen in the corresponding fractions in Figure 71. This figure illustrates that at both high and low concentrations, the majority of cGMP hydrolysis is due to PDE1. Alternatively, cAMP is hydrolyzed by both PDE1 and PDE3 at low substrate concentration, but PDE1 dominates at high substrate concentrations (implying a

lower affinity but higher V_{max} of PDE1 for cAMP). We assume that these two families represent the bulk of cyclic nucleotide hydrolysis in the cytosol and membrane, but allow for different abundances in these two regions. Below we use pertinent experimental measurements to build a model of PDE1 and PDE3 activity in the rabbit SANC.

4.3 PDE Model

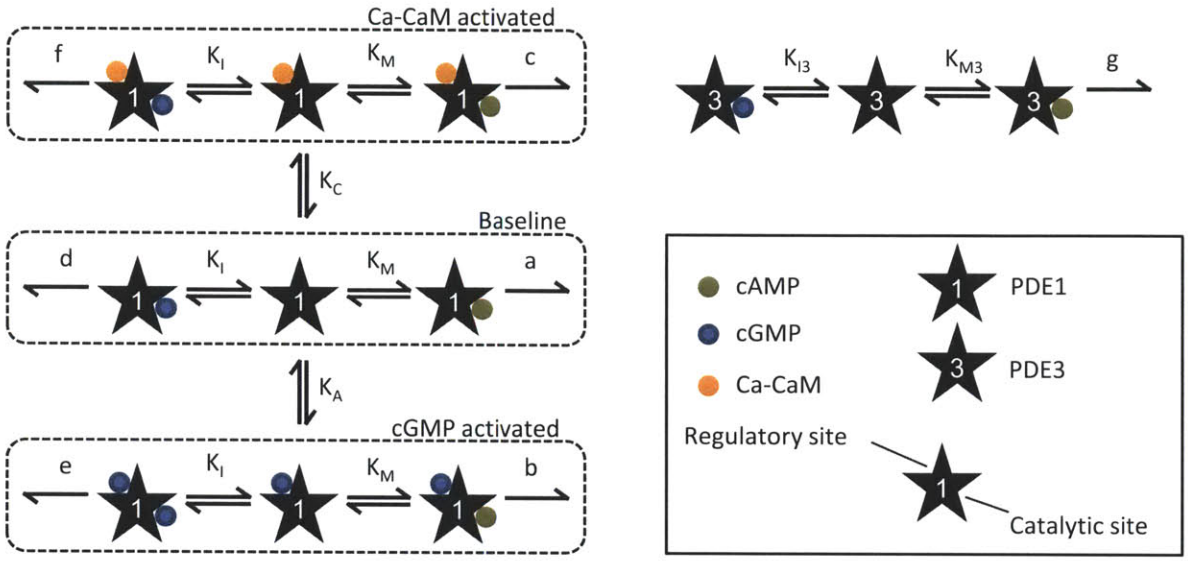

Figure 72 Schematic of PDE1 and PDE3 activity and regulation by cGMP and Ca-CaM. The catalytic site of both PDE1 and PDE3 can bind cAMP and cGMP, which compete with each other (catalytic site reactions shown going left-right). PDE1 also has a regulatory site that can bind cGMP or Ca-CAM and lead to faster catalytic rates (regulatory reactions shown going up-down).

The overall model of PDE1 and PDE3 activity is diagrammed in Figure 72. This model is supported by PDE structure and is the minimal model needed to reproduce all the functional observations quantified by Taniguchi et al. in the rabbit SAN (317, 320). The catalytic site of PDE1 and PDE3 can bind both cAMP and cGMP with affinities K_M and K_I for PDE1, respectively, and K_{M3} and K_{I3} for PDE3. PDE1 also has a regulatory site which can bind either Ca-CaM or cGMP with affinities K_C and K_A, respectively. Both of these regulators have been shown to increase the hydrolysis rate of cAMP or cGMP (317). To keep the model simple, we assume that Ca-CaM and cGMP bind the same regulatory site competitively, and that this binding only affects the catalytic rates (*a-f* in Figure 72) and not the substrate affinities (K_M and K_I). We make these assumptions because insufficient data exist to permit estimation of the additional parameters required by a more general model where both cGMP and Ca-CaM can be bound at the same time. A final detail which is not represented in Figure 72 is that the PDEs are distributed between the membrane and the cytoplasm; this distribution is specified by the fraction of PDE1 and PDE3 in the membrane M_1 and M_3, respectively. The parameter values are set as described in Table 11.

Table 10 Cyclic nucleotide hydrolysis data from (317), at 30 °C and 0.4 μM substrate concentration.

	cAMP hydrolysis (pmol/min/mg protein)	cGMP hydrolysis (pmol/min/mg protein)
Total	32±1 (100%)	120±10 (100%)
Soluble	9±1 (28%)	60±10 (50%)
Membrane-bound	26±2 (81%)	80±10 (67%)

Table 11 PDE complete model parameters for rabbit SANC model at 37°C.

Parameter	Source
K_M=8.3 μM K_I=2 μM K_{M3}=0.8 μM K_{I3}=0.1 μM	Affinities reported by Taniguchi et al. (317)
M_1=0.5	PDE1 is the only PDE that hydrolyzes cGMP (see Figure 71), and cGMP hydrolysis was measured to be roughly equal between the cytosolic and membrane-bound fractions at low cGMP concentration (see Table 10).
M_3=0.8 a=17.4 μM/min g=12 μM/min	In the absence of cGMP and Ca-CaM, and at 0.4 μM cAMP: 1) total cAMP hydrolysis has been measured as 4.8 μM/min (see Table 12). 2) ~0.75 of the total cAMP hydrolysis happens in the membrane-bound fraction (see Table 10). 3) in the cytosolic fraction, cAMP hydrolysis by PDE3 is about 2× that by PDE1 (see Figure 71). These three observations allow us to write three equations, which can be solved for M_3, a, and g: $a\left(0.4/\left(0.4+K_M\right)\right)+g\left(0.4/\left(0.4+K_{M3}\right)\right)=4.8$ $aM_1\left(0.4/\left(0.4+K_M\right)\right)+gM_3\left(0.4/\left(0.4+K_{M3}\right)\right)=0.75\cdot 4.8$ $2a\left(1-M_1\right)\left(0.4/\left(0.4+K_M\right)\right)=g\left(1-M_3\right)\left(0.4/\left(0.4+K_{M3}\right)\right)$
b=54 μM/min K_A=0.3 μM	These values reproduce the data in Figure 73B (b=3.1a) (see reproduction in Figure 74). The Hill coefficient for this reaction is 2
c=35 μM/min	A saturating concentration of Ca-CaM causes cAMP hydrolysis rate to double, c=2a (317)
K_C=2 μM	This dissociation constant and a Hill coefficient of 2 reproduce the data in Figure 73A, see reproduction in Figure 74A. We assume that the affinity of PDE1 for Ca-CaM is the same as that of PDE2, since only data for PDE2 are available.
d=130 μM/min	In the absence of cAMP and Ca-CaM, and at 0.4 μM cGMP, total cGMP hydrolysis rate is 22 μM/min (see Table 12): $d\left(0.4/\left(0.4+K_I\right)\right)=22$
e=130 μM/min	Taniguchi et al. report standard Michaelis-Menten kinetics for cGMP hydrolysis by PDE1 (317); this implies that cGMP binding the regulatory site does not affect cGMP hydrolysis rate, so e=d.
f=180 μM/min	A saturating concentration of Ca-CaM causes cGMP hydrolysis rate to increase by 1.4-fold, f=1.4d (317)

Table 12 Measured hydrolysis rates at 0.4 μM substrate concentration, 30°C, rabbit SANC homogenate.

Nucleotide	Reported hydrolysis rate, 30 °C (μmol/min/mg protein)	Converted hydrolysis rate, 37°C (μM/min)*	Source
cAMP	19.9	3.6	(320)
	27	4.8	(317)
	32	5.7	(317)
cGMP	120	22	(317)

* see section 9.2 for unit conversions

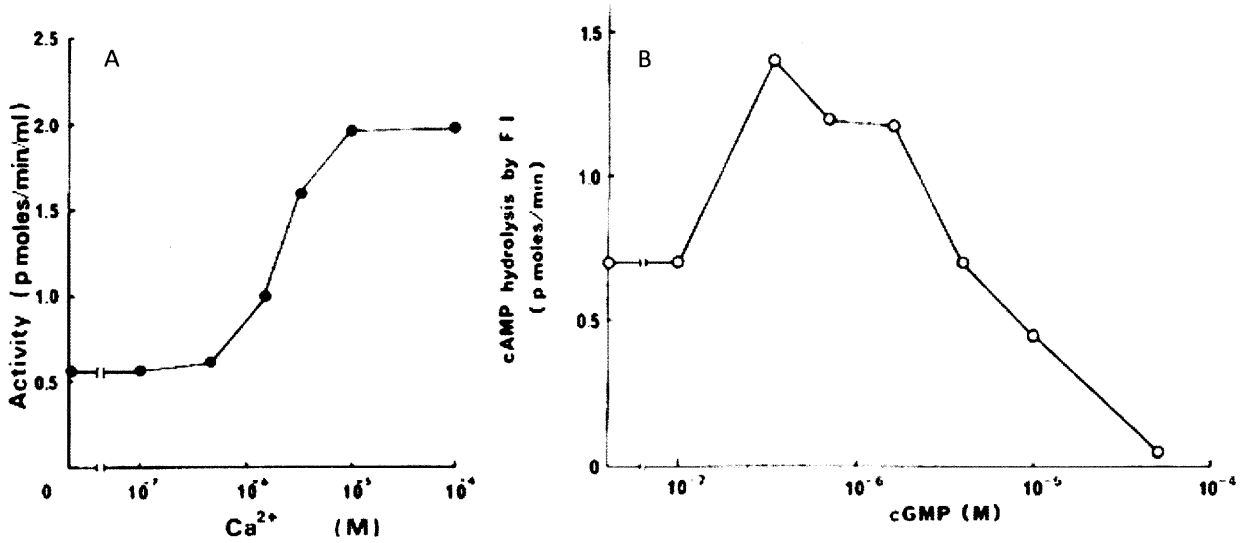

Figure 73 Modulation of PDE2 and PDE1 by Ca-CaM and cGMP. Figures from (317). A. rate of cGMP hydrolysis ([cGMP]=0.4 μM) by PDE2 is shown as a function of saturating amounts of calmodulin (the "activator of the rabbit brain" referred to by Taniguchi et al. (317) is a protein first purified by Cheung (62) and later shown to be calmodulin by Means and Dedman (236)) and the indicated concentration of Ca^{2+}. The effect of saturating concentration of Ca^{2+} and varying amounts of calmodulin produced a similar curve. cGMP hydrolysis by PDE2 was most sensitive to Ca-CaM activation (4× baseline); the effect on cAMP and cGMP hydrolysis by PDE1 was 2× and 1.4× baseline, respectively (317). B) rate of cAMP hydrolysis ([cAMP]=0.4 μM) by PDE1 as a function of cGMP concentration. All measurements at 30°C.

The PDE1 and PDE3 models are specified by equations (12). f_{cGMP}, f_{CaM} and f_{base} are the fractions of PDE1 activated by cGMP or Ca-CaM, and at baseline, respectively. v_{cAMP1} and v_{cGMP1} are the hydrolysis velocities of cAMP and cGMP by PDE1 (soluble plus membrane-bound), and v_{cAMP3} is the hydrolysis velocity of cAMP by PDE3 (soluble plus membrane-bound). To obtain only the membrane-bound PDE activity, the total activities in these equations can be multiplied by M_1 or M_3 (or 1-M_1 and 1-M_3 for soluble portion).

$$
\begin{aligned}
f_{cGMP} &= [cGMP]^2 / \left([cGMP]^2 + K_A^2 \left(1 + [CaM]^2 / K_C^2 \right) \right) \\
f_{CaM} &= [CaM]^2 / \left([CaM]^2 + K_C^2 \left(1 + [cGMP]^2 / K_A^2 \right) \right) \\
f_{base} &= 1 - f_{cGMP} - f_{CaM} \\
v_{cAMP1} &= \left(af_{base} + bf_{cGMP} + cf_{CaM} \right) \frac{[cAMP]}{[cAMP] + K_M \left(1 + [cGMP] / K_I \right)} \\
v_{cGMP1} &= \left(df_{base} + ef_{cGMP} + ff_{CaM} \right) \frac{[cGMP]}{[cGMP] + K_I \left(1 + [cAMP] / K_M \right)} \\
v_{cAMP3} &= g \frac{[cAMP]}{[cAMP] + K_{M3} \left(1 + [cGMP] / K_{I3} \right)}
\end{aligned}
\tag{12}
$$

4.4 Model Reduction:

The full model presented above contains many details that were necessary in order to quantify its properties based on the available experimental data. For purposes of cAMP regulation within a SANC model however, that level of complexity is unnecessary. We therefore reduce the complete model to a total PDE rate by calculating the actual PDE rate according to the full model at fixed cGMP and Ca-CaM concentrations and fitting that relationship with a Hill function. We used extreme cGMP concentrations measured in the SANC at rest and with maximal ACh stimulation (318), and extreme Ca-CaM concentrations based on their values in the Maltsev model. The resulting cAMP hydrolysis rates were well-fit by a single Hill function (see Figure 76) of the form in equation (13):

$$
v_{PDE} = v_{PDE,max} [cAMP]^{n_{PDE}} / \left([cAMP]^{n_{PDE}} + K_{M,PDE}^{n_{PDE}} \right) \tag{13}
$$

4.5 Results

As we can see in Figure 74, Figure 75, and Table 13, this model reproduces the following features of the experimental system:

1) Activation of PDE1 by Ca-CaM (2× activation of cAMP hydrolysis is shown in Figure 74A; cGMP hydrolysis increased by 1.4×, as reported by Taniguchi et al. (317), not shown).
2) Activation of PDE1 by low concentrations of cGMP; competitive inhibition by high concentrations of cGMP (Figure 74B)
3) Competitive inhibition of PDE3 by cGMP (Figure 75C).

4) Distribution of cAMP and cGMP hydrolysis in the cytosolic and membrane fractions of SANC homogenate (Table 13)

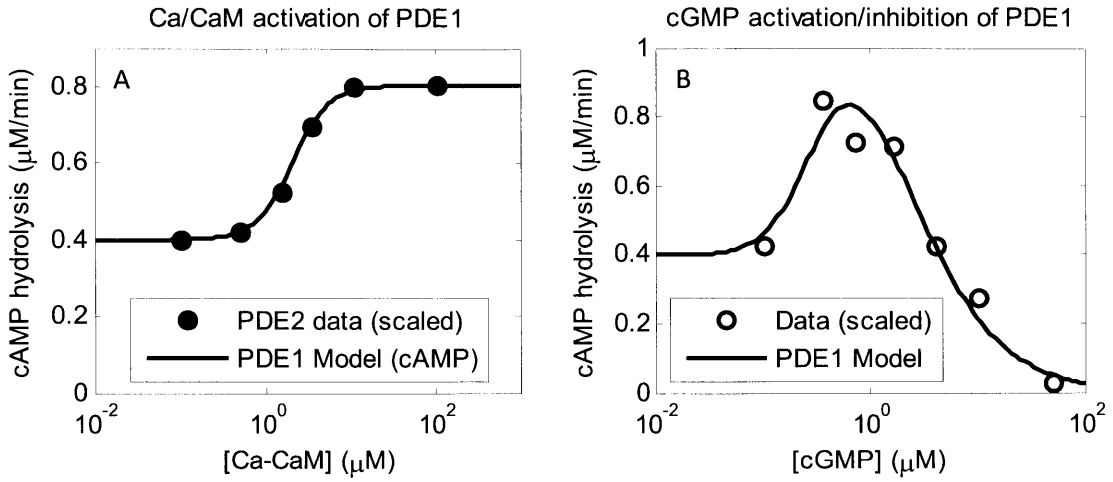

Figure 74 Reproduction of data from Figure 73 using complete PDE1 model. The line in A was generated with [cAMP]=0.4 μM, [cGMP]=0 μM, and [Ca-CaM] as indicated; only the cytosolic activity of PDE1 is shown. The data points in A were digitized from (317) and vertically shifted and scaled to lie on top of the model line (shifting and scaling was necessary because the units and baseline rate of the data were different from the model). The line in B was generated with [cAMP]=0.4 μM, [cGMP] as indicated, and [Ca-CaM]=0 μM; only the cytosolic activity of PDE1 is shown. The data points were scaled to line up with the model (scaling necessary since units of data and model are different).

Figure 74 shows the data that were used to determine the values of parameters K_C, K_A, and b. The model is justified not only by the excellent fits to the data, but also by the molecular structure of PDE1, which contains two regulatory sites (72). The presence of multiple regulatory sites supports cooperative binding (the model uses a Hill coefficient of 2, present as the exponents in equations (12)), which was necessary to replicate the steep up-slopes. The model-generated distribution of PDE activity between the soluble and membrane-bound fractions is shown in Table 13, which can be compared to the data collected by Taniguchi et al. (317) and reproduced in Table 10. The absolute value of the hydrolysis rates is different between the two tables because of disparate units and temperatures, but the percent of cAMP and cGMP hydrolysis occurring in the soluble versus membrane-bound fractions match closely. The values in Table 13 were generated by using equations (12) with the substrate concentration indicated in the table, the presence of a single cyclic nucleotide at a time, and no Ca-CaM. The parameters M_1 and M_3 were used to separate the total PDE1 and PDE3 hydrolysis velocities into soluble and membrane-bound portions. As indicated in the table footnotes, about twice as much cAMP is hydrolyzed by PDE3 compared to PDE1 in the soluble fraction (see Figure 71), and PDE3 dominates cAMP hydrolysis in the membrane-bound fraction at low [cAMP].

Table 13 Cyclic nucleotide hydrolysis model results at 37 °C and 0.4 μM substrate concentration.

	cAMP hydrolysis (μM/min)	cGMP hydrolysis (μM/min)
Total	4.8 (100%)	22 (100%)
Soluble	1.2* (25%)	11 (50%)
Membrane-bound	3.6† (75%)	11 (50%)

* 0.4 due to PDE1, 0.8 due to PDE3. † 0.4 due to PDE1, 3.2 due to PDE3

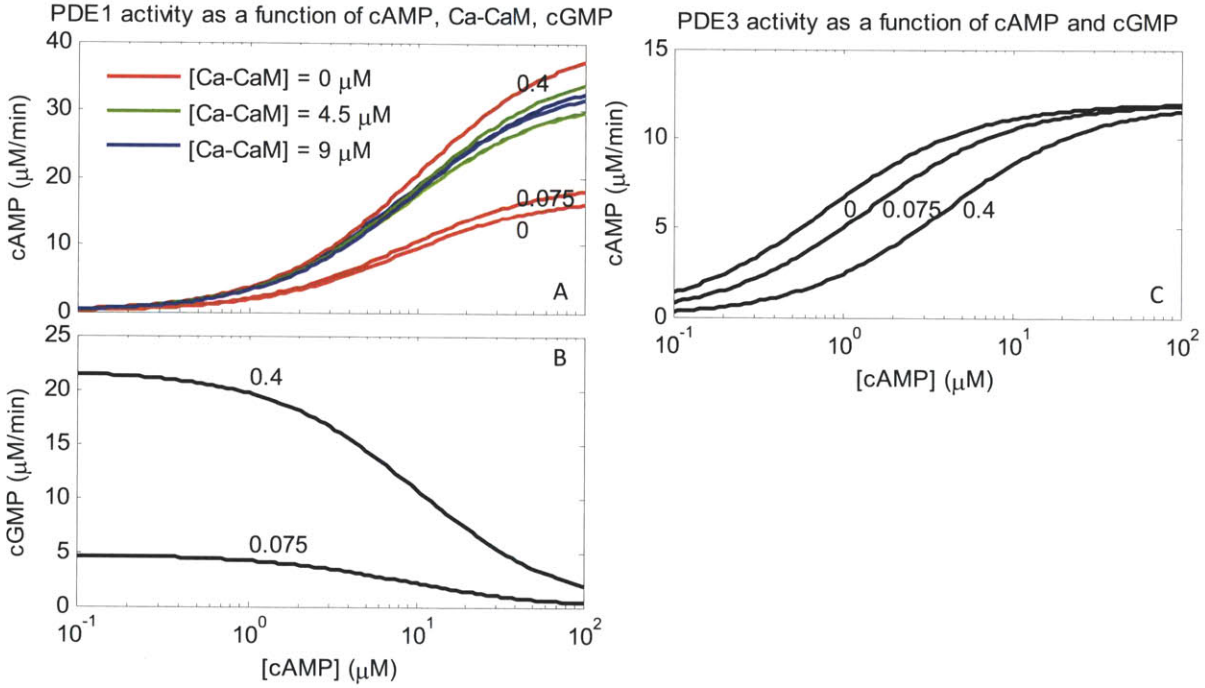

Figure 75 cAMP and cGMP hydrolysis rates by PDE1 and PDE3. In all panels, [cAMP] is on the abscissa, and three [Ca-CaM] and [cGMP] are shown as separate lines. The [Ca-CaM] are indicated in the legend of panel A; the nonzero values were picked because they are the mean [Ca-CaM] in the cytoplasm and sub-membrane space produced by the Maltsev model during steady-state oscillation. [cGMP] are indicated next to each curve (μM). The nonzero [cGMP] are the mean (0.075 μM) and maximum (0.4 μM) concentrations in rabbit SANC at rest and after maximal ACh stimulation, respectively (318). Panels B and C show processes that are insensitive to Ca-CaM so they only include the effect of cGMP. A. cAMP hydrolysis rate by PDE1. B. cGMP hydrolysis rate by PDE1. C. cAMP hydrolysis rate by PDE3.

The summary of PDE1 and PDE3 activity is shown in Figure 75. This figure shows the activation of PDE1-mediated cAMP hydrolysis by both Ca-CaM and low concentrations of cGMP. The results in Figure 75A point to an interesting consequence of this dual regulation: Ca-CaM tunes the sensitivity of PDE1 to cGMP, wherein the effect of increasing [cGMP] is large in the absence of Ca-CaM, but becomes negligible as [Ca-CaM] increases. At the physiological [cGMP] shown in this figure, we appreciate that hydrolysis of cAMP by PDE1 is only stimulated due to the rather low affinity of the PDE1 catalytic site

for cGMP which makes competitive inhibition negligible. On the other hand, PDE3-mediated cAMP hydrolysis is significantly inhibited by physiological [cGMP]. cGMP hydrolysis by PDE1 is inhibited by cAMP in the physiologic [cAMP] range (1-10 μM), as shown in panel B.

Figure 76 shows the total PDE rate under extreme cGMP and Ca-CaM concentrations. The cGMP concentrations are the values at baseline and maximal ACh stimulation as in Figure 75. The Ca-CaM concentrations were calculated by taking the average Ca-CaM concentrations in the subspace and cytosol for the baseline Maltsev model (6.2 and 5 μM, respectively), and scaling them by 0.75 and 1.4 to represent extremes during cholinergic and β-adrenergic stimulation (Ca-CaM changes proportional to intracellular Ca^{2+}, and fig 7 in (227) shows the submembrane space Ca concentration changes by these ratios from the baseline value upon application of Iso and ACh).

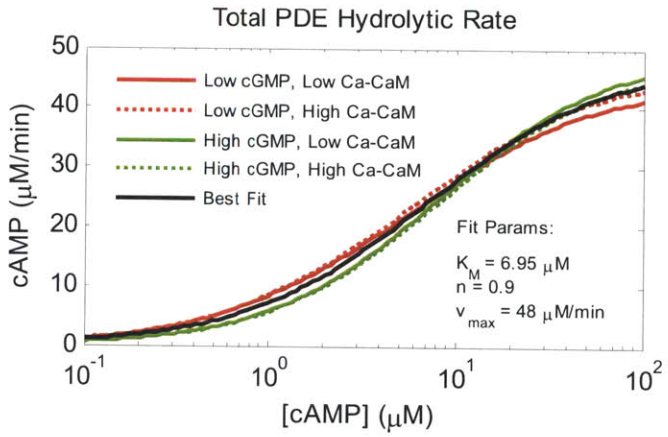

Figure 76 Total PDE hydrolysis at extreme cGMP and Ca-CaM concentrations along with best fit. Low and high cGMP (0.075, 0.4 μM) are each paired with low Ca-CaM (3.8 μM in cytosol, 4.7 μM in submembrane space) or high Ca-CaM (7 μM in cytosol and 8.7 μM in the submembrane space). Parameters were obtained by least-squares fitting (`lsqcurvefit` in Matlab) to all four curves on the displayed cAMP range and are shown on the figure.

The independent effects of vagal and sympathetic stimulation on cAMP rate are shown in Figure 77. Sympathetic stimulation causes an increase in cAMP from the baseline value of 3μM to ~10 μM, with a small difference between the peak and SS value emerging for stimulation frequencies >10 Hz. Vagal stimulation lowers cAMP concentration from the baseline value to ~0.3, and virtually no difference between the steady-state and peak values. The rates of cAMP change tell a similar story as what we saw with β-AR and M2-muscarinic receptor activation, and G_S and G_I activation. The sympathetic effect is still slower than the vagal, with a half-time on the order of 7s and a 0.95 time around 20 seconds. These rates are about the same as what we saw for G_S activation in Figure 67. The vagal effect remains faster,

with a half-time on the order of 1-2s and 0.95 time on the order of 4-5s, a slight slowing from the ~0.5s and 1-2s times, respectively, for G_I activation (Figure 67).

The effect of simultaneous sympathetic and vagal stimulation can be seen in Figure 78. This figure is similar to the figure of AC rate Figure 69, but reflects the equilibrium cAMP concentrations that result from its synthesis by AC and its destruction by PDE. In the absence of simultaneous SS or VS (0 lines), we see the expected sigmoidal decrease in cAMP with ACh, and a sigmoidal increase with NE. Sympathetic stimulation in the presence of moderate ACh concentrations (<0.1 μM) causes cAMP to increase rather effectively, but higher ACh concentrations render this effect virtually negligible. Simultaneous vagal stimulation during NE application produces the expected effect, reducing cAMP with increasing concentrations, and two differences from the ACh/SS simulations: VS reduces cAMP across the whole NE range, and it becomes more powerful with increasing VS (0-5 Hz VS causes a downward shift in the cAMP curves, whereas 7 Hz also shifts the curve to the right).

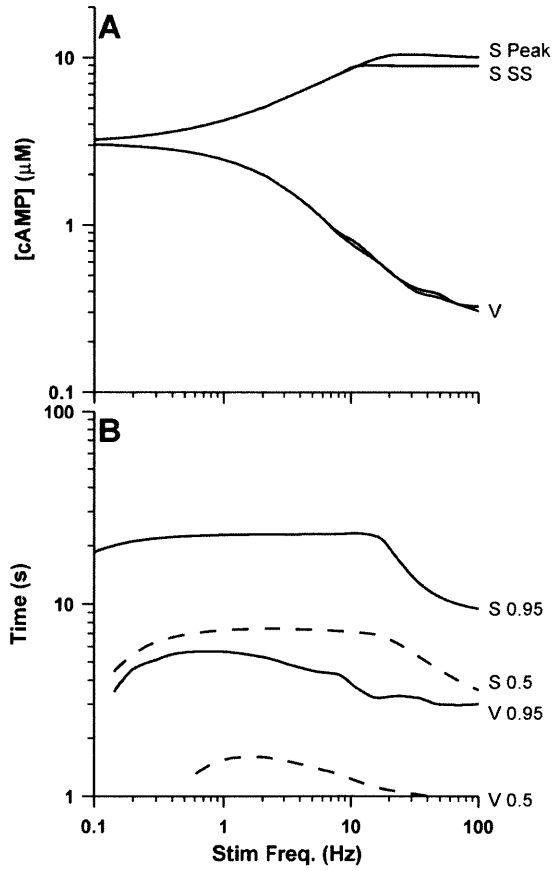

Figure 77 cAMP sensitivity and rate of activation/inactivation (model simulation). A. Steady-state (SS) and peak cAMP concentrations are shown as functions of sympathetic (S) and vagal (V) stimulation frequency, respectively. B. The rates of activation from a baseline level (~3 μM cAMP) to the peak/min values indicated in A. did not follow an exponential time course, so we show the time required to reach 0.5 and 0.95 of peak value. Missing values indicate frequencies where the first stimulus surpassed either the 0.5 or 0.95 point.

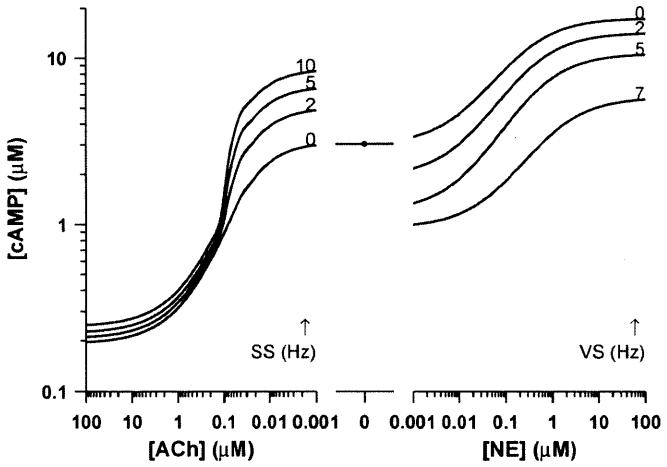

Figure 78 cAMP concentration is modulated by both sympathetic and parasympathetic activity (model simulation). Note the reverse ACh scale; showing maximal cholinergic effect on the left and maximal adrenergic effect on the right. In the ACh regime, four sets of simulations were done, with simultaneous sympathetic stimulation (SS) at 0, 2, 5, and 10 Hz as labeled. In the NE regime, simultaneous vagal stimulation (VS) frequencies are similarly indicated. The baseline panel shows the cAMP concentration in the absence of neurotransmitter. neurotransmitter concentrations were clamped in the neuroeffector junction and EJS (no effect of reuptake / absorption / hydrolysis).

4.6 Discussion

We developed a PDE model for the SANC which uses measured affinities, regulation by cGMP and Ca-CaM, and hydrolysis rates (total, and their distribution between the cytosol and submembrane space). The complete model was then reduced to a simple relationship between cAMP concentration and hydrolysis rate, similar to the PDE model used by Demir et al. (81). We use the reduced PDE model together with our AC model in order to produce steady-state cAMP concentrations that show the expected increase with adrenergic stimulation and decrease with cholinergic stimulation (Figure 77 and Figure 78). The baseline cAMP concentration produced by our model is 3μM. This value falls within the range of measured cAMP concentrations listed in Table 14. Furthermore, the maximum cAMP value generated by the model under maximal adrenergic stimulation (~17 μM) matches the cAMP concentration (~18 μM) obtained by blocking PDE activity in rabbit SANC (342). In our model, complete blockage of PDE would result in infinite cAMP concentration because PDE is the only mechanism for removing cAMP synthesized by AC; we say these numbers match because they at least give us confidence that maximal cAMP concentration should be on the order of 10 μM since unopposed cAMP production in the real cell produces a concentration of 18 μM. Of course, there are experimental considerations such as incomplete blockage of PDE, or whether the system reached steady state (it appears that PDE inhibition proceeded for 5 minutes before cAMP was measured), but this data point is good enough to provide some support for the overall order of magnitude of cAMP concentrations produced by our model.

Table 14 cAMP measurements in mammalian cells. For unit conversions, see section 9.2

Source	System	cAMP Measurement (pmol/mg protein)	Concentration estimate (μM)
Webb et al. 2001 (350)	A7r5*	100	12.4
	Cultured VSMC†	44	5.4
Vinogradova et al. 2006 (341)	Rabbit SANC	100	12.4
Vinogradova et al. 2008 (342)	Rabbit SANC	20	2.5
Taniguchi 1977 (320)	Rabbit SANC	40.6	5

* Arterial smooth muscle cell line. † rat aortic vascular smooth muscle cell

Our model also produced rates of cAMP change that are reasonable: for sympathetic-mediated changes, the rate limiting factor is still the activation of β-ARs; however a slight decrease in activation rate was seen for vagally-mediated changes. This implies that the rate of AC synthesis/breakdown starts to be a rate-determining step in the parasympathetic modulation of HR.

Finally, our model compares favorably with another published PDE model. The maximal baseline cAMP hydrolysis rate in our model is 48 μM/min (reduced model total PDE rate). This value is in agreement with the value used by Banks et al.: 8×10^{-6} mol/min/kg tissue, which converts to ~17 μM/min per cell using the mass and cytoplasmic volume of one SANC model cell (11). The cAMP affinity used by Banks et al. (1 μM) is also close to that in our model. On the other hand, the Demir et al. model used a much higher maximal rate of 20 μM/s (per second!) (81). This value appears to have been picked arbitrarily in order to counterbalance the large baseline cAMP generation rate of 8 μM/s and to reproduce the desired steady-state [cAMP] of 3 μM. As the purpose of PDE in the Demir et al. model was to maintain cAMP homeostasis, the absolute value of the maximal rates were not critical. However, since our model is based on actual experimental data describing PDE kinetics we maintain that our parameters are more correct in an absolute sense. We also note that the maximal PDE rate of 48 μM/min is greater than the maximal AC rate that our model generates (<35/min, Figure 69), which ensures that cAMP concentration cannot increase without bound.

Despite developing a detailed PDE model and using it to reproduce experimental data as well as believable cellular cAMP concentrations, we made a number of simplifying assumptions that need to be discussed. For example, our complete PDE model was not built to reproduce cGMP hydrolysis rate at high substrate concentration (100 μM cGMP). Taniguchi et al. show that at such a high concentration, the cGMP hydrolysis rate is significantly faster (1,470 pmol/min/mg protein) than at 0.4 μM [cGMP] (see Table 12) (317). This implies the presence of a low-affinity, high catalytic rate PDE. We did not include

this species because physiologic cGMP concentration, even under maximal ACh stimulation, does not exceed 1 μM (318).

In our SANC model, we do not explicitly include cGMP concentration, synthesis, or hydrolysis. This decision was made in order to simplify this already complex system and because we reasoned that the effect of this exclusion would not be significant. cGMP changes have been documented in response to cholinergic stimulation of rabbit SANCs (318), and cGMP affects the rate of cAMP hydrolysis by PDE (see complete model developed here, Figure 72). However, the minimal and maximal cGMP concentrations (0.075 and 0.4 μM (318)) do not have a large effect on PDE rate in our model (Figure 75,Figure 76). As we show in Figure 75, the regulatory effect of cGMP on PDE is made negligible by the presence of relatively high Ca-CaM concentrations in the rabbit SANC. Furthermore, including an explicit cGMP synthesis and hydrolysis system would have required the introduction of a number of rate constants and affinities that would come with their own uncertainties attached (especially because the cGMP system does not seem as well-understood as the AC/cAMP system). Finally, the Demir model also considered cGMP concentration to be constant and did not mention that any limitations were caused by this assumption. We do concede however, that if the effect of cGMP on the cAMP balance is not negligible, its exclusion in our model would tend to underestimate the effects of vagal stimulation on cAMP concentration.

We excluded PDE2/4 from this model because the FII peak, which corresponds to PDE2 and PDE4 (see Fig. 5 and 6 in(293)), had very low hydrolytic rate for both cAMP and cGMP according to Taniguchi et al. (317). Another discrepancy between the rabbit SANC and rabbit ventricular PDE1 is that the effect of Ca-CaM is significantly greater in the ventricle (16× activation (293)) than the SAN (2× activation (317)). We replicated the rabbit SANC data and explain the difference as arising from cell-type specific PDE differences; however, the possibility remains that differing experimental conditions or calmodulin quality may be the true cause of this disparity.

Of the two PDE types we model, PDE1 and PDE3 differ in a number of ways: PDE1 has a higher V_{max} than PDE3 but a lower affinity for cAMP, and PDE3 is more selectively localized to the membrane. Furthermore, membrane-bound PDE3 is localized to the SR in humans (221), a prime location for regulating the cycling of Ca^{2+} that has recently been shown to have a major impact on SANC oscillation rate (227). In fact, PDE inhibition studies in human and rabbit cardiac myocytes show a clear impact of PDE3 on HR and contractility (168, 263, 266). A similar result was seen in rabbit SANC, where inhibition of PDE3 increased Ca^{2+} cycling and spontaneous firing rate (342). These properties and

observations imply specific and different purposes for PDE1 and PDE3: the former is suited for regulating bulk [cAMP] in the cytoplasm and may have an effect on PKA activation and downstream effects on ion channels ("membrane clock"), whereas the latter exerts specific control over the cAMP effects on the SR and Ca^{2+} cycling ("calcium clock"). For now, this is just a hypothesis, and more experimental data and a focused modeling study would be required to elucidate the unique roles (if any) played by the different PDE families.

The biggest limitation of the PDE model as presented here, is that we do not consider compartmentalization of PDE and cAMP in the cell. There has been much evidence pointing to the potential functional implications of local cAMP pools which are created because localized PDE creates diffusion barriers or otherwise limits the spread of cAMP from the site of synthesis ((13, 14, 188, 251), see (72, 321, 365) for reviews). We did not model all this complexity due to insufficient data regarding the size of these microdomains and unknown mechanisms of how PDE accomplishes this cAMP-localization task. Beavo et al. also argued that (18) compartmentalization of cAMP was not necessary in order to reproduce its functional effects. However, we did find a need to abstractly incorporate the effect of compartmentalization, by including a cAMP speedup factor of 10 (see section 6.7). This rate was necessary in order to reproduce high-level vagal and sympathetic stimulation data, and implies that the molecular rates of cAMP synthesis and degradation as we have modeled them here are not necessarily applicable when we consider cAMP to be diffused and equal within the entire cytosol. From our experience with this model, the compartmentalization of second messengers is a feature that must be included in future versions, when it is better understood mechanistically and functionally.

4.7 Conclusion

We constructed a detailed model of PDE1 and PDE3 activity in the rabbit SANC, based on experimental data that reported specific affinities, hydrolysis rates, and subcellular distribution of the enzyme. We used a number of simplifying assumptions to reduce the model to a simple relationship that was appropriate for the rabbit SANC, and verified that it works together with our AC model to generate reasonable cAMP concentrations in response to adrenergic and cholinergic stimulation.

Our PDE model converts cAMP synthesis rate to steady-state cAMP concentration (the synthesis rate equals the hydrolysis rate at steady-state), and compares favorably to previous PDE models. However, it also has a number of limitations: it assumes a constant cGMP concentration, when cGMP is known to change with cholinergic stimulation; it does not model all the PDE families known to exist in cardiac cells and which may have distinct effects on cAMP concentration in specific locations; it assumes an even

distribution of PDE throughout the cell and therefore does not create localized cAMP pools or differentially regulate membrane from cytosolic components. Despite these limitations, our model is able to reproduce the phenomena of HR regulation by the ANS. However, in the quest for a true understanding of the molecular processes at play in the SANC response to ANS drive, we must continue to include new data and mechanisms as they are made available, focusing our efforts by addressing the major model limitations first. As with most models, the reward of such work would not be an improvement in the "what," since relatively simple phenomenological models can reproduce input-output relationships very well, but rather in the "how," as we would gain a rigorous mechanistic explanation for how cells function.

5 PHOSPHOKINASE-A (EC 2.7.11.11)

5.1 Overview

This chapter describes the activation of phosphokinase-A by cAMP, as highlighted in Figure 79.

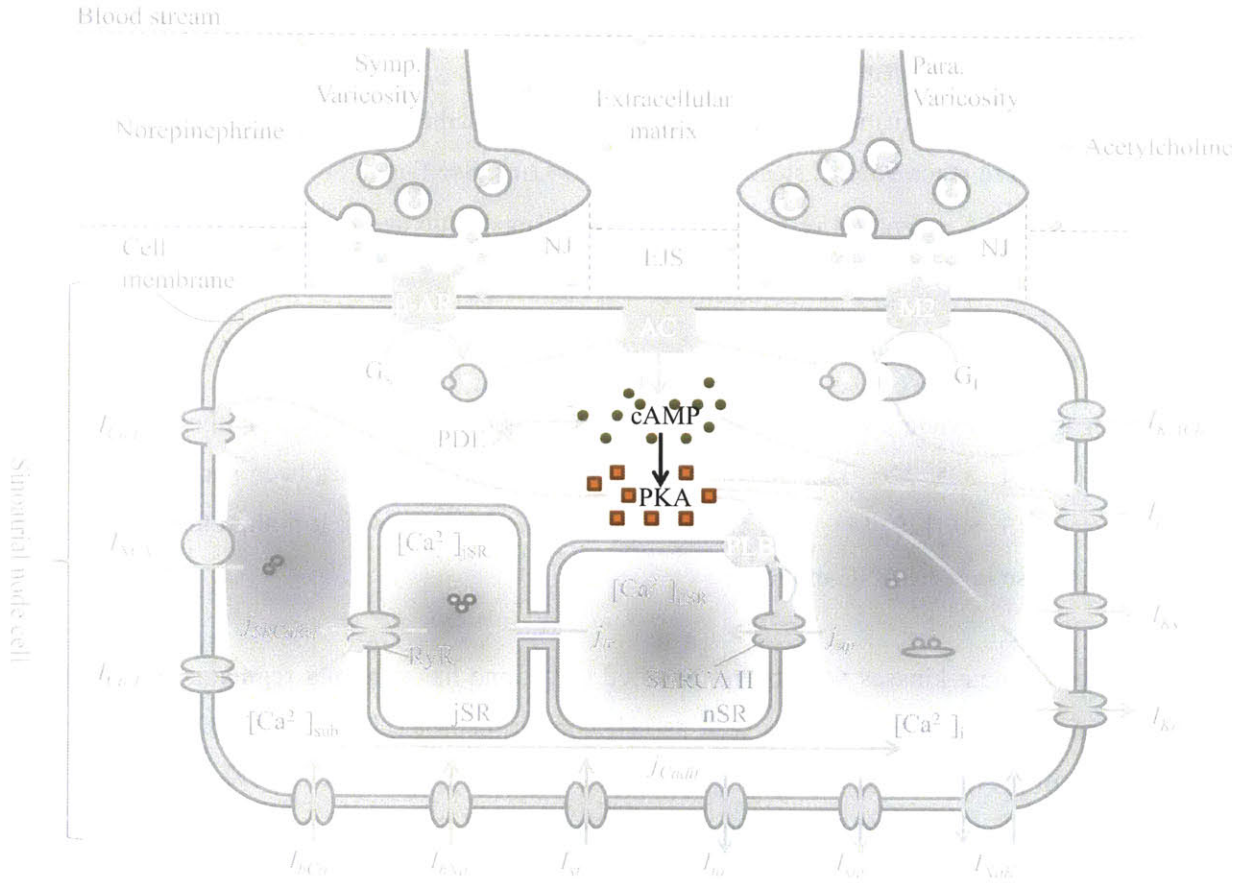

Figure 79. High level illustration of phosphokinase-A activation by cAMP in the context of the entire model originally shown in Figure 4 (see original figure for key).

Model

- Phosphokinase A is composed of two identical regulatory subunits and two identical catalytic subunits. Binding of 2 cAMP molecules per regulatory subunit releases the associated catalytic subunit which can then phosphorylate target proteins
- Phosphokinase A is a very complicated molecule, we present a minimal model
- Activation of phosphokinase A catalytic subunits by cAMP is modeled using a standard Hill function to describe steady-state activation. Total phosphokinase A abundance, half-activation cAMP concentration and Hill coefficient based on experimental measurements.
- The rate of phosphokinase A catalytic subunit activation is based on experimental values

- The phosphokinase A model reproduces experimental data on PKA activation/inactivation due to time-varying cAMP concentration (see Figure 85)

Results

- A wide range of phosphokinase A parameters are published; we summarize the data and provide a theoretical explanation for this variance as a function of the phosphokinase A concentration used in individual experiments
- Phosphokinase A activation is rate-limiting for parasympathetic stimulation, slowing down the time required to reach 95% of steady-state value to ~10 s. See Figure 86
- Phosphokinase A activation reflects the effects of sympathetic and parasympathetic activity (see Figure 87)

5.2 Introduction

Protein kinases phosphorylate a vast array of molecular targets and thereby modulate their function (for reviews see (112, 321, 325, 326, 332, 365)). In the heart, phosphorylation has been shown to influence membrane currents (3, 60, 129, 141, 270) and Ca^{2+} cycling machinery (341). It is therefore important to include protein kinase in our SANC model.

Over 60 different protein kinases have been identified (325), and have varying regulatory mechanisms, phosphorylation targets, and cell type as well as cell compartment specificity (112, 321). The protein kinase family most prevalent in heart tissue is cAMP-dependent protein kinase (cAPK, or protein kinase A, PKA). In its inactive state, PKA exists as R_2C_2, comprising two identical regulatory (*R*) subunits and two identical catalytic (*C*) subunits. Upon binding 4 molecules of cAMP (two per *R*), the *C* subunits are released and available to phosphorylate targets: $R_2C_2 + 4cAMP \leftrightarrow R_2cAMP_4 + 2C$ ((75), (112, 321) for review).

The R subunits interact with cAMP and structural proteins in the cell (202, 321, 332, 362) and can undergo phosphorylation themselves (113, 152). There are two types of R subunit (each one with an α and β subtype, (321, 332)): RI and RII, which define two functionally distinct forms of PKA: PKA I and PKA II. RI and RII differ in affinity for cAMP (152, 321) and structural proteins (144). Because RII has a much higher affinity than RI for structural proteins (144), PKA II can be localized in specific cellular compartments whereas PKA I is soluble (74, 321). It has also been shown that cardiac myocytes contain mostly PKA II whereas skeletal muscle contains PKA I (152). Finally, R subunits can be phosphorylated leading to changes in apparent cAMP affinity (152) and kinetics of reassociation with C (279, 280). Since the rate of R-C reassociation is decreased by phosphorylation, Buxbaum and Dudai have shown that it is a

possible mechanism for long-term PKA activation/memory through autophosphorylation of RII (50). On the other hand, RI does not undergo autophosphorylation (112, 152).

A number of *C* subunit forms exist, but "have similar chemical, physical, catalytic, and immunological properties, as well as similar K_m for ATP, protein substrate specificity, and the ability to interact with either type I or type II *R* subunit" (112). *C* binds ATP with high affinity (K_m=3-18 μM (4, 112)) and various phosphorylation targets with similar affinity (K_m=30-66 μM (4) or 200 μM (126)). The phosphorylation reaction involves the transfer of a phosphate from ATP to the target (fast, >80 /s – 500 /s depending on target, (4, 126, 371)), followed by the rate-limiting release of ADP (24-35/s (371)) that sets overall phosphorylation turnover rate to ~20 /s (4, 371).

The activity of PKA is counterbalanced by protein phosphatases (PPs) that remove the phosphate groups added by PKA. We implicitly model PP activity as playing a role in determining the steady-state phosphorylation state of various protein targets.

5.3 Model

A thorough model of PKA regulation in *Drosophila* has been developed (50); however, brain RII in that model is different from heart RII that we are modeling (351). Also, detailed models for catalytic subunit activity exist (4, 126, 371). While we appreciate the importance of PKA in modulating SANC function, a review of experimental data makes apparent the great complexity of this molecule and its sensitivity to experimental conditions: for example, the concentration of enzyme used in experiments can shift the apparent half-activation concentration of cAMP (K_a) by orders of magnitude ((18), Table 17), phosphorylation and the presence of ATP significantly affect R-C reassociation kinetics (279, 280), and Mg^{2+} (73) and NaCl (249) affect maximal catalytic velocity. A complete PKA model would therefore be overly complicated and would require many assumptions due to the lack of comprehensive experimental data. We also note that other models of SANC modulation by the ANS do not include PKA explicitly (81, 96). We are concerned with the dynamics of SANC modulation, so to capture the contribution of PKA in the second messenger cascade, we include only a minimal model featuring activation of *C* subunit by cAMP. In defining this model, we use data to estimate physiologic PKA concentration, the physiological K_a, and the rate of the activation reaction for the phosphorylated RII subunit (x). A model of phosphorylation is also presented wherein the balance of phosphorylated and dephosphorylated protein targets is a function of *C* and *PP* activity. We assume that *PP* is constant, so steady-state phosphorylation is modeled as a function of *C* only (see section 6.5 for phosphorylation specification; here we focus on

catalytic subunit activation). Our PKA activation model is shown on the right in Figure 80 and is described by equation (14).

$$\frac{dC}{dt} = (2R_{2T} - C)\frac{x}{K_a}[cAMP] - xC \tag{14}$$

Activation

$$R_2C_2 + cAMP \underset{}{\overset{K_D}{\rightleftharpoons}} R_2C_2cAMP_4 \underset{r_{off}/K}{\overset{r_{off}}{\rightleftharpoons}} R_2cAMP_4 + 2C \quad \Longrightarrow \quad R\,C + cAMP \underset{x}{\overset{x/K_a}{\rightleftharpoons}} R\,cAMP + C$$

Phosphorylation

$$\begin{matrix} C + T & \overset{K_T}{\rightleftharpoons} & C\,T & \overset{r_P}{\rightarrow} & C + TP \\ P + PP + T & \overset{r_D}{\leftarrow} & PP\,TP & \overset{K_P}{\rightleftharpoons} & PP + TP \end{matrix} \quad \Longrightarrow \quad T \underset{p(PP)}{\overset{f(C)}{\rightleftharpoons}} TP$$

Figure 80 Model of PKA activation by cAMP and balance of phosphorylation by the C subunit and dephosphorylation by PP. **Activation**: The R subunits are in rapid equilibrium with cAMP described by dissociation constant K_D. It is assumed that C cannot dissociate when cAMP is not bound to R; when R is saturated by cAMP, the C subunits are released with Michaelis-Menten coefficient K and dissociation rate r_{off}. The minimal model of C subunit activation is shown to the right of the empty arrow: cAMP liberates C with an apparent activation constant K_a; the overall rate of the reaction is limited by x, the reassociation rate of R and C. **Phosphorylation**: The phosphorylation and dephosphorylation of target proteins (T) are diagrammed in detail on the left, and a simplified model is shown on the right. We encapsulate phosphorylation with the functional changes it causes, so the modeling aspects are discussed in section 6.5; we provide this diagram to illustrate the mechanism of phosphorylation/dephosphorylation. The C subunits bind T with rapid equilibrium constant K_T, followed by a phosphorylation reaction with rate r_P. The reverse reaction proceeds similarly, with the phosphorylated protein target (TP) binding PP with Michaelis-Menten constant K_P, followed by the dephosphorylation reaction with rate r_D. In the simplified model, the phosphorylation reaction rate is a function of C, $f(C)$, and the dephosphorylation rate is a function of protein phosphatase $p(PP)$.

The assumptions in our model are similar to those used by Buxbaum and Dudai (50): RII is treated as a monomer that binds a single cAMP molecule and releases a single C. This contrasts the fact that the regulatory unit exists as a dimer (R_2C_2), each R binds 2 molecules of cAMP, and releases 2 C subunits upon dissociation, but this simplified model captures the necessary functionality with the benefit of a reduced number of states and rate constants. We further assume that PKA does not dissociate in the absence of cAMP; this is supported by the very high affinity of the RII and C subunits (<0.1 nM in the presence of Mg^{2+} (143)). Finally, we assume that all regulatory subunits exist in a phosphorylated form (see reasoning below), so we only model the phosphorylated kinetics. The model for C subunit activity is also simplified compared to (4, 126, 371) by not modeling specific affinities and phosphorylation rates for the various targets, but rather using just the concentration of activated C subunit to define the steady-state phosphorylation balance for various protein targets (see section 6.5). The use of steady-state functions is

justified by the presence of multiple phosphorylation sites on a single target protein, and complex effects of phosphorylated sites on target protein conformation and function as well as interaction with other cellular machinery that relies on phosphorylation as a signal for removal or up-regulation of specific proteins. The PKA activation model parameters are summarized in Table 15 along with a brief description of how they were obtained. A more thorough explanation can be found in the text.

Table 15 PKA model parameters for rabbit SANC model at 37 °C.

Parameter	Source
R_{2T}=0.5 μM	Measurements of kinase activity (correlated to abundance of C subunit), as well as measurements of cAMP binding (correlated to abundance of R subunit) conducted in rabbit heart tissue homogenate both indicate ~0.9-1 μM for each subunit (74). PKA is a homodimer with two regulatory and two catalytic subunits (R2C2), so R_{2T}=0.5 μM.
K_a=5 μM	Apparent half-activation concentrations of cAMP from a number of studies were used to infer the dependence of K_a on experimental PKA concentration (see Table 17) and this linear relationship was evaluated at physiologic [PKA] to yield K_a. A similar analysis yielded a Hill coefficient of unity, implying that the binding reaction is not cooperative.
x=0.2/min	Obtained by fitting the R-C reassociation time course from (280) (see Figure 85). A rate of 0.07/min fit the experimental data which were collected at 23 °C; this value was converted to 0.2/min at 37 °C using a Q_{10} of 1.7.

We calculate the abundance of PKA in rabbit SANCs from data published by Corbin et al. (74) and reproduced in Table 16. Using either the activity of the C subunit or the amount of cAMP binding protein, the total R subunit concentration in rabbit SANC is ~0.9-1 μM giving a PKA holoenzyme concentration of 0.5 μM (PKA holoenzyme is R_2C_2). This value is greater than that estimated in rabbit skeletal muscle (0.23 μM (18)) but lower than that in rat and cow heart (0.55 and 0.8, respectively (74)). Furthermore, this concentration lies in the middle of the PKA concentration range generally thought to exist in cells (0.2-0.7 μM (112)).

Table 16 also shows that the total PKA activity is split equally between the membrane/protein bound (particulate) and soluble (supernatant) portions. The distribution of RI and RII in these fractions is shown in more detail in Figure 81. This figure shows that the membrane/protein associated PKA is exclusively type II, whereas the soluble fraction contains both types. From the areas under the RI and RII peaks in Figure 81, we compute that roughly 1/3 of the supernatant PKA is type I, whereas the entire particulate fraction and 2/3 of the supernatant are type II. This means that PKA II is about 5× more abundant than PKA I in rabbit heart; an observation supported by other studies (152). We therefore assume that all PKA in rabbit SANC is type II and do not include a model of PKA I. Table 16 also shows the PKA activity

ratio in the presence (+cAMP) and absence (base) of saturating cAMP; these values were used in conjunction with Figure 81 to compute the relative abundances of RI and RII discussed above.

Table 16 Measurements of R and C subunit concentrations and PKA activation in rabbit SANC, reproduced from (74).

	PKA Activity (C subunit)		cAMP binding protein (R subunit)		PKA activity ratio
	U/g tissue	μM*	nmol/ g tissue	μM†	base/+cAMP
Homogenate	53,500	0.97	0.42	0.91	0.15
Supernatant	33,100	0.60	0.21	0.46	0.09
Particulate	26,100	0.47	0.19	0.41	0.24

* converted from U/g tissue using $3x10^6$ U/mg C, 40,000 g/mol C, $3.5x10^{-6}$ mg/cell, $1.6x10^{-12}$ L cytoplasm/cell. † converted from nmol/ g tissue using the weight of the cell and volume of cytoplasm as above

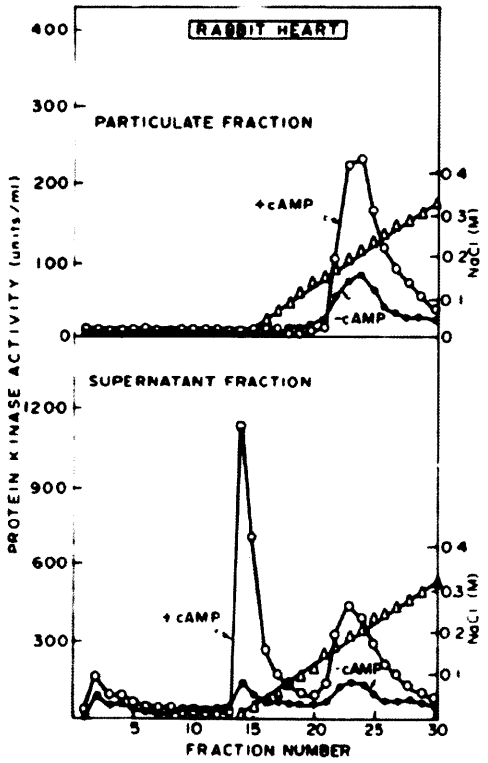

Figure 81 Separation of RI and RII in rabbit heart particulate and supernatant fractions shows that the particulate (membrane/organelle bound) PKA activity is entirely due to RII (second peak) while the supernatant fraction (soluble PKA) is a mixture of RI (first peak) and RII. Figure taken from (74). The protein kinase activity in the absence of cAMP (•) and in the presence of 2 μM cAMP (○) (this concentration is saturating at the low [PKA] in the experiment) are also shown.

The apparent half-activation cAMP concentration K_a depends on the concentration of PKA (18). This is so because standard binding assays assume total enzyme concentration $\ll K_D$, but this is not always the case experimentally, especially for high-affinity interactions like that between R and cAMP. The PKA-

specific apparent activation constants and experimental enzyme concentrations are shown in Table 17 and plotted in Figure 82. The K_a data are well fit by a linear relationship with slope 10, allowing us to estimate K_a at 0.5 μM PKA to be 5 μM. The effect of [PKA] on the Hill coefficient for the cAMP activation is more complicated, as shown in Figure 82B. The three values of PKA I are all ~1, but we were unable to find any data in the range where PKA II exhibited strong cooperative binding. Therefore, it is unclear whether the Hill coefficients for PKA I and II peak around 0.1 μM. From this figure, we conclude that the activation of PKA II by cAMP is not cooperative at physiological [PKA] and has Hill coefficient 1. This observation is in line with the detailed PKA model of Buxbaum and Dudai (50). In Figure 83, we offer a simple illustration of the phenomena of apparent half-activation concentration shift and Hill coefficient increase with total enzyme concentration.

Table 17 Experimental PKA concentration affects apparent K_a and Hill coefficient for activation by cAMP.

[PKA] μM	½ activation [cAMP] μM	Hill coefficient	PKA source	Ref.
0.009	0.3	1.1*	Rabbit skeletal PKAI	(18)
0.15	1.3	1.2*		
0.18	2.8	0.85	Bovine cardiac PKA II	(152)
0.03	0.1	2*	Bovine cardiac PKA II	(279)
0.075	0.3*	4.4*		
0.140	0.4*	2.8*		
2.3	25	1*	Bovine cardiac PKA II	(280)
0.02	0.105	1.5-1.7	Recombinant RI	(143)

* not explicitly reported in papers; calculated by digitizing figures and fitting with Hill functions, see Figure 84 and Figure 85.

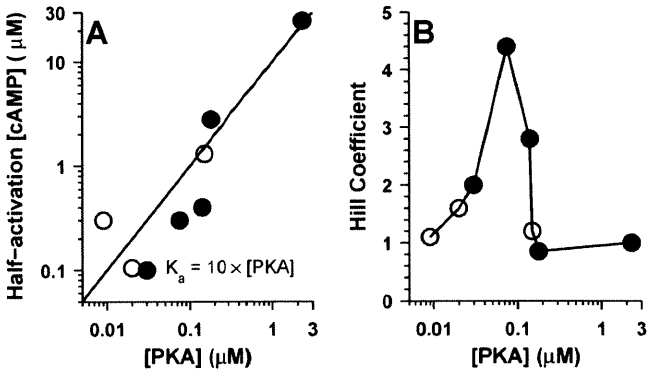

Figure 82 Plots of the data in Table 17. A. K_a for cAMP activation of PKAI (○) and PKAII (●); the equation of the plotted best fit line is shown on the figure (fit to PKA I and II data using `polyfit` in Matlab). B. Hill coefficient as a function of [PKA]; trend is illustrated by a line connecting all the data points.

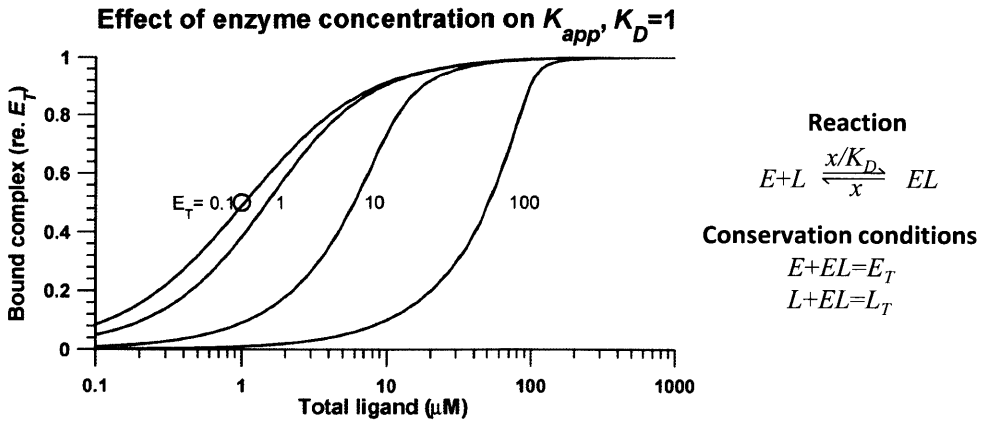

Figure 83 The simple binding reaction shown on the right, with enzyme-ligand dissociation constant K_D and conditions specifying the conservation of the total amount of ligand and enzyme, is solved for bound complex EL. The figure shows the EL/E_T for the indicated amounts of E_T. The actual K_D=1, indicated by ○, but we see that for $E_T>K_D$, the apparent binding curve shifts right and becomes steeper. Cooperative binding of multiple ligand molecules may make these phenomena more pronounced (the figure uses a Hill coefficient of 1, implying non-cooperative binding). The solution is $EL=1/2(E_T+L_T+K_D-[(E_T+L_T+K_D)^2-4E_TL_T]^{1/2}$.

RII can (but RI cannot) undergo autophosphorylation by C (112, 152, 279) via an intramolecular mechanism (108). A number of studies have explored the effect of phosphorylation on RII function (113, 152, 279, 280) and the conclusion is that phosphorylation does not affect affinity for cAMP (279, 280), but does decrease the rate of reassociation of the R and C subunits (which causes the apparent shifts in K_a, as explained by Buxbaum and Dudai (50)). Furthermore, as argued by Rangel-Aldao and Rosen (279) based on the high physiological ATP concentration in cells and the selective action of *PP* on dissociated R_2 (rather than PKA holoenzyme R_2C_2), the majority of PKA in SANCs is likely phosphorylated. We adopt this idea in our model, obtaining the R-C dissociation rate x=0.2/min for the phosphorylated R subunit. This was done by choosing parameters to reproduce an experiment done by Rangel-Aldao and Rosen shown in Figure 85. In this experiment, PKA was incubated with a high [cAMP] (4 mM) to steady state, and then cAMP was hydrolyzed by the addition of PDE (280). As [cAMP] decreases with time, PKA holoenzyme reassociates as quantified through measurement of the catalytic rate of the sample. The data and model reproduction are shown in Figure 85. This figure shows that the rate of R-C dissociation is ~0.07/min for phosphorylated R at 23 °C (0.2/min at 37 °C), and is at least 6 times faster for unphosphorylated R (0.4/min is shown in the figure at 23 °C, but faster rates yielded similar curves). This decrease in R-C reassociation rate due to phosphorylation is similar to the >5× decrease reported in another experiment, where the ratio is again a lower bound due to experimental limitations (279).

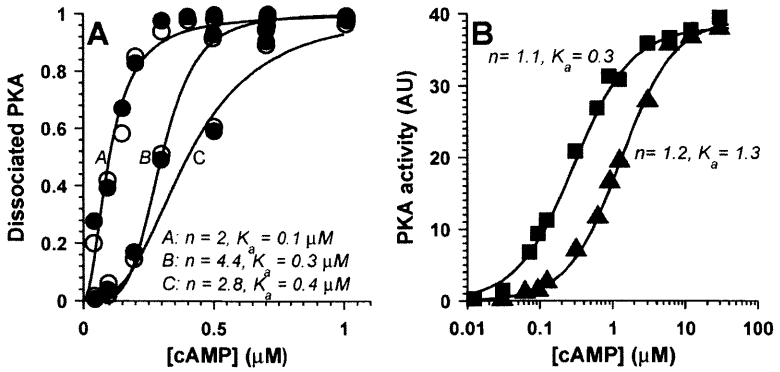

Figure 84 Reproduction of figures from reference papers (18, 279) to estimate the value of Hill coefficient and K_a shown in Table 17. A. fraction of dissociated PKA for phosphorylated (•) and unphosphorylated (○) protein. B. PKA activity in arbitrary units (AU) as a function of cAMP for 0.009 μM (■) and 0.15 μM (▲) PKA.

5.4 Results

Our simple PKA model reproduces data showing dynamic catalytic subunit dissociation from regulatory subunits in response to a changing cAMP concentration (Figure 85). In reproducing this data, we also considered more complicated models, where cAMP-binding and R-C dissociation were separate steps. The more complicated models did not provide a better fit than what is shown in Figure 85, where we considered only a single-step in which cAMP binds and R-C dissociates, and they had the drawback that best fit parameters were not unique.

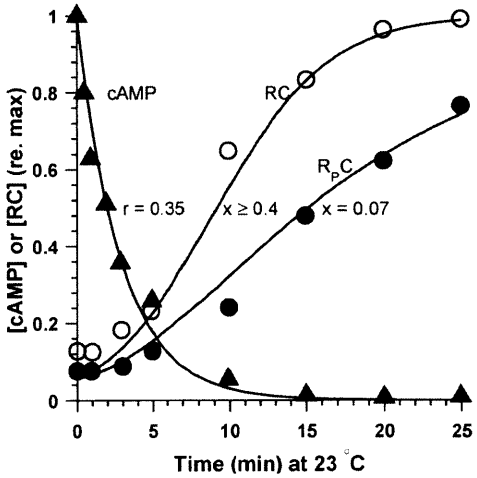

Figure 85 Model reproduction of data from Fig. 1 in (280). cAMP concentration (▲), reassociated unphosphorylated kinase (○), and reassociated phosphorylated kinase (•) are shown relative to their maximum values. Model reproduction is plotted with lines. The rate of cAMP decay was fit to the data (r=0.35 /min). A K_a=25μM and R_{2T}=2.3 μM were reported in the paper. The only free variables were the R-C dissociation rates x, which were fit as indicated next to each curve (units of /min). The model solved the following differential equations: $d[cAMP]/dt=-r[cAMP]$, and $dC/dt = (2R_{2T}-C)x/K_a[cAMP] - xC$, with $[RC]=2R_{2T}-C$, and initial condition $[cAMP]$=400μM, and C= 2×2.3×400/(400+25)= 4.33 μM. For unphosphorylated PKA (curve labeled RC), the minimum rate is shown because all faster rates yielded good fits to the data. For phosphorylated PKA (R_PC), the best fit was obtained with rate 0.07/min. Experiment was conducted at a temperature of 23 °C.

The peak and steady-state C concentration as a function of vagal or sympathetic stimulation follow the expected trends, increasing with sympathetic stimulation, with a slight peak vs. steady-state difference caused by neurotransmitter depletion above 10 Hz, and decreasing with vagal stimulation, with almost no depletion effects (Figure 86). An interesting disparity starts to become visible here as well, in that maximal sympathetic stimulation increases C concentration by less than a factor of 2, whereas vagal stimulation reduces C concentration by almost a factor of 7. The kinetic data for C subunit activation continues to emphasize the difference between sympathetic and vagal rates, with vagal effects being faster than sympathetic. While the sympathetic times for half- and 95%- activation remain about the same as they were for β-AR activation, the vagal effect experiences more slowing down, now with a half-time of ~3 s, and a 95%-time between 5 and 10 s. The time courses are still not purely exponential, as the ratio of 0.95-time/0.5-time is closer to 3 rather than the 4.3 one would expect for a single-exponential approach to steady state.

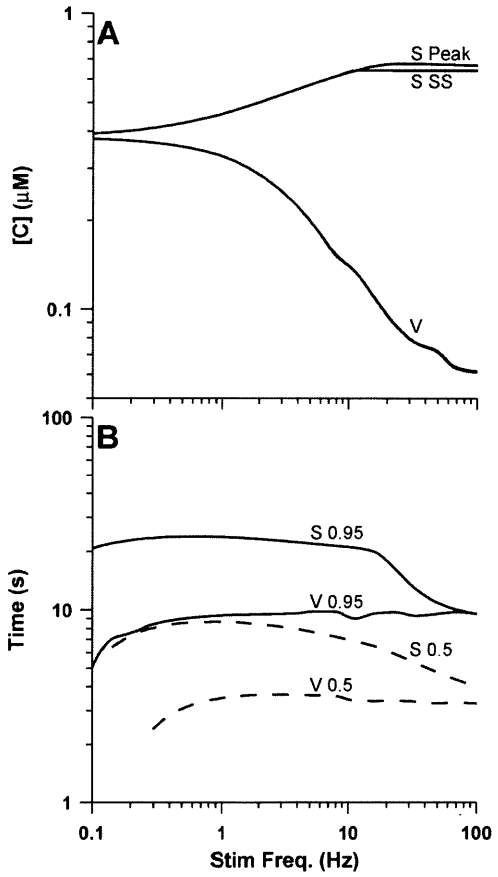

Figure 86 PKA catalytic subunit sensitivity and rate of activation/inactivation (model simulation). A. Steady-state (SS) and peak *C* concentrations are shown as functions of sympathetic (S) and vagal (V) stimulation frequency, respectively. B. The rates of activation from a baseline level (~0.38 μM) to the peak/min values indicated in A. did not follow an exponential time course, so we show the time required to reach 0.5 and 0.95 of peak value. Missing values indicate frequencies where the first stimulus surpassed the 0.5point.

The joint effects of adrenergic and cholinergic stimulation are shown in Figure 87. We again see the large changes effected by cholinergic stimulation (about twice as great as that of adrenergic stimulation), and the effective elimination of an adrenergic effect at high ACh concentrations. At low ACh concentrations however, the adrenergic effect is strong, with 10 Hz sympathetic stimulation raising the C concentration to almost the same level as maximal independent adrenergic stimulation. The effect of vagal stimulation during simultaneous adrenergic activation strongly inhibits C activation, and the effect becomes more powerful with greater rates of vagal stimulation: in the presence of 5 Hz vagal stimulation, the greatest physiological sympathetic stimulation (~10 Hz, equivalent to about 0.1μM NE) barely raises C above the baseline level.

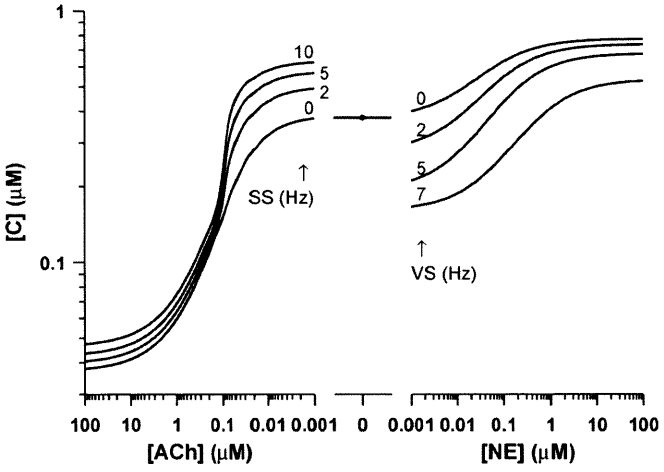

Figure 87 PKA catalytic subunit concentration is modulated by both sympathetic and parasympathetic activity (model simulation). Note the reverse ACh scale; showing maximal cholinergic effect on the left and maximal adrenergic effect on the right. In the ACh regime, four sets of simulations were done, with simultaneous sympathetic stimulation (SS) at 0, 2, 5, and 10 Hz as labeled. In the NE regime, simultaneous vagal stimulation (VS) frequencies are similarly indicated. The baseline panel shows the cAMP concentration in the absence of neurotransmitter. neurotransmitter concentrations were clamped in the neuroeffector junction and EJS (no effect of reuptake / absorption / hydrolysis).

5.5 Discussion

We present a very simple model of a very complicated molecule. Even as such, our PKA activation model reproduces *in-vitro* experimental data (see Figure 84) as well as the following observations made in rabbit SANC. Application of Iso and PDE inhibitor caused a 3 and 9-fold increase in cAMP level, respectively, and resulted in a 1.5 and 2.5-fold increase in PKA-dependent phosphorylation, respectively (342). The baseline [cAMP] in these experiments was ~2 μM, which using our model predicts 1.9× and 2.7× increase in activated C subunit concentration. At baseline (concentration of 3 μM cAMP), our model indicates PKA is 38% activated. This is higher than the 20% baseline activity estimated in skeletal muscle (18), but we argue is reasonable given the strong effect of PKA inhibition on SANC rate (341).

We also quantified the dependence of the apparent half-activation cAMP concentration on experimental conditions; a phenomenon that had been previously noted (18), but not described mathematically using published data from various experiments (18, 143, 152, 279, 280). We described this dependence with a linear relationship that fits the data well on the range 0.01-3μM cAMP, and used this relationship to determine the value of K_a at the estimated cellular concentration of PKA in the SANC.

The effects of adrenergic and cholinergic stimulation on PKA catalytic subunit activation produced by our model are qualitatively correct, with the expected sigmoidal increases with adrenergic activation, and decreases with cholinergic activation. We have been unable to find direct measurements of PKA activity in response to such stimulation, so we cannot definitively state that the values shown in Figure 86 and Figure 87 are accurate. Furthermore, the Demir and Dokos models of SANC rate modulation by vagal stimulation do not include explicit PKA activation, so we cannot compare performance against these models either. However, we constructed our PKA model bottom-up, using a reasonable mechanism and experimentally measured parameters which gives us a fair amount of certainty about its accuracy.
A number of limitations exist in the model due to its simplicity. For example, the model presents no intrinsic mechanism to explain the observed dependence of half-activating cAMP concentration on total PKA concentration, although we do provide a plausible experimental methodology-based explanation for these results. While this exclusion limits our understanding of the system, it does not impair the function of the model in predicting the phenomena of interest. Another limitation is that we do not model PKA I. This molecule may have a different affinity to cAMP and a different rate of activation, which could lead to more complex downstream effects. On the other hand, given its low abundance relative to PKA II, and that we were able to reproduce high-level data using the present PKA II model, we argue that this omission is forgivable.

The biggest limitation is that we do not model subcellular compartmentalization of PKA. It has been shown that compartmentalization may be critical to targeted PKA function ((55, 74, 144), for review see (60, 233, 272, 298, 362, 365)). The consequences of a compartmentalized model would be to allow higher concentrations of PKA in the vicinity of selected structures , which would allow faster phosphorylation and possibly independent dynamics from the rest of the cell. Coupled with localized cAMP pools, the rates of C activation, and the magnitude of the activation could be much greater than in our whole-cell model. In fact, we found it necessary to include an abstract feature of PKA/cAMP compartmentalization in our model, through the use of a speedup factor C_{sf}=100 (see section 6.7 for more detail). Enough data does not exist to formulate a complete compartmental model at this time, but recent advances in

measurement of localized cAMP pools (for review see (176)) and a growing understanding of PKA localization (233, 298, 362) may make the necessary data available in the near future.

5.6 Conclusion

We presented a simple model of PKA catalytic subunit activation, along with simplifying assumptions that would allow the use of C concentration as a determinant of target protein phosphorylation. The model parameters were based on direct measurements of cAMP affinity and deactivation rate. In determining model parameters, we provided an explanation for the large variance in reported K_a values and were able to deduce the value of this parameter in a way consistent with all the data rather than picking an arbitrary value on the observed range.

The model reproduces data collected in cell-free experiments as well as in experiments on rabbit SANCs. However, it is not without its limitations, as it is largely a phenomenological model that ignores the complexity of the interaction between the regulatory and catalytic subunits. The largest limitation of the model presented here is that we consider PKA concentration to be uniform throughout the SANC, ignoring any local differences. Given the structure of PKA regulatory subunits, in particular those of PKA II which are known to contain residues that can anchor it to the cell membrane or other cellular organelles, this is a limitation that will have to be addressed in any mechanistically-correct model of PKA activation and function in the cell.

6 Modification of Ion Channels and Calcium-Cycling Machinery by Second Messengers

6.1 Overview

This chapter describes the interaction of all the second-messengers with the sinoatrial node cell components that they affect. These interactions are illustrated in Figure 88. Elements A and B in this figure were fit using explicit data; 1-6 used implicit data and a global optimization algorithm (details in bullets below). This chapter also includes a thorough comparison of the experimental data and functions used by other models and explores/eliminates an unexpected instability we discovered in the Maltsev model.

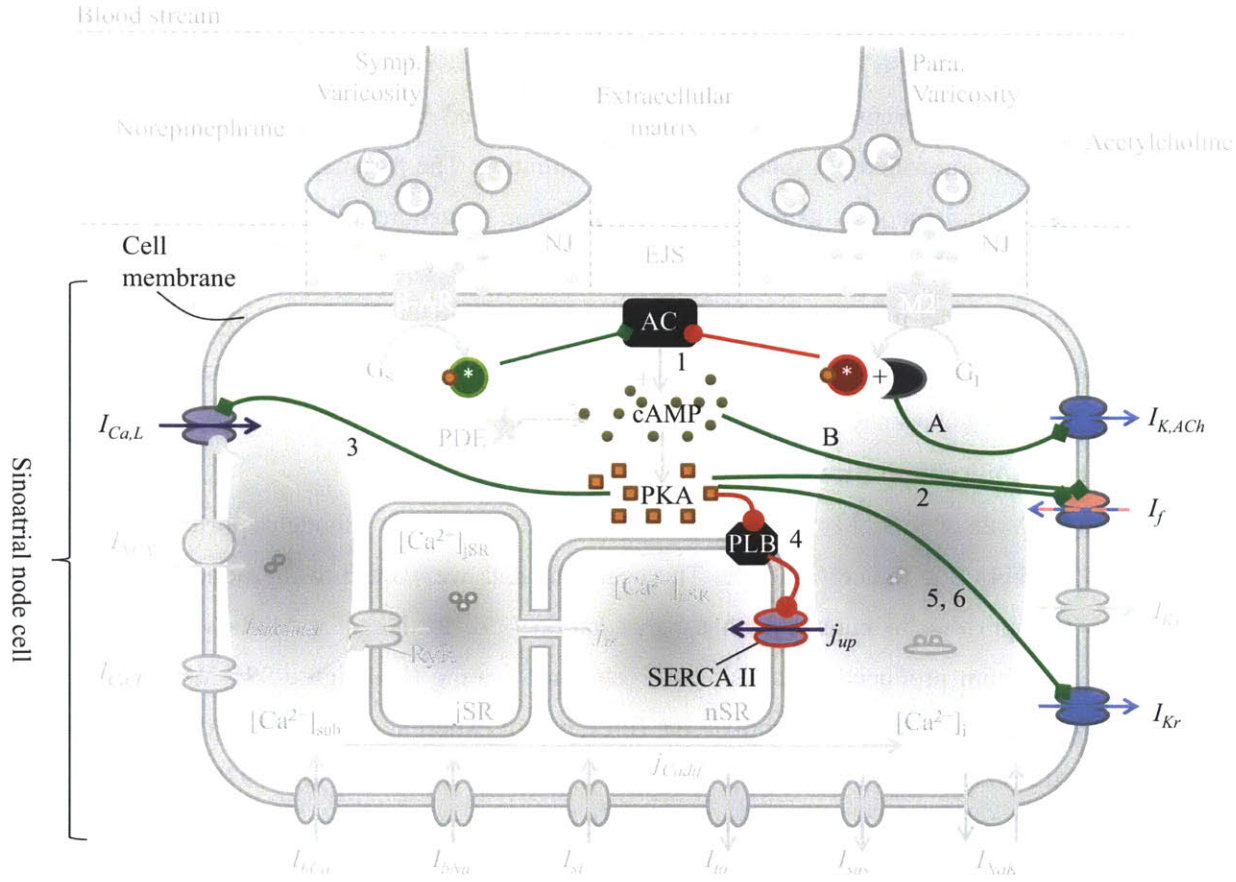

Figure 88. High level illustration of second messenger-mediated effects on sinoatrial node cell components in the context of the entire model originally shown in Figure 4 (see original figure for key). 1: modulation of adenylate cyclase (AC) by stimulatory and inhibitory G-proteins; 2: shift of "funny" current I_f activation gate by phosphokinase A; 3: stimulation of L-type Ca^{2+} current $I_{Ca,L}$ by phosphokinase A; 4: phosphokinase A mediated increase in Ca^{2+} uptake flux j_{up} through SERCA II pump; 5 and 6: stimulation of rapid delayed rectifier K^+ current I_{Kr} conductance and kinetics. A: activation of acetylcholine-sensitive K^+ current $I_{K,ACh}$ by inhibitory G-protein βγ subunit. B: shift of "funny" current I_f activation gate by cAMP.

Second messenger effects on sinoatrial node cell components

- Many (likely, all) of the ion channels are modified by second messengers released through sympathetic and parasympathetic stimulation of the sinoatrial node cell, see Table 18. We follow the example of previous models and change the properties of the major "pacemaking currents"
- $\beta\gamma_I$-mediated activation of $I_{K,ACh}$ (A in Figure 88) and cAMP-mediated shift of I_f activation gate (B in Figure 88) are based on *explicit* data for these reactions. Data for A showed $I_{K,ACh}$ current in response to acetylcholine concentration (we used our G-protein model to compute the $\beta\gamma_I$ concentration corresponding to each acetylcholine concentration, see Figure 89). Data for B showed the shift in I_f activation as a function of experimentally-controlled cAMP concentration (see Figure 91).
- The effect of G-proteins on adenylate cyclase (1 in Figure 88), and the cAMP and phosphokinase A-mediated effects (2-6 in Figure 88) are based on *implicit* data. For example, the effects of acetylcholine and norepinephrine on $I_{Ca,L}$ were measured rather than the explicit effect of experimentally-controlled phosphokinase A concentration. The parameters for all these functions were chosen simultaneously using a global optimization procedure to best-fit all the experimental data at once. The obtained fits are very good; see Figure 105. Our model reproduces experimental data better than other models: see Figure 89, Figure 91-Figure 93, Figure 95, and Figure 96.
- Speedup factors representing rate increases due to subcellular compartmentalization of second messengers were chosen to reproduce dynamic heart rate data (see Figure 106)

Maltsev model instability/limitations

- We use the Maltsev model as the baseline sinoatrial cell model. This model reported heart rates as low as 111 bpm due to acetylcholine. The heart rate data we wanted to reproduce show rates as low as 65 bpm due to parasympathetic stimulation (33). Pushing the Maltsev model to rates below ~100 bpm produced un-physiologic "chaotic" beating (see Figure 97). We were able to correct this aberrant behavior, simulate the full range of experimentally observed heart rates, and improve the shape of the model-generated action potential (compare Figure 97C with Figure 98) by modeling changes in rapid delayed rectifier K+ channel (I_{Kr}) kinetics. These changes were not explored in the Maltsev model but are supported by experimental data.
- A component contributing to the instability is a fixed-frequency subthreshold oscillation due to the L-type Ca^{2+} current ($I_{Ca,L}$). We identify necessary and sufficient conditions for the existence of this oscillation (Figure 100) but do not eliminate it from the model because this behavior has been experimentally observed (Figure 101)

- Our model can reproduce the full range of sympathetically-mediated heart rates (Figure 102) and has a more correct action potential shape than that produced by the Maltsev model (compare Figure 102B to Figure 103)

6.2 Introduction

The second messengers described in Chapters 3-5 modulate target proteins (ion channels and phospholamban), which in turn affect maximal current densities, ion channel kinetics, and Ca^{2+} cycling. In Table 18, we summarize the known modulation mechanisms and the magnitude of adrenergic and cholinergic effects on the ionic currents known to exist in the rabbit SANC. These currents are all included in the Maltsev SANC model, although the full range of modulations described in the table is usually not modeled. In fact, the Maltsev model only considered changes in $I_{Ca,L}$, $I_{K,ACh}$, I_f, I_{Kr}, and P_{up}, and were able to reproduce some adrenergic and cholinergic effects on SANC rate. The Demir model included changes to the most comprehensive number of ionic currents: $I_{Ca,L}$, I_f, I_K, $I_{K,ACh}$, I_{Na}, and I_{bNa}, but since it did not include a description of sarcoplasmic reticulum Ca^{2+} release (a feature unique to the Maltsev model), it did not model changes in Ca^{2+} cycling. Finally, the Dokos model features changes in only three ionic currents in response to ACh released by vagal stimulation: I_f, $I_{Ca,L}$, and $I_{K,ACh}$.

Our work is an extension of the Maltsev model, so we follow their example and focus on reproducing the effects on $I_{Ca,L}$, $I_{K,ACh}$, I_f, I_{Kr}, and P_{up}. We also found it necessary to change the kinetics of I_{Kr}, instead of just its current density as was done by Maltsev et al.. This extra feature allows our model to reproduce the full range of HR observed in vagal stimulation experiments on perfused rabbit hearts (33), and improves the shape of the diastolic depolarization in response to ACh stimulation.

Table 18. Mechanisms and magnitude of the modulation of SANC ionic currents, based largely on the excellent review by Mangoni and Nargeot (231).

Current	Modulation mechanism	Adrenergic effect	Cholinergic effect
$I_{K,ACh}$	Activated by G-protein βγ subunit (358)		Increases with ACh and can stop pacemaking (88, 160, 264, 339)
I_f	cAMP (26, 90); Phosphorylation (3)	Activation curve shifts 9.5-9.6 mV (26), 11 mV (90), or 9.6mV (367). Phosphatase inhibition increased I_f current density by 39.6± 6.4%, and Iso-induced activation curve shift by a factor of 1.5 (3)	Activation curve shifts -9.9 mV (367), -7mV with ACh (88)
$I_{Ca,L}$	PKA phosphorylation (231, 270). G_I-mediated cAMP cascade (145), Nitric oxide-cGMP (111)	Enhanced 103±33% (131) and 54.19% (367) by Iso. NE increases peak current 108±32% and shifts activation threshold to left by 6 mV in mice (230)	~55% decrease by ACh (270). 31% decrease by ACh (367). No effect (145). No effect on baseline, but reverses the effect of Iso (154)
P_{up}	PKA phosphorylation (341)	Iso enhances amplitude and frequency of localized Ca^{2+} releases (338), 2× increase to model Iso effect (227)	Localized Ca^{2+} releases are abolished by inhibition of PKA activity (341). 70% decrease to produce ACh effect (227)
I_{Kr}	PKA and PKC (141, 348)	1.7× increase in I_K due to adrenaline (44). 47±12% increase due to Iso in ventricular myocytes (141). I_K activation speeds up (120) and deactivation slows down (347) with Iso.	
I_{Ks}	Likely same as I_{Kr}, PKA and PKC phosphorylation (348)	PKA and PKC dependent increase in I_K (348)	
I_{st}	PKA phosphorylation (231). Pharmacologic sensitivity similar to $I_{Ca,L}$ (129). AC/cAMP cascade (330)	×2 due to Iso (129, 242). Up 100% due to Iso, EC_{50}= 2.6 nM, also shifts activation to left (330)	10.5± 2% decrease from baseline by 1μM ACh. Can undo stimulation by Iso with IC_{50}=133.9 nM (330)
$I_{Ca,T}$	Coupled with Ca^{2+} release through RyR and NCX (211, 215). G_I-mediated cAMP cascade (145)	4.8±3.4% increase due to Iso (131)	No effect (145)
$I_{bCa/Na}$	Current identified by Hagiwara (132), plays a		

	role in pacemaking (254), specific modulation mechanism not known		
I_{NaK}	Voltage and $[Na]_i$ (289); direct stimulation by Iso (84); mechanism is unclear, but modeled as cAMP effect (81)	May be linked to I_f regulation (231). 27.8±2.4% increase with Iso (84). 2.6× max increase to model Iso effect (81)	ACh decreases I_{NaK} in sheep purkinje (158). Up to 20% increase in K^+ uptake with ACh ((216); this K+ movement is attributed to I_{NaK} (158)). Maximum modeled decrease of 1% (81)
I_{NCX}	Changed passively by RyR modulation by PKA (22)		ACh reduced net slow inward current by 50% (121) which has a component due to I_{NCX} (231)
I_{to}	KChIP2 (Ca sensitive protein) (7); drugs (209)	KChIP1 and 2 increase it more than 10× (7)	May be reduced by lower Ca^{2+} concentration (7)
I_{sus}	Current is similar to I_{to} but with slow kinetics (231); May share similar modulation		

6.3 $I_{K,ACh}$ activation by $G_{\beta\gamma}$

6.3.1 Background

One of the first observations of an ACh-sensitive potassium current was made in tortoise sinus venosus by Harris and Hutter who noted that cells loaded with radioactive K^+ released this isotope much more rapidly upon application of ACh or in response to vagal stimulation (138). An early phenomenological model of $I_{K,ACh}$ was developed by Osterrieder, Noma, and Trautwein (ONT model (264)), where the activation rate of the $I_{K,ACh}$ channel was treated as a function of ACh concentration. This model was subsequently modified and used by Demir et al. (81) and Maltsev and Lakatta (227) in their SANC models. Dokos, Celler, and Lovell (DCL model, (96)) on the other hand, used data from Inomata et al. (160) to formulate a different $I_{K,ACh}$ model. As explained by Dokos et al., the difference between the ONT and DCL models is that the former attributes the lag between ACh application and $I_{K,ACh}$ activation to neurotransmitter diffusion, whereas the latter attributes this latency to the gating of the channel itself (96). A feature that both of these models share is that the channels open as a result of direct interaction with ACh; however, it was shown that $I_{K,ACh}$ channels are controlled by binding of G-protein βγ subunits (220, 358), which in turn are released through ACh-stimulated, M2-muscarinic receptor mediated activation of G_I (see Chapter 3). Thus, in our model the apparent $I_{K,ACh}$ latency is due to the delay in activation of the second messenger $G_{\beta\gamma}$, as well as channel gating. Below, we describe a new model of $I_{K,ACh}$ activation by $G_{\beta\gamma}$. Using our model of neurotransmitter release (Chapter 2), we also provide an explanation for some of

the apparent discrepancies in the experimental data on this channel, which had led different groups to develop inconsistent models.

6.3.2 Model description

We model $I_{K,ACh}$ similar to the original ONT model (osterrieder 1980), as an equilibrium between a closed and open state of the channel, where the opening rate β is a function of $\beta\gamma_I$ (the βγ subunit liberated from inhibitory G-protein), and the closing rate α is a function of transmembrane voltage (V_m):

$$C \underset{\alpha(V_m)}{\overset{\beta(\beta\gamma_I)}{\rightleftharpoons}} O$$

In contrast to the form used by ONT, Demir, and Maltsev, where β is an instantaneous function of ACh, we impose a nonzero time constant on the rate of change of β. This modification was necessary in order to improve the fit to the half-time of activation data (see Figure 89C) and preserve model stability: using an instantaneous relationship for β results in a 3-4 bpm oscillation in HR for low-frequency vagal stimulation.

$$\beta_\infty = 12.32 a_{IKACh} \frac{(\beta\gamma_I)^{n_{IKACh}}}{(\beta\gamma_I)^{n_{IKACh}} + K_{d,IKACh}^{n_{IKACh}}}$$

$$\beta_\tau = \beta_{\tau a} / (\beta\gamma_I)^{n_{IKACh}}$$

$$\frac{d\beta}{dt} = \frac{\beta_\infty - \beta}{\beta_\tau}$$

With a_{IKACh}=1.47, $K_{d,IKACh}$=1.097 μM, n_{IKACh}=3, and $\beta_{\tau a}$=6×10^{-9} ms×mM^3.We used the same formulation for $\alpha(V_m)$ as was used by Maltsev and Lakatta (227):

$$\alpha = 17 e^{0.0133(V_m + 40)}$$

In defining the parameters of $G_{\beta\gamma}$ activation of $I_{K,ACh}$, we use experimental data from three studies: DiFrancesco et al. (88), Inomata et al. (160), and Osterrieder et al. (264). These three sets of experiments differ in SANC preparation: DiFrancesco et al. and Inomata et al. used cells isolated from the rabbit and guinea-pig SAN, respectively, whereas Osterrieder et al. used slices of rabbit SAN tissue. These data are plotted in Figure 89B, and we make two observations: 1) there does not appear to be a large species difference between steady-state activation of rabbit and guinea pig $I_{K,ACh}$, as the data of DiFrancesco and Inomata are in very close agreement with each other 2) ACh hydrolysis by AChE is significant in whole-tissue slices, but does not seem significant in isolated cells. The second point is illustrated most clearly by comparing the Osterrieder "control" data with that of the isolated cell preparations: the Osterrieder data is shifted to the right, indicating a less potent effect of ACh on $I_{K,ACh}$ activation. However, when Osterrieder et al. blocked the activity of AChE using the inhibitor neostigmine, their data shift back to the same range

observed by DiFrancesco et al. and Inomata et al.. We hypothesize that the effect of AChE is apparent in tissue slices but not in isolated cells because the cell-isolation procedure either damages AChE activity or effectively removes all ECM from the cells and therefore allows more accurate control over the ACh concentration at the cell surface. As we showed in Figure 27, our model produces this effect for both β-AR and M2 muscarinic receptor activation when neurotransmitter concentration is fixed at the cell surface (directly in the neuroeffector junction/EJS compartments) versus on the opposite side of the ECM (in the BS compartment). Although our diffusion and AChE models were not constructed with the Osterrieder data in mind, Figure 89B shows that we can reproduce at least some of the rightward shift in $I_{K,ACh}$ by applying ACh in the BS compartment rather than the neuroeffector junction and EJS.

More specifically, Figure 89 summarizes the performance of our $I_{K,ACh}$ model with regard to experimental data and the SANC models of Dokos, Demir, and Maltsev. In panel A, we show the steady-state concentration of $\beta\gamma_I$ subunit in response to ACh concentration applied directly at the cell surface versus in the BS. Panel B shows the steady-state current (or open probability of the channel). We picked model parameters n_{IKACh}, $K_{d,IKACh}$ and a_{IKACh} in order to reproduce the data of DiFrancesco et al. (88), Inomata et al. (160), and the neostigmine data of Osterrieder at al. (264), as well as the maximal value of β used by Maltsev and Lakatta (227) and Demir et al. (81). We can see that our steady-state value is very similar to that of the Dokos model, but produces a more sensitive $I_{K,ACh}$ than that of the Demir and Maltsev models. We also see the modeled effect of a physically distant ACh concentration, which more closely matches the models of Demir and Maltsev, as well as the control data of Osterrieder et al.. Panel C shows the half-time of $I_{K,ACh}$ activation in response to a step in ACh concentration (ACh was applied in the neuroeffector junction/EJS for our model). Our model matches the half-times reported by Inomata et al. and the function used by Dokos et al., but is roughly one order of magnitude slower than the data of Osterrieder et al. and the models of Demir and Maltsev. We chose to use the Inomata et al. data because of the issues with the Osterrieder preparation discussed above. The Inomata et al. kinetic data were collected at 26 °C, but following the example of Dokos et al., we did not temperature-correct them to 37 °C. We conducted simulations using an $I_{K,ACh}$ formulation based on the temperature-corrected data (using the reported Q_{10} of 2.11 (160)), but the slower kinetics shown in Figure 89 produced more physiological HR responses to low-frequency vagal stimulation.

The final parameter of $I_{K,ACh}$ is the maximum current density. DiFrancesco et al. (88) show a maximum $I_{K,ACh}$ of roughly 2 pA/pF at -40 mV. The reversal potential of $I_{K,ACh}$ in our model is -87 mV, which gives a driving force of 47 mV and implies a measured maximal conductance of 0.043 nS/pF, which we use in our model. This value is close to that used by Demir (0.02 nS/pF for bath application of ACh, calculated

from the values of 1.119 nS and cell capacitance of 55×10^{-6} μF, (81)) and Dokos (1.3 pA/pF at -75 mV, from max $I_{K,ACh}$ of 40.5 pA, cell capacitance of 32 pF). Our $I_{K,ACh}$ conductance is smaller than the value used by Maltsev and Lakatta (0.14241818 nS/pF, (227)), which we suspect they chose to offset their less-sensitive $I_{K,ACh}$ activation profile.

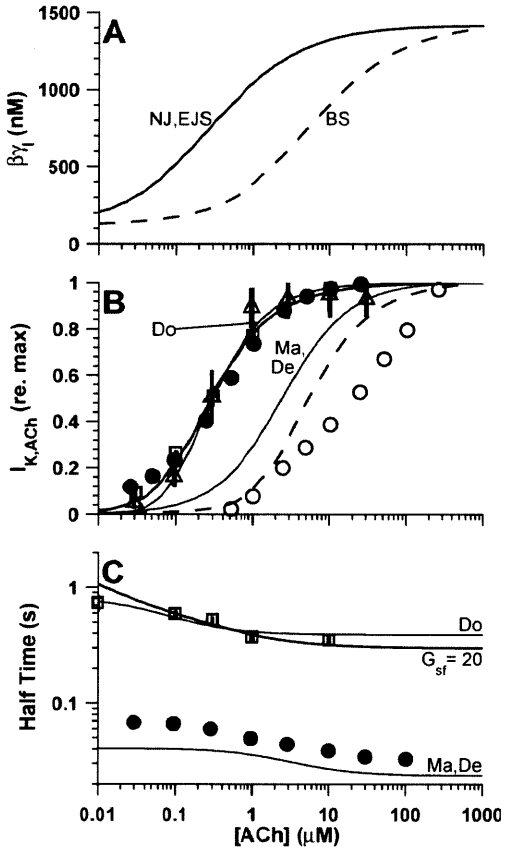

Figure 89 $I_{K,ACh}$ steady-state activation and half-time are reproduced by our model, as well as the rightward shift that most likely occurs due to differences in experimental preparation. A. Concentration of $\beta\gamma_1$ as a function of ACh concentration in the neuroeffector junction and EJS (solid line) versus in the BS (dashed line). B. Experimental data and model reproductions by our model (thick lines, solid is for ACh in the neuroeffector junction and EJS, dashed is for ACh in the BS) the Dokos model (line labeled "Do"), and the Maltsev ("Ma") and Demir ("De") models. The model lines show the steady-state open probability of the $I_{K,ACh}$ channel scaled by the maximum value. Steady-state $I_{K,ACh}$ data from DiFrancesco et al. (88) (Δ), Inomata et al. (160) (□), and Osterrieder et al. (264) (● control, ○ neostigmine) were individually fit by Hill functions and scaled down by the amplitude of the Hill function fit. C. Time to half-activation of $I_{K,ACh}$ in response to steps in ACh concentration. Our model is shown with a thick line for a G-protein speedup factor G_{sf}=20. The Dokos model curve "Do", was computed as $t_{1/2}$=-log(1-0.5$^{1/4}$)/(α_u+β_u) using the equations for α_u and β_u in (96). The Maltsev and Demir model curve "Ma, De" was computed as log(2)/(α+β) using the equations for α and β in (81, 227) at -40 mV because the rates were based on (264), which was collected at -40 mV. As mentioned in the text of (81), the α rate was sped up relative to what was reported by Osterrieder et al.; this is why the curve does not lie on top of the Osterrieder et al. data. The Osterrieder et al. half-times (●) were computed from the α and β values from Fig. 7 in (264) as $t_{1/2}$=log(2)/(α+β). The Inomata et al. (160) data and error bars (□) are shown as reported in the paper, without a temperature correction.

6.3.3 *Discussion*

We model activation of $I_{K,ACh}$ by only the βγ subunits derived from inhibitory G protein ($\beta\gamma_I$). This is at odds with the observation that the βγ subunits are identical between inhibitory and stimulatory G-proteins (178), but was necessary in order to make $I_{K,ACh}$ activation only sensitive to ACh. Using the total βγ concentration derived from both G_S and G_I results in NE-induced activation of $I_{K,ACh}$ due to the βγ subunits liberated in the process of G_S activation. We could not find any reports of adrenergic activation of $I_{K,ACh}$, so we specified its activation by only the βγ subunits from G_I. This approach is reasonable because there may be physical co-localization of $I_{K,ACh}$ channels and M2-muscarinic receptors, which would imply mainly G_I-derived βγ concentration in the vicinity of the channels.

We obtained the value of $K_{d,IKACh}$=1.097 μM by fitting the data shown in Figure 89B. This value is higher than the βγ-$I_{K,ACh}$ dissociation constants directly measured by Wickman et al. (3-30 nM (358)). This discrepancy may be due to a number of factors: Wickman et al. used recombinant $G_{\beta\gamma}$ subunits from rat brain and the $I_{K,ACh}$ channels were from rat atrial myocytes rather than rabbit SANC. Furthermore, Wickman et al. showed that $G_{I\alpha}$GDP has an inhibitory effect on $I_{K,ACh}$ channels; since our model predicts relatively high $G_{I\alpha}$GDP levels in the presence of ACh, this may explain the need for higher $G_{\beta\gamma}$ concentrations to activate $I_{K,ACh}$ (358).

In describing the kinetics of $I_{K,ACh}$ activation by $\beta\gamma_I$, we used the same half-time data used by Dokos et al. (96), although these data were collected at 26 °C rather than the physiologic temperature of 37°C. Our model is capable of reproducing the temperature-corrected data, by increasing the G-protein speedup factor G_{sf} and decreasing the β time constant scalar $\beta_{\tau a}$. The temperature-corrected data and our model fit are shown in Figure 90A. This figure also shows the global effect of these fast $I_{K,ACh}$ kinetics on the model: for slow vagal stimulation frequencies, the HR develops an oscillation, as shown in Figure 90B. The amplitude of this oscillation is greatly reduced by using the slower $I_{K,ACh}$ kinetics we described above. Furthermore, the $I_{K,ACh}$ formulation we use produces virtually the same temporal effect on HR as the faster formulation when the latter is stimulated by an ACh clamp rather than pulsatile vagal stimulation. The origin of the HR oscillation is illustrated in Figure 90C. The top line shows the value of β (the $I_{K,ACh}$ channel's opening rate constant). Due to the very fast response of M2-muscarinic receptors, and the greater G_{sf} needed to reproduce the temperature-corrected $I_{K,ACh}$ half-times, β undergoes a rapid rise and decay with each vagal stimulus, thus the frequency of the β waveform is f_1=2 Hz. The membrane potential (V_m) shows the SANC AP. As we can see in panel B, the HR oscillates between 122 and 128 bpm, so the frequency of the V_m signal is about f_2=2.03-2.17 Hz. The $I_{K,ACh}$ trace is a function of these two processes: the open probability of the channel (determined by β) and the driving force for the current through the

channel (determined by V_m). Thus, $I_{K,ACh}$ exhibits a beat pattern, depending on whether β and V_m are constructively or destructively interfering. Given the frequencies of β and V_m, the expected frequency of this beat is $|f_1-f_2|$=0.03-0.17 Hz, which corresponds to periods of 6-30 seconds. The actual period of the $I_{K,ACh}$ envelope is roughly in the middle of this range, at about 11 s. Finally, because $I_{K,ACh}$ influences the rate of depolarization and therefore the HR, the HR signal reflects the frequency of the $I_{K,ACh}$ envelope, oscillating with a period of about 11s. The HR oscillation is significantly reduced when $I_{K,ACh}$ kinetics are slower because the slower kinetics eliminate much of the β oscillation, as can be seen in the thin line β trace in panel C.

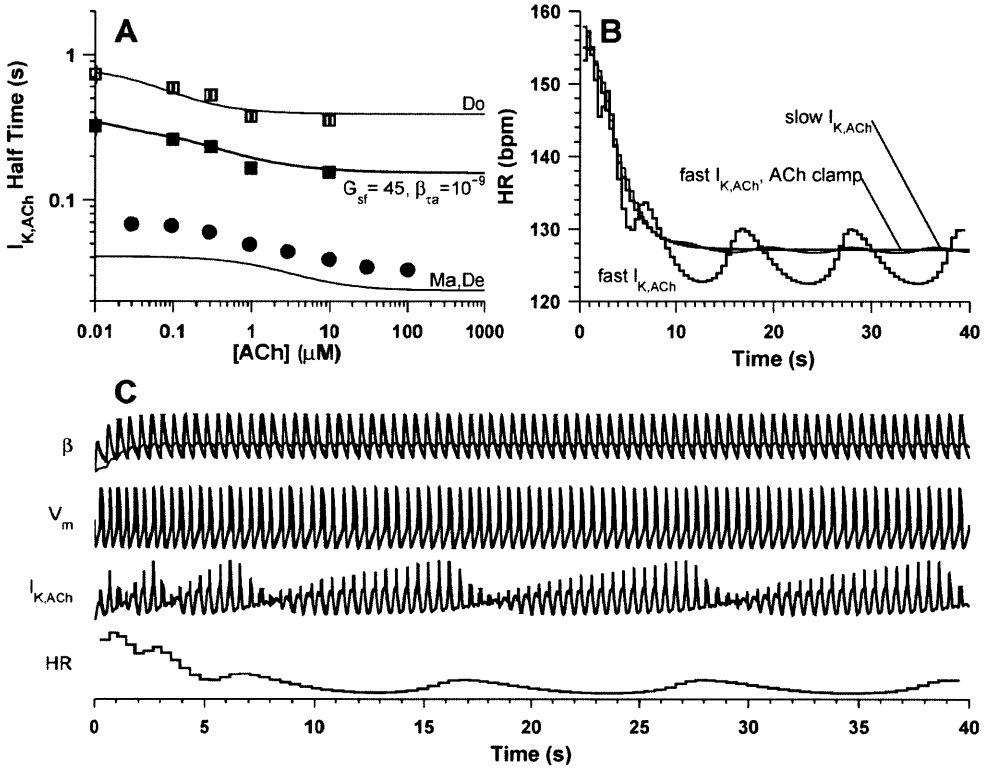

Figure 90. The combination of fast $I_{K,ACh}$ kinetics and uniform-frequency, pulsatile ACh release induces a non-physiologic HR oscillation (model simulation). A. Same as Figure 89C, but includes temperature-corrected half-time data from (160) (■) and shows the model reproduction of that data using G_{sf} and $\beta_{\tau a}$ values shown on the figure. B. HR as a function of time for 2 Hz vagal stimulation using the fast kinetics from panel A (fast $I_{K,ACh}$), the slower kinetics from Figure 89 (slow $I_{K,ACh}$), and fast kinetics but ACh concentration clamp in the neuroeffector junction/EJS instead of 2 Hz vagal stimulation (fast $I_{K,ACh}$, ACh clamp). In the last simulation, ACh concentration was stepped from the baseline level to $0.0082\times2^{1.188}$ μM at time 0, according to the stimulation-frequency → ACh function in Figure 26. C. Thick lines show the value of β, V_m, $I_{K,ACh}$, and HR from the 'fast $I_{K,ACh}$' simulation in panel B. The thin line shows the β value from the 'slow $I_{K,ACh}$' simulation. The y-axis is arbitrary; each trace was scaled to have a similar relative range and shifted vertically for clarity.

The preceding analysis brings into question our early assumption that we can lump all cholinergic varicosities into one. This was done in order to reduce the number of ODEs we would have to solve: ACh release from a single varicosity is described by 6 equations, and there are 14.5 cholinergic varicosities per

SANC, so treating each varicosity individually would mean solving 90 simultaneous equations for ACh release alone! Lumping all the varicosities into one allowed us to gain computational feasibility, but removed the ability to model inhomogeneities that doubtless exist in the system. For example, the distance from the brain to each varicosity is different, so a finite neural conduction rate implies that some varicosities would release neurotransmitter before others. Also, we model the release of multiple varicosities as an instantaneous process, but some temporal jitter likely exists there as well. If we were able to include these effects in the model of ACh release, it would result in a more gradual M2-muscarinic activation profile with each stimulus and a more gradual G-protein activation even with the high G_{sf} required to reproduce the temperature-corrected $I_{K,ACh}$ half-times. Thus, a more accurate ACh release model would have allowed us to more accurately model $I_{K,ACh}$ without running into the HR oscillation we see in Figure 90. However, we made the simplifying assumption at the level of ACh release, and therefore must use slower $I_{K,ACh}$ kinetics in order to avoid the non-physiologic HR oscillation. However, although our $I_{K,ACh}$ formulation does not exactly reproduce the most accurate kinetic data, the effect on HR appears to be negligible, as we can see by the close agreement between the 'slow $I_{K,ACh}$', and 'fast $I_{K,ACh}$, ACh clamp' data in Figure 90B.

In all, our $I_{K,ACh}$ model is mechanistically correct as it is activated by $G_{\beta\gamma}$, it reproduces the steady-state activation profile recorded in a number of studies (86, 160, 264), has similar activation kinetics as used by Dokos et al. (96), and has a maximum conductance based on a measured value (88) and close to the values used in the Dokos (96) and Demir (81) models. The process we followed in developing this model also led to a plausible explanation for the lower ACh sensitivity reported by Osterrieder et al. (264), and brought to our attention the need for explicitly modeling ACh release from individual varicosities or even vesicles (or some approximate way of temporally-smearing ACh release).

6.4 I_f activation curve shift by cAMP ($I_{f,ShiftC}$)

The hyperpolarization-activated Na^+ current, or "funny" current I_f, is known to be affected by adrenergic and cholinergic agonists (88, 91, 92, 367). The effect that is most well-characterized is the shift in the I_f activation curve, which is known to be directly controlled by cAMP concentration (90). The data showing the I_f shift due to cAMP are reproduced in Figure 91. Our model uses the fit published by DiFrancesco and Tortora (90):

$$I_{f,ShiftC} = s_{max}\left[cAMP\right]^{n_f} / \left(\left[cAMP\right]^{n_f} + K_{0.5,f}^{n_f}\right)$$

with s_{max}=11mV, $K_{0.5,f}$=0.211μM, and n_f=0.85. This function is shown in Figure 91, as well as the function used in the Demir model. The function used by Demir differs from the experimental data in two ways: the steepness of the curve is much greater, and the range is roughly twice as large. The Dokos and Maltsev models did not explicitly model cAMP, so we cannot plot their functions here for comparison. We assume that cAMP is in rapid equilibrium with I_f channels, and that the binding reaction produces an immediate effect on the channels so the above relationship is instantaneous. The models of Demir and Maltsev used a similar instantaneous formulation, whereas Dokos used fourth-order kinetics to relate ACh concentration to $I_{f,Shift}$. Dokos et al. mention that their choice of fourth-order kinetics was arbitrary; also, it is pertinent to note that their formulation treats the whole cascade from ACh to $I_{f,Shift}$ as a single process, whereas the latency and delay in our model arise from the intermediate steps of receptor and G-protein activation, and cAMP synthesis.

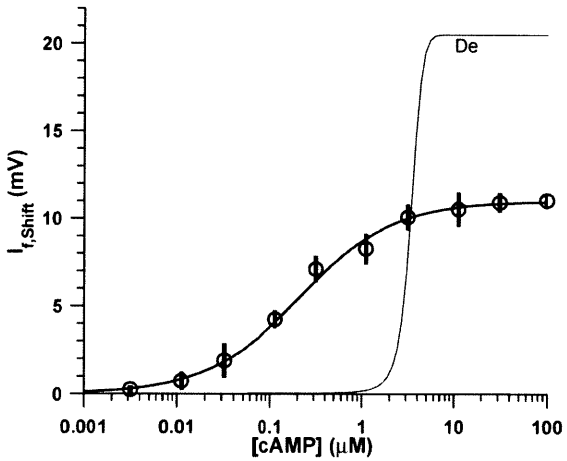

Figure 91. The I_f activation curve shifts with cAMP. Data (○) from (90) are reproduced along with the function used in our model (thick line) and the function used by Demir et al. (thin line labeled 'De') (81).

The function used by Demir deserves further discussion, as it illustrates an attempt to deal with an inconsistency in the experimental data. As we can see from the data in Figure 91, cAMP accounts for a maximal shift of 11 mV; however, experiments have shown that I_f activation shifts maximally by 9.5 to 11 mV (26, 90, 367) upon adrenergic stimulation and -7 to -9.9 mV (88, 367) with cholinergic stimulation (see Table 18 for details), implying a ~20 mV range of shifts. Demir et al. dealt with this inconsistency by expanding the range of their cAMP→$I_{f,ShiftC}$ function to 21 mV. We considered this approach as well, but upon a further review of the literature we found data showing that the I_f channels are also modified by phosphorylation (3), which affects both I_f current density and the shift in the activation curve (see Table 18 for details). We therefore express the total activation curve shift as a sum of a cAMP- and a PKA-mediated effect: $I_{f,Shift}=I_{f,ShiftC}+I_{f,ShiftP}$. We use the exact cAMP→$I_{f,ShiftC}$ relationship reported by DiFrancesco and Tortora (90), and we fit the parameters of the PKA→$I_{f,ShiftP}$ function in order to

reproduce the full range of $I_{f,Shift}$ data in response to adrenergic and cholinergic stimulation (367). We present the details in the following section, since we used a consistent framework to represent all the PKA effects.

6.5 PKA Effects

PKA phosphorylates various target proteins and in this way affects their function. In our model, we developed mechanistically-motivated descriptions of the signal transduction cascade from autonomic nerve impulses to the activation of PKA catalytic subunit *C*. In describing how *C* affects the properties of various ion channels and other functionally-important proteins in the SANC, we step away from mechanisms and focus on the important phenomena instead. This abstraction is necessary because the effects of phosphorylation are very complex, and therefore require more data than are currently unavailable. For example, phosphorylation involves a number of steps: binding of *C* to the phosphorylation sites (likely a plurality of sites per protein), the phosphorylation reaction itself wherein a phosphate is transferred from a donor ATP to the target site, the concurrent dephosphorylation of these same sites by a number of protein phosphatases (PPs), and the final change in protein function as a consequence of phosphorylation, which can either be a direct effect due to a conformational change in the protein or the result of interaction with other cellular machinery that relies on phosphorylation as a signal for removal or up-regulation of specific proteins. Thus, to describe all these reactions, we would need information regarding the number of phosphorylation sites on each protein of interest, the affinities and rates of phosphate transfer for each of these sites, the affinities and rates of dephosphorylation by PPs, a description of other regulatory proteins that interact with these sites, and the final quantitative measurement of the effect of phosphorylation on the function of the target protein.

Given that an explicit mechanistic model of PKA effects on SANC function is too complicated to parameterize confidently, we adopt the simplest model that is still based on the above mechanisms and can reproduce the high-level data of interest. We define steady-state functions to describe the change (either relative or absolute) in the phosphorylation-modulated model parameters. Based on the mechanisms mentioned above, these steady-state functions are expected to be monotonic with C, and can be arbitrarily complicated given the number of steps involved. We use the sum of Hill functions to describe each steady-state relationship; in most cases only two functions were necessary:

$$I_{f,ShiftP,SS} = a_{0S} + a_{1S}\frac{C^{n_{1S}}}{C^{n_{1S}} + K_{1S}^{n_{1S}}} + a_{2S}\frac{C^{n_{2S}}}{C^{n_{2S}} + K_{2S}^{n_{2S}}}$$

$$R_{gCaL,SS} = a_{0C} + a_{1C}\frac{C^{n_{1C}}}{C^{n_{1C}} + K_{1C}^{n_{1C}}} + a_{2C}\frac{C^{n_{2C}}}{C^{n_{2C}} + K_{2C}^{n_{2C}}}$$

$$R_{Pup,SS} = a_{0P} + a_{1P}\frac{C^{n_{1P}}}{C^{n_{1P}} + K_{1P}^{n_{1P}}} + a_{2P}\frac{C^{n_{2P}}}{C^{n_{2P}} + K_{2P}^{n_{2P}}}$$

$$R_{gKr,SS} = a_{0K} + a_{1K}\frac{C^{n_{1K}}}{C^{n_{1K}} + K_{1K}^{n_{1K}}} + a_{2K}\frac{C^{n_{2K}}}{C^{n_{2K}} + K_{2K}^{n_{2K}}}$$

$$pa_{sf,SS} = a_{0p} + a_{1p}\frac{C^{n_{1p}}}{C^{n_{1p}} + K_{1p}^{n_{1p}}} + a_{2p}\frac{C^{n_{2p}}}{C^{n_{2p}} + K_{2p}^{n_{2p}}} + a_{3p}\frac{C^{n_{3p}}}{C^{n_{3p}} + K_{3p}^{n_{3p}}}$$

Given the complexity of the system, some delay is expected so we include a single time constant τ_P to define the differential equations:

$$\frac{dI_{f,ShiftP}}{dt} = \left(I_{f,ShiftP,SS} - I_{f,ShiftP}\right)/\tau_P$$

$$\frac{dR_{gCaL}}{dt} = \left(R_{gCaL,SS} - R_{gCaL}\right)/\tau_P$$

$$\frac{dR_{Pup}}{dt} = \left(R_{Pup,SS} - R_{Pup}\right)/\tau_P$$

$$\frac{dR_{gKr}}{dt} = \left(R_{gKr,SS} - R_{gKr}\right)/\tau_P$$

$$\frac{d\,pa_{sf}}{dt} = \left(pa_{sf,SS} - pa_{sf}\right)/\tau_P$$

We describe the meaning of each of these variables below, and discuss the experimental data that justify each variable's dependence on PKA phosphorylation. The optimization method we used to compute the best-fit parameters for the above equations is discussed in section 6.6.

6.5.1 Shift in I_f activation ($I_{f,ShiftP}$)

As we discussed above, the I_f activation function is known to shift with adrenergic and cholinergic stimulation. We modeled the direct cAMP effect to reproduce the pertinent data (Figure 91), and we include a PKA-mediated shift based on the observations of Accili et al. that phosphorylation also contributes to a shift in I_f activation (3). We use data from a study by Zaza et al. (367), where $I_{f,Shift}$ was directly measured in isolated rabbit SANC cells in response to the adrenergic agonist Iso, and the

cholinergic neurotransmitter ACh. To convert the Iso data to equivalent NE concentrations, we shifted the data one order of magnitude to the right (see Figure 32).

The Demir, Dokos, and Maltsev models do not explicitly include a phosphorylation-mediated change in I_f. Demir et al. ascribe the full effect to cAMP, at the expense of not reproducing the cAMP data of DiFrancesco and Tortora (90). On the positive side however, the Demir model provides smooth $I_{f,Shift}$ with both ACh and Iso application (81). Maltsev and Dokos use functions that directly translate ACh concentration to $I_{f,Shift}$, so they neither espouse not denounce a PKA-mediated mechanism. They also do not provide functions for adrenergically-mediated changes: Dokos does not include an adrenergic model at all, and Maltsev simply uses a constant shift of 7.8 mV to simulate a maximal β-adrenergic effect (227). The experimental data from (367), our model reproduction of that data, and the models of Demir, Dokos, and Maltsev are summarized in Figure 92.

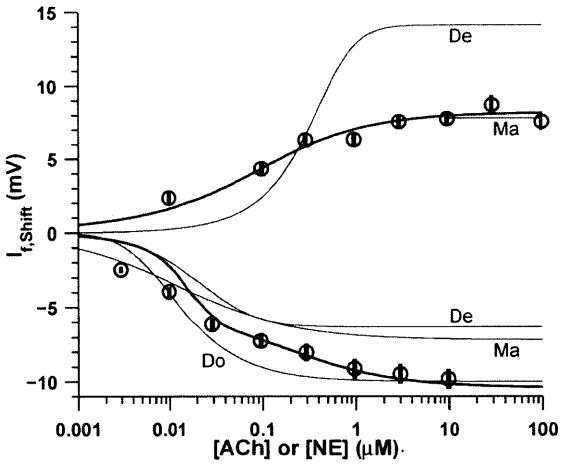

Figure 92. Our model reproduces experimental data on the shift in I_f activation due to adrenergic and cholinergic stimulation. Data from Zaza et al. (○) (367) are shown with the decreasing points showing the ACh effect and the increasing points showing adrenergic effect. The study used the adrenergic agonist Iso, which is about 10× as potent as NE, so the original Iso data are shifted by a factor of 10 to the right to correspond to the NE scale. Thick lines show our model reproduction of the data when the neuroeffector junction and EJS concentrations are clamped to the corresponding ACh or NE concentrations. The $I_{f,Shift}$ model of Demir et al. (81) for both ACh and Iso is labeled 'De' and the Iso curve is shifted to the right by a factor of 10 as we did with the Zaza et al. data. The Dokos steady-state ACh response is labeled 'Do' (96), and the Maltsev model relationships are labeled 'Ma' (227). Maltsev and Lakatta only modeled a maximal adrenergic effect using a constant $I_{f,Shift}$; this value is shown as a line between 10 and 100 μM.

6.5.2 $I_{Ca,L}$ Conductance (R_{gCaL})

The L-type Ca^{2+} channel is modulated by PKA-dependent phosphorylation (for review, see (231)). This mechanism agrees with the observations that ACh reduces peak $I_{Ca,L}$ (270, 367), while Iso enhances it (367). As discussed by Maltsev and Lakatta (227), a wide range of $I_{Ca,L}$ sensitivities to ACh have been reported (154, 270, 367), also see Table 18 for details. We follow their example in reproducing the data of Zaza et al. (zaza 1996). Although this study reported a 31% decrease in $I_{Ca,L}$ due to high ACh (300 μM), a minimal effect is seen for concentrations below 10 μM, which is in agreement with the observation of Honjo et al. that 10 μM ACh had no effect on $I_{Ca,L}$ (154). These figures contrast the strong inhibition observed by Petit-Jacques et al.: 56% at 10μM ACh (270). We did not use the Petit-Jacques et al. data because strong $I_{Ca,L}$ inhibition of this magnitude caused cessation of spontaneous SANC activity at moderate ACh concentrations in our model, which is at odds with the commonly accepted mechanism (that SANCs stop beating due to an increased potassium conductance). Zaza et al. also provide data on the effect of Iso in stimulating $I_{Ca,L}$.

The Zaza et al. and Petit-Jacques et al. data on the relative change in L-type channel conductance (R_{gCaL}) are summarized in Figure 93, along with our model reproduction of the data, and the models used by Maltsev, Dokos, and Demir. As is the case for $I_{f,Shift}$, Demir used a function of cAMP to directly modulate the L-type calcium current conductance, although they note that the actual mechanism involves PKA. Their description matches the Petit-Jacques data for applications of ACh, and the amplitude of their Iso-stimulated function is similar to the Zaza et al. Iso data, but shifted to the right. Maltsev and Dokos model changes in $I_{Ca,L}$ as direct ACh effects: Maltsev uses an instantaneous function of ACh that appears to have a half-activation similar to the Petit-Jacques data, but a maximum value from the Zaza data, whereas Dokos used a first-order reaction (again, introducing some delay between ACh application and $I_{Ca,L}$ change) with steady-state value that matches the Petit-Jacques data. To simulate a β-adrenergic effect, Maltsev used a constant value of 1.75× baseline. Our model fits the Zaza data very well for concentrations below 10 μM, but deviates from the high-ACh data points. We do not consider this deviation important for two reasons: 1) physiological ACh concentrations are below 0.1 μM ACh (corresponding to 10 Hz maximal vagal spike rate), and 2) SANC cells stop spontaneously depolarizing at ACh>10 μM, so these measurements were recorded on essentially dysfunctional cells and may not be valid.

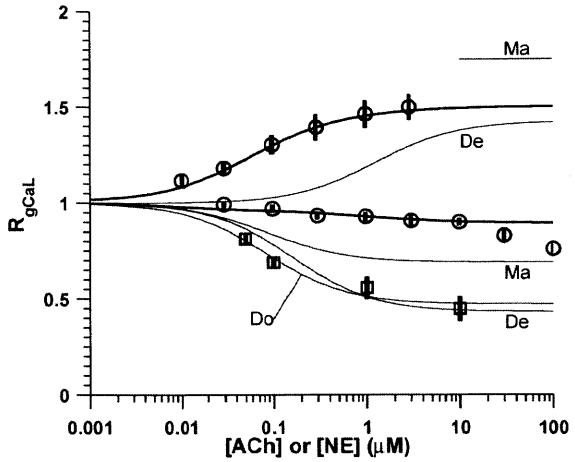

Figure 93. Data and models of the relative change in L-type calcium current conductance. ACh and Iso data from Zaza et al. (○) (367), Iso data is increasing and has been shifted to the right by a factor of 10 to convert Iso concentration to equivalent NE concentration, ACh data is decreasing. ACh data from Petit-Jacques et al. (□) (270). Thick lines show our model reproduction of the data when the neuroeffector junction and EJS concentrations are clamped to the corresponding ACh or NE concentrations. Functions used by the Maltsev ('Ma'), Dokos ('Do'), and Demir ('De') models are shown with thin lines. The Demir Iso curve is shifted to the right by a factor of 10 in order to convert it to equivalent NE concentration, as was done with the Zaza et al. Iso data.

6.5.3 PLB Phosphorylation and SERCA Pumping rate (R_{Pup})

Phospholamban (PLB) is a protein that inhibits the activity of the sarcoplasmic reticulum Ca^{2+} pump (SERCAII). The inhibitory activity of PLB is a function of its own phosphorylated state: phosphorylated PLB is not an effective inhibitor of SERCAII function, whereas unphosphorylated PLB is. Therefore, adrenergic stimulation increases PKA activation, increasing PLB phosphorylation, decreasing the effectiveness of PLB, and increasing the Ca^{2+} pumping rate by SERCAII. The opposite is true for cholinergic stimulation. The effect of cholinergic agonist carbachol (CCh) on PLB phosphorylation was quantified by Lyashkov et al. (222), who showed that cholinergic activation reduces the amount of phosphorylated PLB and that this reduction happens in concert with the observed reduction in SANC oscillation rate (see Figure 94). Maltsev et al. include this effect in their SANC model by modifying the parameter P_{up}, which is a measure of SERCAII pumping rate (227). They also show that this change in P_{up} and the resulting effect on spontaneous Ca^{2+} release in their SANC model is a major contributor to changes in SANC spontaneous oscillation rate. Given its potentially important role in HR regulation by the autonomic nervous system, we included modulation of P_{up} in our model as well. The Dokos and Demir models on the other hand, were developed before the role of the "calcium clock" was fully understood so they do not include these effects.

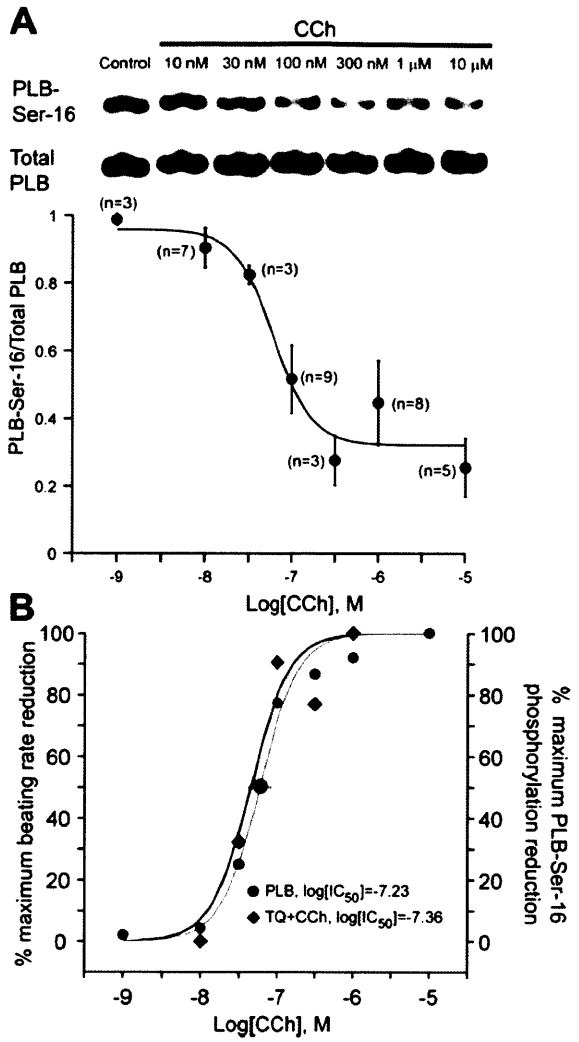

Figure 94. Effect of CCh on PLB phosphorylation and SANC beating rate, figure taken from (222). A. Phosphorylated PLB (PLB-Ser-16) as a fraction of total PLB is shown for a range of CCh concentrations. B. The effect of CCh on PLB phosphorylation overlaps its effect on SANC beating rate reduction, implying an important functional role of PLB regulation.

We model adrenergic and cholinergic effects on P_{up} through the relative change in this parameter's value R_{Pup}. In defining the cholinergic effect, we follow the example of Maltsev et al. and use the Lyashkov et al. PLB data (222). In doing this, we are making two assumptions: 1) that the effectiveness of CCh is not vastly different from that of ACh, and 2) that the fraction of phosphorylated PLB is directly proportional to SERCAII function. The first assumption appears to be justified, judging by the similar effect of CCh and ACh on HR (see Figure 105k). The latter assumption is the more questionable of the two, since it does not consider the affinity of the PLB-SERCAII interaction. Different affinities would effectively shift the PLB curve left or right along the ACh/CCh axis; on the other hand, the close agreement of PLB phosphorylation reduction and HR reduction (Figure 94B) imply that no such shift is necessary.

We were unable to find detailed data relating adrenergic stimulation to PLB phosphorylation. For the β-adrenergic effect in their model, Maltsev and Lakatta used a constant value of 2× the baseline value of P_{up}. This value was chosen in order to produce a desired increase in HR with β-adrenergic stimulation (227). We followed this example and computed the necessary R_{Pup} values that would yield HRs measured under sympathetic nerve stimulation in rabbit heart by Brack et al. (33). This procedure is detailed in section 6.5.6. These data, the fits achieved by our model and the function used by Maltsev are shown in Figure 95. The ACh functions are very similar, but our NE function rises to about 3.5× baseline, whereas Maltsev et al. used a value of 2× baseline (227). This difference is mainly due to the larger HR range we were reproduced: in the Maltsev model, maximal β-adrenergic stimulation causes a 25.8% increase in HR (from a baseline of 184 bpm to a maximum 226 bpm), whereas in our model, maximal β-adrenergic stimulation causes a 73% increase in HR (baseline 156 bpm, maximum 270 bpm).

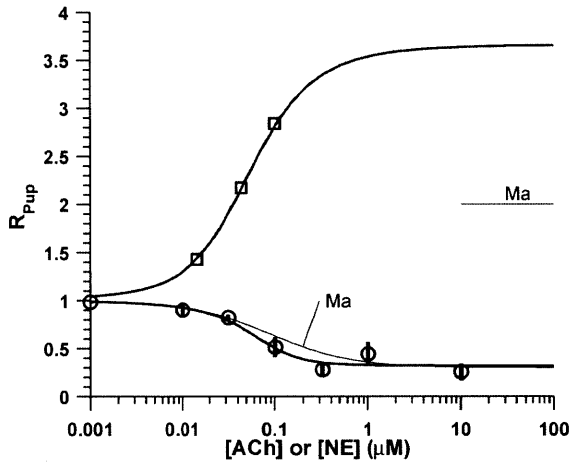

Figure 95. Our R_{Pup} formulation (thick lines) fits the ACh data of Lyashkov et al. (○) (222) and the NE values required to reproduce the HR data from Brack et al. (□) (33). The Lyashkov et al. data were collected using CCh, and are plotted here as a function of ACh without any modification. The Maltsev model (thin lines) uses a function of ACh directly fit to the Lyashkov et al. data as indicated ('Ma'), and the maximal adrenergic effect is simulated using a value 2× baseline.

6.5.4 I_{Kr} Conductance (R_{gKr})

The rapid delayed rectifier potassium current I_{Kr} is known to be modulated by PKA and PKC (141, 348), with 47-70% increase in peak current due to adrenergic stimulation (44, 141) (see Table 18 for details). We were unable to find data showing the specific dependence of the relative change in I_{Kr} conductance (R_{gKr}) on NE or ACh, so we computed R_{gKr} values in order to reproduce the HR data of Brack et al. (33) (see section 6.5.6). The Maltsev model includes a β-adrenergically mediated increase in I_{Kr} of 50% above baseline, and did not change it with ACh. The Demir model also includes a change in the potassium

current I_K, which they modeled as a direct effect of cAMP concentration, but note that this change is PKA-mediated. Demir et al. (81) do not cite any specific data used for defining their I_K modulation equations, so we assume they chose the function in order to reproduce some desired phenomena. The Dokos model did not modulate the potassium current. Figure 96 summarizes the data points we used to fit our R_{gKr} function, and the functions used by Maltsev and Demir. The functions used to describe adrenergic modulation of R_{gKr} vary between 35%-67% maximal increase over baseline value, with our model being much more sensitive to NE than the Demir model. We believe that our model is valid because it fits the values required to reproduce HR changes due to sympathetic stimulation (33), has a sensitivity to NE that is similar to that of I_f and $I_{Ca,L}$ (see Figure 92 and Figure 93), and has a maximum increase close to that reported by Brown and DiFrancesco in rabbit SANC (44). Our R_{gKr} function for ACh modulation lies between the 0 effect used in the Maltsev model, and the 40% maximal decrease in the Demir model. The sensitivity of our formulation to ACh is slightly greater than that of the Demir model, but closely mirrors the sensitivity to NE, and fits the values required to reproduce the vagal stimulation HR data from Brack et al. (33). The R_{gKr} functions we used also help maintain the maximum diastolic potential of our model around the baseline value of -60 mV for a wide range of adrenergic and cholinergic stimulations, in line with experimental observations (see Fig 3 in (88), Fig 6A in (44), Fig 1E in (64), Fig 3 in (328), Fig 1 in (352), Fig 3 in (53)).

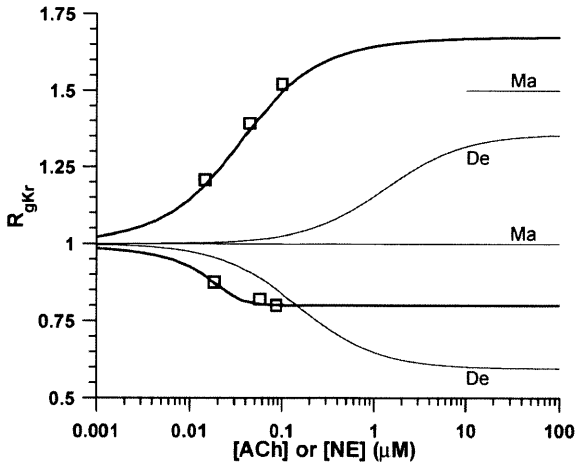

Figure 96 We model the relative conductance change of the rapid delayed rectifier potassium channel by fitting it to values required in order to reproduce the HR data of Brack et al. (□) (33). Our model reproduction of the data is shown with thick lines. The Demir model change in I_K conductance is shown with thin lines ('De') for ACh and Iso effects, with the Iso line shifted to the right by a factor of 10 to convert to equivalent NE concentration. The Maltsev model did not change g_{Kr} with ACh ('Ma' line at 1), and increased it by 50% to model a maximal β-adrenergic effect.

6.5.5 I_{Kr} Kinetics (pa_{sf})

We initially attempted to reproduce the effects of ANS stimulation on HR by following the example of the Maltsev model and only modifying the parameters described above($I_{K,ACh}$, $I_{f,Shift}$, R_{gCaL}, R_{Pup}, and R_{gKr}). The Maltsev model showed that these four parameters were sufficient to reproduce HRs between 111 bpm and 226 bpm (227). We aimed to reproduce the wider HR range obtained in response to vagus and sympathetic nerve stimulation in perfused rabbit heart, which showed minimum and maximum HRs of 67 bpm and 250 bpm, respectively (33). After updating the $I_{K,ACh}$ model (see Figure 89), and adjusting the baseline P_{up} value to reproduce the baseline HR of 156 bpm (33) (see section 6.5.6 for details), we were confronted by a major limitation of the Maltsev model illustrated in Figure 97.

As shown in Figure 97B, the Maltsev model was only explored up to 0.1 μM ACh, at which point it reaches 111 bpm (227). A version of our model in which we do not change I_{Kr} kinetics (pa_{sf}=1 in Figure 97) crosses this threshold however, at which point the HR "bifurcates" into a slow rate and a fast rate. Maltsev and Lakatta did not encounter the bifurcation because the higher baseline HR in their model (184 bpm) and less sensitive $I_{K,ACh}$ formulation did not push their ACh-stimulated HR below 111 bpm, were the HR bifurcation occurs. However, the existence of what they termed "chaotic firing" was noted in their earlier paper (see Figs 10 and 11 in (228)), and is the same phenomenon we observe here. We stress that this phenomenon is a function of the SANC oscillation rate rather than a pathologic setting of particular parameter values. In our attempts to reproduce the low HRs reported by Brack et al., we explored all the currents listed in Table 18 and were able to increase the sensitivity of the HR to ACh, essentially shifting the HR curve in Figure 97B left. However, as soon as the HR dropped below ~100 bpm in these simulations, a bifurcation occurred. We do not show these simulations because they involved manual changes in many parameters and are difficult to describe in enough detail to allow reproduction; by simply clamping pa_{sf} to 1 in our model, we can study the bifurcation behavior, albeit at relatively high ACh. The consequence of the bifurcation is that the set of ACh-modulated changes used in the Maltsev model is incapable of producing uniform HRs between ~50 bpm and 110 bpm. As Figure 97B also shows however, by including changes in I_{Kr} kinetics via pa_{sf}, our full model reproduces the complete range of HR data reported by Brack et al. without encountering this bifurcation. The full model also reproduces the data of Lyashkov et al. (222), although these data were not explicitly used to fit/train the model. Finally, Campbell et al. (53) showed that 20Hz vagal stimulation causes guinea-pig SANCs to stop beating, and this phenomenon is replicated by all three models (however the mechanism is different: our model stops beating due to a high $I_{K,ACh}$, whereas the Maltsev model stops due to a decrease in $I_{Ca,L}$).

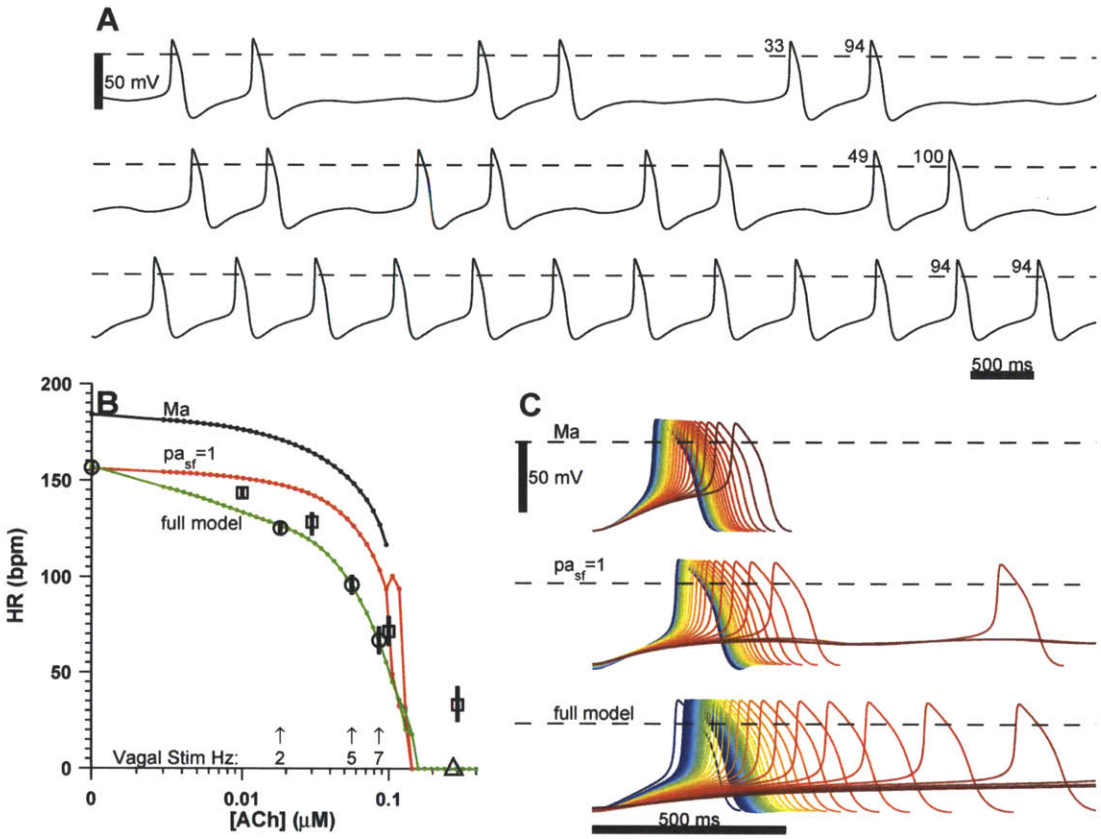

Figure 97. Illustration of HR bifurcation and insufficient change in early DD without pa_{sf} modification. 40-second simulations were run at 50 logarithmically distributed ACh concentrations (0 μM and 49 values between 0.003-0.4 μM) using three SANC models: the Maltsev and Lakatta model ('Ma'), our new model with pa_{sf} clamped to 1 ('pa_{sf}=1'), and our full model ('full model'). A. Membrane potential in the pa_{sf}=1 model during the last 8 seconds for three simulations: immediately before the HR bifurcation (bottom), the first simulation exhibiting bifurcated HR (middle, 0.1063 μM ACh), and the second simulation with a bifurcated HR (top, 0.1177 μM ACh). The numbers between the last two APs indicate the HR between those two beats in bpm. Dashed lines show 0 mV. B. HR is plotted as a function of ACh concentration for each model as labeled. The HR computed between each adjacent pair of APs during the last 10 seconds of simulation is plotted (•). The solid lines are drawn for each model, one connecting the maximum HRs at each concentration, and another connecting the minimum HRs to emphasize the bifurcation. The Maltsev model was only explored up to 0.1 μM ACh, so we do not plot behavior beyond this point. HR data from Brack et al. (○) (33) at 0, 2, 5, and 7 Hz vagal stimulation are plotted as a function of equivalent ACh concentration, labeled with arrows. Data from Lyashkov et al. (□), which were collected using CCh as the cholinergic agonist are plotted as a function of ACh assuming equal potency of CCh and ACh. The data were provided as normalized HR, so we scaled them by the baseline HR from Brack et al.. A data point from Campbell et al. (Δ) (53) shows that 20Hz vagal stimulation caused cessation of spontaneous activity in guinea pig SANC. This point is plotted at the ACh concentration equivalent to 20 Hz stimulation. C. The last AP from each simulation is shown for the three models as labeled. Waveforms are lined up so that they begin at the most negative diastolic potential. No trace is shown for simulations that lacked spontaneous activity.

Figure 97A shows the actual membrane voltage traces for simulations immediately preceding and during the bifurcation. Note that in all the traces, there appears to be a ripple at approximately -40 mV with a fixed period of ~0.61 s. When APs successfully fire from each ripple (bottom trace), we see a HR of approximately 60/0.61=98 bpm. If one or two successive ripples fail to cross the AP threshold however,

we observe the bifurcated HRs at approximately ½ and ⅓ the ripple frequency. This phenomenon is quite apparent upon a fine-grained exploration of the bifurcated range, producing alternating HR periods that are integer multiples of each other (data not shown). Since the ripples occur around -40 mV, the rate at which the cell rises from the maximum diastolic potential (MDP) of -60 mV to this level determines whether the cell has had enough time to reset so that it can fire an AP at the peak of the ripple. This rate of early diastolic depolarization (DD) is shown in Figure 97C.

Panel C shows detail on the AP shape produced by the three models. All three maintain a fairly unchanged MDP, around -60 mV. The major difference between our full model and the two models that lack pa_{sf} is that the slope of the early DD changes in our model, whereas it is relatively constant in the other two. If early DD does not change with ACh (as in the Maltsev model), then HR can only be controlled by prolonging late DD. However, as we can see in the top two traces in Figure 97A and the "pa_{sf}=1" model in panel C, prolonging late DD too much causes the AP to "fall off" the ripple caused by the rapid early DD. To eliminate the HR instability described above, we use the pa_{sf} parameter to appropriately slow down early DD (details below). The type of early DD change produced by the full model is also supported by experimental recordings in mammalian SANC in response to both bath-applied and vagally-released ACh, see Figure 98.

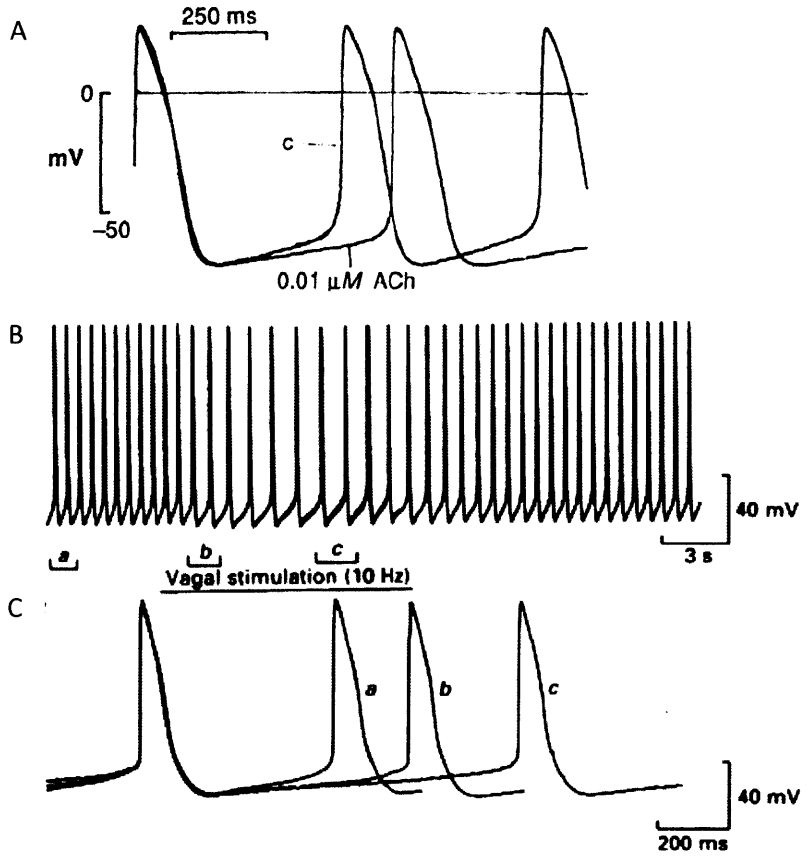

Figure 98. The slope of early DD decreases with bath applied ACh as well as vagal stimulation. A. Membrane potential recordings in isolated rabbit SANCs under control conditions (c) and with 0.01 μM ACh as labeled. Figure taken from Fig 3 in (88). B. the effect of 10Hz vagal stimulation on the APs recorded in guinea-pig SANC. C. Expanded view of APs in A before vagal stimulation (a), and at two points during stimulation (b, c). B and C taken from Fig 3 in (53).

The process though which we identified pa_{sf} as a determinant of early DD is shown in Figure 99. Panel A shows the major time-varying currents active during the first 0.1 s of depolarization: I_{Kr}, I_f, and $I_{Ca,L}$. Note that the total time-varying current is positive, and it is balanced by a negative total instantaneous current (not shown), which changes linearly with cell membrane potential in this range. Due to the sign convention, *negative* currents depolarize the cell, so early DD occurs when I_{Kr} becomes less positive (termed potassium current decay) from its high value immediately following an AP. Panel B shows a series of experiments aimed at slowing early DD by either increasing I_{Kr}, decreasing I_f, or both. These APs show that negative shift in the I_{Kr} activation gate or a positive shift in the inactivation gate to boost I_{Kr} during DD were ineffective in changing early DD, as was complete blockage of I_f. Changes in $I_{Ca,L}$ were also without effect on early DD, and caused cessation of spontaneous activity (not shown). The rate of early DD was only affected by the kinetics of I_{Kr} activation, wherein a pa_{sf} value of 0.3 significantly slowed early DD. In this scenario, the additional elimination of I_f was synergistic. Because the decay in K^+ conductance has long been thought to be the initiator of DD (253), we view its regulation by pa_{sf} a

reasonable modification of the model that is also minimal in the sense that the desired behavior is obtained through a change in a single parameter (we could alter early DD by changing other currents as well, but these changes always required more than one parameter). Also, there is some experimental evidence showing changes in I_{Kr} kinetics with adrenergic agonists through the PKA/PKC pathway (see Table 18), so changes with cholinergic stimulation can reasonably be expected.

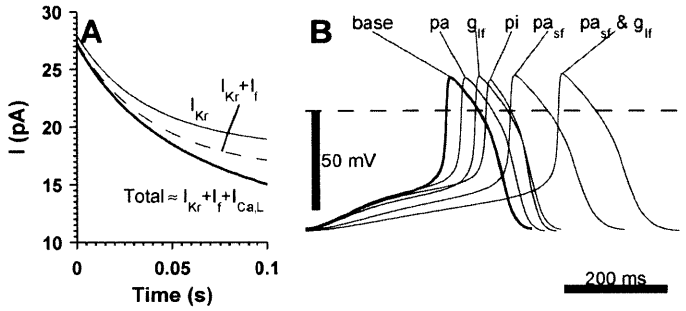

Figure 99. The rate of decay of I_{Kr} determines early DD slope. A. The major time-varying currents during the first 0.1s of diastolic depolarization are I_{Kr}, I_f, and $I_{Ca,L}$. The total time-varying current (thick line) during this period is approximately equal to the sum of these three currents, as indicated. B. Simulated APs under various interventions. In all simulations, P_{up} was reduced to 0.3× baseline in order to prolong late DD and emphasize early DD; this and the parameters specifically listed below were the only changes from baseline values. The baseline simulation is shown with a thick line. The indicated interventions are: a shift in I_{Kr} activation gate p_a 5 mV to the left ('pa'), a shift in I_{Kr} inactivation gate p_i 10 mV to the right ('pi'), complete blockade of I_f by setting conductance g_{If} =0 ('g_{If}'), a slowing of I_{Kr} activation gate kinetics by clamping pa_{sf} to 0.3 ('pa_{sf}'), and the combined effect of I_f blockade and I_{Kr} activation gate slowing ('pa_{sf} & g_{If}'). For the simulations involving pa_{sf}, we also decreased g_{Kr} to 0.8× baseline in order to elevate the MDP to the same level as in the baseline simulation and make it easier to compare early DD. The dashed line indicates 0 mV.

We also explored the nature of the fixed-frequency oscillation to determine its origin and properties, results shown in Figure 100. We show that the oscillation is produced by the L-type Ca^{2+} current $I_{Ca,L}$, and that the necessary and sufficient conditions for the oscillation are a functional activation gate (d_L) and at least one of the two inactivation gates (voltage-sensitive gate f_L, or submembrane Ca^{2+}-sensitive gate f_{Ca}). The "base" trace shows the membrane voltage oscillation at baseline, with a period of 0.61 s. "P_{up}=k_s=0" illustrates that the oscillation is not caused by the Maltsev "Calcium clock", since setting the rate of Ca^{2+} uptake into the SR (P_{up}) and the rate of spontaneous release (k_s) to 0 did not eliminate the oscillation nor significantly change its frequency. The next two traces ("clamp all except d_L and f_L", and "clamp all except d_L, f_{Ca}, Ca_{sub}") show sufficient conditions for the existence of this oscillator: the activation gate d_L and one of the two inactivation mechanisms (f_L, or f_{Ca} and Ca_{sub}) are enough to cause the oscillation. In these simulations, all the other SANC variables are clamped to their baseline values and do not change with time. These two cases differ in one interesting aspect however: if Ca^{2+} is not involved, the

oscillations tend to decrease over time (increasing $g_{Ca,L}$ did not make the waves grow in amplitude) whereas when Ca^{2+} is involved, the oscillations amplify over time and eventually cause an AP.

The necessity of d_L and one of the inactivation mechanisms is shown by the next four lines: Clamping only Ca_{sub} or f_L does not eliminate the oscillation, but clamping both does. Similarly, clamping only d_L also eliminates the oscillation. In both simulations where no oscillation was seen, we tried increasing $g_{Ca,L}$ up to 100-fold to bring the oscillations back, but this was ineffective. The amplitude of the oscillations seems to depend strongly on f_L, since the f_L clamp trace had to be amplified 1,000-fold to have an amplitude comparable to the other traces. Eliminating the f_L gate also had the largest effect on changing the period of the oscillation. The only way to smoothly modulate the period of the oscillation over a large range is to slow down the kinetics of the $I_{Ca,L}$ gates (the top trace shows the effect of slowing d_L and f_L by a factor of 10; slowing d_L alone was enough to produce some change in the oscillation frequency).

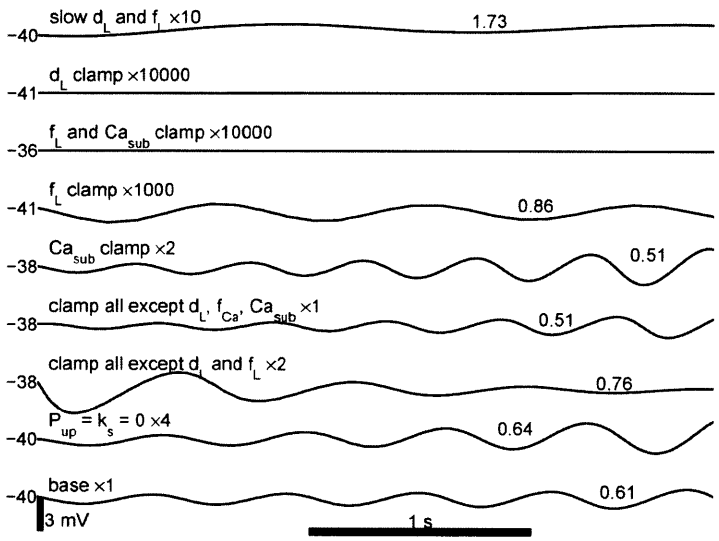

Figure 100. The necessary and sufficient components for the fixed-frequency oscillation are the $I_{Ca,L}$ activation gate d_L and one of the inactivation gates f_L or f_{Ca}. Each line shows transmembrane potential V_m, and was simulated using different conditions, as indicated by the labels on the left. The time bar refers to all the traces; the voltage bar refers to the baseline case. Some of the traces were amplitude-scaled around their mean as indicated by the multiplier at the end of each label. The numbers on the left show the voltage of the leftmost point in each trace. The numbers above the traces show the period (in seconds) between the two nearest peaks. The simulation conditions were: base: ACh=0.144 μM in the neuroeffector junction and EJS, NE=0 in neuroeffector junction and EJS, pa_{sf}=1. One of the points from this simulation was used when clamping the other variables. The variables clamped in the baseline simulation were also set to the same values in all the other simulations. P_{up}=k_s=0: P_{up} and k_s both set to 0. Clamp all except d_L and f_L: all variables were clamped to a single value from the baseline simulation, except d_L and f_L. The other labels are interpreted in a similar way. The two flat lines are scaled by 10,000 to verify the absence of oscillations. Slow d_L and f_L: these gates were slowed by a factor of 10; all other parameters were allowed to change.

This oscillation, whose properties had not previously been characterized, does not appear to be an artifact of the simulated system. In fact, a growing, subthreshold oscillation has been observed in rabbit SANC cells whose automaticity had been pharmacologically stunted as we show in Figure 101.

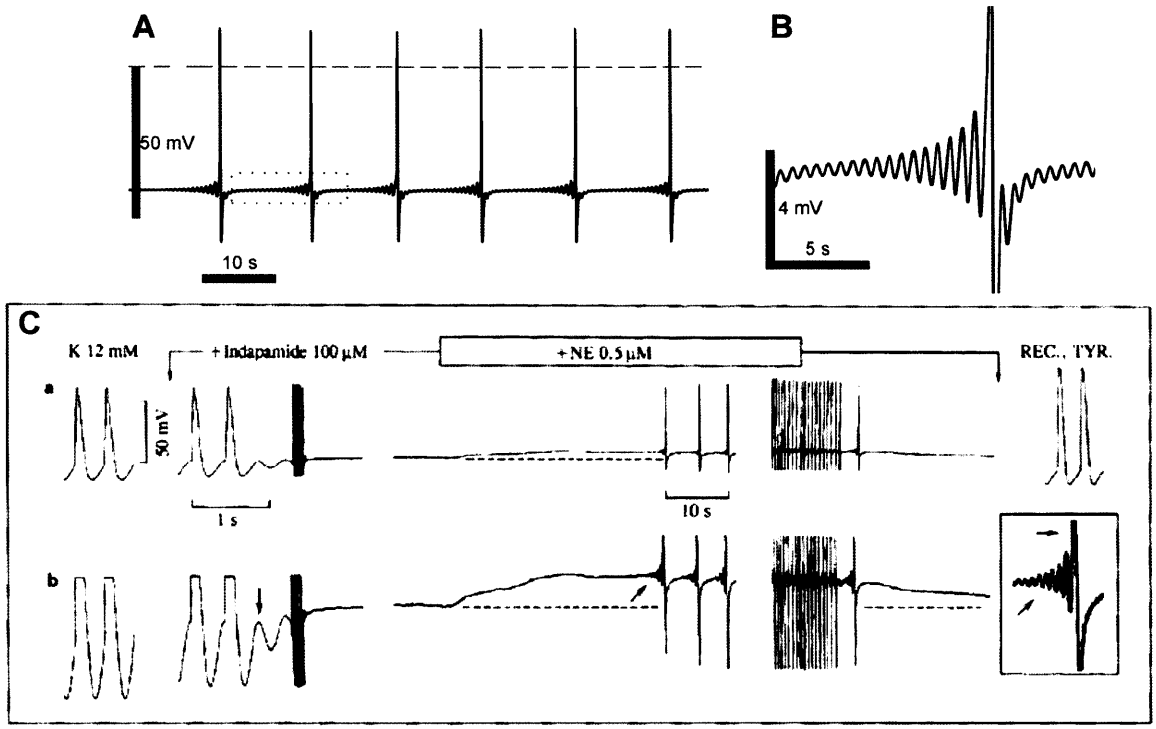

Figure 101. The membrane voltage oscillation is physiological. A. high ACh concentration (0.144 µM) and pa_{sf} clamped at 1 allows our model to produce subthreshold oscillations that grow in amplitude until the threshold is reached. If we do not clamp pa_{sf} at 1, but let it change with ACh, the same behavior is seen at higher ACh, with a slower oscillation frequency. B. A rescaled version of the region shown by a dotted box in A. C. Figure taken from Zhang and Vassalle (370). The traces show the membrane voltage of a guinea-pig SANC cell that was made quiescent using the potassium channel blocker indapimide as indicated at the top. The subsequent addition of NE restored spontaneous activity (NE applied during the box shown at top), and washout of NE made the cell quiescent again. b is an enlarged version of a, showing more detail around the threshold, and the inset is enlarged similar to our model in B.

In the setting of adrenergic stimulation, we did not encounter any unexpected behavior from the Maltsev model. Modulating the $I_{f,Shift}$, R_{gCaL}, R_{Pup}, and R_{gKr} as described above produced the expected saturating increase in SANC oscillation rate. However, the Maltsev model has two undesirable features: 1) the maximal HR is below that measured in perfused rabbit heart in response to sympathetic stimulation, and 2) the MDP becomes more negative with increasing adrenergic stimulation. These phenomena are reproduced by our model when pa_{sf} is clamped to 1, as shown in Figure 102. By including pa_{sf} changes of the kind discussed for cholinergic modulation however, we were able to remedy both limitations. Figure 102A shows that our full model reproduces experimental HR data whereas the pa_{sf}=1 version falls short

by achieving a maximum rate of ~230 bpm. Figure 102B shows detail on the AP shape in the two models: without changes in pa_{sf}, the MDP becomes ~10 mV more negative at maximal [NE] and AP duration increases marginally, whereas the full model shows virtually no change in MDP and the AP duration actually decreases somewhat. The behavior of the full model more closely resembles experimental data, some of which are reproduced in Figure 103. In this figure we see that adrenergic stimulation has virtually no effect on MDP; Choate et al. even report that sympathetic stimulation made the MDP less negative, but only by about 1-2 mV (64). Regarding the AP peak voltage (APP), the traces show conflicting information, with panel A showing an increase in APP with adrenaline, but panel C showing a decrease, however both changes are slight. The AP duration was reported to decrease with sympathetic stimulation (~ 2-3% (328), panel C), and tighter adrenergic APs are also seen in panel A and B.

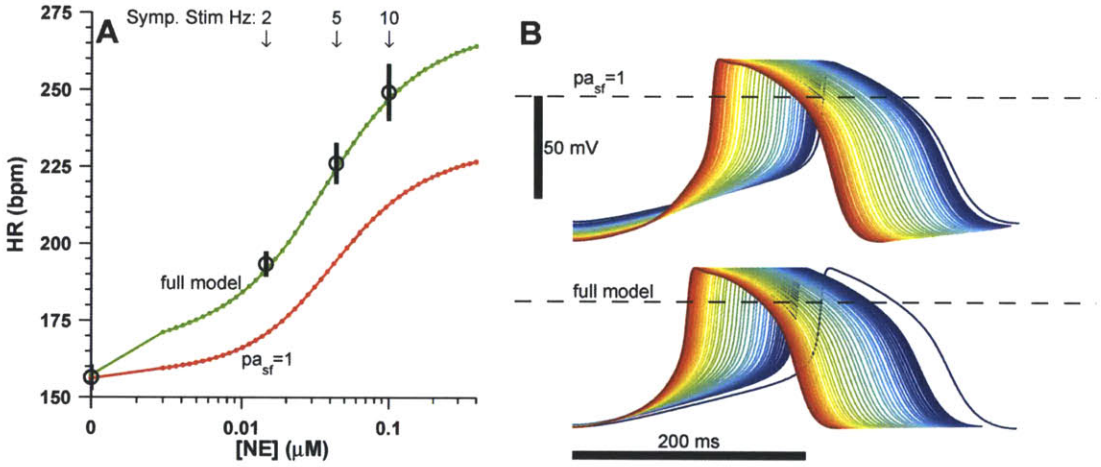

Figure 102. pa_{sf} allows the full model to attain higher HRs and maintain MDP close to the baseline level for a wide [NE] range. A Steady-state HR as a function of NE for full model and a version wherein pa_{sf} is clamped to 1, as labeled. Maltsev model is not shown because it only simulated a maximal adrenergic effect, but the AP shape and maximal HR are similar to that of the pa_{sf}=1 version of our model. 50-second simulations were run for 0 μM NE and 49 logarithmically distributed concentrations between 0.003 and 0.4 μM NE. Each simulation was 50s in duration, and the HR during the last 3 seconds are all plotted (•), and the minimum and maximum rates are connected by lines. Data ○ are from (33) for sympathetic stimulation frequencies as indicated. B. The last AP in each simulation is shown, shifted so the MDPs are lined up. Dashed line shows 0 mV.

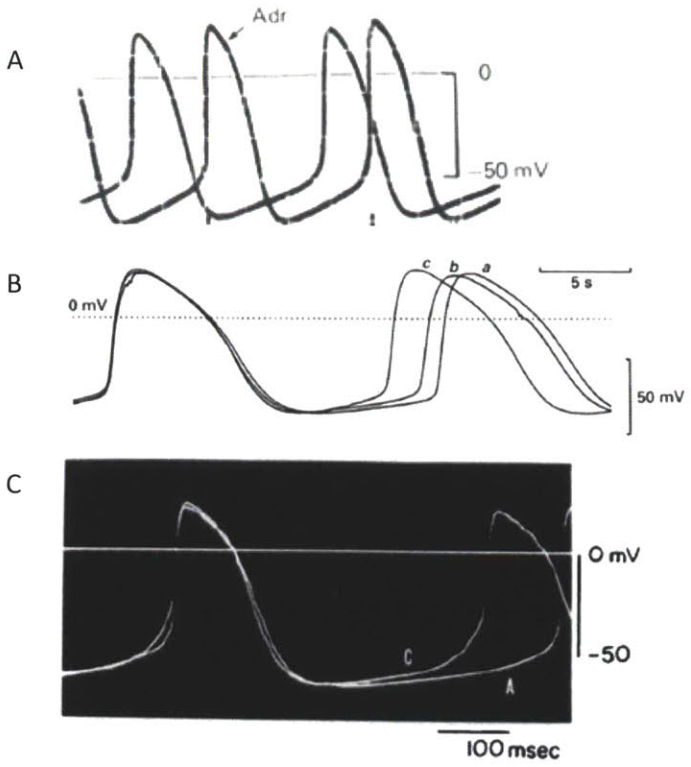

Figure 103 Adrenergic stimulation via neurotransmitter bath application or neural release causes minimal changes in AP shape and MDP. A. Effect of adrenaline applied to rabbit SANC, control and adrenaline (Adr) voltage traces are shown. Taken from Fig 6A in (44). B. Sympathetic stimulation on guinea pig SANC, showing APs before (a), and ~3s (b) and ~10s (c) after 5 Hz stimulation, taken from Fig 1E in (64). C. Sympathetic stimulation on rabbit SANC, before (A) and at maximal effect (C) after 20 Hz stimulation, taken from Fig 5 in (328).

In light of the above cholinergic and adrenergic explorations, we concluded that it was necessary to modulate I_{Kr} kinetics with adrenergic and cholinergic stimulation. This change allowed us to slow early DD and avoid "chaotic" beating in the setting of cholinergic drive, and to reach high HRs and correct subtle changes in the AP with adrenergic drive. We also concluded that the Ca^{2+} current oscillation is not a pathologic consequence of the Maltsev "Calcium clock", but rather a phenomenon that had been observed experimentally. We therefore did not attempt to explicitly change the properties of this oscillation with ACh. We obtained pa_{sf} data points to describe the steady-state function by using the HR data of Brack et al. (33) as described in the next section. Since the Dokos, Demir, and Maltsev models did not alter I_{Kr} kinetics, we cannot compare our formulations beyond what is shown in Figure 97and Figure 102. Our pa_{sf} function and the data it fits can be found in Figure 105i.

6.5.6 *Determining P_{up}, R_{Pup}, R_{gKr}, and pa_{sf} to fit HR data*

The baseline Maltsev model (in the absence of ACh and NE), generates a beating rate of about 184 bpm. Brack et al. showed that for a perfused rabbit heart with no sympathetic or vagus stimulation, the baseline HR is 156 bpm. To achieve this HR, we lowered the value of P_{up} from 12 to 6.5 mM/s. This parameter was originally treated as a means of setting baseline HR by Maltsev and Lakatta (228), so our lowered value does not conflict with any experimental measurements (there are no direct measurements of P_{up} (227)).

The SANC model parameters that change with adrenergic and cholinergic stimulation are: $I_{f,Shift}$, R_{gCaL}, R_{Pup}, R_{gKr}, and pa_{sf}. The $I_{f,Shift}$ and R_{gCaL} values with ACh and NE were fully specified by the experimental data from Zaza et al. (367). The R_{Pup} function was specified for various ACh concentrations using the data of Lyashkov et al. (222). Thus, to be able to simulate the cholinergic effect on HR, we needed to specify only two functions: R_{gKr} and pa_{sf}. Furthermore, since our ultimate modeling objective was to reproduce the HR data from Brack et al. (33), we computed values of R_{gKr} and pa_{sf} that would accomplish this goal.

The Brack et al. data shows HRs of 125, 96 and 66 bpm with 2, 5, and 7 Hz stimulation, respectively. In these experiments, the right vagus was stimulated; Brack et al. also provide HRs for left vagus stimulation, but since this nerve synapses primarily on the AV node rather than the SAN and it produced less extreme changes in HR, we chose to use the right vagus data. We used our neurotransmitter release model to convert these stimulation frequencies to equivalent ACh concentrations and then interpolated the $I_{f,Shift}$, R_{gCaL}, and R_{Pup} data and set those parameters accordingly (each data set was individually fit with a Hill function in a least squares sense and then evaluated at the desired ACh concentrations). For each data point, we then found R_{gKr} and pa_{sf} values to produce the desired HR to within 0.5 bpm. Since these two parameters also altered the MDP, we were able to find unique solutions by requiring that the MDP be no greater than the baseline MDP, and no lower than 1 mV below the baseline MDP (baseline MDP is around -61 mV).

We followed a similar procedure for defining the parameters for NE. We used data from Brack et al. where the sympathetic nerves were stimulated at 2, 5, and 10 Hz, giving HRs of 193, 226, and 249 bpm. In this case however, there were three unknowns: R_{Pup}, R_{gKr}, and pa_{sf}. We first directly fit the three HR points using a Hill function which we evaluated at 10 μM NE as an estimate of the maximum adrenergically-stimulated HR. We then interpolated the $I_{f,Shift}$ and R_{gCaL} data at 10 μM NE and set these parameters accordingly. We also set R_{gKr} to 1.7, based on the measurement showing 70% maximal

increase in I_{Kr} with adrenergic stimulation (44). With the other variables fixed, we found the pa_{sf} and R_{Pup} that reproduced the maximal HR while maintaining the MDP at the baseline level. We defined functions for R_{gKr} and pa_{sf} by scaling and shifting the Hill function that was directly fit to the HRs such that they had value 1 at 0 NE and the computed maximum values at infinity. Since these functions were related by a constant, they ensured that pa_{sf} and R_{gKr} moved in concert and therefore also fixed the MDP. These functions were evaluated at the equivalent NE concentrations of the Brack et al. data, and R_{Pup} was chosen to produce the desired HR at each point.

6.6 Parameter Fitting

6.6.1 Steady-state function parameters

The model parameters (42 total) for which explicit experimental data were unavailable are:

1. AC modulation by G_S and G_I: K_{SAC}, n_{SAC}, K_{IAC}, n_{IAC}
2. $I_{f,ShiftP}$ modulation by C: a_{0S}, a_{1S}, a_{2S}, n_{1S}, n_{2S}, K_{1S}, K_{2S}
3. R_{gCaL} modulation by C: a_{0C}, a_{1C}, a_{2C}, n_{1C}, n_{2C}, K_{1C}, K_{2C}
4. R_{Pup} modulation by C: a_{0P}, a_{1P}, a_{2P}, n_{1P}, n_{2P}, K_{1P}, K_{2P}
5. R_{gKr} modulation by C: a_{0K}, a_{1K}, a_{2K}, n_{1K}, n_{2K}, K_{1K}, K_{2K}
6. pa_{sf} modulation by C: a_{0p}, a_{1p}, a_{2p}, a_{3p}, n_{1p}, n_{2p}, n_{3p}, K_{1p}, K_{2p}, K_{3p}

We would like to point out that despite the large number of free parameters we listed above, the functions that they parameterize are not arbitrary, but were mechanistically motivated. In fact, they are all Hill functions with amplitudes (a), binding affinities (K), and measures of cooperative binding (n). This insistence on appropriate functions increases the number of parameters (for example, good fits for all the C-functions were obtainable using polynomials with a smaller number of parameters), but ensures desirable properties like monotonicity, gives parameter values that have intuitive meanings, and from a practical standpoint, allows us to manually set good initial guesses for the parameters before they are optimized by a numerical error minimization algorithm. The model is also over-determined in the sense that the number of parameters, while large, does not allow perfect fits to the data and therefore does not allow us to fit noise. In all, we fit 60 data points and satisfied 12 equality constraints.

Since our model is sequential (see "Actual cascade used for parameter fitting" in Figure 104), it is not optimal to fit each function individually. For example, the AC function influences all downstream functions so a suboptimal fit to the local AC data may still be globally optimal if it enables better fits downstream. To enable optimization of all the parameters simultaneously, we constructed an error

function that took all 42 parameters as input and produced model reproductions of all the data points. For example, Zaza et al. (367) provide data on R_{gCaL} as a function of NE. To obtain the model reproduction of each data point, we evaluate all the functions linking *NE* to R_{gCaL} in Figure 104: NE to β^*, β^* to G_S^*, G_S^* to AC (since AC is a function of both G_S and G_I, we also have to specify ACh and follow its cascade down to G_I), etc.

In this way, we compute the sum squared error between data and model reproduction for each data set, and this total error is minimized by a constrained minimization algorithm in Matlab (`fmincon`). The constraints we satisfy with equality are: a baseline cAMP concentration of 3μM, baseline $I_{f,Shift}$ of 0 ($I_{f,Shift}=I_{f,ShiftP}+I_{f,ShiftC}$), and baseline R_{gCaL}, R_{Pup}, R_{gKr} and pa_{sf} of 1. Since the pa_{sf} data were calculated in order to reproduce HR data, we also used the 6 pa_{sf} data points as equality constraints.

Alternate optimizations: we explored the idea of distributing fitting error along the function cascade as a way to reduce the number of free parameters. In one attempt ("Alternate cascade 1" in Figure 104), we parameterized the PKA function (arrow from cAMP to *C*) as a sum of Hill functions and allowed the cAMP→$I_{f,ShiftC}$ function to shift left/right, but reduced the complexity of the five relationships depending directly on *C* to single Hill functions. In another attempt ("Alternate cascade 2" in Figure 104), we parameterized the PDE function (arrow from v_{AC} to cAMP) instead of the PKA function, and left the other changes mentioned above intact. In a final attempt ("Alternate cascade 3" in Figure 104), we allowed both PKA and PDE functions to be double Hill functions and left the other changes as in the first alternate attempt. These alternate formulations were motivated by the uncertainty in our PDE and PKA formulations, and the possibility of subcellular sequestration of cAMP which would make different populations of PDE and PKA subject to different cAMP concentrations. The second motivator was the idea that a more complicated function upstream may be able to reduce the necessary complexity of the downstream functions. While these attempts did reduce the number of free parameters by ~10, they produced unacceptable model reproductions of high level data, so the original optimization described above and shown in Figure 104 was used.

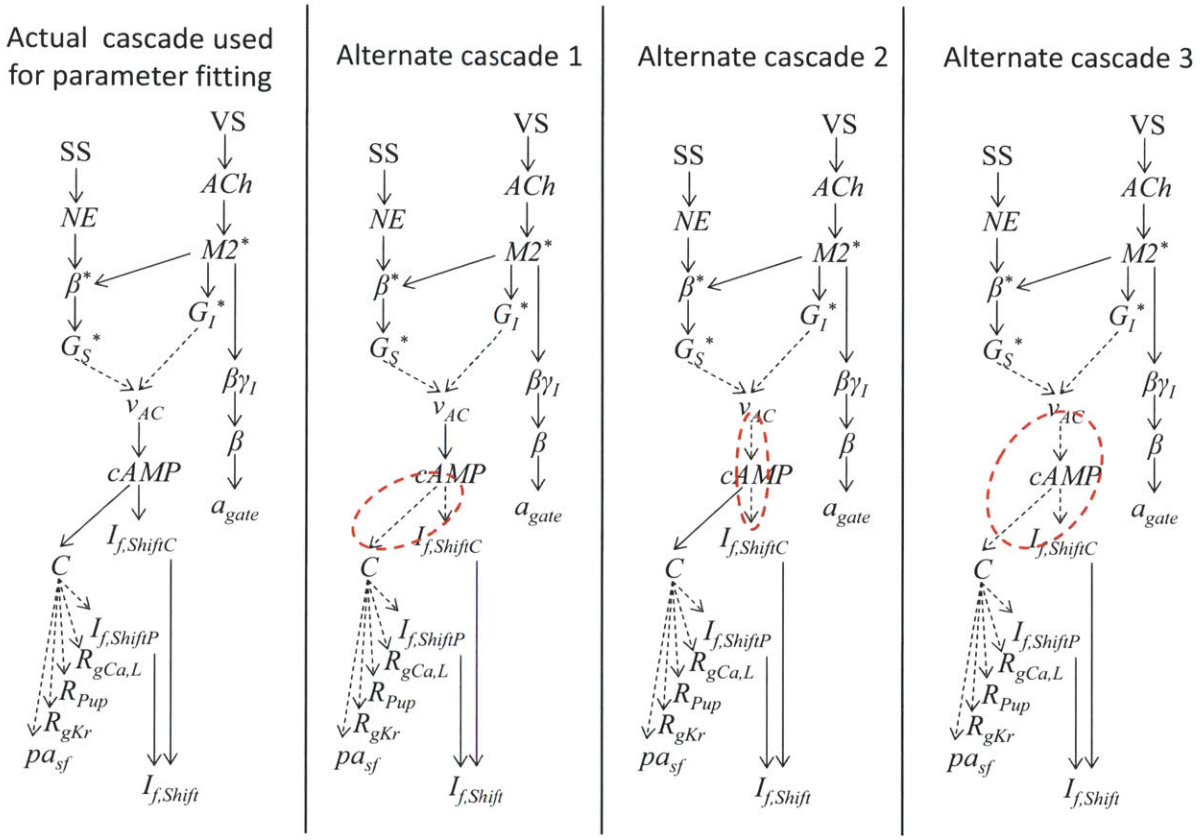

Figure 104. Summary of the signal flow in the overall model. See text for discussion of alternate cascades for optimization. The diffusion, hydrolysis, and reuptake functions are not explicitly shown. Arrows represent functions (simple binding reactions, enzyme kinetics, or more abstract equilibrium functions). Solid lines: functions that are characterized using direct data. Dashed lines: functions defined by fitting parameters to reproduce high-level implicit data. Key: SS: sympathetic stimulation, VS: vagal stimulation, NE: norepinephrine, ACh: acetylcholine, β*: activated β-adrenergic receptor, M2*: activated M2 muscarinic receptor, G_S*: activated stimulatory G-protein; G_I*: activated inhibitory G-protein, $\beta\gamma_I$: liberated βγ subunit from inhibitory G-protein, β: opening rate coefficient for $I_{K,ACh}$ channel, a_{gate}: gate of $I_{K,ACh}$ channel, v_{AC}: cAMP-synthesizing velocity of adenylate cyclase, cAMP: cAMP concentration in cytosol, $I_{f,ShiftC}$: cAMP mediated shift in I_f activation gate, C: activated catalytic subunit of phosphokinase A, $I_{f,ShiftP}$: phosphokinase A mediated shift in I_f activation gate, $I_{f,Shift}$: the total shift of the I_f activation gate (sum of $I_{f,ShiftC}$ and $I_{f,ShiftP}$), R_{gCaL}: relative change in L-type calcium channel conductance, R_{Pup}: relative change in SERCA pumping rate P_{up}, R_{gKr}: relative change in rapidly activating potassium channel conductance, pa_{sf}: speedup factor for I_{Kr} activation gate p_a. The arrow connecting v_{AC} and cAMP is the phosphodiesterase (PDE) function.

A summary of the entire model and the experimental data it reproduces are shown in Figure 105. Various sub-domains of the model are validated by experimental data, as shown by the bulleted lines in the gray box. Some experiments controlled vagal and sympathetic stimulation (VS and SS), but most used direct manipulation of the NTs NE (or Iso) and ACh (or CCh or MCh). Because the data spans various subsets of the model, we are fairly confident that each component system is accurate. Briefly, our model reproduces both the direct cAMP effect on $I_{f,Shift}$ (a), and the effects of ACh and NE (b). Data on the actual cAMP generation rate as a function of NE (c), and the steady-state cAMP concentration as a function of

ACh are reproduced well. The data shown in panel c were collected in whole SAN tissue, so for reasons discussed earlier, we fit this data using NE application in the BS compartment of our model (dashed line). The model reproduces the data on L-type Ca^{2+} current sensitivity that we deemed most trustworthy (e) but we also show the other available data (e, □) for completeness and since other models used that data. The computed data for R_{gKr} (f), R_{Pup} (h) and pa_{sf} (i) are also fit well for both ACh and NE, as well as the explicitly measured data for R_{Pup} with ACh (h, ○). Our $I_{K,ACh}$ formulation fits the steady-state activation data (l), and ACh application in the BS compartment can explain some of the rightward shift seen in whole tissue experiments (l, ○). Finally, the model reproduction of the most important data, and our initial aim, are shown in figures g, j, and k. g shows the effect of sympathetic stimulation in the presence of varying background vagal stimulation, illustrating the inhibitory effect of VS on SS (note the small HR increase due to SS for 7 Hz VS line versus the larger effect for the 0 Hz VS line). In j, we see the opposite: the effect of increasing vagal stimulation in the presence of various background sympathetic stimulations. Note that regardless of background sympathetic tone, the SANC model stops spontaneous oscillation at vagal stimulation rates of roughly 15 Hz. The direct effect of neurotransmitter application is shown in k, where we plot data obtained via direct ACh and NE application as well as the data obtained from nerve stimulation on the same figure. The close agreement of the data (compare ○ and □) validate our neurotransmitter release model but also bring into question the large difference in cell responses to bath-applied versus neural ACh used in the Demir model (where they assumed neural release is only 2% as effective at impacting the cAMP cascade as bath-applied ACh). In this figure we also show data that were not originally used to build the model ("test data", ▲), but are fairly well reproduced nevertheless. These data were collected in whole SAN tissue, and application of neurotransmitter in the BS compartment of our model reproduces the observed rightward shift in HR sensitivity to neurotransmitter.

6.6.2 Phosphorylation rate parameter

The value of τ_P was chosen to be fast enough to allow the reproduction of dynamic HR data (see Figure 106), while also not conflicting with measured rates. We chose a value of $\tau_P = 1$s, which is on the (rather wide) range of observed values: on the fast side is the PKA catalytic subunit with a turnover rate of 20/s (time constant of 0.05s), and on the slow side is the observation by Accili et al., who report that *PP* inhibition causes a change in the I_f current conductance with a time constant of 466 seconds (3).

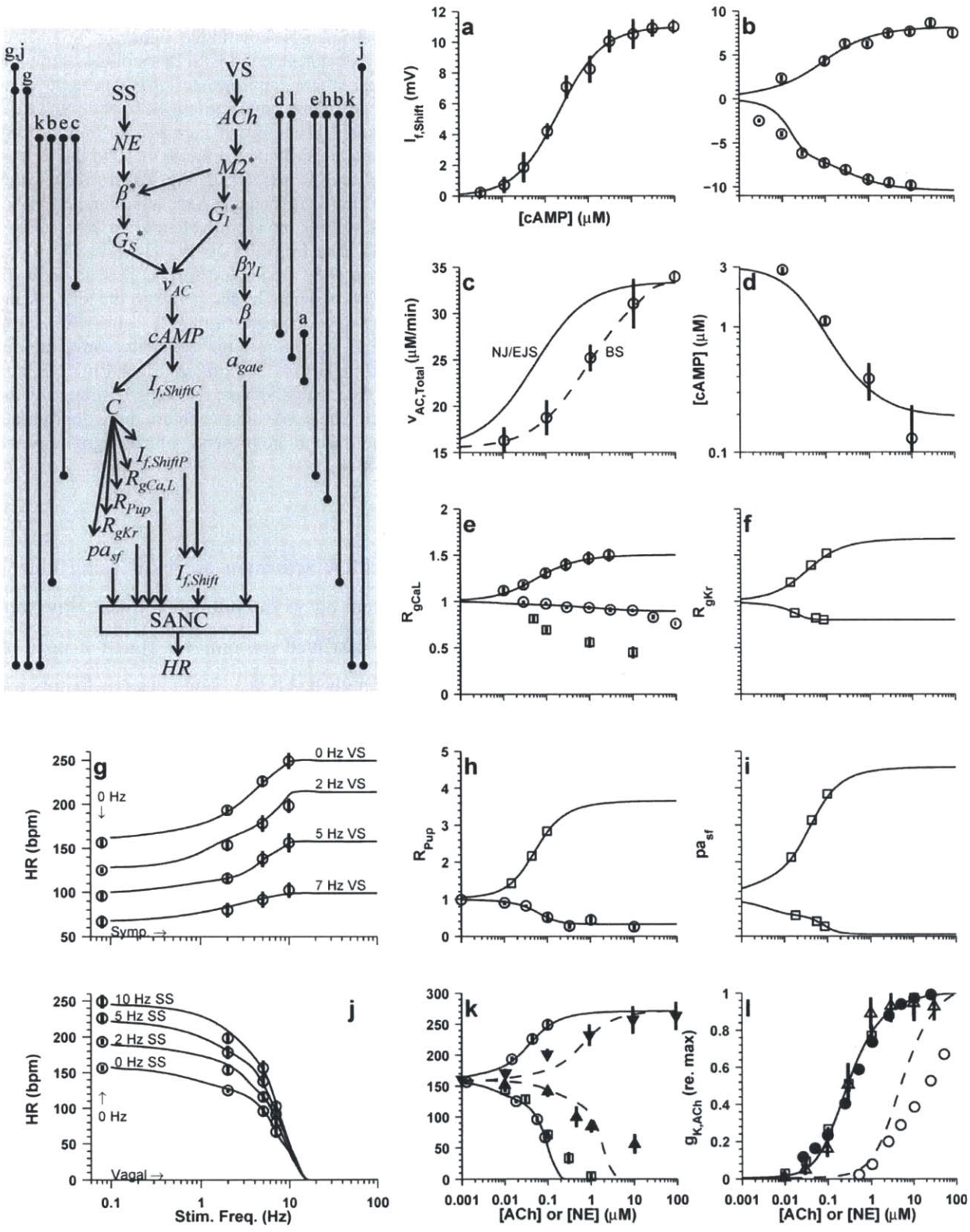

Figure 105. Model reproduction of experimental measurements. The gray box shows the complete cascade-view of our model, with each state variable on a unique vertical level. The bulleted lines on either side illustrate available experimental data which are shown, along with the model reproduction in the panels corresponding to the letter

above each bulleted line. For example the rightmost line shows experimental data where vagal stimulation (VS) was controlled and HR was measured, and the data is shown in panel j. All the panels show model behavior. Solid lines show model responses when ACh or NE is applied directly in the neuroeffector junction/EJS; dashed lines show the responses for neurotransmitter application in the BS. The BS application is more appropriate for experiments done on whole tissue as opposed to isolated cells. The rightmost two columns of figures have a joint [ACh] and [NE] axis; coincidentally, ACh always caused a decrease in the plotted values and NE caused an increase, so they are not individually labeled. Some experiments used Iso instead of NE; these data are shifted by a factor of 10 to the right to show equivalent NE data. Data sources are: a. Fig 3 in (90); b. Fig 2 and 3 in (367); c. Fig 4B in (320) scaled vertically to produce a baseline $v_{AC,Total}$ that gives 3μM cAMP; d. Fig 2D in (336) scaled to have a baseline cAMP of 3μM, original data is collected in response to metacholine (MCh) which we assume is equivalent to ACh; e. ○ Fig 2 and 3 in (367), □ Fig 2A in (270) f, h, i. □ calculated to reproduce HR data from Fig 2B in (33); h. ○ Fig 6A in (222); g. data from Fig 2B in (33), x-axis is sympathetic stimulation (SS) frequency for various amounts of concurrent vagal stimulation (VS) as indicated next to each curve. 0 Hz SS is shown by the arrow on the left; j. same data as panel g, but with VS on x axis and different lines corresponding to concurrent SS rate; k. ○ from Fig 2B in (33) when only SS or VS is nonzero, stimulation frequency converted to neurotransmitter concentration using our neurotransmitter release model, □ Fig 1A in (222) scaled to have a baseline HR of 156 bpm, ▲ Fig 4A in (318) and Fig4A in (319) with ACh data scaled to a baseline rate of 156 bpm, NE data scaled to have the same HR range as the model and shifted to a baseline of 156 bpm. these data were collected in whole SAN tissue so are more appropriate for BS application of neurotransmitter; l. Δ Fig 2C in (88), □ Fig 1B in (160), in the presence of neostigmine • and control ○ from Fig 1A in (264), all data scaled relative to max value.

6.7 Speedup Factors

Our models of G-protein activation, cAMP equilibrium, and PKA activation are built using kinetic information from experimental data. Thus, each component system obeys the published rates. However, once we combined these individual components into the full cascaded system, we found a need to introduce empirical speedup factors to allow the reproduction of high-level data. The speedup factors are multipliers that change the rates of the differential equations. The use of these empirical scalars is justified for two reasons. First, the vast majority of the experimental data from which we determined the initial rate constants were collected in cell-free systems. This is commonly done as an experimental convenience, to allow more systematic control of the experimental environment. However, this also means that potentially important interactions that happen in-vivo are excluded. For example, regulators of G-protein signaling (RGS) or GTPase activating proteins (GAPs) have been shown to bind G_α subunits and cause a significant increase (over 50x) in GTP hydrolysis rate (23, 327). If auxiliary molecules such as these are not included in experimental solutions, kinetic constants would be underestimated. Furthermore, the addition of components that do not exist in the natural system can also retard kinetic rates; for example, the detergent Lubrol PX decreases the catalytic rate of G-proteins (35), but is commonly used in many of the classic G-protein experiments. Finally, the concentrations of certain ions such as Mg^{2+} and Na^{+} may not be at physiologic levels, and even the type of buffer used can affect kinetic rates (see discussion of G_I-GDP dissociation rates in section 3.4.1).

Secondly, we assumed that all the molecules are dissolved in the entire cytoplasmic volume, whereas it is known that second messengers are often localized to spatially-segregated pools. This subcellular

compartmentalization has been noted for G-proteins (166, 250), cAMP (188, 251, 272, 321, 365), PDE (13, 14, 72, 365), and PKA (55, 74, 144, 233, 272, 298, 362). The Kurata model (198) moved toward modeling compartmentalization effect by including an explicit "submembrane space" located adjacent to the sarcolemma and comprising $1/50^{th}$ of the full cytoplasmic volume. The consequence of chemical reactions occurring in smaller volumes is that less time is required to reach a specific concentration. Thus, if the localized pools of G-protein, cAMP and PKA are on the order of the Kurata submembrane space (likely they are even smaller), speedup factors on the order of 50 or greater would be expected.

The G-protein speedup factor G_{sf}=20, was chosen in order to allow the reproduction of $I_{K,ACh}$ half-time data (see Figure 89). Although this data directly pertains only to the inhibitory G-protein, we assume that similar experimental underestimation or spatial effects occur for the stimulatory G-protein. The cAMP ($cAMP_{sf}$=10) and PKA (C_{sf}=100) speedup factors were set to the minimum values that allowed the reproduction of HR changes in response to vagal and sympathetic stimulation, as shown in Figure 106. The model reproduction of the HR dynamics are excellent for the vagal stimulation data, as well as low and high sympathetic stimulation. The 5 Hz sympathetic stimulation data appears to have a faster initial rise, followed by a slower approach to steady-state which our model does not capture perfectly. However, the good fits to the low and high stimulation frequencies imply that this is not a fundamental flaw of the model, and also that it cannot be fixed using the simple speedup factors described here. We reason that the good fits to the extreme stimulation frequencies and the possibility of some variance in experimental method when obtaining the 5 Hz data are valid reasons for avoiding more complex speedup functions.

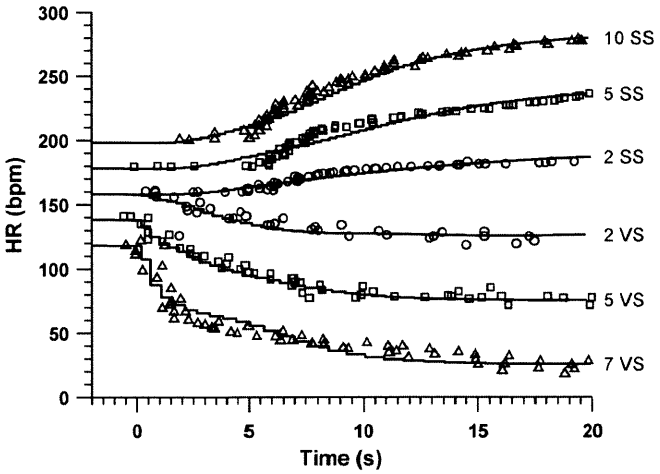

Figure 106. Model reproduction of dynamic HR data from Brack et al. (33). Model HRs in response to 2, 5, and 10 Hz sympathetic stimulation (SS) and 2, 5, and 7 Hz vagal stimulation (VS) starting at 0s, with the medium and high stimulation rates shifted by 20 and 40 bpm up (SS) or down (VS) for clarity. Digitized data from Fig 1B (VS) and Fig 5B (SS) in Brack et al. are shown by symbols for low (○), medium (□), and high (Δ) stimulation frequencies. Symbols have been shifted and scaled to best overlap the model lines.

7 MODEL PROPERTIES

7.1 Overview

In this chapter, we explore high-level model behavior which arises as a consequence of the individual sub-systems we describe in the preceding chapters but which cannot be modeled explicitly. In standard modeling parlance, the previous chapters can be seen as the "training data" for our model and this chapter contains "test data."

Pacemaking currents

- The "classic" pacemaking currents I_f and $I_{Ca,L}$ do not have as large an effect as previously believed on changing the beating rate of sinoatrial node cells in response to sympathetic and parasympathetic stimulation (Figure 107 and Figure 108)
- Changes in Ca^{2+} cycling through the sarcoplasmic reticulum (parameters P_{up} and R_{Pup}) have a large effect on heart rate changes, as shown by Maltsev and Lakatta (227)
- Changes in rapid delayed rectifier K^+ current *kinetics* (parameter pa_{sf}) cause only subtle changes in I_{Kr} shape, but have a very important effect on sinoatrial node cell beating rate. Classically, much attention has been paid to measuring changes in ion channel *conductances*; our results imply that more effort needs to be expended on also quantifying ion channel *kinetics*.

Response to sympathetic and parasympathetic stimulus trains

- Stimulation of sympathetic and parasympathetic nerves at low, moderate, and high frequencies reproduce quantitative and qualitative aspects of analogous experimental data (compare Figure 109 and Figure 110)

Phase response curves

- It has been shown that the timing of parasympathetic nerve stimulation with respect to the sinoatrial node cell action potential affects the "gain" of the stimulus on prolonging cycle period. We generate simulated phase response curves for both parasympathetic and sympathetic stimuli that are similar to those reported in other models and experiments (see Figure 111 and Figure 112).
- We identify the rate of $I_{K,ACh}$ activation as an important factor in determining the shape and amplitude of vagal phase response curves
- Sympathetic phase response curves are fairly flat, as is expected from the slow rate of sympathetically-mediated heart rate changes. The sympathetic phase response is amplified by the presence of background acetylcholine

Vagal and Sympathetic Impulse response functions

- We reproduce experiments conducted in dogs wherein random stimulation (Gaussian white noise) of sympathetic and parasympathetic nerves are converted to heart rate impulse response functions
- Our model produces functions that are similar both qualitatively and quantitatively to the experimental data (see Figure 113 and Figure 114)
- We identify one difference between our simulations and the experimental data: a low frequency component in the vagal impulse response function. We hypothesize that this feature may be absent in the experimental data because of inadvertent sympathetic stimulation during the vagal stimulation protocol (due to physical proximity of some sympathetic nerve fibers and the vagus).

7.2 Results

The detailed approach we took to constructing each sub-system of our overall model (Chapters 2-6), and the final reproduction of steady-state (Figure 105) as well as dynamic (Figure 106) HR data validate our model. In this chapter, we explore some high-level behaviors.

First, we look at the changes in ionic currents during adrenergic and cholinergic stimulation. Figure 107 summarizes the effect of adrenergic and cholinergic stimulation, at NE and ACh concentrations chosen to provide a similar relative increase and decrease from basal as what was shown in the Maltsev model and is shown in Figure 108. With NE application, the main mechanisms of rate increase are increased Ca^{2+} release from the SR ($j_{SRCarel}$) which stimulates the depolarizing Na^{+}/Ca^{2+} exchanger I_{NCX}. This effect was also noted by Maltsev and Lakatta and can be seen in Figure 108A. The $j_{SRCarel}$ curves are qualitatively different in the two models however, with a less extreme effect seen in our model. This is so because Maltsev and Lakatta only simulated "maximal" adrenergic stimulation, so they use a P_{up} value of 24 mM/s whereas our functional representation of Pup and the fact that we reduced the baseline value in order to reproduce baseline HR only give a value of 10.4 mM/s at the NE concentration used in Figure 107. Similarly, $I_{Ca,L}$, is only slightly larger compared to baseline in our model, whereas the difference in $I_{Ca,L}$ is large in the Maltsev model. Because our $I_{Ca,L}$ formulation is based on experimental data, as is our model's HR behavior, we argue that our model's representation of the $I_{Ca,L}$ change is more appropriate. I_f is another current that experienced a large increase with NE in the Maltsev model, but we actually see a NE-mediated decrease in our model. This is so despite the shift in I_f activation with NE: at this concentration, a shift of only 2.25 mV occurs in our model, which appears to be outweighed by the increase in SANC oscillation frequency, which tends to cause more I_f inactivation. $I_{K,ACh}$ plays no part in NE-mediated rate acceleration, so it is about the same as at baseline. Finally, I_{Kr} is slightly larger and has a faster decay during early diastole in our model. This is due to the combined effect of R_{gKr} and pa_{sf}, and

we point out that the effect of pa_{sf} is rather subtle when looking at just the current traces. This implies that the pa_{sf} modification, which is new in our model, is not obviously un-physiologic and may have been present but overlooked experimentally. The Maltsev model shows a similar larger I_{Kr} peak and faster decay, but the greater relative decay rate of our I_{Kr} allows it to fall to a below-baseline value during early diastole, whereas in the Maltsev model the diastolic I_{Kr} is larger with Iso than at baseline. To summarize, our model shows a similar increase in SANC oscillation rate as the Maltsev model, but the major mechanisms shift from being a drastic SR Ca^{2+} release, increases in I_f and $I_{Ca,L}$, to a more moderate SR Ca^{2+} release and a more rapid I_{Kr} decay, with the effect of I_f and $I_{Ca,L}$ being almost negligible.

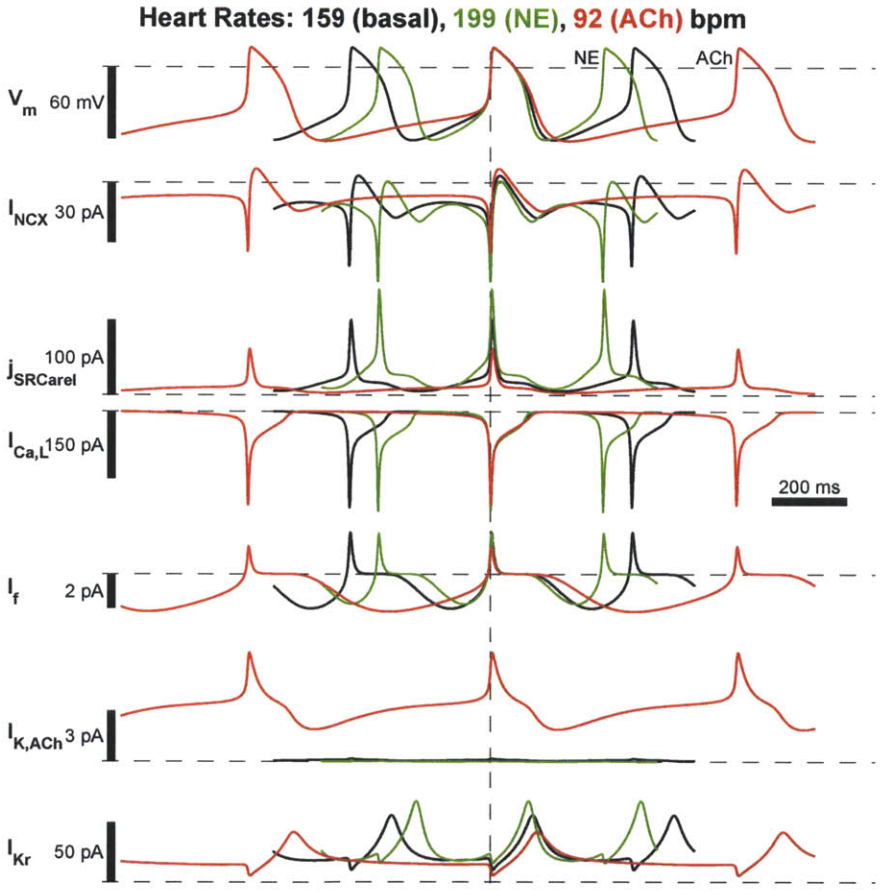

Figure 107. Effect of adrenergic and cholinergic stimulation on the major ionic currents and SR calcium release. Dashed horizontal lines show 0 for each current and V_m, The basal simulation was in the absence of vagal or sympathetic stimulation (but nonzero ACh_{BS} and NE_{BS}); 0.02 μM NE and 0.06 μM ACh (in the neuroeffector junction/EJS) were used for the adrenergic and cholinergic simulations, respectively, which are labeled in the V_m traces. Negative currents are entering the cell (depolarizing), positive flux ($j_{SRCarel}$) is exiting the SR (depolarizing). Time bar corresponds to all traces, which were lined up such that V_m=0 at t=0 (vertical dashed line).

The most apparent means of ACh-mediated rate slowing is the drastic increase in $I_{K,ACh}$., which was also reported to be a key mechanism by Zhang et al. (369). The other changes are opposite to those we

discussed above: SR Ca^{2+} release and I_{NCX} decrease, $I_{Ca,L}$ decreases almost imperceptibly, I_f paradoxically increases, and the rate of I_{Kr} decay slows slightly. The effect of ACh on R_{Pup}, R_{gCaL}, R_{gKr}, and pa_{sf} can explain the associated changes, and the paradoxical increase in I_f is again explained by the prolonged diastolic period, which provides I_f channels more time to open despite increasing deactivation and the negative shift in the activation curve due to ACh. The features of an increased $I_{K,ACh}$ and decreased SR Ca^{2+} release are shared by the Maltsev model, but their model also has a significant decrease in $I_{Ca,L}$ and I_f (see Figure 108B), which are responsible for some of the rate slowing in their model. They also do not even consider the effect of I_{Kr}, since their model did not model changes in *Kr* conductance or kinetics, but these were major players in our model (see section 6.5.5).

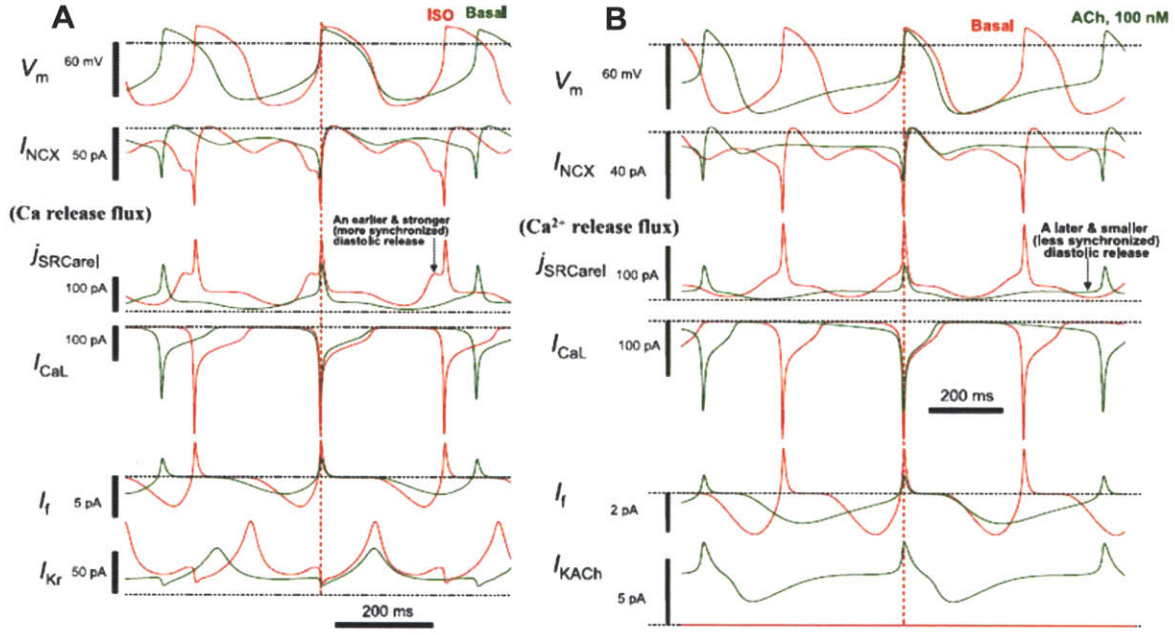

Figure 108. Membrane voltage and currents during adrenergic (A) and cholinergic (B) simulations taken from Maltsev and Lakatta (227) Fig 3A and Fig 6A.

Next, we illustrate the effect of a train of vagal or sympathetic stimuli on beating rate, shown in Figure 109 and compare to experimental data presented in Figure 110. In model simulations and experiments, 2 Hz vagal causes gradual slowing and no change in AP peak or MDP. 10 Hz vagal stimulation causes a drastic slowing of HR and erratic beating. In our model, beating actually stops shortly after start of stimulation, but then starts up again and approaches a steady-state rate (see last beat during stimulation in Figure 109B). In the analogous experiment, HR slows more gradually during this stimulation protocol. Both model and experiment show a decrease in AP peak during stimulation and an increase after. In the experimental data, MDP hyperpolarizes during stimulation and then recovers monotonically, in our model MDP hyperpolarizes slightly during stimulation but recovers to a more positive value before settling to

baseline. 20 Hz vagal stimulation stops beating in both model and experiment, but the recovery is different: the MDP in our model is more positive than at baseline, whereas it is more negative in the experiment. The decrease in AP height during stimulation and its increase afterwards is also more extreme in the experimental data than our model. In terms of HR, recovery starts immediately after stop of stimulation and completes by 30 sec.

The disparity in HR response and AP morphology in response to 10 Hz stimulation may be due to species differences, since the experimental data were collected in guinea-pig. They may also be due to the fact that the experiments were done on intact atria rather than single cells, allowing the coupling between adjacent cells to influence the response of the cell in which the data were collected. We built our single-cell model to reproduce the HR response of the entire SAN; however, the more detailed changes may be different from those seen in whole tissue.

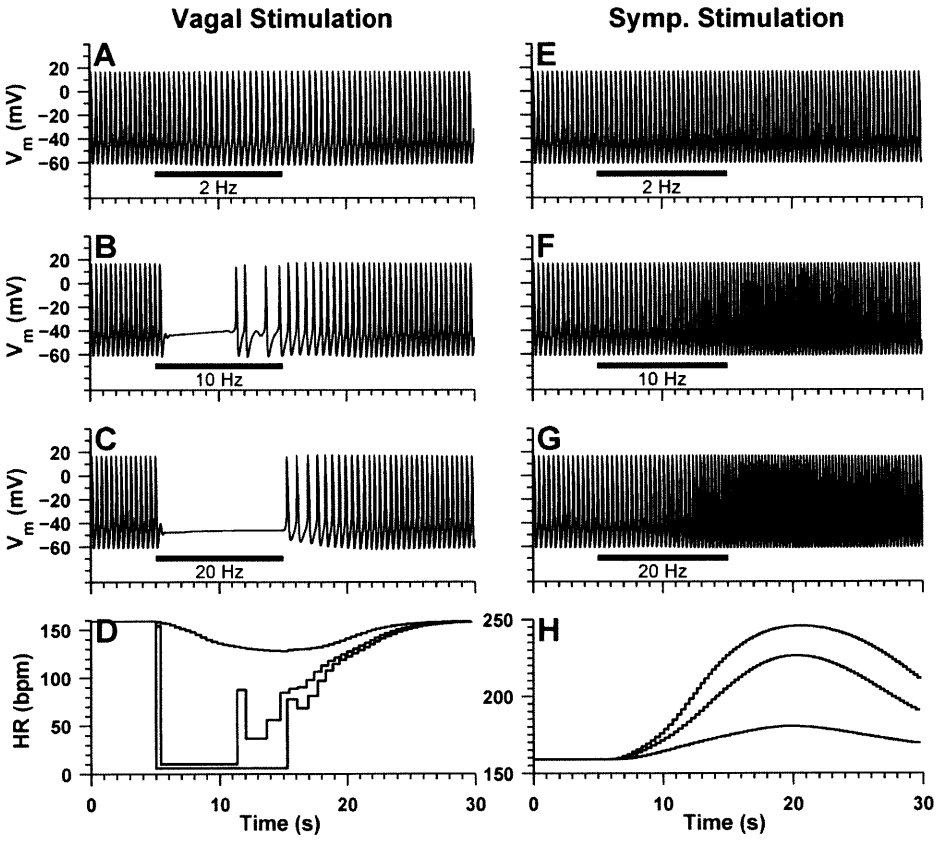

Figure 109. Effect of vagal and sympathetic stimulation on SANC model APs. A-C show the membrane voltage for a 10-s period of vagal stimulation starting at 5s, at the frequencies indicated in the figure. D shows the HR as a function of time for each simulation. E-H are the analogous plots for sympathetic stimulation.

Sympathetic stimulation at 2, 10 and 20 Hz causes no perceptible change in MDP or AP peak in simulation and data. Interestingly, HR continues to increase after cessation of stimulation, reaching a peak about 5 seconds after cessation. The HR recovery is also slow, not reaching steady state within 30 seconds. Both of these observations are similar in the experimental data.

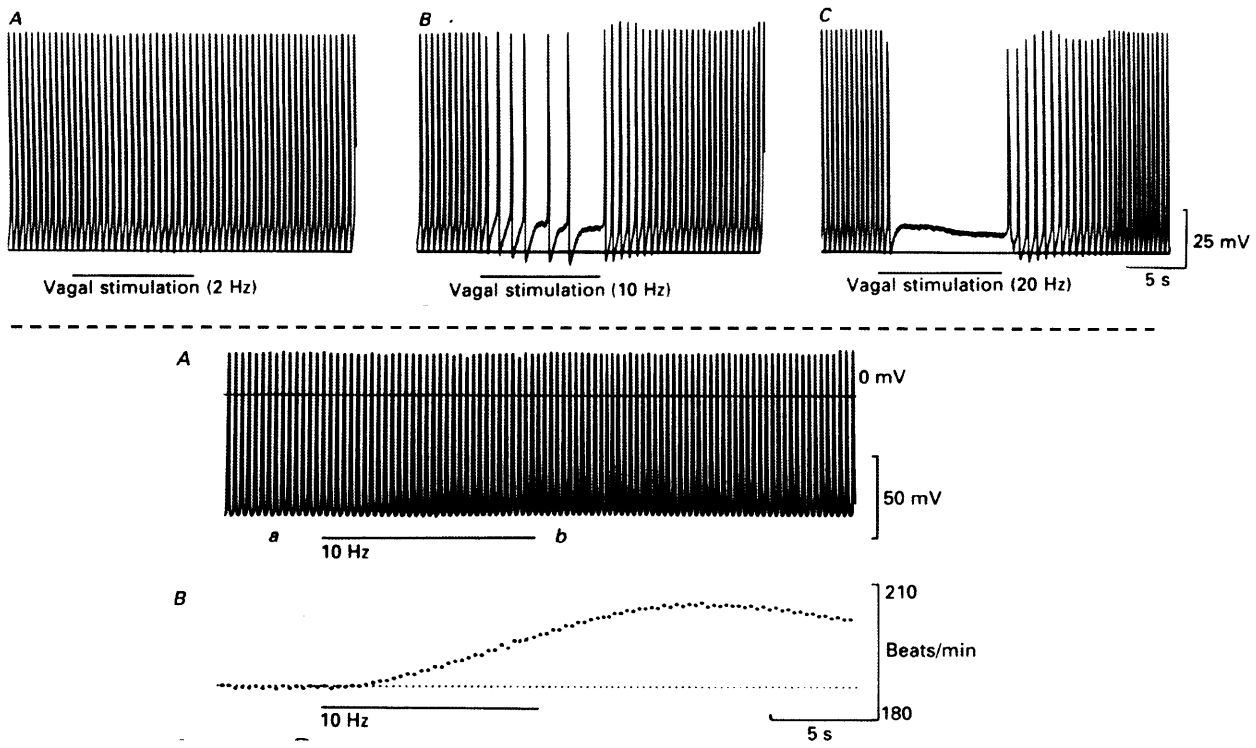

Figure 110. Effect of vagal and sympathetic stimulation, experimental data. A-C above the dashed line are from Fig 2 in (53), showing the effect of right vagus stimulation on guinea-pig SANC membrane voltage. A-B below the dashed line show an experiment from Fig 2 in (64), showing the effect of sympathetic nerve stimulation in guinea-pig SANC; A shows the membrane voltage and B the corresponding HR.

Another interesting phenomenon is the importance of sympathetic/parasympathetic spike timing in altering HR. We produced phase response curves (PRCs) in Figure 111 (see figure caption for explanation of PRC construction) and the figures from other models and experiments are shown in Figure 112. A fast $I_{K,ACh}$ (greater G_{sf} and smaller $\beta_{\tau a}$, see Figure 90) is needed for a peaked PRC similar to those of the Demir and Dokos models. The slower $I_{K,ACh}$ that we use in our model produces less potent (lower magnitude) and less phase-sensitive rate inhibition. The peaked PRCs all have a max around $\Phi = 0.6$, which is similar to the PRCs of the Dokos and Demir models, as well as the experimental data from Slenter et al. (296). The slow $I_{K,ACh}$ PRCs in our model peak around -0.2, meaning that vagal stimulation during the preceding beat is most potent in influencing the current beat; this quantitative observation is not seen in the other models or the data. In our model, the effect of background NE is to reduce the amplitude and phase-sensitivity of

the vagal PRCs when using slow $I_{K,ACh}$. This effect is most likely due to the shortening of the period, which means that a stimulus has less time to have an effect. With fast $I_{K,ACh}$, low dose NE actually increases the PRC amplitude – an example of accentuated antagonism, but high dose NE decreases amplitude and phase dependence significantly. A qualitatively similar effect was seen by Demir, but they did not see accentuated antagonism, which is an interesting feature of our model with fast $I_{K,ACh}$/ G-protein dynamics.

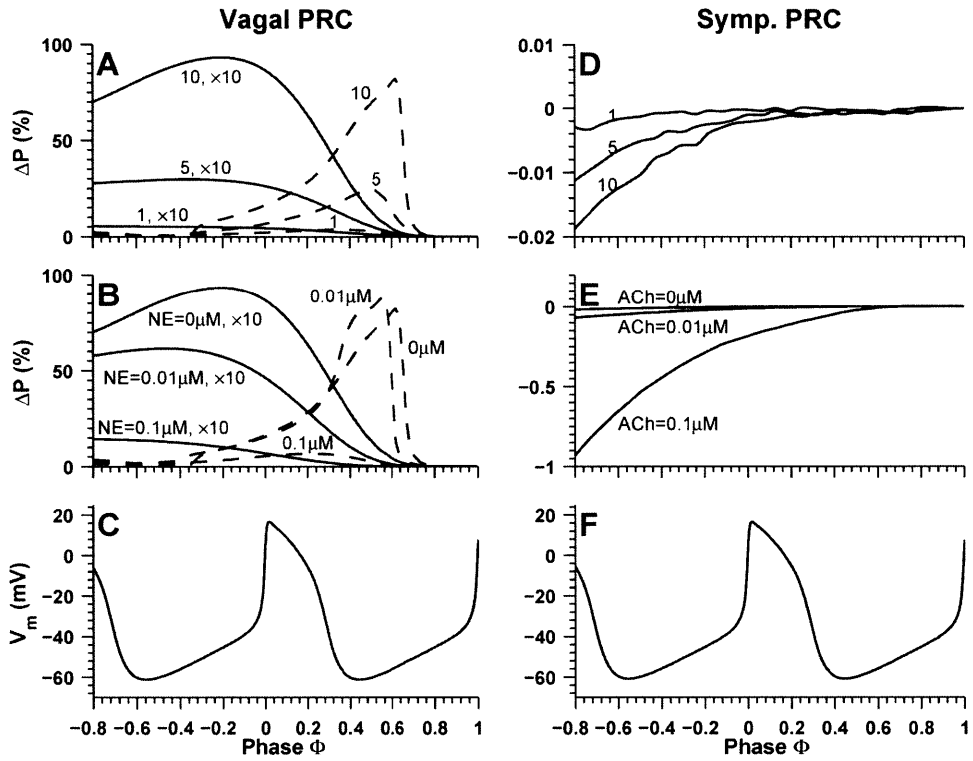

Figure 111. Vagal and sympathetic PRCs. Trains of 1, 5, or 10 vagal or sympathetic stimulations at 200 Hz were delivered at various phases of the AP waveform and the effect on SANC period is quantified as $\Delta P=(P_1-P_0)/P_0$, where P_0 is the baseline period in the absence of stimulation and P_1 is the SANC period with stimulation (plotted as a percent rather than fraction of 1). Phase Φ is defined to be 0 at the point where V_m=0, 1 at the end of that cycle, and negative during the preceding cycle. These definitions are consistent with what was used by Demir et al. (81). A. vagal PRC for standard $I_{K,ACh}$ model (solid line) magnified by 10, and for the fast $I_{K,ACh}$ model (dashed line) for 1, 5, and 10 vagal spikes as labeled. B. Effect of simultaneous adrenergic stimulation on vagal PRC. NE concentrations of 0, 0.01, and 0.1 μM were applied to the neuroeffector junction/EJS during the vagal PRC determination protocol. Dashed and solid lines are as in A, [NE] for each line as labeled. C. The control AP showing the phase range tested. D-F. Analogous plots to A-C, except with sympathetic stimulation and background ACh in E. Note the zoomed y-scale in D and E.

The experimental data show about 30% slowing in response to 10 vagal pulses and 70% with 20 pulses, and it has a fairly flat shape to the left of the PRC peak, which is around 0.5-0.6. This is different from the very tall and peaked PRC shapes shown by Demir and Dokos: in the Demir model, 9 pulses cause 90% maximal rate slowing, and in Dokos, 10 pulses cause an even greater 125% rate slowing. The 10-pulse

PRCs in our model straddle the experimental range, with the slow and fast $I_{K,ACh}$ producing ~10% and 80% maximal slowing, respectively. The qualitative shape of the experimental PRC curves is also less extreme than the shapes produced by the Demir and Dokos models, and lies between the peaked and blunt PRCs produced by fast and slow $I_{K,ACh}$ in our model.

For completeness, we also studied the sympathetic PRC using our model, although we cannot compare the results with other models or experimental data. Sympathetic PRCs are barely existent, being very close to zero and fairly insensitive to phase (Figure 111D). This is expected given the slow rate of β-AR activation. The addition of background ACh increases PRC amplitude (Figure 111E), presumably due to lengthened period which allows the slow NE response to have a greater effect; however, the effect is still very small at <1%.

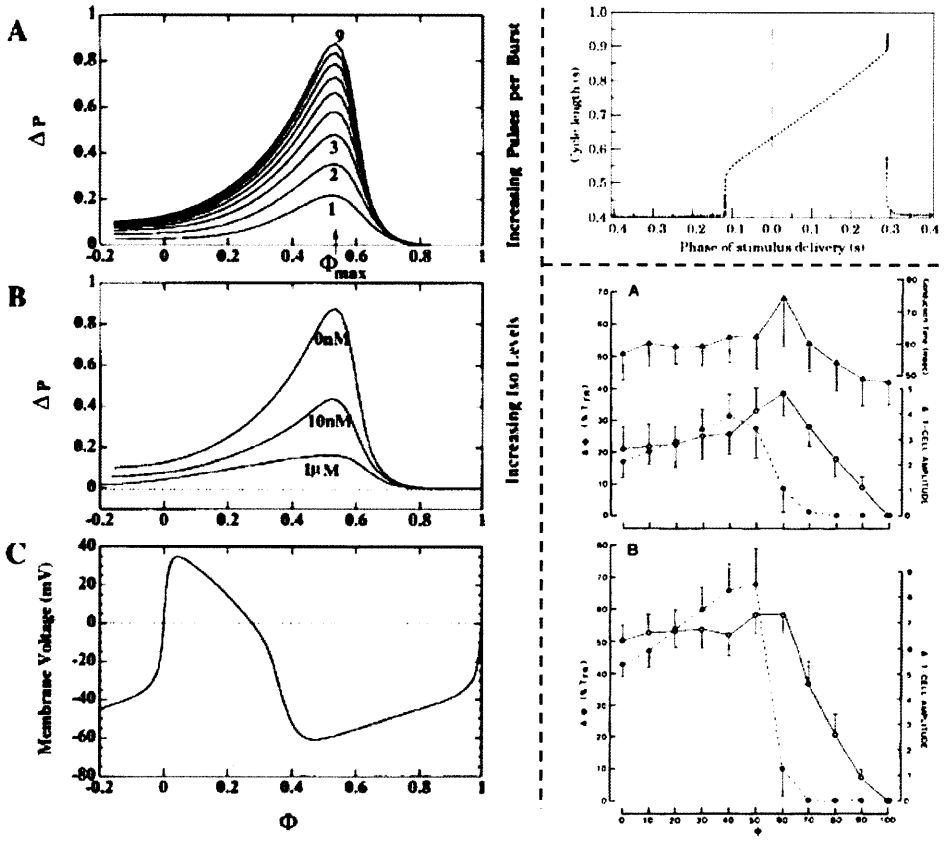

Figure 112. Vagal PRCs from the Demir (A-C to the left of dashed line, from Fig 12 from (81)) and Dokos (top right figure, from Fig 13 in (96)) models, as well as experimental data from Slenter et al. (A-B in bottom right, from Fig 5 in (296)). A-C on left: Figures analogous to Figure 111A-C, with 1-9 vagal stimuli delivered at 200Hz and background Iso concentrations as indicated in B. Top right: Similar PRC curve, but showing phase in seconds (not normalized to cycle length) and actual cycle length instead of ΔP. Vagal stimulation was at 100 Hz for 100 ms. Bottom right: • with dashed lines show ΔP (labeled as ΔΦ) for 10 (A) and 20 (B) vagal pulses at 200 Hz in rabbit SAN.

Finally, we consider the "impulse response" of the HR to individual sympathetic and parasympathetic spikes. We follow the procedure described by Berger et al. (20). In this study, the autonomic nerves in a canine preparation were stimulated according to a Gaussian White Noise (GWN) process and the resulting HR analyzed to produce nerve stimulation → HR impulse responses. The summary figure from our model study is shown in Figure 113 with the analogous figure from Berger et al. in Figure 114.

The results are qualitatively very similar, with the vagal impulse response being a sharp downward spike symmetric around 0, and the sympathetic one being a causal slow rise and fall about 20-30 seconds in duration. The Berger parasympathetic impulse response is slightly wider than ours, but that is likely due to the slower HR in their data (~70 bpm compared to ~110 bpm) which limits how tight the impulse response can be in the time-domain. Our vagal impulse response also contains a small low-frequency component which likely reflects the longer-lasting effect of the G-protein cascade on HR. This feature appears to be absent from the Berger data, although the area immediately to the right of the peak in their plot is also a bit more noisy. Another explanation for this is that sympathetic nerves have been observed to travel in close physical proximity to the vagus (324), so the Berger vagal stimulation data may suffer from contamination by partial activation of sympathetic fibers. If the system is fairly linear, this would have the effect of cancelling out the low-frequency hump in the vagal impulse response, since the sympathetic impulse response is about the same amplitude and shape, but opposite in sign. The difference could also be a rabbit vs. dog species effect, or it could imply that the effect of vagal stimulation on the cAMP cascade is not as large as we modeled, which would be in agreement with the model of Demir. More microanatomical data on the distribution of M2 muscarinic receptors in the neuroeffector junction and EJS spaces and their coupling to G-proteins and AC would be necessary to clear up this issue definitively. Alternatively, experiments similar to those of Berger could be re-run using a β-blocker while collecting the parasympathetic data to ensure no unwanted stimulation of the sympathetic branch. The sympathetic functions are also qualitatively very similar.

One thing that is quite surprising is how similar the experimental and model-generated transfer functions are quantitatively: both show about -2 bpm/Hz vagal stimulation peak and about 0.4 bpm/Hz sympathetic stimulation peak. A difference between the two systems is the amount of nonlinearity (the initial change in HR before it settles around the new set-point), which is fairly large in our model and almost nonexistent in the Berger data. This may again be because of species differences or due to the possibility of simultaneous stimulation of vagus and sympathetic nerves because of their anatomic proximity.

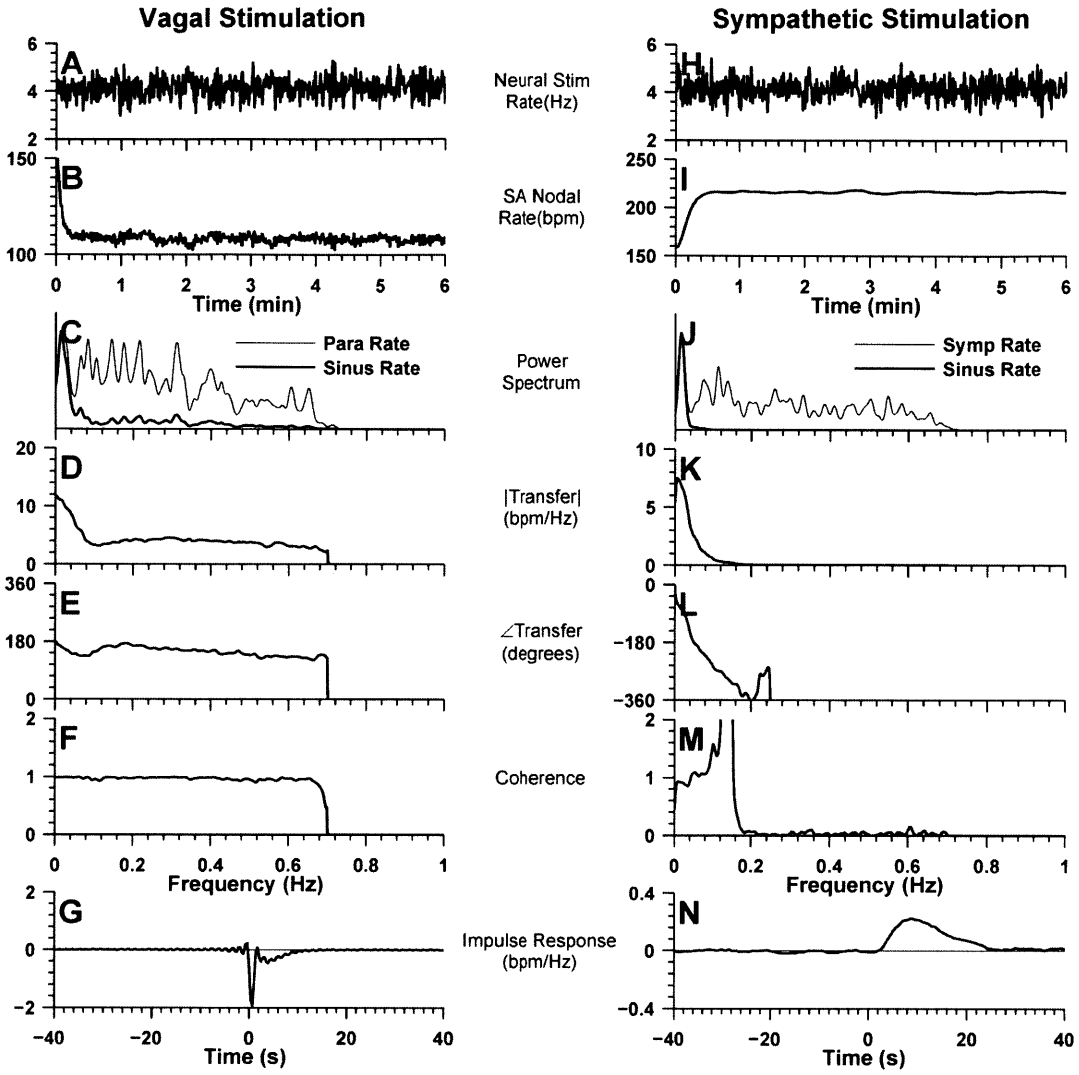

Figure 113. Transfer function analysis of SANC model responses to vagal and sympathetic stimulation, modeled after experiments by Berger et al. (20), see reference for experimental details. Briefly, A. GWN vagal stimulation low-pass filtered to 0.7 Hz, B. SANC model oscillation rate in response to stimulus in A. C. Power spectra of vagal stimulation rate (Para Rate) and SANC oscillation rate (Sinus Rate), normalized to peak value; arbitrary y-scale. D and D. Magnitude and phase of transfer function describing SANC input-output relationship for vagal stimulation. F. Computed coherence function (measure of system linearity). G. Vagal stimulation → HR impulse response in time, computed by averaging 8 experiments. H-N are analogous figures for sympathetic stimulation.

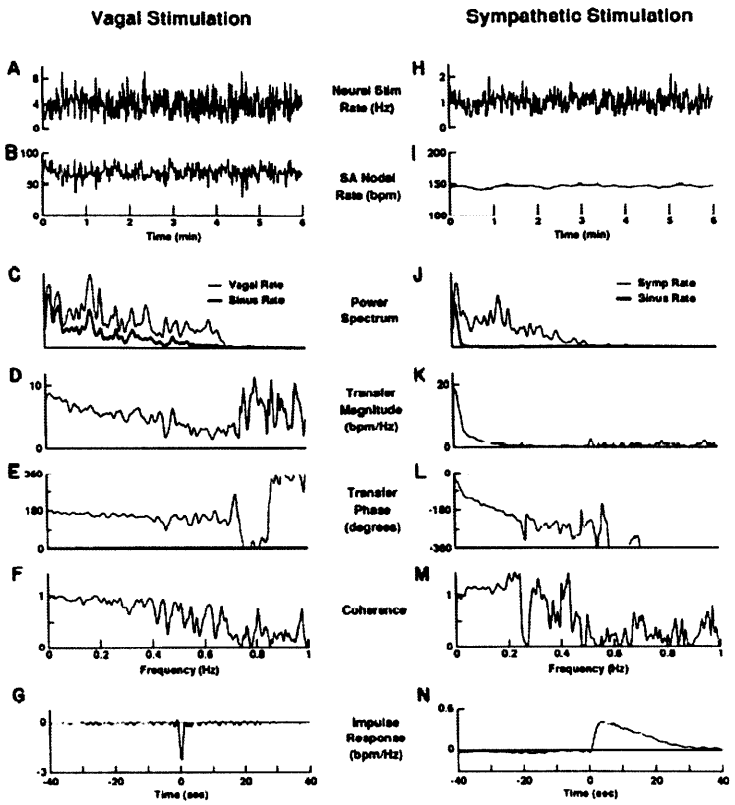

Figure 114. Experimental data on vagal and sympathetic transfer functions obtained in a canine preparation. Taken from Fig 4 in (20).

8 CONCLUSION AND FUTURE WORK

The work described in this thesis is the next natural step in the evolution of mathematical models of SANCs. The very first models applied the HH formalism to spontaneously active cells and provided a plausible mechanism of diastolic depolarization (the idea of potassium current decay in (253)). Next, more physiological realism was added in the form of SANC-specific ionic currents based on voltage clamp studies (82, 89, 95, 360, 368) and subcellular compartmentalization and cycling of Ca^{2+} (198, 228). The effects of adrenergic and cholinergic stimulation were also modeled (81, 96, 227, 369, 370), usually aimed at reproducing specific changes in AP shape or probing the ionic mechanisms of SANC oscillatory rate change. These models were incomplete however, because they described only very specific vagal stimulation protocols, and did not model neutrally-released NE, nor the dynamics of SANC rate change.

Our main objective was to build a complete model of dynamic HR modulation by the ANS; we achieved this goal by developing models of the individual component systems in the signaling cascade and assembling them to produce the desired high-level phenomenon of dynamic HR change. The model reproduces numerous experimental data sets and measured values, as well as high-level behaviors classically associated with ANS control of HR. Below we summarize the unique features of our model, what the model allows us to learn about the system, and future expansions of the model in terms of addressing its limitations and exploring other applications.

8.1 Model summary

Our model is fundamentally different from previous SANC models in our adherence to appropriate molecular mechanisms whenever possible. For example, models that explicitly include ACh release (81, 96) use a single parameter to describe the rate of ACh hydrolysis by AChE; in contrast, our model of ACh hydrolysis is based on experimentally measured AChE abundance, and the accepted catalytic mechanism wherein ACh binds AChE with a certain affinity and is then hydrolyzed at a specific rate. As a consequence, our model has more parameters. This may at first seem a disadvantage; however, these parameters describe real chemical processes and have been measured experimentally. This means that we have more confidence about the particular parameter values and therefore the overall function of various model components. The other components of our model are specified in a similarly detailed manner, and parameter values are supported by numerous experimental measurements. The explicit nature of our model also enables future refinements because more current measurements/estimates of particular parameters can easily be updated without having to change the overall model framework.

A second consequence of our focus on mechanisms is that our model features novel descriptions of a number of sub-systems that are absent in other models. We model 1) neurotransmitter release from the adrenergic and cholinergic varicosities, as well as the ACh- and NE-specific clearance mechanisms 2) the activation of β-AR and M2 muscarinic receptors 3) the activation of G-proteins and their effect on AC 4) the function of PDE in establishing an equilibrium cAMP concentration 5) the activation of PKA by cAMP 6) the effect of second messengers on SANC function, and 7) direct inhibition of adrenergic activity by high levels of ACh. Some of these sub-systems are useful independently of the whole cascade: for example, we used the neurotransmitter release model to combine data from experiments that used neural stimulation and those that used bath applications of NTs. The explicit nature of the entire cascade is also useful: if experimental data on SANC changes resulting from PDE or PKA inhibition, or cAMP application are available, the experimental conditions can be easily reproduced using our model in order to evaluate the simulated responses against the actual data and update the model if necessary.

To summarize each novel component:

1) Neurotransmitter release and clearance are based on first principles of binding/unbinding/catalysis reactions, diffusion, and SANC/autonomic varicosity geometry. The same basic framework is used for cholinergic and adrenergic stimulation, and allows simultaneous activation of both branches of the ANS, conversion from stimulation rate to neurotransmitter concentration, and neurotransmitter application directly at the cell's surface as well as on the far side of the ECM (in the BS).

2) The activation of β-AR and M2 muscarinic receptors by binding the appropriate neurotransmitter is modeled using measured rate constants and affinities, and includes two receptor populations (neuroeffector junction and EJS), with receptor abundances and distribution deduced from experimental measurements.

3) The G-protein model has independent sets of reactions for G_S and G_I, based on direct experimental data. The intrinsic GTP turnover cycle of each species is modeled, as well as GPCR-mediated facilitation of guanine nucleotide exchange and subunit dissociation. The activated G_S and G_I α subunits competitively bind AC and enhance or inhibit its rate of cAMP production according to the measured AC abundance and experimentally documented effects of adrenergic/cholinergic stimulation.

4) The complete PDE model features the two PDE subtypes most abundant in the SANC and their modulation by Ca-CaM and cGMP, and is based on experimental data. A reduced model appropriate for the particular Ca-CaM and cGMP concentrations in the SANC is also presented.

5) The catalytic subunit of PKA is liberated by binding cAMP according to a specific affinity and rate deduced from a number of experimental measurements appropriate for the SANC environment.

6) Second messengers cause a number of changes in ion channel parameters and SERCA function: a) our novel $I_{K,ACh}$ model is activated by $G_{\beta\gamma I}$, has a correct ACh sensitivity, and can reproduce correct kinetics (we use slower kinetics to compensate for the simplified nature of our neurotransmitter release model); b) the shift in the I_f activation gate is attributed to both a direct cAMP mechanism and a phosphorylation-dependent mechanism and allows the reproduction of explicit cAMP data as well as the overall adrenergic/cholinergic effects; c) changes in $I_{Ca,L}$ conductance are mediated by PKA and reproduce overall cholinergic/adrenergic data; d) SERCA pumping rate parameter P_{up} is mediated by PKA (through the implicit inactivation of PLB) and reproduces experimental data on PLB dephosphorylation by cholinergic agonists; e) I_{Kr} conductance and kinetics are PKA mediated, and change in accordance with maximal measured values and allow the reproduction of the full range of HRs using the baseline Maltsev model.

7) Adrenergic activity is directly inhibited by high levels of cholinergic agonists via a postsynaptic process.

The model fits all of the experimental data used in its construction, as well as some phenomena that we did not explicitly try to fit: the rightward shifts in $I_{K,ACh}$ and HR changes in response to NTs applied to whole-tissue preparations, the general shape and amplitude of vagal PRCs, and vagal and sympathetic impulse response functions. By incorporating changes in the kinetics of I_{Kr}, our model also eliminates a major limitation of the Maltsev model and enables smooth HR changes below 100 bpm without eliciting "chaotic" behavior. The use of pa_{sf} to modulate I_{Kr} kinetics also allows our model to generate more correct AP shapes than those produced by the Maltsev model.

8.2 Model implications

Our model allows us to draw multiple conclusions about the mechanisms of HR control by the ANS. Because the model is very detailed, the inferences we make can be equally specific and can be tested through targeted experiments. For example, it is generally understood that parasympathetically-mediated HR changes happen more quickly than sympathetically-mediated ones (5). Our model provides evidence regarding the mechanism responsible for this unique feature of the system: the rate-limiting step in adrenergic modulation of SANC properties occurs very early in the signal transduction cascade, in the slow activation of β-ARs. On the other hand, the rate limiting steps for cholinergically-mediated changes only occur downstream of cAMP, but still remain faster than the maximal adrenergic rate. To test this explanation, experiments comparing the rate of HR change in response to step application of NE versus step application of intracellular cAMP can be conducted. The hypothesis supported by our model is that direct application of cAMP would result in a faster approach to steady-state. The mechanistic explanation

offered by our model may also have clinical implications: since adrenergic changes are limited at the level of the receptors, the β-ARs are good drug targets. Conversely, drugs targeting M2 muscarinic receptors may not be as effective as ones targeting downstream systems such as PDE and PKA.

Along the same lines, the impulse response of our model to vagal and sympathetic stimulation matches that recorded in dog: the vagal response has the classic peaked shape whereas the sympathetic response is much more gradual increase followed by a decrease. However, the parasympathetic response from our model also contains a slow component. This difference may imply that the model overstates the slower cAMP-mediated mechanisms. It may also be due to differences between the rabbit and canine SANCs. However, the phenomenon could also be real, arising from contamination of the vagal stimuli by inadvertent activation of sympathetic fibers traveling in close proximity to the vagus ((171), reviewed by (324)). It would also imply that there is a greater low-frequency component to parasympathetic stimulation than previously believed, and would call into question heart rate variability (HRV) methods that rely on spectral separation of parasympathetic and sympathetic activity. To test these hypotheses, experiments like those done by Berger et al. (20) in dog should be repeated in rabbit to eliminate possible species differences. To test the hypothesis that electric stimulation of the vagus also causes stimulation of sympathetic fibers, the vagal stimulation experiments can be done in the presence and absence of β-blockers.

The disparity in the speed of vagally versus sympathetically mediated HR changes was also studied in terms of PRCs. The slow effect of sympathetic activity was manifested as the very small (<0.02%) maximal change in cycle length for stimuli applied during the preceding beat. On the other hand, vagal PRCs produced by the model had much larger maximum cycle length effects (10-80%) and the peak value was observed either during the current or preceding cycle. The model implies that the mechanism underlying peaked vagal PRC is primarily the rate of $I_{K,ACh}$ activation, with faster channel kinetics causing sharper and taller PRCs. Comparing the shape of the PRCs produced by our model to experimental data also implies that the appropriate rate of $I_{K,ACh}$ activation lies between the "fast" and "slow" kinetics we tested. The fast and slow kinetics were based on data from guinea-pig atrial $I_{K,ACh}$ (160), similar experiments should be conducted in rabbit SANCs to better determine the activation rate; from our model results, we would expect times between 200-800 ms for half-maximal $I_{K,ACh}$ activation in response to step applications of ACh.

Our model also allows us to critically evaluate data on the sensitivity of $I_{K,ACh}$ to ACh. Due to the explicit nature of our neurotransmitter release model, we are able to reconcile the disparate $I_{K,ACh}$ activation data

of Osterrieder et al. (264) versus those of Inomata et al. (160) and DiFrancesco et al. (88) and attribute the differences to experimental technique (whole SAN tissue vs. isolated cells) and the effect of AChE. We were able to further support this hypothesis by reproducing the rightward shifts in HR curves observed in whole SAN tissue experiments versus those on isolated cells (see Figure 105k). Previous models with less specific descriptions of the extracellular space and neurotransmitter diffusion were unable to systematically deduce the more appropriate data set, and this led to a number of unique descriptions of $I_{K,ACh}$ (see Figure 89B, Dokos vs. Maltsev and Demir models). To completely resolve this issue, our hypothesis should be tested experimentally: by quantifying the $I_{K,ACh}$ sensitivity to ACh in an isolated cell versus whole SAN tissue in the presence and absence of AChE inhibitors (the effect of AChE inhibitors was tested by Osterrieder et al. (264) and the result is in agreement with our hypothesis).

Because of the thorough description of both adrenergic and cholinergic systems, our model allows us to deduce how they interact when simultaneously activated. In the literature, both direct and indirect mechanisms have been proposed; our model shows that both are necessary, but active under different regimes. In the setting of low and moderate vagal activity, the sympathetic/parasympathetic interaction occurs indirectly, via competitive inhibition or activation of AC. At high vagal rates however, a direct inhibition of adrenergic stimulation was necessary to reproduce experimental data. The mechanism of this direct inhibition is modeled abstractly due to a lack of data. We chose an intracellular mechanism wherein activated M2 muscarinic receptors effectively reduce the number of active β-ARs. However, presynaptic mechanisms that result in diminished release of NE are also possible. To differentiate these two mechanisms, studies of direct NE release or spillover in the setting of constant sympathetic stimulation and varying levels of simultaneous vagal stimulation would need to be conducted. Also, to verify that such a direct mechanism exists, experiments in recombinant cells lacking functional G_I could be conducted to explore whether a cholinergic effect can be elicited at high vagal rates and nonzero sympathetic rates; our model predicts that an effect would be observed.

Our model uses a unified framework to change SANC parameter values in response to ANS stimulation. This allows us to assess the importance of various pacemaker mechanisms relative to each other in a way that was previously not possible. The major conclusions we make are that the classically considered "pacemaker currents" I_f and $I_{Ca,L}$ exert a smaller effect on the rate of SANC depolarization than previously believed, and that more subtle changes like those in I_{Kr} kinetics can have a significant impact. This is so largely because the experimentally measured changes in I_f and $I_{Ca,L}$ (Figure 105 b and e) only reach about half of their maximal values at neurotransmitter concentrations that elicit near-maximal HR changes (Figure 105k). Thus, models such as the Maltsev model, which assume the maximal change in I_f and $I_{Ca,L}$

parameters to simulate moderate HR changes overestimate their effect. In our model, the modification of I_{Kr} kinetics was necessary in order to allow reproduction of the full experimentally observed HR range, and is therefore of critical importance. However, its importance is not obvious from the subtle changes in I_{Kr} current traces over the course of an AP (compare I_{Kr} in Figure 107 versus Figure 108A). While the particular changes in I_{Kr} kinetics may be somewhat arbitrary in our model, it illustrates the importance of kinetics over conductances. Most other models do not include any changes in channel kinetics due to adrenergic or cholinergic activity (81, 96, 227); this may be because these changes are more difficult to measure than those in maximum current. However, our model suggests that more experimental efforts gathering channel kinetic data would be very valuable for understanding the mechanisms of ANS control of HR.

Our model shows a diminished importance of $I_{Ca,L}$ in altering SANC depolarization rate; however, further exploration identified it as necessary and sufficient for maintaining a growing membrane voltage oscillation at very low HRs. This oscillation appears to be physiologic since it has been observed experimentally, and it points to a new function of $I_{Ca,L}$, as a possible mechanism to prevent complete cessation of pacemaking. From a clinical perspective, this same mechanism could have the negative consequence of acting as a proarrhythmic. In this case, Ca^{2+} channel blockers may be of clinical value not only as methods of rate- but also rhythm-control and more testing of such applications could be called for.

Finally, we identified processes that need to be modeled in detail and are therefore likely to be critical for SANC function. Our neurotransmitter release model assumes that a number of vesicles are released from all varicosities at the same instant. By studying the effect of this assumption on the behavior of $I_{K,ACh}$ and HR (see section 6.3.3), we concluded that it would be necessary to model a more stochastic vesicle release process. The dynamics of vesicle release can be studied experimentally to determine the distribution of lag times between neural stimulus and the fusion of a number of vesicles in a single varicosity. Also, the effect of stimulus conduction delays as a function of distance to individual varicosities should be experimentally explored. Another aspect that requires a more explicit treatment is that of subcellular localization of second messengers. Our detailed models of G-proteins, cAMP and PKA do not allow the reproduction of appropriate HR dynamics without the use of empirical speedup factors. The same effect could be achieved by modeling second messenger localization to smaller volumes; the spatial localization and dimensions of these pools would have to be determined through direct experimentation or to reproduce the same phenomenon achieved by our speedup factors.

8.3 Future work: model limitations and applications

A considerable amount of effort was expended to develop our model in adherence to the known mechanisms and experimental data. As with all models however, ours has a number of limitations that should be addressed. Below is a list of suggestions for best remedying these limitations:

1. Add stochastic element to neurotransmitter release. This can be done by either modeling each varicosity separately, or using a temporally-smeared function. Modeling each varicosity independently would be easiest from a functional point of view since all the same equations could be used. It would however be much more computationally intensive because this would add almost 100 more state variables to the ODE system. The second option would be computationally simpler since we would maintain a "single" adrenergic and cholinergic varicosity, but the equations describing release would have to change. A good choice for vesicle release function would have the shape of a Poisson distribution, under the assumption that the signal for vesicle fusion arrives instantaneously, but N different vesicles fuse with the varicosity membrane and release neurotransmitter in a random manner (Poisson arrivals). The parameters for this distribution can be obtained empirically to eliminate the HR oscillation when using fast $I_{K,ACh}$, theoretically by looking at the spatial distribution of vesicles within a varicosity and estimating the variance of their fusion lags, or experimentally by actually measuring neurotransmitter concentration in a neuroeffector junction as a function of time in response to a stimulus. The improved model should allow for fast $I_{K,ACh}$ kinetics without causing the HR oscillation/beat pattern we observed with the model presented here.
2. Improve $I_{K,ACh}$ model to reflect actual kinetics. Inomata et al. data (160) or more appropriate rabbit data can be used to pick appropriate G_{sf} and $\beta_{\tau a}$. Speeding up G_{sf} may require slowing down some of the downstream speedup factors to maintain overall vagal HR dynamics Figure 106. The faster $I_{K,ACh}$ kinetics should also produce PRCs that are more similar to the experimental data of Slenter et al. (296).
3. Add compartmentalization of cAMP, PKA, and PDE based on experimental data to replace the empiric speedup factors we used. Some data are available (see references in section 6.7), and it seems that more will become available in the near future as experimental methods improve and the scientific community gains a greater appreciation for the importance of compartmentalization in cell function. Initial modeling attempts will have to be rudimentary due to the computational complexity they would otherwise introduce; a reasonable first attempt would be to introduce local volumes (based on experimental data) specific to G-proteins, cAMP, PDE, and PKA, to allow faster kinetics similar to what we modeled with our speedup factors.

4. Describe alternate and interacting second messenger systems that are known to exist in the SANC, like cGMP, PKC, and NO.
5. Obtain more data to better describe and test our model representation of: a) the direct pathway of ACh-induced inhibition of adrenergic activity, b) $I_{f,Shift}$ phenomena due to cAMP and PKA, c) the parameters for which we did not have explicit data and instead fit to HR data (g_{Kr}, R_{Pup}, pa_{sf})

Despite the above limitations, we showed that our model reproduces some high-level phenomena, and there are many other studies for which the model could be used. For example, it would be interesting to study the mechanisms responsible for the AP refractory period and its dependence on cycle length as experimentally measured by Mendez et al. (238); to evaluate the appropriateness of modeling the SAN as an integrate-and-fire model (integral pulse frequency modulation/IPFM) with regard to incoming sympathetic and parasympathetic impulses (59, 63, 246); to study in more detail the contribution of individual second messengers and membrane currents on AP shape and SANC beating rate; or to evaluate the effect of sympathetic and parasympathetic stimulation rates and individual spike statistics on the variability in heart rate. As an extension of the last point, our model could also be used to generate a synthetic data set with explicit sympathetic and parasympathetic inputs for the systematic evaluation and comparison of the numerous HRV estimation methods, all of which aim to solve the inverse problem of deducing ANS tone from an observation of HR or other physiological signals (a number of HRV methods that could be studied in this way are described in (1)). Also along the lines of ANS tone estimation, the forward model that we describe here can be used to systematically design an optimal (in some well-defined mathematical sense) algorithm for the inference problem of estimating sympathetic and parasympathetic rates from an observation of heart beat times.

One way to approach this goal of designing an estimation algorithm is to first reduce the model to a collection of functions that describe steady-state values and the time constants for approaching those values. These functions could eliminate many "unnecessary" components of the system; for example, all the neurotransmitter reuptake, diffusion, and hydrolysis functions, and the explicit β-adrenergic and M2-muscarinic binding reactions could be replaced by a two steady-state functions (that express steady-state fraction of each bound receptor as a function of sympathetic or parasympathetic nerve stimulation frequency) and two time constant functions (to express the lag between nerve stimulation and receptor activation; it may be necessary to use more than one time constant since the approaches to steady-state were not single-exponential). These functions could be obtained in a straightforward manner by running the full model with various inputs, and fitting functions of necessary complexity to the generated data. Once the system is reduced to a smaller number of equations and a consistent equation format

(essentially, the differential equation for each variable v would look like $dv/dt=(v_{ss}(u)-v)/\tau_v(u)$, with v being the particular variable, $v_{ss}(u)$ being the steady state function as a function of upstream variables u, and $\tau_v(u)$ being the time constant function), it should be easier to define the relationship between the inputs (sympathetic and parasympathetic stimulation frequency) and the resulting heart rates. Certain components of the system could even be removed at this point, if their time constants are fast relative to those of the other variables. This reduced and simplified form may have a well-defined estimation approach already defined (I am not familiar with any specific algorithms, but it seems reasonable that a few may exist to solve the inverse problem for a cascaded system of steady-state functions and lags), or a specific algorithm can be derived for this purpose.

In developing this model, we encountered many interesting experimental data which it would be interesting to reproduce. We reproduced many of them (see Figure 105); below, we list others that should be reproduced to either verify the correct functioning of the model ("test data") or to provide improved estimates of certain model parameters ("training data"):

1. Acetylcholinesterase function in a quiescent cell (Fig. 10 in (192))
2. Adenylate cyclase activation by Iso, can be converted to NE by shifting an order of magnitude to the right (Fig 2 in (41))
3. Phosphodiesterase and G-protein effects on I_f, (various figures in (92))
4. Phosphokinase A inhibition (Fig 2 in (341))
5. To estimate baseline parasympathetic rate in rabbits, reproduce the observation that in rabbits, atropoine (which can be modeled by setting parasympathetic stimulation rate to 0) caused a 39.6% increase in HR (193)
6. cAMP dynamics and effect on rabbit heart rate, and simultaneous acetylcholine and norepinephrine effects on heart rate (various figures in (317-320))
7. cGMP dynamics (cGMP is not included in the present model; if it is added, these data could be used to formulate its behavior: (318, 319))
8. Desensitization to acetylcholine (the current model does not include desensitization to acetylcholine, data in Fig 2 in (154) could be used to formulate it)
9. cAMP effect on heart rate (Fig 1 in (363))
10. Sympathetic stimulation and NE effect on heart rate (Fig 2 in (328))
11. Time course of ACh and NE effects on heart rate and AP shape (Fig 2-4 and 6-7 in (352))
12. Dynamics of sympathetic stimulation on HR in guinea pig (Fig 4 in (64))

9 APPENDIX

9.1 Temperature correction

We aim to reproduce SANC activity *in-vivo*, at a temperature of 37 °C. However, many of the available experimental data were collected at other temperatures, most commonly room temperature (20-25 °C). To compensate measured kinetic values (time constants and rates) for temperature effects, the concept of a Q_{10} is frequently used ((reference)-Q_{10} used: (368)-1.7, (76)-3, (212)-1.7, (198)-1.7, (69)-2.3):

$$r_2 = r_1 (Q_{10})^{\frac{T_2 - T_1}{10}}$$

Where r_1 is the measured rate at temperature T_1, and r_2 is the rate corrected to temperature T_2. In essence, the rate is Q_{10} times faster for each 10 °C increase in temperature. A wide range of Q_{10} values have been measured for various systems, ranging from ~1.2 for diffusion of small molecules (196) to 2.3 for movement of sodium channel activation gates (69), and values as high as 3 have been assumed by modelers for certain ion channels (76). For the present model, we use an intermediate Q_{10} of 1.7 as used in a number of other models (198, 212, 368) unless a specific Q_{10} value for the reaction of interest is reported in an experimental paper.

9.2 Unit conversions

We gathered experimental data from a large number of studies. This section provides the numerical details on how units were converted to allow comparison across these disparate sources. Table 19 contains the conversion factors we used; when computing concentrations of intracellular molecules, the volume of the cytosol was used (not whole cell volume, which includes the nucleus and other organelles).

Table 19. Conversion factors for translating experimental results to SANC-specific values

Value	Units	Source (if applicable)
169.18	g /mol NE	
146.21	g /mol ACh	
6×10^{23}	molecules/mol	
1	g /mL wet tissue	(186, 357)
3.5×10^{-12}	L wet tissue/SANC	Volume of cell calculated using cell dimensions
1.6×10^{-12}	L cytosol/SANC	Cytosol occupies 46% of cell volume (82)
1760	μm^2/SANC	Surface area of cell calculated using cell dimensions
52.5	mg protein/g wet tissue	*
13,000	ACh molecules/s/AChE	AChE catalytic rate constant, see section 2.3.4

* The "total protein" in certain experiments refers to mostly membrane protein, after cells have been homogenized and sarcoplasmic, nuclear, and contractile protein has been removed (39, 123). We estimate the membrane protein content of cardiac cells to be $2x10^{-7}$ mg/cell. This figure was obtained from a measurement of protein fractions in mouse ventricular muscle by Medugorac (237). This study reports 52.5 mg stromal protein per 1 g wet weight of myocardium (237). For comparison, a study on human cardiac patients without ventricular dysfunction reported 11-16 mg protein/gram wet weight (115), and a study by Delforge et al. quotes 10% protein per tissue weight (100 mg protein/g wet weight) as a standard value (80). On this range from 11-100 mg protein/gram wet weight, we choose the intermediate value of 52.5 mg protein/g wet weight.

The values in the above table are used to convert units using standard dimensional analysis; for example to convert µg NE/g wet tissue to molecules of NE/SANC:

$$\frac{\mu g\ NE}{g\ wet\ tissue}\times\frac{1\times10^{-6}g}{\mu g}\times\frac{mol\ NE}{169.18g\ NE}\times1\frac{g\ wet\ tissue}{mL\ wet\ tissue}\times3.518\times10^{-9}\frac{mL\ wet\ tissue}{SANC}\times6\times10^{23}\frac{molecules\ NE}{mol\ NE}$$

9.3 Summary of previous neurotransmitter diffusion models

In this section, we summarize each previous model pointing out their unique assumptions and differences from our model. In the figures used to summarize each model, $[ACh]_{ms}$ is the "main store" of neurotransmitter (the varicosity), $[ACh]_{cell}$ is the concentration at the cell membrane, and $[ACh]_{ex}$ is the concentration in the extrajunctional space.

Among the earliest models is that developed by Warner and Cox (349) to explain changes in canine HR in response to vagal and sympathetic stimulation.

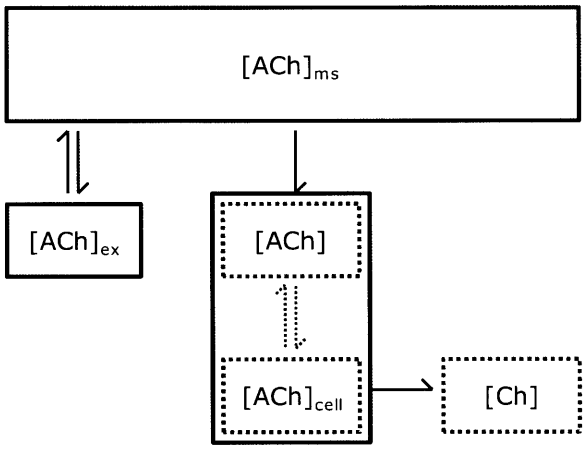

Figure 115 Warner 1962 model (349).

This model features vagus nerves containing a number of vesicles which are released into the neuroeffector junction at a rate proportional to the frequency of vagus nerve spiking or external stimulation (349)). ACh is diluted in the volume of the neuroeffector junction and hydrolyzed by AChE (349). The neuronal store of vesicles is replenished through a diffusion-like process from a constant vesicle store (349), a feature that we also included in our model. As shown above, the model does not explicitly define diffusion through the neuroeffector junction, and instead considers the nerve end and cell end of the junction as a single compartment. The model also does not include washout from the neuroeffector junction, so hydrolysis is the only method for removing ACh. This model can accurately reproduce changes in HR that result from step inputs; however, model parameters were chosen in order to fit every recording independently and not all are reported in the paper (349). This implies that the model is rich enough to explain a particular phenomenon, but not a general class of phenomena across multiple experiments, which in turn implies that it may be an oversimplification.

In 1971, Chess and Calaresu (61) published a model of HR changes in response to left and right vagus stimulation.

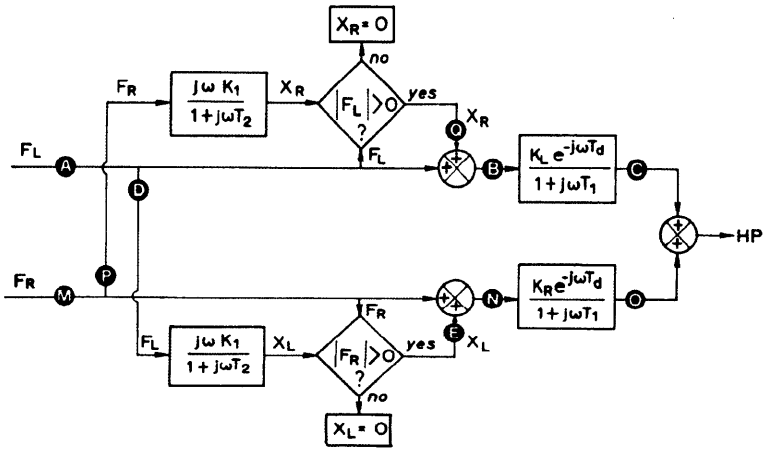

FIG. 2. Block diagram of frequency response model of vagus-heart period system. F_L and F_R are variations in rate of left and right vagal stimulation, X_L and X_R are interaction terms, and HP is variation in heart period. For bilateral stimulation, parallel first-order systems for left and right vagi are mutually connected by rate-sensitive elements whose outputs (X_L and X_R) are routed to contralateral paths. For unilateral stimulation of either vagus, both X_L and X_R are zero and model reduces to a simple first-order system.

Figure 116. Model of Chess and Calaresu 1971, figure taken from (61). See original caption for abbreviations.

The model contains transfer functions from vagus stimulation frequency to change in HR, but does not explicitly model the ACh concentration (61). It is mentioned here for completeness and to emphasize the fact that the dynamics of HR in response to ACh are better modeled as a third order system. This implies that models with simple ACh removal dynamics (such as the Warner model) cannot account for HR changes observed experimentally (see page 25 in (96) for discussion).

In 1977, Purves published a collection of equations describing the diffusion of molecules away from a point source as a function of time and distance (276). For ACh in particular, several equations are given, which include passive diffusion as well as hydrolysis by AChE (276). Despite being an idealization that does not fit the physical description of the neuroeffector junction (the diffusion model assumes a point source diffusing through an infinite, homogeneous space), the Purves model has been used by Osterrieder et al. (265), Pott (274), and Demir (81). Interestingly, all of these groups used equation 38 from Purves, which assumes that hydrolysis occurs in the medium (276):

$$C = \frac{M}{8(\pi Dt)^{1.5}} \exp\left(-k_h t - \frac{x^2}{4Dt}\right)$$

As Loffelholz and Pappano point out however, only cell membrane-bound AChEs participate in hydrolysis (219). Purves 1977 also provides a solution for this case (Equation 40 in (276)), however it is more complicated and involves computing the error function compliment at each time or distance point:

$$S = M\left\{\frac{\exp(-x^2/4Dt)}{(\pi Dt)^{\frac{1}{2}}} - \frac{k_h'}{D}\exp\left[\frac{k_h' x + k_h'^2 t}{D}\right]\operatorname{erfc}\left[\frac{x}{2\sqrt{Dt}} + k_h'\sqrt{\frac{t}{D}}\right]\right\}$$

The Osterrieder et al. and Pott models were used to reproduce membrane voltage hyperpolarizations of rabbit (Osterrieder) and guinea pig (Pott) SA node cells in response to pipette-administered ACh, so the models do not include replenishment of the main ACh store (265, 274). As shown in the diagram below, these two models feature a diffusion distance of 30-100 microns, which may have accurately described the distance between the ACh pipette tip and the cells, but is orders of magnitude larger than neuroeffector junction widths measured with electron microscopy, which are less than 0.1μm (65, 219).

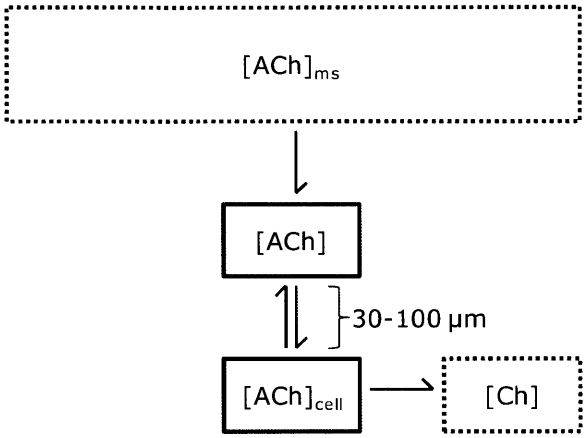

Figure 117 Osterrieder 1981 and Pott 1983 models

In his 1989 paper, Celler used an ACh release and hydrolysis model similar to that of Warner, which included release of a fraction of the sequestered ACh with each vagal stimulus pulse, and hydrolysis of the free ACh in the neuroeffector junction (56). As with the Warner model, diffusion and washout were not considered. The major difference between these two models however, is that the Celler model made explicit that the total amount of ACh was constant (hydrolyzed ACh replenished the sequestered store) rather than being withdrawn from a limitless pool as in the Warner model (56, 349). We incorporated this feature in our model as well; however, we did not limit the model to the local ACh supply only, and also included the Warner-like term for ACh synthesis from the blood stream.

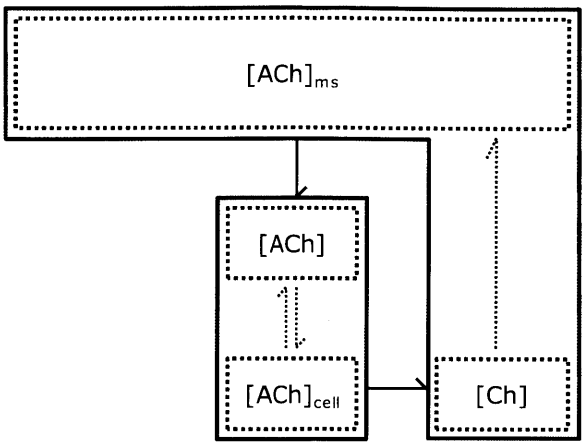

Figure 118 Celler 1989 model (56).

Also in 1989, Dexter et al. analyzed a detailed model of ACh hydrolysis by AChE, washout, and binding to receptors to conclude that ACh concentration would decay with a single exponential time course, where the time constant is a function of all three ACh removal processes (86).

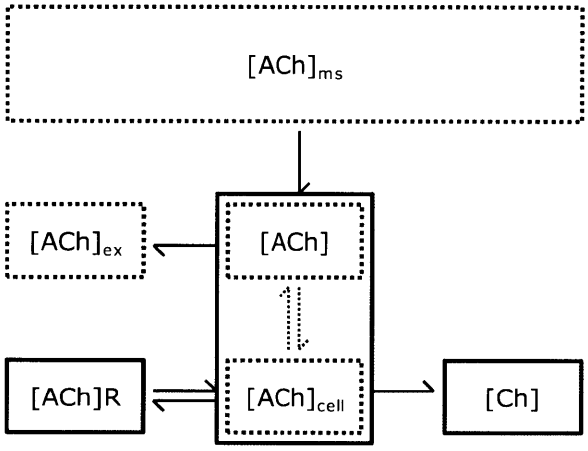

Figure 119 Dexter 1989 model (86).

Dokos developed a fairly comprehensive ACh model, for the first time introducing an explicit extrajunctional third compartment (96). The rationale behind their model description and comparisons with previous models is thoroughly described in the paper; to summarize, the three compartment model was chosen in order to reproduce 1) the observed fast and slow components of HR recovery after vagal stimulation and 2) the differing effects produced by the timing of vagal stimulation relative to the beginning of the heart period (96). The model contains three compartments: the main ACh store $[ACh]_{ms}$, ACh released into the neuroeffector junction [ACh], and ACh in the extrajunctional space $[ACh]_{ex}$. Each vagal stimulus instantaneously releases a fraction of ACh from the main store, with a fraction being released into the neuroeffector junction and EJS simultaneously. The ACh in the neuroeffector junction is

hydrolyzed with a rate 14/s and is reabsorbed and synthesized into ACh in the main store. ACh diffuses between the neuroeffector junction and EJS with rate 0.5/s. Finally, ACh from the extrajunctional space "escapes" unhydrolized and returns to the main store with rate 0.5/s. This is the most thorough compartmental model, capturing the three important processes (synthesis, diffusion, hydrolysis). Similar to our model, it shares the undesirable (but in our opinion, physiologic) feature of discontinuous jumps in concentration with each stimulus (release and diffusion from the varicosity to the cell is assumed to be instantaneous).

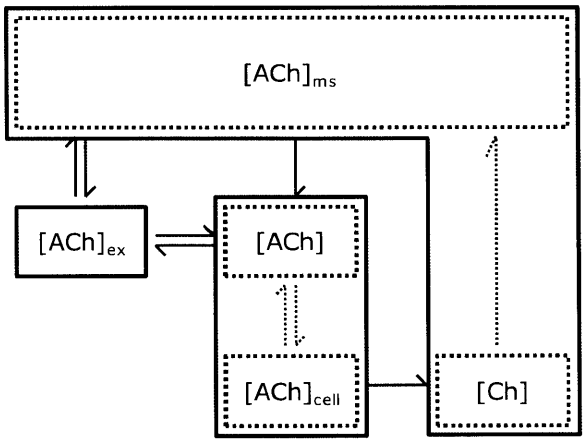

Figure 120. Dokos 1996 model (96).

The most recent SANC model with explicit ACh dynamics was published by Demir (81). This model used the Purves equation for diffusion within the neuroeffector junction and hydrolysis, but it also modeled depletion of ACh from the nerve varicosity such that after the first three releases (which release a constant amount of ACh), the amount of ACh released per stimulus decays exponentially (81). While some amount of depletion may occur, this model does not include any mechanisms for ACh synthesis/replenishment, so once all the ACh stores are depleted (which happens after about 10 releases), further vagal stimulation has no effect on ACh concentration in the neuroeffector junction. This is a serious drawback of this model, which makes it inappropriate for the type of prolonged vagal stimulations that occur in-vivo. This model is similar to those of Osterrieder and Pott, however Demir uses a much more physiological neuroeffector junction distance of 75nm. The diffusivity constant Demir assumes however, is 5 orders of magnitude smaller than those used by Osterrieder and Pott, who used the more reasonable value of $8 \times 10^{-6} cm^2/s$.

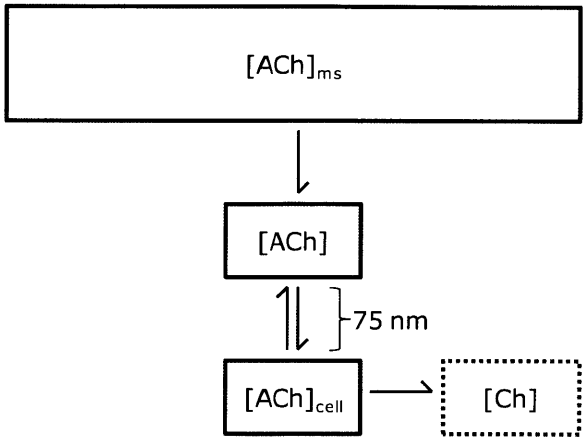

Figure 121. Demir 1999 model (81)

Table 20. A list of parameters assumed or measured in previous studies.

	Hydrolysis (/s)	Synthesis (/s)	D (cm^2/s)	Distance to cell (nm)	Peak ACh after 1 pulse (mM)
Warner 1962 (349)	0.87*	2.75			
Osterrieder 1980 (264)	2.5				
Osterrieder 1981 (265)			8×10^{-6}	30,000-100,000	
Nilsson 1970 (252), Trautwein 1963 (331)				<60	
Lindmar 1982 (214)	0.2773*				
Pott 1983 (274)	1		8×10^{-6}	100,000	
Celler 1989 (56)	0.57*				
Dexter 1989 (86)	0.2567*				
Celler 1991 (57)	0.2260*				
Dokos 1996 (96)	14	0.5 EJS→ms 14 NJ→ms			4×10^{-4}
Demir 1999 (81)	50	0	5.1469×10^{-11}	75	2×10^{-3}

* experimentally measured

9.4 Diffusion within the SANC

The second messengers in our model are either synthesized at the cell membrane (cAMP generation by AC) or are tethered to the membrane by anchoring proteins prior to release (catalytic subunit of PKA, G-protein α subunits). Thus, we explored the rate of diffusion from submembrane space (defined as a space 0.02 μm immediately inside the cell membrane (198)) into the general cytosol. Molecular Monte-Carlo simulations of a cell cross section Figure 122 illustrate that unhindered diffusion within the cell is very rapid over a large range of assumed diffusivities. We initially modeled all second messengers as being instantly diffused within the entire SANC volume; however, G-proteins, cAMP, and PKA appear to be localized to cell compartments by the action of PDEs or membrane anchoring proteins. Subcellular localization is expected to result in faster rates of change compared to a system where the second messengers instantly fill the entire cell volume. To model this feature, we included speed-up factors for G-proteins, cAMP, and PKA, whose values were set in order to reproduce HR time courses in response to vagus and sympathetic nerve stimulation in an isolated rabbit heart preparation (see section 6.7).

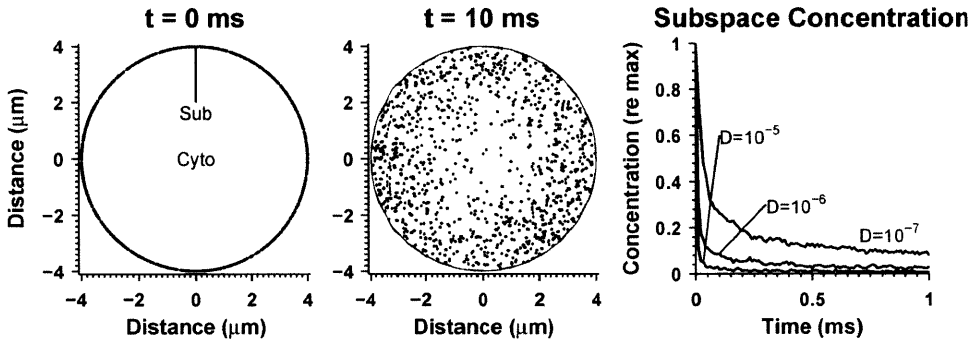

Figure 122 Monte-Carlo simulation of unhindered diffusion from cell membrane. The panels on the left illustrate the initial condition (all molecules in submembrane space) and the location of the molecules at 10 ms for the intermediate diffusivity of 10^{-6} cm^2/s. The right panel shows the normalized number of molecules within the submembrane space as a function of time for the three diffusivities indicated on the figure (in cm^2/s).

9.5 *Model specification*

9.5.1 *State variables*

Table 21. Model state variables and initial values suitable for 0 Hz sympathetic and parasympathetic stimulation.

Order	Variable	Initial value	Units	Description
1	$N_{v,ACh}$	6075	number	Number of ACh-filled vesicles
2	$[ACh]_{NJ}$	1.404E-07	mM	ACh concentration in neuroeffector junction
3	$[AChM]_{NJ}$	4.646E-05	mM	M2 muscarinic receptors bound to ACh in the NJ
4	$[ACh]_{EJS}$	1.640E-07	mM	ACh concentration in extrajunctional space
5	$[AChM]_{EJS}$	2.278E-06	mM	M2 muscarinic receptors bound to ACh in the EJS
6	$[ACh]_{ECM}$	8.575E-07	mM	ACh concentration in the extracellular matrix
7	X	3.625E-07	mM	Activated M2 muscarinic receptor concentration in cytosol
8	$N_{v,NE}$	675	number	Number of NE-filled vesicles
9	$[NE]_{NJ}$	3.097E-08	mM	NE concentration in neuroeffector junction
10	$[NE\beta]_{NJ}$	1.284E-05	mM	β-adrenergic receptors bound to NE in the NJ
11	$[NE]_{EJS}$	3.018E-07	mM	NE concentration in extrajunctional space
12	$[NE\beta]_{EJS}$	5.234E-07	mM	β-adrenergic receptors bound to NE in the EJS
13	$[NE]_{ECM}$	9.616E-07	mM	NE concentration in the extracellular matrix
14	$[G_{S\alpha\beta\gamma}\,GDP]$	1.824E-03	mM	Un-dissociated G_S bound to GDP (concentration in cytosol)
15	$[G_{S\alpha\beta\gamma}\,GTP]$	7.264E-05	mM	Un-dissociated G_S bound to GTP (concentration in cytosol)
16	$[G_{S\alpha}\,GTP]$	3.394E-05	mM	Dissociated $G_{S\alpha}$ subunit bound to GTP (concentration in cytosol)
17	$[G_{I\alpha\beta\gamma}\,GDP]$	9.531E-03	mM	Un-dissociated G_I bound to GDP (concentration in cytosol)
18	$[G_{I\alpha\beta\gamma}\,GTP]$	3.466E-04	mM	Un-dissociated G_I bound to GTP (concentration in cytosol)
19	$[G_{I\alpha}\,GTP]$	4.072E-05	mM	Dissociated $G_{I\alpha}$ subunit bound to GTP (concentration in cytosol)
20	$[cAMP]$	3.105E-03	mM	cAMP concentration in cytosol
21	C	3.831E-04	mM	Activated PKA catalytic subunit concentration in cytosol
22	$I_{f,ShiftP}$	-9.812	mV	Shift in I_f activation gate due to phosphorylation
23	$R_{gCa,L}$	1.006	scalar	Relative change in Ca^{2+} L-type channel conductance
24	R_{Pup}	1.012	scalar	Relative change in SERCA pumping rate P_{up}
25	R_{gKr}	1	scalar	Relative change in rapidly activating delayed rectifier K^+ channel conductance
26	pa_{sf}	1.084	scalar	Speedup factor for I_{Kr} activation gate p_a
27	Ca_i	2.644E-04	mM	Ca^{2+} concentration in cytosol
28	Ca_{sub}	1.581E-04	mM	Ca^{2+} concentration in submembrane space
29	Ca_{jSR}	0.102	mM	Ca^{2+} concentration in junctional SR
30	Ca_{nSR}	0.9886	mM	Ca^{2+} concentration in network SR
31	f_{TC}	0.05061	fraction	Fractional occupancy of the troponin Ca^{2+} site by Ca^{2+} in cytosol
32	f_{TMC}	0.5687	fraction	Fractional occupancy of the troponin Mg^{2+} site by Ca^{2+} in cytosol

33	f_{TMM}	0.3809	fraction	Fractional occupancy of the troponin Mg^{2+} site by Mg^{2+} in cytosol
34	f_{CMi}	0.1008	fraction	Fractional occupancy of calmodulin by Ca^{2+} in cytosol
35	f_{CMs}	0.06267	fraction	Fractional occupancy of calmodulin by Ca^{2+} in submembrane space
36	f_{CQ}	0.1063	fraction	Fractional occupancy of calsequestrin by Ca^{2+} in junctional SR
37	R	0.5981	fraction	Ryanodine receptor (RyR) reactivated (closed) state
38	O	2.758E-07	fraction	RyR open state
39	I	1.853E-07	fraction	RyR inactivated state
40	RI	0.4019	fraction	RyR RI state (described in (294, 304))
41	V_m	-60.92	mV	Transmembrane voltage
42	d_L	0.0003702	fraction	$I_{Ca,L}$ activation gate
43	f_L	0.6014	fraction	$I_{Ca,L}$ voltage-dependent inactivation gate
44	f_{Ca}	0.6126	fraction	$I_{Ca,L}$ Ca^{2+}-dependent inactivation gate
45	p_{aF}	0.3349	fraction	I_{Kr} fast activation gate
46	p_{aS}	0.5871	fraction	I_{Kr} slow activation gate
47	p_i	0.8687	fraction	I_{Kr} inactivation gate
48	n	0.04394	fraction	I_{Ks} activation gate
49	y	0.065	fraction	I_f activation gate
50	d_T	0.003112	fraction	$I_{Ca,T}$ activation gate
51	f_T	0.2976	fraction	$I_{Ca,T}$ inactivation gate
52	q	0.5671	fraction	I_{to} inactivation gate
53	r	0.004759	fraction	I_{to} and I_{sus} activation gate
54	q_a	0.3186	fraction	I_{st} activation gate
55	q_i	0.4066	fraction	I_{st} inactivation gate
56	β	0.00002503	/ms	$I_{K,ACh}$ activation rate
57	a_{gate}	0.00145	fraction	$I_{K,ACh}$ activation gate (function of β)

9.5.2 *Model equations*

ACh release, clearance, and activation of M2 muscarinic receptors. In these equations, I_{stim} is the impulse (Dirac delta function) corresponding to each stimulus.

$$M2^* = \left(\left[AChM \right]_{NJ} V_{NJ,ACh} + \left[AChM \right]_{EJS} V_{EJS} \right) / V_{cyto}$$

$$k_{hNJ} = \frac{v_{maxNJ,AChE}}{V_{NJ,ACh} \left(\left[ACh \right]_{NJ} + K_{app,AChE} \right)}$$

$$k_{hEJS} = \frac{v_{maxEJS,AChE}}{V_{EJS} \left(\left[ACh \right]_{EJS} + K_{app,AChE} \right)}$$

$$k_{onM,NJ} = \left(\left[ACh \right]_{NJ} / K_{MM} \right)^{n_M} k_{offM}$$

$$k_{onM,EJS} = \left(\left[ACh \right]_{EJS} / K_{MM} \right)^{n_M} k_{offM}$$

$$\frac{dN_{v,ACh}}{dt} = \frac{k_{hNJ} \left[ACh \right]_{NJ} V_{NJ,ACh} 6 \times 10^5}{Q_{ACh}} + \frac{N_{vMax,ACh} - N_{v,ACh}}{\tau_{ACh}} + U_{EJS} \frac{k_{hEJS} \left[ACh \right]_{EJS} V_{EJS} 6 \times 10^5}{Q_{ACh}} - \left\lfloor \frac{N_{v,ACh} k_r}{N_{var,ACh}} \right\rfloor N_{var,ACh} I_{stim}$$

$$\frac{d\left[ACh \right]_{NJ}}{dt} = \frac{Q_{ACh}}{6 \times 10^5 V_{NJ,ACh}} \left\lfloor \frac{N_{v,ACh} k_r}{N_{var,ACh}} \right\rfloor N_{var,ACh} I_{stim} + k_{dNJ,ACh} \left[ACh \right]_{EJS} + k_{offM} \left[AChM \right]_{NJ} - \left(k_{dNJ,ACh} + k_{hNJ} \right) \left[ACh \right]_{NJ} - k_{onM,NJ} \left(\left[M_t \right]_{NJ} - \left[AChM \right]_{NJ} \right)$$

$$\frac{d\left[AChM \right]_{NJ}}{dt} = k_{onM,NJ} \left(\left[M_t \right]_{NJ} - \left[AChM \right]_{NJ} \right) - k_{offM} \left[AChM \right]_{NJ}$$

$$\frac{d\left[ACh \right]_{EJS}}{dt} = \frac{k_{dNJ,ACh}}{V_{EJS} / V_{NJ,ACh}} \left[ACh \right]_{NJ} + k_{dEJS} \left[ACh \right]_{ECM} + k_{offM} \left[AChM \right]_{EJS} - \left(\frac{k_{dNJ,ACh}}{V_{EJS} / V_{NJ,ACh}} + k_{dEJS} + k_{hEJS} \right) \left[ACh \right]_{EJS} - k_{onM,EJS} \left(\left[M_t \right]_{EJS} - \left[AChM \right]_{EJS} \right)$$

$$\frac{d\left[AChM \right]_{EJS}}{dt} = k_{onM,EJS} \left(\left[M_t \right]_{EJS} - \left[AChM \right]_{EJS} \right) - k_{offM} \left[AChM \right]_{EJS}$$

$$\frac{d\left[ACh \right]_{ECM}}{dt} = \frac{k_{dEJS}}{V_{ECM} / V_{EJS}} \left[ACh \right]_{EJS} + k_{dECM} \left[ACh \right]_{BS} - \left(k_{dECM} + \frac{k_{dEJS}}{V_{ECM} / V_{EJS}} \right) \left[ACh \right]_{ECM}$$

$$\frac{dX}{dt} = \frac{M2^* - X}{\tau_X}$$

NE release, clearance, and activation of β-AR

$$\beta^* = \left(\left[NE\beta \right]_{NJ} V_{NJ,NE} + \left[NE\beta \right]_{EJS} V_{EJS} \right) / V_{cyto} \times \left(1 - I_{M^*,max} \frac{X^{nM^*}}{X^{nM^*} + K_{M^*}^{nM^*}} \right)$$

$$k_n = \frac{v_{maxn}}{V_{NJ,NE} \left(\left[NE \right]_{NJ} + K_{Dn} \right)}$$

$$k_{aNJ} = \frac{v_{maxNJ,a}}{V_{NJ,NE} \left(\left[NE \right]_{NJ} + K_{Da} \right)}$$

$$k_{aEJS} = \frac{v_{maxEJS,a}}{V_{EJS} \left(\left[NE \right]_{EJS} + K_{Da} \right)}$$

$$k_{on\beta,NJ} = \left(\left[NE \right]_{NJ} / K_{M\beta} \right)^{n_\beta} k_{off\beta}$$

$$k_{on\beta,EJS} = \left(\left[NE \right]_{EJS} / K_{M\beta} \right)^{n_\beta} k_{off\beta}$$

$$\frac{dN_{v,NE}}{dt} = \frac{N_{vMax,NE} - N_{v,NE}}{\tau_{NE}} + \frac{k_n \left[NE \right]_{NJ} V_{NJ,NE} 6 \times 10^5}{Q_{NE}} - \left\lfloor \frac{N_{v,NE} k_r}{N_{var,NE}} \right\rfloor N_{var,NE} I_{stim}$$

$$\frac{d\left[NE \right]_{NJ}}{dt} = \frac{Q_{NE}}{6 \times 10^5 V_{NJ,NE}} \left\lfloor \frac{N_{v,NE} k_r}{N_{var,NE}} \right\rfloor N_{var,NE} I_{stim} + k_{dNJ,NE} \left[NE \right]_{EJS} + k_{off\beta} \left[NE\beta \right]_{NJ}$$
$$- \left(k_{dNJ,NE} + k_n + k_{aNJ} \right) \left[NE \right]_{NJ} - k_{on\beta,NJ} \left(\left[\beta_t \right]_{NJ} - \left[NE\beta \right]_{NJ} \right)$$

$$\frac{d\left[NE\beta \right]_{NJ}}{dt} = k_{on\beta,NJ} \left(\left[\beta_t \right]_{NJ} - \left[NE\beta \right]_{NJ} \right) - k_{off\beta} \left[NE\beta \right]_{NJ}$$

$$\frac{d\left[NE \right]_{EJS}}{dt} = \frac{k_{dNJ,NE}}{V_{EJS} / V_{NJ,NE}} \left[NE \right]_{NJ} + k_{dEJS} \left[NE \right]_{ECM} + k_{off\beta} \left[NE\beta \right]_{EJS}$$
$$- \left(\frac{k_{dNJ,NE}}{V_{EJS} / V_{NJ,NE}} + k_{dEJS} + k_{aEJS} \right) \left[NE \right]_{EJS} - k_{on\beta,EJS} \left(\left[\beta_t \right]_{EJS} - \left[NE\beta \right]_{EJS} \right)$$

$$\frac{d\left[NE\beta \right]_{EJS}}{dt} = k_{on\beta,EJS} \left(\left[\beta_t \right]_{EJS} - \left[NE\beta \right]_{EJS} \right) - k_{off\beta} \left[NE\beta \right]_{EJS}$$

$$\frac{d\left[NE \right]_{ECM}}{dt} = \frac{k_{dEJS}}{V_{ECM} / V_{EJS}} \left[NE \right]_{EJS} + k_{dECM} \left[NE \right]_{BS} - \left(\frac{k_{dEJS}}{V_{ECM} / V_{EJS}} + k_{dECM} \right) \left[NE \right]_{ECM}$$

G-Protein activation, modulation of AC, and cAMP generation

Instantaneous relationships

$$v_{PDE} = v_{PDE,max}\left[cAMP\right]^{n_{PDE}} / \left(\left[cAMP\right]^{n_{PDE}} + K_{M,PDE}^{n_{PDE}}\right)$$

$$R_{\beta} = \left[\beta^{*}\right] v_{max,\beta} \frac{\left[G_{S\alpha\beta\gamma}GDP\right]}{\left[G_{S\alpha\beta\gamma}GDP\right] + K_{GS}} + \left(\beta_{T} - \left[\beta^{*}\right]\right) v_{max,\beta 0} \frac{\left[G_{S\alpha\beta\gamma}GDP\right]}{\left[G_{S\alpha\beta\gamma}GDP\right] + K_{GS0}}$$

$$R_{M} = \left[M2^{*}\right] v_{max,M} \frac{\left[G_{I\alpha\beta\gamma}GDP\right]}{\left[G_{I\alpha\beta\gamma}GDP\right] + K_{GI}}$$

$$\left[G_{S\alpha}GDP\right] = \left[G_{S}\right]_{T} - \left[G_{S\alpha\beta\gamma}GDP\right] - \left[G_{S\alpha\beta\gamma}GTP\right] - \left[G_{S\alpha}GTP\right]$$

$$\left[G_{I\alpha}GDP\right] = \left[G_{I}\right]_{T} - \left[G_{I\alpha\beta\gamma}GDP\right] - \left[G_{I\alpha\beta\gamma}GTP\right] - \left[G_{I\alpha}GTP\right]$$

$$\left[\beta\gamma\right]_{I} = \left[G_{I\alpha}GTP\right] + \left[G_{I\alpha}GDP\right]$$

$$\left[\beta\gamma\right] = \left[G_{S\alpha}GTP\right] + \left[G_{S\alpha}GDP\right] + \left[\beta\gamma\right]_{I}$$

$$k_{aSD} = k_{aSD,max} \frac{\left[\beta\gamma\right]}{\left[\beta\gamma\right] + K_{M,aSD}}$$

$$k_{aID} = \frac{k_{aID,max}}{1 + e^{-\left(\left[\beta\gamma\right] - K_{M,aID}\right)/s_{aID}}}$$

$$k_{aST} = k_{aST,max} \frac{\left[\beta\gamma\right]}{\left[\beta\gamma\right] + K_{M,aST}}$$

$$k_{dST} = k_{dST,max}\left(1 - \frac{\left[\beta\gamma\right]}{\left[\beta\gamma\right] + K_{M,dST}}\right)$$

$$AC^{*} = AC_{T} \frac{\left[G_{S\alpha}GTP\right]^{n_{SAC}}}{\left[G_{S\alpha}GTP\right]^{n_{SAC}} + K_{SAC}^{n_{SAC}}\left(1 + \frac{\left[G_{I\alpha}GTP\right]^{n_{IAC}}}{K_{IAC}^{n_{IAC}}}\right)}$$

$$AC^{-} = AC_{T} \frac{\left[G_{I\alpha}GTP\right]^{n_{IAC}}}{\left[G_{I\alpha}GTP\right]^{n_{IAC}} + K_{IAC}^{n_{IAC}}\left(1 + \frac{\left[G_{S\alpha}GTP\right]^{n_{SAC}}}{K_{SAC}^{n_{SAC}}}\right)}$$

$$AC = AC_{T} - AC^{*} - AC^{-}$$

$$v_{AC,Total} = v_{AC^{*}}\left[AC^{*}\right] + v_{AC}\left[AC\right] + v_{AC^{-}}\left[AC^{-}\right]$$

Differential equations

$$\frac{d\left[G_{S\alpha\beta\gamma}GDP\right]}{dt} = G_{sf}\left(k_{aSD}\left[G_{S\alpha}GDP\right] + k_{cat,Sb}\left[G_{S\alpha\beta\gamma}GTP\right] - k_{Sb}\left[G_{S\alpha\beta\gamma}GDP\right] - R_{\beta}\right)$$

$$\frac{d\left[G_{S\alpha\beta\gamma}GTP\right]}{dt} = G_{sf}\left(k_{Sb}\left[G_{S\alpha\beta\gamma}GDP\right] + k_{aST}\left[G_{S\alpha}GTP\right] - \left(k_{cat,Sb} + k_{dST}\right)\left[G_{S\alpha\beta\gamma}GTP\right]\right)$$

$$\frac{d\left[G_{S\alpha}GTP\right]}{dt} = G_{sf}\left(k_{dST}\left[G_{S\alpha\beta\gamma}GTP\right] + k_{Sf}\left[G_{S\alpha}GDP\right] + R_{\beta} - \left(k_{cat,Sf} + k_{aST}\right)\left[G_{S\alpha}GTP\right]\right)$$

$$\frac{d\left[G_{I\alpha\beta\gamma}GDP\right]}{dt} = G_{sf}\left(k_{aID}\left[G_{I\alpha}GDP\right] + k_{cat,Ib}\left[G_{I\alpha\beta\gamma}GTP\right] - k_{Ib}\left[G_{I\alpha\beta\gamma}GDP\right] - R_{M}\right)$$

$$\frac{d\left[G_{I\alpha\beta\gamma}GTP\right]}{dt} = G_{sf}\left(k_{Ib}\left[G_{I\alpha\beta\gamma}GDP\right] + k_{aIT}\left[G_{I\alpha}GTP\right] - \left(k_{cat,Ib} + k_{dIT}\right)\left[G_{I\alpha\beta\gamma}GTP\right]\right)$$

$$\frac{d\left[G_{I\alpha}GTP\right]}{dt} = G_{sf}\left(k_{dIT}\left[G_{I\alpha\beta\gamma}GTP\right] + k_{If}\left[G_{I\alpha}GDP\right] + R_{M} - \left(k_{cat,If} + k_{aIT}\right)\left[G_{I\alpha}GTP\right]\right)$$

$$\frac{d\left[cAMP\right]}{dt} = cAMP_{sf}\left(v_{AC,Total} - v_{PDE}\right)$$

The βγ equations above ignore the subunits that may be involved in the hypothesized intermediate states, for simplicity. Otherwise, the βγ concentration is the solution to the following implicit form that arises because of the hypothesized $G_{S\alpha(\beta\gamma)(\beta\gamma)}GTP$ state shown in Figure 52. The implicit equation and solution are:

$$[\beta\gamma] = \left(\begin{array}{l}\left[G_S\right]_T + \left[G_I\right]_T - \left[G_{S\alpha\beta\gamma}GDP\right] - \left(1 + \dfrac{[\beta\gamma]}{[\beta\gamma] + K_{M,dST}}\right)\left[G_{S\alpha\beta\gamma}GTP\right] \\ -\left[G_{I\alpha\beta\gamma}GDP\right] - \left[G_{I\alpha\beta\gamma}GTP\right]\end{array}\right)$$

$$X = \left[G_S\right]_T + \left[G_I\right]_T - \left[G_{S\alpha\beta\gamma}GDP\right] - \left[G_{S\alpha\beta\gamma}GTP\right] - \left[G_{I\alpha\beta\gamma}GDP\right] - \left[G_{I\alpha\beta\gamma}GTP\right]$$

$$a = 1, \quad b = K_{M,dST} - X + \left[G_{S\alpha\beta\gamma}GTP\right], \quad c = -K_{M,dST}X$$

$$[\beta\gamma] = \frac{-b + \sqrt{b^2 - 4ac}}{2a}$$

$[G_{S\alpha}GDP]$ and $[G_{I\alpha}GDP]$ are not expressed as differential equations but rather reflect conservation of G-protein. These functions were chosen to ensure that numerical errors do not lead to drift in the abundance of G_S and G_I.

cAMP-mediated I_f shift $I_{f,ShiftC}$

$$I_{f,ShiftC} = s_{max}\left[cAMP\right]^{n_f} / \left(\left[cAMP\right]^{n_f} + K_{0.5,f}^{n_f}\right)$$

PKA

$$I_{f,ShiftP,SS} = a_{0S} + a_{1S}\frac{C^{n_{1S}}}{C^{n_{1S}} + K_{1S}^{n_{1S}}} + a_{2S}\frac{C^{n_{2S}}}{C^{n_{2S}} + K_{2S}^{n_{2S}}}$$

$$R_{gCaL,SS} = a_{0C} + a_{1C}\frac{C^{n_{1C}}}{C^{n_{1C}} + K_{1C}^{n_{1C}}} + a_{2C}\frac{C^{n_{2C}}}{C^{n_{2C}} + K_{2C}^{n_{2C}}}$$

$$R_{Pup,SS} = a_{0P} + a_{1P}\frac{C^{n_{1P}}}{C^{n_{1P}} + K_{1P}^{n_{1P}}} + a_{2P}\frac{C^{n_{2P}}}{C^{n_{2P}} + K_{2P}^{n_{2P}}}$$

$$R_{gKr,SS} = a_{0K} + a_{1K}\frac{C^{n_{1K}}}{C^{n_{1K}} + K_{1K}^{n_{1K}}} + a_{2K}\frac{C^{n_{2K}}}{C^{n_{2K}} + K_{2K}^{n_{2K}}}$$

$$pa_{sf,SS} = a_{0p} + a_{1p}\frac{C^{n_{1p}}}{C^{n_{1p}} + K_{1p}^{n_{1p}}} + a_{2p}\frac{C^{n_{2p}}}{C^{n_{2p}} + K_{2p}^{n_{2p}}} + a_{3p}\frac{C^{n_{3p}}}{C^{n_{3p}} + K_{3p}^{n_{3p}}}$$

$$\frac{dC}{dt} = C_{sf}\left(\left(2R_{2T} - C\right)\frac{x}{K_a}\left[cAMP\right] - xC\right)$$

$$\frac{dI_{f,ShiftP}}{dt} = \left(I_{f,ShiftP,SS} - I_{f,ShiftP}\right)/\tau_P$$

$$\frac{dR_{gCa,L}}{dt} = \left(R_{gCaL,SS} - R_{gCa,L}\right)/\tau_P$$

$$\frac{dR_{Pup}}{dt} = \left(R_{Pup,SS} - R_{Pup}\right)/\tau_P$$

$$\frac{dR_{gKr}}{dt} = \left(R_{gKr,SS} - R_{gKr}\right)/\tau_P$$

$$\frac{d\,pa_{sf}}{dt} = \left(pa_{sf,SS} - pa_{sf}\right)/\tau_P$$

Integration with Maltsev SANC model

$$g_{Ca,L,new} = R_{gCa,L}g_{Ca,L}$$

$$I_{f,Shift} = I_{f,ShiftC} + I_{f,ShiftP}$$

$$V_{If,1/2} = V_{If,1/2,basal} + I_{f,Shift}$$

$$P_{up,new} = R_{Pup}P_{up}$$

$$g_{Kr,new} = R_{gKr}g_{Kr}$$

The rest of the Maltsev and Lakatta equations are as specified in the supplement to (227). Note that the differential equations in the original paper are /ms, whereas our equations are /s. For consistency with the original model, we multiply all the Maltsev and Lakatta differential equations by 1000 to convert the time to /s rather than changing each rate or time constant individually. This allows for easier comparison against the original equations to ensure proper implementation.

L-Type Ca^{2+} current ($I_{Ca,L}$):

$$I_{Ca,L} = C_m g_{Ca,L,new}\left(V_m - E_{Ca,L}\right) d_L f_L f_{Ca}$$

$$d_{L,\infty} = 1/\left(1 + e^{-(V_m+13.5)/6}\right)$$

$$f_{L,\infty} = 1/\left(1 + e^{(V_m+35)/7.3}\right)$$

$$\alpha_{dL} = -0.02839\left(V_m + 35\right)/\left(e^{-(V_m+35)/2.5} - 1\right) - 0.0849 V_m/\left(e^{-V_m/4.8} - 1\right)$$

$$\beta_{dL} = 0.01143\left(V_m - 5\right)/\left(e^{(V_m-5)/2.5} - 1\right)$$

$$\tau_{dL} = 1/\left(\alpha_{dL} + \beta_{dL}\right)$$

$$\tau_{fL} = 257.1 e^{-\left((V_m+32.5)/13.9\right)^2} + 44.3$$

$$f_{Ca,\infty} = K_{mfCa}/\left(K_{mfCa} + Ca_{sub}\right)$$

$$\tau_{fCa} = f_{Ca,\infty}/\alpha_{fCa}$$

$$\frac{dd_L}{dt} = 1000 \times \left(d_{L,\infty} - d_L\right)/\tau_{dL}$$

$$\frac{df_L}{dt} = 1000 \times \left(f_{L,\infty} - f_L\right)/\tau_{fL}$$

$$\frac{df_{Ca}}{dt} = 1000 \times \left(f_{Ca,\infty} - f_{Ca}\right)/\tau_{fCa}$$

T-type Ca^{2+} current ($I_{Ca,T}$)

$$I_{Ca,T} = C_m g_{Ca,T}\left(V_m - E_{Ca,T}\right) d_T f_T$$

$$d_{T,\infty} = 1/\left(1 + e^{-(V_m+26.3)/6}\right)$$

$$f_{T,\infty} = 1/\left(1 + e^{(V_m+61.7)/5.6}\right)$$

$$\tau_{dT} = 1/\left(1.068 e^{(V_m+26.3)/30} + 1.068 e^{-(V_m+26.3)/30}\right)$$

$$\tau_{fT} = 1/\left(0.0153 e^{-(V_m+61.7)/83.3} + 0.015 e^{(V_m+61.7)/15.38}\right)$$

$$\frac{dd_T}{dt} = 1000 \times \left(d_{T,\infty} - d_T\right)/\tau_{dT}$$

$$\frac{df_T}{dt} = 1000 \times \left(f_{T,\infty} - f_T\right)/\tau_{fT}$$

Rapidly activating delayed rectifier K^+ current (I_{Kr})

$$I_{Kr} = C_m g_{Kr,new}\left(V_m - E_K\right)\left(0.6p_{aF} + 0.4p_{aS}\right)p_i$$

$$p_{a,\infty} = 1/\left(1+e^{-(V_m+23.2)/10.6}\right)$$

$$p_{i,\infty} = 1/\left(1+e^{(V_m+28.6)/17.1}\right)$$

$$\tau_{paF} = 0.84655354/\left(0.0372e^{V_m/15.9} + 0.00096e^{-V_m/22.5}\right)$$

$$\tau_{paS} = 0.84655354/\left(0.0042e^{V_m/17} + 0.00015e^{-V_m/21.6}\right)$$

$$\tau_{pi} = 1/\left(0.1e^{-V_m/54.645} + 0.656e^{V_m/106.157}\right)$$

$$\frac{dp_{aF}}{dt} = pa_{sf}\times 1000\times\left(p_{a,\infty} - p_{aF}\right)/\tau_{paF}$$

$$\frac{dp_{aS}}{dt} = pa_{sf}\times 1000\times\left(p_{a,\infty} - p_{aS}\right)/\tau_{paS}$$

$$\frac{dp_i}{dt} = 1000\times\left(p_{i,\infty} - p_i\right)/\tau_{pi}$$

Slowly activating delayed rectifier K^+ current (I_{Ks})

$$I_{Ks} = C_m g_{Ks}\left(V_m - E_{Ks}\right)n^2$$

$$\alpha_n = 0.014/\left(1+e^{-(V_m-40)/9}\right)$$

$$\beta_n = 0.001/\left(1+e^{-V_m/45}\right)$$

$$n_\infty = \alpha_n/\left(\alpha_n+\beta_n\right)$$

$$\tau_n = 1/\left(\alpha_n+\beta_n\right)$$

$$\frac{dn}{dt} = 1000\times\left(n_\infty - n\right)/\tau_n$$

4-aminopyridine-sensitive currents (I_{to} and I_{sus})

$$I_{to} = C_m g_{to}\left(V_m - E_K\right)qr$$

$$I_{sus} = C_m g_{sus}\left(V_m - E_K\right)r$$

$$q_\infty = 1/\left(1+e^{(V_m+49)/13}\right)$$

$$r_\infty = 1/\left(1+e^{-(V_m-19.3)/15}\right)$$

$$\tau_q = 39.102/\left(0.57e^{-0.08(V_m+44)} + 0.065e^{0.1(V_m+45.93)}\right) + 6.06$$

$$\tau_r = 14.40516/\left(1.037e^{0.09(V_m+30.61)} + 0.369e^{-0.12(V_m+23.84)}\right) + 2.75352$$

$$\frac{dq}{dt} = 1000\times\left(q_\infty - q\right)/\tau_q$$

$$\frac{dr}{dt} = 1000\times\left(r_\infty - r\right)/\tau_r$$

Hyperpolarization-activated, "funny" current

$$I_{fNa} = C_m 0.3833 g_{lf} \left(V_m - E_{Na}\right) y^2$$
$$I_{fK} = C_m 0.6167 g_{lf} \left(V_m - E_K\right) y^2$$
$$I_f = I_{fNa} + I_{fK}$$
$$y_\infty = 1 / \left(1 + e^{\left(V_m - V_{lf,1/2}\right)/13.5}\right)$$
$$\tau_y = 0.7166529 / \left(e^{-(V_m + 386.9)/45.302} + e^{(V_m - 73.08)/19.231}\right)$$
$$\frac{dy}{dt} = 1000 \times \left(y_\infty - y\right) / \tau_y$$

Sustained inward current (I_{st})

$$I_{st} = C_m g_{st} \left(V_m - E_{st}\right) q_a q_i$$
$$q_{a,\infty} = 1 / \left(1 + e^{-(V_m + 57)/5}\right)$$
$$\alpha_{qa} = 1 / \left(0.15 e^{-V_m/11} + 0.2 e^{-V_m/700}\right)$$
$$\beta_{qa} = 1 / \left(16 e^{V_m/8} + 15 e^{V_m/50}\right)$$
$$\tau_{qa} = 1 / \left(\alpha_{qa} + \beta_{qa}\right)$$
$$\alpha_{qi} = 1 / \left(3100 e^{V_m/13} + 700 e^{V_m/70}\right)$$
$$\beta_{qi} = 1 / \left(95 e^{-V_m/10} + 50 e^{-V_m/700}\right) + 0.000229 / \left(1 + e^{-V_m/5}\right)$$
$$\tau_{qi} = 6.65 / \left(\alpha_{qi} + \beta_{qi}\right)$$
$$q_{i,\infty} = \alpha_{qi} / \left(\alpha_{qi} + \beta_{qi}\right)$$
$$\frac{dq_a}{dt} = 1000 \times \left(q_{a,\infty} - q_a\right) / \tau_{qa}$$
$$\frac{dq_i}{dt} = 1000 \times \left(q_{i,\infty} - q_i\right) / \tau_{qi}$$

Na^+-dependent background current (I_{bNa})

$$I_{bNa} = C_m g_{bNa} \left(V_m - E_{Na}\right)$$

Na^+/K^+ pump current (I_{NaK})

$$I_{NaK} = C_m I_{NaK,max} / \left(\left(1 + \left(K_{mKp} / K_o\right)^{1.2}\right)\left(1 + \left(K_{mNap} / Na_i\right)^{1.3}\right)\left(1 + e^{-(V_m - E_{Na} + 120)/30}\right)\right)$$

Ca^{2+}-dependent background current (I_{bCa})

$$I_{bCa} = C_m g_{bCa} \left(V_m - E_{Ca,L}\right)$$

Na^+/Ca^{2+} exchanger current (I_{NCX})

$$d_o = 1 + \left(Ca_o / K_{co}\right)\left(1 + e^{Q_{co}V_m/E_T}\right) + \left(Na_o / K_{1no}\right)\left(1 + \left(Na_o / K_{2no}\right)\left(1 + Na_o / K_{3no}\right)\right)$$

$$k_{43} = Na_i / \left(K_{3ni} + Na_i\right)$$

$$k_{41} = e^{-Q_n V_m/(2E_T)}$$

$$k_{34} = Na_o / \left(K_{3no} + Na_o\right)$$

$$k_{21} = \left(Ca_o / K_{co}\right) e^{Q_{co}V_m/E_T} / d_o$$

$$k_{23} = \left(Na_o / K_{1no}\right)\left(Na_o / K_{2no}\right)\left(1 + Na_o / K_{3no}\right) e^{-Q_n V_m/(2E_T)} / d_o$$

$$k_{32} = e^{Q_n V_m (2E_T)}$$

$$x_1 = k_{34}k_{41}\left(k_{23} + k_{21}\right) + k_{21}k_{32}\left(k_{43} + k_{41}\right)$$

$$d_i = 1 + \left(Ca_{sub} / K_{ci}\right)\left(1 + e^{-Q_{ci}V_m/E_T} + Na_i / K_{cni}\right) + \left(Na_i / K_{1ni}\right)\left(1 + \left(Na_i / K_{2ni}\right)\left(1 + Na_i / K_{3ni}\right)\right)$$

$$k_{12} = \left(Ca_{sub} / K_{ci}\right) e^{-Q_{ci}V_m/E_T} / d_i$$

$$k_{14} = \left(Na_i / K_{1ni}\right)\left(Na_i / K_{2ni}\right)\left(1 + Na_i / K_{3ni}\right) e^{Q_n V_m/(2E_T)} / d_i$$

$$x_2 = k_{43}k_{32}\left(k_{14} + k_{12}\right) + k_{41}k_{12}\left(k_{34} + k_{32}\right)$$

$$x_3 = k_{43}k_{14}\left(k_{23} + k_{21}\right) + k_{12}k_{23}\left(k_{43} + k_{41}\right)$$

$$x_4 = k_{34}k_{23}\left(k_{14} + k_{12}\right) + k_{21}k_{14}\left(k_{34} + k_{32}\right)$$

$$I_{NCX} = C_m k_{NCX}\left(k_{21}x_2 - k_{12}x_1\right) / \left(x_1 + x_2 + x_3 + x_4\right)$$

Acetylcholine-activated K^+ current ($I_{K,ACh}$)

$$I_{K,ACh} = C_m a_{gate} g_{KACh,max}\left(V_m - E_K\right)$$

$$\beta_\infty = 0.001 \times 12.32 \times a_{IKACh} \frac{\left([\beta\gamma]_I\right)^{n_{IKACh}}}{\left([\beta\gamma]_I\right)^{n_{IKACh}} + K_{d,IKACh}^{n_{IKACh}}}$$ *** different from Maltsev equation**

$$\beta_\tau = \beta_{\tau a} / \left([\beta\gamma]_I\right)^{n_{IKACh}}$$ *** different from Maltsev equation**

$$\frac{d\beta}{dt} = \frac{\beta_\infty - \beta}{\beta_\tau}$$ *** different from Maltsev equation**

$$\alpha = 0.001 \times 17 e^{0.0133(V_m + 40)}$$

$$a_{gate,\infty} = \beta / \left(\alpha + \beta\right)$$

$$\tau_{a,gate} = 1 / \left(\alpha + \beta\right)$$

$$\frac{da_{gate}}{dt} = \frac{a_{gate,\infty} - a_{gate}}{\tau_{a,gate}}$$

Ca^{2+} release flux ($j_{SRCarel}$) from SR via RyRs

$$j_{SRCarel} = k_s O\left(Ca_{jSR} - Ca_{sub}\right)$$

$$k_{CaSR} = MaxSR - \left(MaxSR - MinSR\right) / \left(1 + \left(EC_{50\_SR} / Ca_{jSR}\right)^{HSR}\right)$$

$$k_{oSRCa} = k_{oCa} / k_{CaSR}$$

$$k_{iSRCa} = k_{iCa} k_{CaSR}$$

$$\frac{dR}{dt} = 1000 \times \left(\left(k_{im} RI - k_{iSRCa} Ca_{sub} R\right) - \left(k_{oSRCa} Ca_{sub}^2 R - k_{om} O\right)\right)$$

$$\frac{dO}{dt} = 1000 \times \left(\left(k_{oSRCa} Ca_{sub}^2 R - k_{om} O\right) - \left(k_{iSRCa} Ca_{sub} O - k_{im} I\right)\right)$$

$$\frac{dI}{dt} = 1000 \times \left(\left(k_{iSRCa} Ca_{sub} O - k_{im} I\right) - \left(k_{om} I - k_{oSRCa} Ca_{sub}^2 RI\right)\right)$$

$$\frac{dRI}{dt} = 1000 \times \left(\left(k_{om} I - k_{oSRCa} Ca_{sub}^2 RI\right) - \left(k_{im} RI - k_{iSRCa} Ca_{sub} R\right)\right)$$

Ca^{2+} diffusion flux (j_{Ca_dif})

$$j_{Ca\_dif} = \left(Ca_{sub} - Ca_i\right) / \tau_{difCa}$$

The rate of Ca^{2+} uptake (j_{up}) by pumping into the SR

$$j_{up} = P_{up,new} / \left(1 + K_{up} / Ca_i\right)$$

Ca^{2+} flux between network and junctional SR compartments (j_{tr})

$$j_{tr} = \left(Ca_{nSR} - Ca_{jSR}\right) / \tau_{tr}$$

Ca^{2+} buffering

$$\frac{df_{TC}}{dt} = 1000 \times \left(k_{fTC} Ca_i \left(1 - f_{TC}\right) - k_{bTC} f_{TC}\right)$$

$$\frac{df_{TMC}}{dt} = 1000 \times \left(k_{fTMC} Ca_i \left(1 - f_{TMC} - f_{TMM}\right) - k_{bTMC} f_{TMC}\right)$$

$$\frac{df_{TMM}}{dt} = 1000 \times \left(k_{fTMM} Mg_i \left(1 - f_{TMC} - f_{TMM}\right) - k_{bTMM} f_{TMM}\right)$$

$$\frac{df_{CMi}}{dt} = 1000 \times \left(k_{fCM} Ca_i \left(1 - f_{CMi}\right) - k_{bCM} f_{CMi}\right)$$

$$\frac{df_{CMs}}{dt} = 1000 \times \left(k_{fCM} Ca_{sub} \left(1 - f_{CMs}\right) - k_{bCM} f_{CMs}\right)$$

$$\frac{df_{CQ}}{dt} = 1000 \times \left(k_{fCQ} Ca_{jSR} \left(1 - f_{CQ}\right) - k_{bCQ} f_{CQ}\right)$$

Dynamics of Ca^{2+} concentrations in cell compartments. The derivatives that appear in these equations are divided by 1000 to convert back to original Maltsev units of /ms, and the whole expression is then scaled back to /s)

$$\frac{dCa_i}{dt} = 1000 \times \left(\left(j_{Ca\_dif} V_{sub} - j_{up} V_{nSR} \right) / V_i - \left(CM_{tot} \frac{df_{CMi}}{dt} / 1000 + TC_{tot} \frac{df_{TC}}{dt} / 1000 + TMC_{tot} \frac{df_{TMC}}{dt} / 1000 \right) \right)$$

$$\frac{dCa_{sub}}{dt} = 1000 \times \left(j_{SRCarel} V_{jSR} / V_{sub} - \left(I_{Ca,L} + I_{Ca,T} + I_{bCa} - 2I_{NCX} \right) / \left(2FV_{sub} \right) - \left(j_{Ca\_dif} + CM_{tot} \frac{df_{CMs}}{dt} / 1000 \right) \right)$$

$$\frac{dCa_{jSR}}{dt} = 1000 \times \left(j_{tr} - j_{SRCarel} - CQ_{tot} \frac{df_{CQ}}{dt} / 1000 \right)$$

$$\frac{dCa_{nSR}}{dt} = 1000 \times \left(j_{up} - j_{tr} V_{jSR} / V_{nSR} \right)$$

Transmembrane voltage (V_m)

$$\frac{dV_m}{dt} = -1000 \times \left(I_{Ca,L} + I_{Ca,T} + I_f + I_{st} + I_{Kr} + I_{Ks} + I_{to} + I_{sus} + I_{NaK} + I_{NCX} + I_{bCa} + I_{bNa} + I_{K,ACh} \right) / C_m$$

9.5.3 *Parameter values and descriptions*

Table 22. Model parameters

Parameter	Value	Units	Description
$[ACh]_{BS}$	3 E-6	mM	ACh concentration in the blood stream
$[G_I]_T$	0.01	mM	Total concentration of GI in cytosol
$[G_S]_T$	2 E-3	mM	Total concentration of G_S in cytosol
$[M_t]_{EJS}$	4.4 E-4	mM	Total M2 muscarinic receptor concentration in the EJS
$[M_t]_{NJ}$	0.010	mM	Total M2 muscarinic receptor concentration in the cholinergic NJ
$[NE]_{BS}$	3 E-6	mM	NE concentration in the blood stream
$[\beta_t]_{EJS}$	2 E-4	mM	Total β-adrenergic receptor concentration in the EJS
$[\beta_t]_{NJ}$	0.024	mM	Total β-adrenergic receptor concentration in the NJ
a_{0C}	-7.59	unitless	Offset for R_{gCaL} function
a_{0K}	0.8	unitless	Offset for R_{gKr} function
a_{0P}	0.319	unitless	Offset for R_{Pup} function
a_{0p}	0.05	unitless	Offset for pa_{sf} function
a_{0S}	-15.7	unitless	Offset for $I_{f,ShiftP}$ function
a_{1C}	8.56	unitless	Amplitude 1 for R_{gCaL} function
a_{1K}	0.167	unitless	Amplitude 1 for R_{gKr} function
a_{1P}	0.72	unitless	Amplitude 1 for R_{Pup} function
a_{1p}	0.5476	unitless	Amplitude 1 for pa_{sf} function
a_{1S}	5.78	unitless	Amplitude 1 for $I_{f,ShiftP}$ function
a_{2C}	0.75	unitless	Amplitude 2 for R_{gCaL} function
a_{2K}	0.79	unitless	Amplitude 2 for R_{gKr} function
a_{2P}	2.83	unitless	Amplitude 2 for R_{Pup} function
a_{2p}	0.776	unitless	Amplitude 2 for pa_{sf} function
a_{2S}	28.25	unitless	Amplitude 2 for $I_{f,ShiftP}$ function
a_{3p}	3.4	unitless	Amplitude 3 for pa_{sf} function
AC_T	6.25 E-6	mM	Total concentration of AC in cytosol
a_{IKACh}	1.47	unitless	Amplitude scale for maximum β rate
$cAMP_{sf}$	10	unitless	Factor by which the cAMP reactions are accelerated
C_{sf}	100	unitless	Factor by which the activation of C is accelerated
G_{sf}	20	unitless	Factor by which the G-protein reactions are accelerated
$I_{M^*,max}$	0.9	unitless	Maximum inhibition of β-adrenergic activity by direct pathway (X)
K_{1C}	0.00000186	mM	Michaelis-Menten coefficient 1 for R_{gCaL} function
K_{1K}	0.000288	mM	Michaelis-Menten coefficient 1 for R_{gKr} function
K_{1P}	0.0002	mM	Michaelis-Menten-coefficient 1 for R_{Pup} function
K_{1p}	0.000172	mM	Michaelis-Menten coefficient 1 for pa_{sf} function
K_{1S}	0.0003	mM	Michaelis-Menten coefficient 1 for $I_{f,ShiftP}$ function

K_{2C}	0.000657	mM	Michaelis-Menten coefficient 2 for R_{gCaL} function
K_{2K}	0.000573	mM	Michaelis-Menten coefficient 2 for R_{gKr} function
K_{2P}	0.0006	mM	Michaelis-Menten coefficient 2 for R_{Pup} function
K_{2p}	0.000379	mM	Michaelis-Menten-coefficient 2 for pa_{sf} function
K_{2S}	0.001	mM	Michaelis-Menten coefficient 2 for $I_{f,ShiftP}$ function
K_{3p}	0.000578	mM	Michaelis-Menten coefficient 3 for pa_{sf} function
K_a	0.005	mM	cAMP concentration that causes half-maximal activation of PKA
$k_{aID,max}$	0.367	/sec	Maximum rate of association for $G_{I\alpha}$GDP with βγ
k_{aIT}	0	/sec	Maximum rate of association for $G_{I\alpha}$GTP with βγ
$K_{app,AChE}$	0.10	mM	Apparent Michaelis-Menten coefficient for AChE
$k_{aSD,max}$	0.0617	/sec	Maximum rate of association for $G_{S\alpha}$GDP with βγ
$k_{aST,max}$	3.33 E-4	/sec	Maximum rate of association for $G_{S\alpha}$GTP with βγ
$k_{cat,Ib}$	0.167	/sec	GTPase rate constant of $G_{I\alpha\beta\gamma}$
$k_{cat,If}$	0.167	/sec	GTPase rate of free $G_{I\alpha}$
$k_{cat,Sb}$	0.167	/sec	GTPase rate constant of $G_{S\alpha\beta\gamma}$
$k_{cat,Sf}$	0.167	/sec	GTPase rate constant of free $G_{S\alpha}$
$K_{d,IKACh}$	0.001097	mM	Dissociation constant for $\beta\gamma_I$ and $I_{K,ACh}$
K_{Da}	0.252	mM	Michaelis-Menten coefficient for cellular absorption of NE
k_{dECM}	0.4	/s	Rate constant for diffusion between the ECM and blood stream
k_{dEJS}	20	/s	Rate constant for diffusion between the EJS and ECM
k_{dIT}	0.0167	/sec	Maximum rate constant of dissociation for $G_{I\alpha\beta\gamma}$GTP into $G_{I\alpha}$GTP and βγ
K_{Dn}	0.00027	mM	Michaelis-Menten coefficient for neuronal reuptake of NE
$k_{dNJ,ACh}$	7800	/s	Rate constant for diffusion between the cholinergic NJ and EJS
$k_{dNJ,NE}$	8800	/s	Rate constant for diffusion between the adrenergic NJ and EJS
$k_{dST,max}$	3.83 E-3	/sec	Maximum rate of dissociation for $G_{S\alpha\beta\gamma}$GTP into $G_{S\alpha}$GTP and βγ
K_{GI}	0.03	mM	Michaelis-Menten coefficient for liganded M2 muscarinic receptor and $G_{I\alpha\beta\gamma}$GDP
K_{GS}	6 E-3	mM	Michaelis-Menten coefficient for liganded β-adrenergic receptor and $G_{S\alpha\beta\gamma}$GDP
K_{GS0}	0.026	mM	Michaelis-Menten coefficient for unliganded beta adrenergic receptor and $G_{S\alpha\beta\gamma}$GDP
K_{IAC}	2.14 E-4	mM	Dissociation constant for $G_{I\alpha}$GTP and AC
k_{Ib}	6.67 E-3	/sec	GDP dissociation rate constant for $G_{I\alpha\beta\gamma}$
k_{If}	1.67 E-3	/sec	GDP dissociation rate constant for free $G_{I\alpha}$
K_{M*}	2 E-5	mM	Michaelis-Menten coefficient for direct inhibition of β-adrenergic activity by direct pathway (X)
$K_{M,aID}$	2.76 E-4	mM	Michaelis-Menten coefficient for association of $G_{I\alpha}$GDP with βγ
$K_{M,aSD}$	3 E-5	mM	Michaelis-Menten coefficient for association of $G_{S\alpha}$GDP with

			βγ
$K_{M,aST}$	1 E-4	mM	Michaelis-Menten coefficient for association of $G_{S\alpha}GTP$ with βγ
$K_{M,dST}$	6 E-5	mM	Michaelis-Menten coefficient for binding of $G_{S\alpha\beta\gamma}GTP$ with another βγ (slows down dissociation rate)
$K_{M,PDE}$	0.00695	mM	Michaelis-Menten coefficient for hydrolysis of cAMP by PDE
K_{MM}	0.0003	mM	Michaelis-Menten coefficient for M2 muscarinic receptor and ACh
$K_{M\beta}$	0.0015	mM	Michaelis-Menten coefficient for β-adrenergic receptor and NE
k_{offM}	2100	/s	Dissociation rate constant for ACh bound to M2 muscarinic receptor
$k_{off\beta}$	0.15	/s	Dissociation rate constant for NE bound to β-adrenergic receptors
k_r	0.01	unitless	Fraction of available vesicles that are released per stimulus
K_{SAC}	4.59 E-5	mM	Dissociation constant for $G_{S\alpha}GTP$ and AC
k_{Sb}	6.67 E-3	/sec	GDP dissociation rate constant for $G_{S\alpha\beta\gamma}$
k_{Sf}	0.0267	/sec	GDP dissociation rate for free $G_{S\alpha}$
n_{1C}	1.57	unitless	Hill coefficient 1 for R_{gCaL} function
n_{1K}	9.64	unitless	Hill coefficient 1 for R_{gKr} function
n_{1P}	3.67	unitless	Hill coefficient 1 for R_{Pup} function
n_{1p}	5.11	unitless	Hill coefficient 1 for pa_{sf} function
n_{1S}	10.27	unitless	Hill coefficient 1 for $I_{f,ShiftP}$ function
n_{2C}	5.437	unitless	Hill coefficient 2 for R_{gCaL} function
n_{2K}	7.06	unitless	Hill coefficient 2 for R_{gKr} function
n_{2P}	9.86	unitless	Hill coefficient 2 for R_{Pup} function
n_{2p}	16.57	unitless	Hill coefficient 2 for pa_{sf} function
n_{2S}	4.1	unitless	Hill coefficient 2 for $I_{f,ShiftP}$ function
n_{3p}	9.294	unitless	Hill coefficient 3 for pa_{sf} function
n_{IAC}	1.74		Hill coefficient for $G_{I\alpha}GTP$ and AC
n_{IKACh}	3	unitless	Hill coefficient for $\beta\gamma_I$ and $I_{K,ACh}$
n_M	0.7	unitless	Hill Coefficient for M2 muscarinic receptor and ACh
n_{M*}	16	unitless	Hill coefficient for direct inhibition of β-adrenergic activity by direct pathway (X)
n_{PDE}	0.9	unitless	Hill coefficient for cAMP hydrolysis by PDE
n_{SAC}	1		Hill coefficient for $G_{S\alpha}GTP$ and AC
$N_{var,ACh}$	13.5	unitless	Number of cholinergic varicosities per cell
$N_{var,NE}$	4.5	number	Number of adrenergic varicosities per cell
$N_{vMax,ACh}$	6075	number	Maximum number of ACh-containing vesicles in all cholinergic varicosities
$N_{vMax,NE}$	675	number	Maximum number of NE-containing vesicles in all adrenergic varicosities
n_β	0.7	unitless	Hill Coefficient for β-adrenergic receptor and NE

Q_{ACh}	5000	molecules	Number of ACh molecules in a cholinergic vesicle
Q_{NE}	20000	molecules	Number of NE molecules in an adrenergic vesicle
R_{2T}	0.0005	mM	Total concentration of R2 subunit concentration (equivalently, one half of maximal C concentration)
s_{aID}	4 E-5	mM	slope factor for logistic function for association of $G_{I\alpha}GDP$ with $\beta\gamma$
U_{EJS}	0.5	unitless	Fraction of Ch hydrolyzed in EJS that is restored to varicosity
v_{AC}	1	/sec	Baseline rate of cAMP production by AC
v_{AC-}	0.5	/sec	Rate constant of cAMP production for inhibited ($G_{I\alpha}GTP$-bound) AC
v_{AC*}	100	/sec	Rate constant of cAMP production for activated ($G_{S\alpha}GTP$-bound) AC
V_{cyto}	1600	fL	Volume of cytosol inside sinoatrial node cell
V_{ECM}	2800	fL	Volume of ECM
V_{EJS}	173	fL	Volume of EJS
$v_{max,M}$	10	/sec	Maximum activation velocity of GI by liganded M2 muscarinic receptor
$v_{max,\beta}$	10	/sec	Maximum activation velocity of G_S by liganded β-adrenergic receptor
$v_{max,\beta 0}$	1.54	/sec	Maximum activation velocity of G_S by unliganded beta adrenergic receptor
$v_{maxEJS,a}$	115.566	amol/s	Maximum velocity of cellular absorption of NE from the EJS
$v_{maxEJS,AChE}$	1014	amol/s	Maximum AChE velocity in the EJS
v_{maxn}	18.7	amol/s	Maximum velocity of neuronal reuptake of NE per cell
$v_{maxNJ,a}$	0.374	amol/s	Maximum velocity of cellular absorption of NE from the NJ (all varicosities together)
$v_{maxNJ,AChE}$	525	amol/s	Maximum AChE velocity in the NJ (all varicosities together)
$V_{NJ,ACh}$	4	fL	Total volume of cholinergic NJ
$V_{NJ,NE}$	0.9	fL	Total volume of adrenergic NJ
$v_{PDE,max}$	0.0008	mM/sec	Maximum cAMP hydrolysis rate constant by PDE
x	0.00333	/sec	Rate of PKA catalytic+regulatory subunit reassociation
β_T	3.57 E-5	mM	Total β-adrenergic receptor concentration in the cytosol
$\beta_{\tau a}$	6 E-9	ms mM^3	Scale for β time constant
τ_{ACh}	5	s	Time constant for ACh synthesis in cholinergic nerves
τ_{NE}	30	s	Time constant for synthesis of NE in sympathetic nerves
τ_P	1	sec	Time constant for phosphorylation by C
τ_X	3	s	Time constant by which X lags M2*
			Maltsev model parameters:
Ca_o	2	mM	Extracellular Ca^{2+} concentration
K_o	5.4	mM	Extracellular K^+ concentration
Na_o	140	mM	Extracellular Na^+ concentration
Na_i	10	mM	Intracellular Na^+ concentration
Mg_i	2.5	mM	Intracellular Mg^{2+} concentration
C_m	32	pF	Cell membrane electric capacitance

V_{sub}	0.0351	pL	Volume of submembrane space
V_{jSR}	0.0042	pL	Volume of junctional SR (Ca^{2+} release store)
V_i	1.58	pL	Volume of the cytosol excluding submembrane space
V_{nSR}	0.04	pL	Volume of network SR (Ca^{2+} uptake store)
E_T	26.72655	mV	(RT/F) factor in calculating Nernst potentials
F	96485	C/mol	Faraday constant
E_{Na}	70.5329	mV	Equilibrium potential for Na^+
E_K	-87.0014	mV	Equilibrium potential for K^+
E_{Ks}	-49.4464	mV	Reversal potential for I_{Ks}
$E_{Ca,L}$	45	mV	Apparent reversal potential of $I_{Ca,L}$
$E_{Ca,T}$	45	mV	Apparent reversal potential of $I_{Ca,T}$
E_{st}	37.4	mV	Apparent reversal potential of I_{st}
$g_{Ca,L}$	0.58	nS/pF	Maximum L-type Ca^{2+} current conductance
$g_{Ca,T}$	0.1832	nS/pF	Maximum T-type Ca^{2+} current conductance
g_{If}	0.15	nS/pF	Maximum "funny" current conductance
$V_{If,1/2,basal}$	-64	mV	Baseline half-activation voltage for I_f
g_{st}	0.003	nS/pF	Maximum sustained non-selective current conductance
g_{Kr}	0.08113973	nS/pF	Maximum conductance of rapid delayed rectifier K^+ current
g_{Ks}	0.0259	nS/pF	Maximum conductance of slow delayed rectifier K^+ current
g_{to}	0.252	nS/pF	Maximum conductance of 4-aminopyridine sensitive transient K^+ current
g_{sus}	0.02	nS/pF	Maximum conductance of 4-aminopyridine sensitive sustained K^+ current
$I_{NaK,max}$	2.88	pA/pF	Maximum Na^+/K^+ pump current
k_{NCX}	187.5	pA/pF	Maximum Na^+/Ca^{2+} exchanger current
g_{bCa}	0.0006	nS/pF	Maximum conductance of background Ca^{2+} current
g_{bNa}	0.00486	nS/pF	Maximum conductance of background Na^+ current
$g_{KACh,max}$	0.043	nS/pF	Maximum conductance of acetylcholine-activated K^+ current
K_{mfCa}	0.00035	mM	Dissociation constant of Ca^{2+}-dependent $I_{Ca,L}$ inactivation
K_{mKp}	1.4	mM	Extracellular K^+ concentration for half-maximal I_{NaK}
K_{mNap}	14	mM	Intracellular Na^+ concentration for half-maximal I_{NaK}
α_{fCa}	0.021	/ms	Ca^{2+} dissociation rate constant for $I_{Ca,L}$
s_{max}	11	mV	Maximal shift in I_f activation gate due to cAMP
n_f	0.85	unitless	Hill coefficient for cAMP-dependent shift in I_f activation gate
$K_{0.5,f}$	2.11 E-4	mM	cAMP concentration needed for half-maximal shift in I_f activation gate
K_{1ni}	395.3	mM	Intracellular Na^+ dissociation constant for first site on NCX
K_{2ni}	2.289	mM	Intracellular Na^+ dissociation constant for second site on NCX
K_{3ni}	26.44	mM	Intracellular Na^+ dissociation constant for third site on NCX
K_{1no}	1628	mM	Extracellular Na^+ dissociation constant for first site on NCX
K_{2no}	561.4	mM	Extracellular Na^+ dissociation constant for second site on NCX

K_{3no}	4.663	mM	Extracellular Na^+ dissociation constant for third site on NCX
K_{ci}	0.0207	mM	Intracellular Ca^{2+} dissociation constant for NCX
K_{co}	3.663	mM	Extracellular Ca^{2+} dissociation constant for NCX
K_{cni}	26.44	mM	Intracellular dissociation constant for simultaneous Na^+ and Ca^{2+} binding to NCX
Q_{ci}	0.1369	unitless	Intracellular Ca^{2+} occlusion reaction of NCX
Q_{co}	0	unitless	Extracellular Ca^{2+} occlusion reaction of NCX
Q_n	0.4315	unitless	Na^+ occlusion reactions of NCX
τ_{difCa}	0.04	ms	Time constant of Ca^{2+} diffusion from the submembrane space to cytosol
τ_{tr}	40	ms	Time constant for Ca^{2+} transfer from the network to junctional SR
K_{up}	6 E-4	mM	Half-maximal intracellular Ca_i for Ca^{2+} uptake in the network SR
P_{up}	0.0065	mM/ms	Rate constant for Ca^{2+} uptake by the Ca^{2+} pump in the network SR
k_{oCa}	10	/mM^2/ms	RyR parameter
k_{om}	0.06	/ms	RyR parameter
k_{iCa}	0.5	/mM/ms	RyR parameter
k_{im}	0.005	/ms	RyR parameter
EC_{50_SR}	0.45	mM	RyR parameter
k_s	250000	/ms	RyR parameter
MaxSR	15	unitless	RyR parameter
MinSR	1	unitless	RyR parameter
HSR	2.5	unitless	RyR parameter
k_{bCM}	0.542	/ms	Ca^{2+} dissociation constant for calmodulin
k_{bCQ}	0.445	/ms	Ca^{2+} dissociation constant for calsequestrin
k_{bTC}	0.446	/ms	Ca^{2+} dissociation constant for the troponin-Ca^{2+} site
k_{bTMC}	0.00751	/ms	Ca^{2+} dissociation constant for the troponin-Mg^{2+} site
k_{bTMM}	0.751	/ms	Mg^{2+} dissociation constant for the troponin-Mg^{2+} site
k_{fCM}	227.7	/mM/ms	Ca^{2+} association constant for calmodulin
k_{fCQ}	0.534	/mM/ms	Ca^{2+} association constant for calsequestrin
k_{fTC}	88.8	/mM/ms	Ca^{2+} association constant for troponin
k_{fTMC}	227.7	/mM/ms	Ca^{2+} association constant for the troponin-Mg^{2+} site
k_{fTMM}	2.277	/mM/ms	Mg^{2+} association constant for the troponin-Mg^{2+} site
TC_{tot}	0.031	mM	Total concentration of the troponin-Ca^{2+} site
TMC_{tot}	0.062	mM	Total concentration of the troponin-Mg^{2+} site
CQ_{tot}	10	mM	Total calsequestrin concentration
CM_{tot}	0.045	mM	Total calmodulin concentration

Table 23. Low-level model parameters that are used to calculate some higher-level parameters in table Table 22.

Parameter	Value	Units	Description

L_{Cell}	70	μm	Length of sinoatrial node cell
d_{Cell}	8	μm	Diameter of sinoatrial node cell
$major_{DChol}$	1.38	μm	Major diameter of cholinergic varicosities
$minor_{DChol}$	0.48	μm	Minor diameter of cholinergic varicosities
$major_{DAdr}$	1.26	μm	Major diameter of adrenergic varicosities
$minor_{DAdr}$	0.38	μm	Minor diameter of adrenergic varicosities
$H_{NJ,ACh}$	0.195	μm	Height of cholinergic NJ (distance from cell surface to bottom of varicosity)
$H_{NJ,NE}$	0.166	μm	Height of adrenergic NJ (distance from cell surface to bottom of varicosity)
$N_{Vesicles,ACh}$	450	number	Number of ACh-containing vesicles per varicosity
$N_{Vesicles,NE}$	150	number	Number of NE-containing vesicles per varicosity
H_{EJS}	0.1	μM	Height of EJS (distance from cell membrane to ECM)
H_{ECM}	20	μM	Height of ECM (distance from edge of EJS to blood stream compartment)
N_{Cells}	8	number	Number of cells in a cross-section of sinoatrial node
D_{NJ}	0.000007	cm^2/s	ACh and NE diffusivity in the NJ
D_{EJS}	0.000007	cm^2/s	ACh and NE diffusivity in the EJS
D_{ECM}	0.0000008	cm^2/s	ACh and NE diffusivity in the ECM

9.6 *Basic chemical reactions*

Our model explicitly describes chemical reactions between various molecules. Because the model is fairly low-level, the equations that describe these reactions are fairly simple. In this section, we cover three elementary reactions which form the basis for almost all of the functions that appear in the body of this thesis. The elementary reactions are: 1) simple binding, 2) enzyme kinetics, and 3) cooperative binding.

9.6.1 Steady-state binding reaction

Given the reaction

$$R + L \underset{b}{\overset{a}{\rightleftharpoons}} RL \tag{15}$$

And the total amounts of receptor and ligand $R+RL=R_T$, $L+RL=L_T$, what is the steady state concentration of RL?

We can rewrite equation (15) using R_T and L_T

$$(R_T - RL) + (L_T - RL) \underset{b}{\overset{a}{\rightleftharpoons}} RL \tag{16}$$

At steady state, the rate of creation of RL and its rate of destruction is equal:

$$a(R_T - RL)(L_T - RL) = bRL \tag{17}$$

Solving equation (17) with a straightforward application of the quadratic formula gives:

$$\begin{aligned} RL &= \frac{1}{2}\left(R_T + L_T + \frac{b}{a} - \sqrt{\left(R_T + L_T + \frac{b}{a} \right)^2 - 4R_T L_T} \right) \\ &= \frac{R_T + L_T + \frac{b}{a}}{2}\left(1 - \sqrt{1 - \frac{4R_T L_T}{\left(R_T + L_T + \frac{b}{a} \right)^2}} \right) \end{aligned} \tag{18}$$

If $L_T \gg R_T$ or $R_T \gg L_T$, the second term in the square root becomes small, so we can use the first term of the Taylor expansion for the square root around 1 to obtain:

$$\begin{aligned} RL &\approx \frac{R_T + L_T + \frac{b}{a}}{2} \frac{4R_T L_T}{2\left(R_T + L_T + \frac{b}{a} \right)^2} \\ &= \frac{R_T L_T}{R_T + L_T + \frac{b}{a}} \end{aligned}$$

If $L_T \gg R_T$, we obtain the standard equation:

$$RL \approx R_T \frac{L_T}{L_T + \frac{b}{a}}$$

If, on the other hand, $R_T \gg L_T$, we obtain:

$$RL \approx L_T \frac{R_T}{R_T + \frac{b}{a}}$$

If R_T and L_T are on the same order: $R_T \approx L_T = X$, and b/a is small, the expression under the radical in equation (18) approaches 0, so we get:

$$RL \approx \frac{R_T + L_T}{2}$$

If b/a is large, we get:

$$RL \approx 0$$

And if $b/a \approx R_T \approx L_T = X$, we get:

$$RL \approx \frac{3-\sqrt{5}}{6}\left(R_T + L_T + \frac{b}{a}\right)$$
$$\approx \frac{R_T + L_T + \frac{b}{a}}{8}$$

9.6.2 Enzyme Kinetics

Given a typical enzyme reaction:

$$E + S \underset{b}{\overset{a}{\rightleftharpoons}} ES \xrightarrow{c} E + P \tag{19}$$

Where E is the enzyme, S is the substrate, ES is the enzyme-substrate complex, P is the product of the catalytic reaction. For a fixed concentration of enzyme $E_T = E + ES$, equation (19) can be written as

$$(E_T - ES) + S \underset{b}{\overset{a}{\rightleftharpoons}} ES \xrightarrow{c} (E_T - ES) + P$$

The differential equations are:

$$\begin{aligned} \frac{dES}{dt} &= a(E_T - ES)S - (b+c)ES \\ \frac{dS}{dt} &= -a(E_T - ES)S + bES \\ \frac{dP}{dt} &= cES \end{aligned} \tag{20}$$

If S is maintained at a constant level, or if it is abundant relative to the time course of the binding/unbinding reaction, we can easily solve for the steady-state concentration of ES by solving the first equation with $\frac{dES}{dt} = 0$:

$$
\begin{aligned}
0 &= a\left(E_T - ES\right)S - \left(b+c\right)ES \\
ES &= \frac{aE_T S}{aS+b+c} \\
&= E_T \frac{S}{S+K_{app}}
\end{aligned}
\tag{21}
$$

The last equation is in the familiar Michaelis-Menten form, where $K_{app} = \frac{b+c}{a}$ is the apparent dissociation constant. From (21), it follows that the steady-state rate of P generation, or velocity (v) is:

$$
\begin{aligned}
v &= \frac{dP}{dt} \\
&= \underbrace{cE_T}_{V_{max}} \frac{S}{S+K_{app}}
\end{aligned}
$$

If the product is itself an enzyme and reverts back to the substrate and some byproduct B with some rate constant d:

$$
E + S \underset{b}{\overset{a}{\rightleftharpoons}} ES \xrightarrow{c} E + P \xrightarrow{d} S + B \tag{22}
$$

If we assume that the amount of substrate and product is a constant $S + P = SP_T$, and similarly for the total amount of enzyme as before $E + E_S = E_T$ equation (22) becomes:

$$
\left(E_T - ES\right) + \left(SP_T - P\right) \underset{b}{\overset{a}{\rightleftharpoons}} ES \xrightarrow{c} E + P \xrightarrow{d} \left(SP_T - P\right) + B \tag{23}
$$

Which gives the following differential equations:

$$
\begin{aligned}
\frac{dES}{dt} &= a\left(E_T - ES\right)\left(SP_T - P\right) - \left(b+c\right)ES \\
\frac{dP}{dt} &= cES - dP \\
\frac{dB}{dt} &= dP
\end{aligned}
\tag{24}
$$

Setting the derivatives of ES and P equal to 0 and solving gives:

$$
\begin{aligned}
P &= \frac{c}{d}ES \\
ES &= \frac{dSP_T + cE_T + d\frac{b+c}{a} - \sqrt{\left(dSP_T + cE_T + d\frac{b+c}{a}\right)^2 - 4dSP_T cE_T}}{2c}
\end{aligned}
\tag{25}
$$

In deriving the above, we used the quadratic equation, which has a $\pm$ preceding the radical; we chose the minus because when $SP_T = 0$, we expect the concentration of ES to be 0.

Equation (25) lets us calculate the overall rate of production of B:

$$\frac{dB}{dt} = dP = cES$$
$$= \frac{1}{2}\left(dSP_T + cE_T + d\frac{b+c}{a} - \sqrt{\left(dSP_T + cE_T + d\frac{b+c}{a} \right)^2 - 4dSP_T cE_T} \right)$$

9.6.3 Cooperative Binding

When one molecule can bind two ligands, the opportunity for cooperative binding exists. The simplest case is shown below, where the molecule of interest (X) has two binding sites for ligand (Y). When no ligand is bound, the affinity is K_D, and when one ligand is bound, the affinity is increased by a factor f (K_D/f). The two binding sites are assumed to be identical.

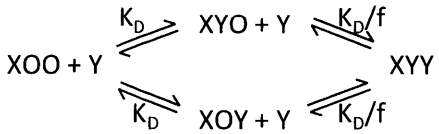

Figure 123 Reaction diagram for binding of 2 ligands (Y) to a molecule X with two binding sites (O). The empty binding sites are shown as O in order to differentiate the two intermediate states. The dissociation constant is K_D when no ligand is bound, and changes to K_D/f after one ligand has bound.

The above diagram can be reduced to the following form by grouping the intermediate states:

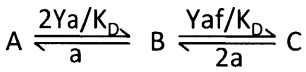

Figure 124 Simplified form of the diagram in Figure 123. The states are named A, B, and C for simplicity, where B is the sum of the two intermediate states. This simplification causes the rate constants entering state B to double. The arbitrary dissociation rate a was introduced to allow writing of differential equations; it is assumed not to change when the affinity changes. The association rate is expressed in terms of a and K_D to ensure that the dissociation constant is K_D.

If the total amount of molecule X is T, then $A+B+C=T$. We can also write the differential equations for A and B:

$$\frac{dA}{dt} = -2Ya / K_D A + aB$$
$$\frac{dB}{dt} = -\left(a + Yaf / K_D\right)B + 2Ya / K_D A + 2aC$$

Solving the two differential equations at steady state, and using the equation for T, we can solve for A, B, and C at steady state:

$$A = T\frac{1}{1+2\frac{Y}{K_D}+f\left(\frac{Y}{K_D}\right)^2}$$

$$B = T\frac{2\frac{Y}{K_D}}{1+2\frac{Y}{K_D}+f\left(\frac{Y}{K_D}\right)^2} \quad (26)$$

$$C = T\frac{f\left(\frac{Y}{K_D}\right)^2}{1+2\frac{Y}{K_D}+f\left(\frac{Y}{K_D}\right)^2}$$

The functions for f=1 are shown in

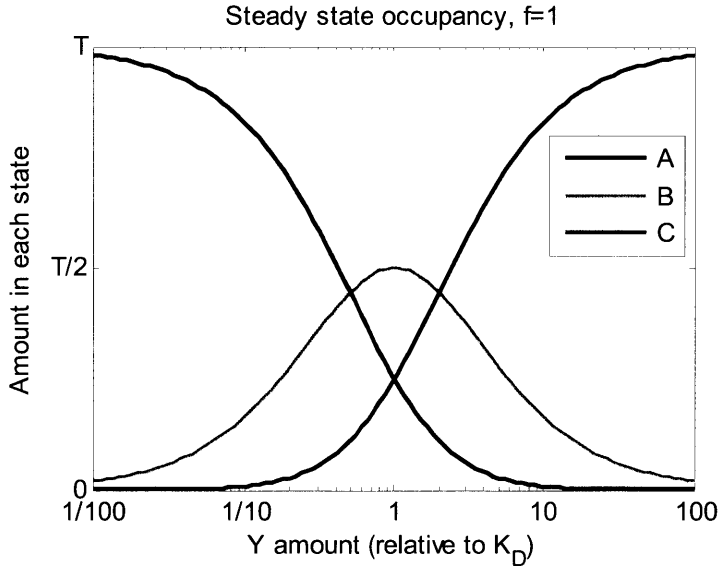

Figure 125 Steady state occupancy of each state in Figure 124.

For cooperative binding, the amount of bound ligand (relative to the total possible amount) is expressed using the Hill equation with an apparent dissociation constant K_{app} and a Hill coefficient n:

$$Y_{bound} = \frac{Y^n}{Y^n + K_{app}^n} \quad (27)$$

Using equations (26) and normalizing by $2T$ since that's the total possible amount of Y that can be bound, we obtain:

$$Y_{bound} = \frac{1}{2T}(B + 2C)$$
$$= \frac{\frac{Y}{K_D} + f\left(\frac{Y}{K_D}\right)^2}{1 + 2\frac{Y}{K_D} + f\left(\frac{Y}{K_D}\right)^2} \tag{28}$$

Note that if f=1, equation (28) reduces to $Y/(Y+K_D)$, which is exactly the Hill equation with coefficient n=1, and K_{app}=K_D. This makes sense since a Hill coefficient of 1 implies independent binding, which is exactly the condition of f=1. To convert equation (28) into a form like equation (27) for any value of f, we can first calculate the apparent dissociation constant (ie. value of Y that gives Y_{bound}=1/2):

$$\frac{\frac{K_{app}}{K_D} + f\left(\frac{K_{app}}{K_D}\right)^2}{1 + 2\frac{K_{app}}{K_D} + f\left(\frac{K_{app}}{K_D}\right)^2} = \frac{1}{2} \quad \Rightarrow \quad \boxed{K_{app} = \frac{K_D}{\sqrt{f}}} \tag{29}$$

We can use the slope of the Y_{bound} function at Y=K_{app} to calculate n. The slope of Y_{bound} at Y=K_{app} is

$$\left.\frac{dY_{bound}}{dY}\right|_{Y=K_{app}} = \frac{n}{4K_{app}} \tag{30}$$

Therefore, taking the derivative of equation (28) with respect to Y, evaluating at Y=K_{app}, and multiplying by 4K_{app}, we obtain:

$$n = \left.\frac{dY_{bound}}{dY}\right|_{Y=K_{app}} 4K_{app} = \frac{1}{K_D}\frac{2 + 2\sqrt{f}}{\left(2 + 2/\sqrt{f}\right)^2} 4\frac{K_D}{\sqrt{f}} \quad \Rightarrow \quad \boxed{n = \frac{2\sqrt{f}}{1 + \sqrt{f}}} \tag{31}$$

Interestingly for the cooperative binding of two molecules as in this model, the asymptotic value of n as $f \rightarrow \infty$ is 2.

To verify that equations (29) and (31) are correct, we plot the Y_{bound} ratio using equation (28) as well as equation (27) using K_{app} and n as defined in (29) and (31) for f=0.1, f=1, and f=10. As we can see, the calculations are correct at the intended point (around Y_{bound}=0.5), but deviate away from that point, especially for f<1 (negatively cooperative binding).

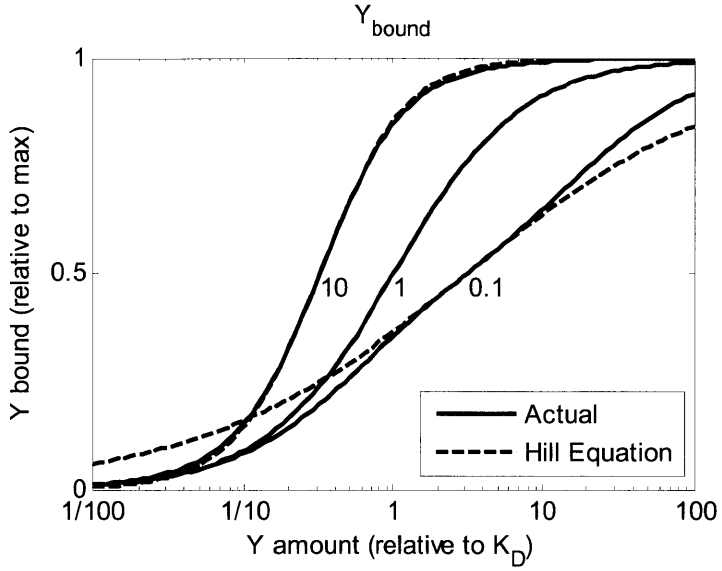

Figure 126. Plots of Y_{bound} for three values of f (indicated next to each curve). The solid lines show the actual amount of Y bound using equation (28), and the dashed lines are the Hill equation approximations using equations (29) and (31) to calculate K_{app} and n.

To conclude, the Hill equation is pretty good for positively cooperative binding, but for negatively cooperative binding, it may be better to just use equation (28) and fit the f and K_D parameters to data. The advantage of the Hill equation is a cleaner form however, and the parameters K_{app} and n can just as easily be fit to data.

10 REFERENCES

1. Heart rate variability. Standards of measurement, physiological interpretation, and clinical use. Task Force of the European Society of Cardiology and the North American Society of Pacing and Electrophysiology. *Eur Heart J* 17: 354-381, 1996.
2. The top 10 causes of death World Health Organization. http://www.who.int/mediacentre/factsheets/fs310/en/index.html#. [07/14/2011, 2011].
3. **Accili EA, Redaelli G, and DiFrancesco D**. Differential control of the hyperpolarization-activated current (i(f)) by cAMP gating and phosphatase inhibition in rabbit sino-atrial node myocytes. *J Physiol* 500 (Pt 3): 643-651, 1997.
4. **Adams JA, and Taylor SS**. Energetic limits of phosphotransfer in the catalytic subunit of cAMP-dependent protein kinase as measured by viscosity experiments. *Biochemistry* 31: 8516-8522, 1992.
5. **Akselrod S, Gordon D, Ubel FA, Shannon DC, Berger AC, and Cohen RJ**. Power spectrum analysis of heart rate fluctuation: a quantitative probe of beat-to-beat cardiovascular control. *Science* 213: 220-222, 1981.
6. **Alexander RW, Williams LT, and Lefkowitz RJ**. Identification of cardiac beta-adrenergic receptors by (minus) [3H]alprenolol binding. *Proc Natl Acad Sci U S A* 72: 1564-1568, 1975.
7. **An WF, Bowlby MR, Betty M, Cao J, Ling HP, Mendoza G, Hinson JW, Mattsson KI, Strassle BW, Trimmer JS, and Rhodes KJ**. Modulation of A-type potassium channels by a family of calcium sensors. *Nature* 403: 553-556, 2000.
8. **Angelakos ET, Fuxe K, and Torchiana ML**. Chemical and Histochemical Evaluation of the Distribution of Catecholamines in the Rabbit and Guinea Pig Hearts. *Acta Physiol Scand* 59: 184-192, 1963.
9. **Armour JA, Murphy DA, Yuan BX, Macdonald S, and Hopkins DA**. Gross and microscopic anatomy of the human intrinsic cardiac nervous system. *Anat Rec* 247: 289-298, 1997.
10. **Bailey JJ, Hodges M, and Church TR**. Decision to implant a cardioverter defibrillator after myocardial infarction: the role of ejection fraction v. other risk factor markers. *Med Decis Making* 27: 151-160, 2007.
11. **Banks HT, Miech RP, and Olson SL**. A comparison of mathematical models for a recycling cascade in glycogenolysis. *Mathematical Modelling* 1: 13-26, 1980.
12. **Bar KJ, Letzsch A, Jochum T, Wagner G, Greiner W, and Sauer H**. Loss of efferent vagal activity in acute schizophrenia. *J Psychiatr Res* 39: 519-527, 2005.
13. **Barber R, Goka TJ, and Butcher RW**. Role of high affinity cAMP phosphodiesterase activities in the response of S49 cells to agonists. *Mol Pharmacol* 32: 753-759, 1987.
14. **Barnes AP, Livera G, Huang P, Sun C, O'Neal WK, Conti M, Stutts MJ, and Milgram SL**. Phosphodiesterase 4D forms a cAMP diffusion barrier at the apical membrane of the airway epithelium. *J Biol Chem* 280: 7997-8003, 2005.
15. **Bartol TM, Jr., Land BR, Salpeter EE, and Salpeter MM**. Monte Carlo simulation of miniature endplate current generation in the vertebrate neuromuscular junction. *Biophys J* 59: 1290-1307, 1991.
16. **Basbaum CB, Grillo MA, and Widdicombe JH**. Muscarinic receptors: evidence for a nonuniform distribution in tracheal smooth muscle and exocrine glands. *J Neurosci* 4: 508-520, 1984.
17. **Beau SL, Hand DE, Schuessler RB, Bromberg BI, Kwon B, Boineau JP, and Saffitz JE**. Relative densities of muscarinic cholinergic and beta-adrenergic receptors in the canine sinoatrial node and their relation to sites of pacemaker activity. *Circ Res* 77: 957-963, 1995.
18. **Beavo JA, Bechtel PJ, and Krebs EG**. Activation of protein kinase by physiological concentrations of cyclic AMP. *Proc Natl Acad Sci U S A* 71: 3580-3583, 1974.
19. **Bennett MR**. Autonomic neuromuscular transmission at a varicosity. *Prog Neurobiol* 50: 505-532, 1996.

20. **Berger RD, Saul JP, and Cohen RJ**. Transfer function analysis of autonomic regulation. I. Canine atrial rate response. *Am J Physiol* 256: H142-152, 1989.
21. **Berne RM**. *Physiology*. St. Louis: Mosby, 1998, p. xiv, 1131 p.
22. **Bers DM**. Cardiac excitation-contraction coupling. *Nature* 415: 198-205, 2002.
23. **Berstein G, Blank JL, Jhon DY, Exton JH, Rhee SG, and Ross EM**. Phospholipase C-beta 1 is a GTPase-activating protein for Gq/11, its physiologic regulator. *Cell* 70: 411-418, 1992.
24. **Bevan JA, Chesher GB, and Su C**. Release of adrenergic transmitter from terminal nerve plexus in artery. *Agents Actions* 1: 20-26, 1969.
25. **Bevan JA, and Torok J**. Movement of norepinephrine through the media of rabbit aorta. *Circ Res* 27: 325-331, 1970.
26. **Bois P, Renaudon B, Baruscotti M, Lenfant J, and DiFrancesco D**. Activation of f-channels by cAMP analogues in macropatches from rabbit sino-atrial node myocytes. *J Physiol* 501 (Pt 3): 565-571, 1997.
27. **Bokoch GM, Bickford K, and Bohl BP**. Subcellular localization and quantitation of the major neutrophil pertussis toxin substrate, Gn. *J Cell Biol* 106: 1927-1936, 1988.
28. **Bokoch GM, Katada T, Northup JK, Hewlett EL, and Gilman AG**. Identification of the predominant substrate for ADP-ribosylation by islet activating protein. *J Biol Chem* 258: 2072-2075, 1983.
29. **Bokoch GM, Katada T, Northup JK, Ui M, and Gilman AG**. Purification and properties of the inhibitory guanine nucleotide-binding regulatory component of adenylate cyclase. *J Biol Chem* 259: 3560-3567, 1984.
30. **Bouairi E, Neff R, Evans C, Gold A, Andresen MC, and Mendelowitz D**. Respiratory sinus arrhythmia in freely moving and anesthetized rats. *J Appl Physiol* 97: 1431-1436, 2004.
31. **Bouvier M, Hausdorff WP, De Blasi A, O'Dowd BF, Kobilka BK, Caron MG, and Lefkowitz RJ**. Removal of phosphorylation sites from the beta 2-adrenergic receptor delays onset of agonist-promoted desensitization. *Nature* 333: 370-373, 1988.
32. **Boyett MR, Honjo H, and Kodama I**. The sinoatrial node, a heterogeneous pacemaker structure. *Cardiovasc Res* 47: 658-687, 2000.
33. **Brack KE, Coote JH, and Ng GA**. Interaction between direct sympathetic and vagus nerve stimulation on heart rate in the isolated rabbit heart. *Exp Physiol* 89: 128-139, 2004.
34. **Brandt DR, Asano T, Pedersen SE, and Ross EM**. Reconstitution of catecholamine-stimulated guanosinetriphosphatase activity. *Biochemistry* 22: 4357-4362, 1983.
35. **Brandt DR, and Ross EM**. Catecholamine-stimulated GTPase cycle. Multiple sites of regulation by beta-adrenergic receptor and Mg2+ studied in reconstituted receptor-Gs vesicles. *J Biol Chem* 261: 1656-1664, 1986.
36. **Brandt DR, and Ross EM**. GTPase activity of the stimulatory GTP-binding regulatory protein of adenylate cyclase, Gs. Accumulation and turnover of enzyme-nucleotide intermediates. *J Biol Chem* 260: 266-272, 1985.
37. **Brann MR**. *Molecular biology of G-protein-coupled receptors*. Boston: Birkhäuser, 1992, p. xvi, 326 p.
38. **Breitwieser GE, and Szabo G**. Mechanism of muscarinic receptor-induced K+ channel activation as revealed by hydrolysis-resistant GTP analogues. *J Gen Physiol* 91: 469-493, 1988.
39. **Bristow MR, Ginsburg R, Strosberg A, Montgomery W, and Minobe W**. Pharmacology and inotropic potential of forskolin in the human heart. *J Clin Invest* 74: 212-223, 1984.
40. **Bristow MR, Ginsburg R, Umans V, Fowler M, Minobe W, Rasmussen R, Zera P, Menlove R, Shah P, Jamieson S, and et al.** Beta 1- and beta 2-adrenergic-receptor subpopulations in nonfailing and failing human ventricular myocardium: coupling of both receptor subtypes to muscle contraction and selective beta 1-receptor down-regulation in heart failure. *Circ Res* 59: 297-309, 1986.
41. **Bristow MR, Hershberger RE, Port JD, Minobe W, and Rasmussen R**. Beta 1- and beta 2-adrenergic receptor-mediated adenylate cyclase stimulation in nonfailing and failing human ventricular myocardium. *Mol Pharmacol* 35: 295-303, 1989.

42. **Bristow MR, Minobe W, Rasmussen R, Larrabee P, Skerl L, Klein JW, Anderson FL, Murray J, Mestroni L, Karwande SV, and et al.** Beta-adrenergic neuroeffector abnormalities in the failing human heart are produced by local rather than systemic mechanisms. *J Clin Invest* 89: 803-815, 1992.
43. **Brodde OE, Konschak U, Becker K, Ruter F, Poller U, Jakubetz J, Radke J, and Zerkowski HR**. Cardiac muscarinic receptors decrease with age. In vitro and in vivo studies. *J Clin Invest* 101: 471-478, 1998.
44. **Brown H, and Difrancesco D**. Voltage-clamp investigations of membrane currents underlying pace-maker activity in rabbit sino-atrial node. *J Physiol* 308: 331-351, 1980.
45. **Buchheit M, Simon C, Charloux A, Doutreleau S, Piquard F, and Brandenberger G**. Relationship between very high physical activity energy expenditure, heart rate variability and self-estimate of health status in middle-aged individuals. *Int J Sports Med* 27: 697-701, 2006.
46. **Burnstock G**. The autonomic neuroeffector junction. In: *Primer on the Autonomic Nervous System*, edited by Robertson D, Low P, and Burnstock G. Amsterdam: Elsevier, 2004, p. 29-33.
47. **Burnstock G**. Autonomic neurotransmission: 60 years since sir Henry Dale. *Annu Rev Pharmacol Toxicol* 49: 1-30, 2009.
48. **Burnstock G, and Holman ME**. Spontaneous potential at sympathetic nerve endings in smooth muscle. *J Physiol* 160: 446-460, 1962.
49. **Burnstock G, and Holman ME**. The transmission of excitation from autonomic nerve to smooth muscle. *J Physiol* 155: 115-133, 1961.
50. **Buxbaum JD, and Dudai Y**. A quantitative model for the kinetics of cAMP-dependent protein kinase (type II) activity. Long-term activation of the kinase and its possible relevance to learning and memory. *J Biol Chem* 264: 9344-9351, 1989.
51. **Bylund DB, and Snyder SH**. Beta adrenergic receptor binding in membrane preparations from mammalian brain. *Mol Pharmacol* 12: 568-580, 1976.
52. **Calebiro D, Nikolaev VO, Gagliani MC, de Filippis T, Dees C, Tacchetti C, Persani L, and Lohse MJ**. Persistent cAMP-signals triggered by internalized G-protein-coupled receptors. *PLoS Biol* 7: e1000172, 2009.
53. **Campbell GD, Edwards FR, Hirst GD, and O'Shea JE**. Effects of vagal stimulation and applied acetylcholine on pacemaker potentials in the guinea-pig heart. *J Physiol* 415: 57-68, 1989.
54. **Cassel D, Levkovitz H, and Selinger Z**. The regulatory GTPase cycle of turkey erythrocyte adenylate cyclase. *J Cyclic Nucleotide Res* 3: 393-406, 1977.
55. **Catalucci D, Latronico MV, Ceci M, Rusconi F, Young HS, Gallo P, Santonastasi M, Bellacosa A, Brown JH, and Condorelli G**. Akt increases sarcoplasmic reticulum Ca2+ cycling by direct phosphorylation of phospholamban at Thr17. *J Biol Chem* 284: 28180-28187, 2009.
56. **Celler BG**. Characteristics of Cardiac Period Responses to Prolonged Vagal-Stimulation in Dogs. *Medical & Biological Engineering & Computing* 27: 595-602, 1989.
57. **Celler BG, and Lovell NH**. Dynamics of cardiac period responses after prolonged vagal stimulation in the dog. *Ann Biomed Eng* 19: 273-289, 1991.
58. **Cerione RA, Codina J, Benovic JL, Lefkowitz RJ, Birnbaumer L, and Caron MG**. The mammalian beta 2-adrenergic receptor: reconstitution of functional interactions between pure receptor and pure stimulatory nucleotide binding protein of the adenylate cyclase system. *Biochemistry* 23: 4519-4525, 1984.
59. **Chen F, and Zhang Y**. An Efficient Algorithm to Reconstruct Heart Rate Signal Based on an IPFM Model for the Spectral Analysis of HRV. *Conf Proc IEEE Eng Med Biol Soc* 1: 936-939, 2005.
60. **Chen L, Kurokawa J, and Kass RS**. Phosphorylation of the A-kinase-anchoring protein Yotiao contributes to protein kinase A regulation of a heart potassium channel. *J Biol Chem* 280: 31347-31352, 2005.
61. **Chess GF, and Calaresu FR**. Model of dynamic behavior of heart period during bilateral vagal stimulation in the cat. *Am J Physiol* 221: 593-596, 1971.
62. **Cheung WY**. Cyclic 3',5'-nucleotide phosphodiesterase. Evidence for and properties of a protein activator. *J Biol Chem* 246: 2859-2869, 1971.

63. **Chiu HW, and Kao T**. A mathematical model for autonomic control of heart rate variation. *IEEE Eng Med Biol Mag* 20: 69-76, 2001.
64. **Choate JK, Edwards FR, Hirst GD, and O'Shea JE**. Effects of sympathetic nerve stimulation on the sino-atrial node of the guinea-pig. *J Physiol* 471: 707-727, 1993.
65. **Choate JK, Klemm M, and Hirst GD**. Sympathetic and parasympathetic neuromuscular junctions in the guinea-pig sino-atrial node. *J Auton Nerv Syst* 44: 1-15, 1993.
66. **Clapham DE, and Neer EJ**. G protein beta gamma subunits. *Annu Rev Pharmacol Toxicol* 37: 167-203, 1997.
67. **Clapham DE, and Neer EJ**. New roles for G-protein beta gamma-dimers in transmembrane signalling. *Nature* 365: 403-406, 1993.
68. **Coggan JS, Bartol TM, Esquenazi E, Stiles JR, Lamont S, Martone ME, Berg DK, Ellisman MH, and Sejnowski TJ**. Evidence for ectopic neurotransmission at a neuronal synapse. *Science* 309: 446-451, 2005.
69. **Colatsky TJ**. Voltage clamp measurements of sodium channel properties in rabbit cardiac Purkinje fibres. *J Physiol* 305: 215-234, 1980.
70. **Coleman DE, and Sprang SR**. How G proteins work: a continuing story. *Trends Biochem Sci* 21: 41-44, 1996.
71. **Communal C, Singh K, Sawyer DB, and Colucci WS**. Opposing effects of beta(1)- and beta(2)-adrenergic receptors on cardiac myocyte apoptosis : role of a pertussis toxin-sensitive G protein. *Circulation* 100: 2210-2212, 1999.
72. **Conti M, and Beavo J**. Biochemistry and physiology of cyclic nucleotide phosphodiesterases: essential components in cyclic nucleotide signaling. *Annu Rev Biochem* 76: 481-511, 2007.
73. **Cook PF, Neville ME, Jr., Vrana KE, Hartl FT, and Roskoski R, Jr.** Adenosine cyclic 3',5'-monophosphate dependent protein kinase: kinetic mechanism for the bovine skeletal muscle catalytic subunit. *Biochemistry* 21: 5794-5799, 1982.
74. **Corbin JD, Sugden PH, Lincoln TM, and Keely SL**. Compartmentalization of adenosine 3':5'-monophosphate and adenosine 3':5'-monophosphate-dependent protein kinase in heart tissue. *J Biol Chem* 252: 3854-3861, 1977.
75. **Corbin JD, Sugden PH, West L, Flockhart DA, Lincoln TM, and McCarthy D**. Studies on the properties and mode of action of the purified regulatory subunit of bovine heart adenosine 3':5'-monophosphate-dependent protein kinase. *J Biol Chem* 253: 3997-4003, 1978.
76. **Courtemanche M, Ramirez RJ, and Nattel S**. Ionic mechanisms underlying human atrial action potential properties: insights from a mathematical model. *Am J Physiol* 275: H301-321, 1998.
77. **Craven PA, Neidig M, and DeRubertis FR**. Properties of multiple kinetic forms of soluble cyclic nucleotide phosphodiesterase activity of rat colonic mucosa. *Biochim Biophys Acta* 744: 265-275, 1983.
78. **Dahlstrom A, Haggendal J, and Hokfelt T**. The noradrenaline content of the varicosities of sympathetic adrenergic nerve terminals in the rat. *Acta Physiol Scand* 67: 289-294, 1966.
79. **de Champlain J, Farley L, Cousineau D, and van Ameringen MR**. Circulating catecholamine levels in human and experimental hypertension. *Circ Res* 38: 109-114, 1976.
80. **Delforge J, Syrota A, Lancon JP, Nakajima K, Loc'h C, Janier M, Vallois JM, Cayla J, and Crouzel C**. Cardiac beta-adrenergic receptor density measured in vivo using PET, CGP 12177, and a new graphical method. *J Nucl Med* 32: 739-748, 1991.
81. **Demir SS, Clark JW, and Giles WR**. Parasympathetic modulation of sinoatrial node pacemaker activity in rabbit heart: a unifying model. *Am J Physiol* 276: H2221-2244, 1999.
82. **Demir SS, Clark JW, Murphey CR, and Giles WR**. A mathematical model of a rabbit sinoatrial node cell. *Am J Physiol* 266: C832-852, 1994.
83. **DeQuattro V, and Chan S**. Raised plasma-catecholamines in some patients with primary hypertension. *Lancet* 1: 806-809, 1972.
84. **Desilets M, and Baumgarten CM**. Isoproterenol Directly Stimulates the Na+-K+ Pump in Isolated Cardiac Myocytes. *American Journal of Physiology* 251: H218-H225, 1986.

85. **Dessauer CW, Scully TT, and Gilman AG**. Interactions of forskolin and ATP with the cytosolic domains of mammalian adenylyl cyclase. *Journal of Biological Chemistry* 272: 22272-22277, 1997.
86. **Dexter F, Saidel GM, Levy MN, and Rudy Y**. Mathematical model of dependence of heart rate on tissue concentration of acetylcholine. *Am J Physiol* 256: H520-526, 1989.
87. **Dieterich HA, Lindmar R, and Loffelholz K**. Role of Choline in Release of Acetylcholine in Isolated Hearts. *N-S Arch Pharmacol* 301: 207-215, 1978.
88. **DiFrancesco D, Ducouret P, and Robinson RB**. Muscarinic modulation of cardiac rate at low acetylcholine concentrations. *Science* 243: 669-671, 1989.
89. **DiFrancesco D, and Noble D**. A model of cardiac electrical activity incorporating ionic pumps and concentration changes. *Philos Trans R Soc Lond B Biol Sci* 307: 353-398, 1985.
90. **DiFrancesco D, and Tortora P**. Direct activation of cardiac pacemaker channels by intracellular cyclic AMP. *Nature* 351: 145-147, 1991.
91. **DiFrancesco D, and Tromba C**. Acetylcholine inhibits activation of the cardiac hyperpolarizing-activated current, if. *Pflugers Arch* 410: 139-142, 1987.
92. **DiFrancesco D, and Tromba C**. Muscarinic control of the hyperpolarization-activated current (if) in rabbit sino-atrial node myocytes. *J Physiol* 405: 493-510, 1988.
93. **Dionne VE**. Characterization of drug iontophoresis with a fast microassay technique. *Biophys J* 16: 705-717, 1976.
94. **Dobrzynski H, Li J, Tellez J, Greener ID, Nikolski VP, Wright SE, Parson SH, Jones SA, Lancaster MK, Yamamoto M, Honjo H, Takagishi Y, Kodama I, Efimov IR, Billeter R, and Boyett MR**. Computer three-dimensional reconstruction of the sinoatrial node. *Circulation* 111: 846-854, 2005.
95. **Dokos S, Celler B, and Lovell N**. Ion currents underlying sinoatrial node pacemaker activity: a new single cell mathematical model. *J Theor Biol* 181: 245-272, 1996.
96. **Dokos S, Celler BG, and Lovell NH**. Vagal control of sinoatrial rhythm: a mathematical model. *J Theor Biol* 182: 21-44, 1996.
97. **Dunant Y, and Muller D**. Quantal release of acetylcholine evoked by focal depolarization at the Torpedo nerve-electroplaque junction. *J Physiol* 379: 461-478, 1986.
98. **Dunlap ME, Bibevski S, Rosenberry TL, and Ernsberger P**. Mechanisms of altered vagal control in heart failure: influence of muscarinic receptors and acetylcholinesterase activity. *Am J Physiol Heart Circ Physiol* 285: H1632-1640, 2003.
99. **Eccles JC, and Jaeger JC**. The relationship between the mode of operation and the dimensions of the junctional regions at synapses and motor end-organs. *Proc R Soc Lond B Biol Sci* 148: 38-56, 1958.
100. **Eckberg DL**. Human sinus arrhythmia as an index of vagal cardiac outflow. *J Appl Physiol* 54: 961-966, 1983.
101. **Edwards FR, Bramich NJ, and Hirst GD**. Analysis of the effects of vagal stimulation on the sinus venous of the toad. *Philos Trans R Soc Lond B Biol Sci* 341: 149-162, 1993.
102. **Eisenhofer G**. Sympathetic nerve function--assessment by radioisotope dilution analysis. *Clin Auton Res* 15: 264-283, 2005.
103. **Eisenhofer G, Cox HS, and Esler MD**. Noradrenaline reuptake and plasma dihydroxyphenylglycol during sustained changes in sympathetic activity in rabbits. *J Auton Nerv Syst* 32: 217-231, 1991.
104. **Eisenhofer G, Goldstein DS, and Kopin IJ**. Plasma dihydroxyphenylglycol for estimation of noradrenaline neuronal re-uptake in the sympathetic nervous system in vivo. *Clin Sci (Lond)* 76: 171-182, 1989.
105. **Eisenhofer G, Kopin IJ, and Goldstein DS**. Catecholamine metabolism: a contemporary view with implications for physiology and medicine. *Pharmacol Rev* 56: 331-349, 2004.
106. **Ellman GL, Courtney KD, Andres V, Jr., and Feather-Stone RM**. A new and rapid colorimetric determination of acetylcholinesterase activity. *Biochem Pharmacol* 7: 88-95, 1961.

107. **Engelman K, Portnoy B, and Sjoerdsma A**. Catecholamines-cyclic amp-angiotensin receptors. Plasma catecholamine concentrations in patients with hypertension. *Circ Res* 27: 141-146, 1970.
108. **Erlichman J, Rosenfeld R, and Rosen OM**. Phosphorylation of a cyclic adenosine 3':5'-monophosphate-dependent protein kinase from bovine cardiac muscle. *J Biol Chem* 249: 5000-5003, 1974.
109. **Esler M, Jennings G, Korner P, Blombery P, Sacharias N, and Leonard P**. Measurement of total and organ-specific norepinephrine kinetics in humans. *Am J Physiol* 247: E21-28, 1984.
110. **Ferrandon S, Feinstein TN, Castro M, Wang B, Bouley R, Potts JT, Gardella TJ, and Vilardaga JP**. Sustained cyclic AMP production by parathyroid hormone receptor endocytosis. *Nat Chem Biol* 5: 734-742, 2009.
111. **Fischmeister R, Castro L, Abi-Gerges A, Rochais F, and Vandecasteele G**. Species- and tissue-dependent effects of NO and cyclic GMP on cardiac ion channels. *Comp Biochem Phys A* 142: 136-143, 2005.
112. **Flockhart DA, and Corbin JD**. Regulatory mechanisms in the control of protein kinases. *CRC Crit Rev Biochem* 12: 133-186, 1982.
113. **Flockhart DA, Watterson DM, and Corbin JD**. Studies on functional domains of the regulatory subunit of bovine heart adenosine 3':5'-monophosphate-dependent protein kinase. *J Biol Chem* 255: 4435-4440, 1980.
114. **Ford CE, Skiba NP, Bae H, Daaka Y, Reuveny E, Shekter LR, Rosal R, Weng G, Yang CS, Iyengar R, Miller RJ, Jan LY, Lefkowitz RJ, and Hamm HE**. Molecular basis for interactions of G protein betagamma subunits with effectors. *Science* 280: 1271-1274, 1998.
115. **Fowler MB, Laser JA, Hopkins GL, Minobe W, and Bristow MR**. Assessment of the beta-adrenergic receptor pathway in the intact failing human heart: progressive receptor down-regulation and subsensitivity to agonist response. *Circulation* 74: 1290-1302, 1986.
116. **Freeman J**. Q&A: Emotions - Heart, Mind, and Body http://www.6seconds.org/2009/05/09/qa-emotions-heart-mind-and-body/. [07/11/2011, 2011].
117. **Fujii T, Yamada S, Yamaguchi N, Fujimoto K, Suzuki T, and Kawashima K**. Species differences in the concentration of acetylcholine, a neurotransmitter, in whole blood and plasma. *Neurosci Lett* 201: 207-210, 1995.
118. **Gerhardt G, and Adams RN**. Determination of Diffusion-Coefficients by Flow-Injection Analysis. *Anal Chem* 54: 2618-2620, 1982.
119. **Giessler C, Dhein S, Ponicke K, and Brodde OE**. Muscarinic receptors in the failing human heart. *Eur J Pharmacol* 375: 197-202, 1999.
120. **Giles W, Nakajima T, Ono K, and Shibata EF**. Modulation of the delayed rectifier K+ current by isoprenaline in bull-frog atrial myocytes. *J Physiol* 415: 233-249, 1989.
121. **Giles W, and Noble SJ**. Changes in membrane currents in bullfrog atrium produced by acetylcholine. *J Physiol* 261: 103-123, 1976.
122. **Gilman AG**. G proteins: transducers of receptor-generated signals. *Annu Rev Biochem* 56: 615-649, 1987.
123. **Ginsburg R, Esserman LJ, and Bristow MR**. Myocardial performance and extracellular ionized calcium in a severely failing human heart. *Ann Intern Med* 98: 603-606, 1983.
124. **Girod R, Eder-Colli L, Medilanski J, Dunant Y, Tabti N, and Poo MM**. Pulsatile release of acetylcholine by nerve terminals (synaptosomes) isolated from Torpedo electric organ. *J Physiol* 450: 325-340, 1992.
125. **Gnagey AL, Forte M, and Rosenberry TL**. Isolation and characterization of acetylcholinesterase from Drosophila. *J Biol Chem* 262: 13290-13298, 1987.
126. **Grant BD, and Adams JA**. Pre-steady-state kinetic analysis of cAMP-dependent protein kinase using rapid quench flow techniques. *Biochemistry* 35: 2022-2029, 1996.
127. **Gray AL, Johnson TA, Ardell JL, and Massari VJ**. Parasympathetic control of the heart. II. A novel interganglionic intrinsic cardiac circuit mediates neural control of heart rate. *J Appl Physiol* 96: 2273-2278, 2004.

128. **Graziano MP, Freissmuth M, and Gilman AG**. Expression of Gs alpha in Escherichia coli. Purification and properties of two forms of the protein. *J Biol Chem* 264: 409-418, 1989.
129. **Guo J, Ono K, and Noma A**. A sustained inward current activated at the diastolic potential range in rabbit sino-atrial node cells. *J Physiol* 483 (Pt 1): 1-13, 1995.
130. **Haga K, Haga T, Ichiyama A, Katada T, Kurose H, and Ui M**. Functional reconstitution of purified muscarinic receptors and inhibitory guanine nucleotide regulatory protein. *Nature* 316: 731-733, 1985.
131. **Hagiwara N, Irisawa H, and Kameyama M**. Contribution of two types of calcium currents to the pacemaker potentials of rabbit sino-atrial node cells. *J Physiol* 395: 233-253, 1988.
132. **Hagiwara N, Irisawa H, Kasanuki H, and Hosoda S**. Background current in sino-atrial node cells of the rabbit heart. *J Physiol* 448: 53-72, 1992.
133. **Halbrugge T, Ungell AL, Wolfel R, and Graefe KH**. Total body, systemic and pulmonary clearance and fractional extraction of unlabelled and differently 3H-labelled noradrenaline in the anaesthetized rabbit. *Naunyn Schmiedebergs Arch Pharmacol* 338: 361-367, 1988.
134. **Hall ZW**. Multiple forms of acetylcholinesterase and their distribution in endplate and non-endplate regions of rat diaphragm muscle. *J Neurobiol* 4: 343-361, 1973.
135. **Hancock JC, Hoover DB, and Hougland MW**. Distribution of muscarinic receptors and acetylcholinesterase in the rat heart. *J Auton Nerv Syst* 19: 59-66, 1987.
136. **Harden TK, Wolfe BB, and Molinoff PB**. Binding of iodinated beta adrenergic antagonists to proteins derived from rat heart. *Molecular Pharmacology* 12: 1-15, 1976.
137. **Hardouin S, Bourgeois F, Toraasson M, Oubenaissa A, Elalouf JM, Fellmann D, Dakhli T, Swynghedauw B, and Moalic JM**. Beta-adrenergic and muscarinic receptor mRNA accumulation in the sinoatrial node area of adult and senescent rat hearts. *Mech Ageing Dev* 100: 277-297, 1998.
138. **Harris EJ, and Hutter OF**. The Action of Acetylcholine on the Movements of Potassium Ions in the Sinus Venosus of the Heart. *Journal of Physiology-London* 133: P58-P59, 1956.
139. **Harvey RD, and Belevych AE**. Muscarinic regulation of cardiac ion channels. *Br J Pharmacol* 139: 1074-1084, 2003.
140. **Haubrich DR, Wang PF, and Wedeking PW**. Distribution and metabolism of intravenously administered choline[methyl- 3-H] and synthesis in vivo of acetylcholine in various tissues of guinea pigs. *J Pharmacol Exp Ther* 193: 246-255, 1975.
141. **Heath BM, and Terrar DA**. Protein kinase C enhances the rapidly activating delayed rectifier potassium current, IKr, through a reduction in C-type inactivation in guinea-pig ventricular myocytes. *J Physiol* 522 Pt 3: 391-402, 2000.
142. **Hedberg A, Minneman KP, and Molinoff PB**. Differential distribution of beta-1 and beta-2 adrenergic receptors in cat and guinea-pig heart. *J Pharmacol Exp Ther* 212: 503-508, 1980.
143. **Herberg FW, Dostmann WR, Zorn M, Davis SJ, and Taylor SS**. Crosstalk between domains in the regulatory subunit of cAMP-dependent protein kinase: influence of amino terminus on cAMP binding and holoenzyme formation. *Biochemistry* 33: 7485-7494, 1994.
144. **Herberg FW, Maleszka A, Eide T, Vossebein L, and Tasken K**. Analysis of A-kinase anchoring protein (AKAP) interaction with protein kinase A (PKA) regulatory subunits: PKA isoform specificity in AKAP binding. *J Mol Biol* 298: 329-339, 2000.
145. **Hescheler J, Kameyama M, and Trautwein W**. On the mechanism of muscarinic inhibition of the cardiac Ca current. *Pflugers Arch* 407: 182-189, 1986.
146. **Higashijima T, Ferguson KM, Smigel MD, and Gilman AG**. The effect of GTP and Mg2+ on the GTPase activity and the fluorescent properties of Go. *J Biol Chem* 262: 757-761, 1987.
147. **Higashijima T, Ferguson KM, Sternweis PC, Ross EM, Smigel MD, and Gilman AG**. The effect of activating ligands on the intrinsic fluorescence of guanine nucleotide-binding regulatory proteins. *J Biol Chem* 262: 752-756, 1987.
148. **Higashijima T, Ferguson KM, Sternweis PC, Smigel MD, and Gilman AG**. Effects of Mg2+ and the beta gamma-subunit complex on the interactions of guanine nucleotides with G proteins. *J Biol Chem* 262: 762-766, 1987.

149. **Hilf G, and Jakobs KH**. Activation of cardiac G-proteins by muscarinic acetylcholine receptors: regulation by Mg2+ and Na+ ions. *Eur J Pharmacol* 172: 155-163, 1989.
150. **Hirsch J, Leibel RL, Mackintosh R, and Aguirre A**. Heart rate variability as a measure of autonomic function during weight change in humans. *Am J Physiol* 261: R1418-1423, 1991.
151. **Hodgkin AL, and Huxley AF**. A quantitative description of membrane current and its application to conduction and excitation in nerve. *J Physiol* 117: 500-544, 1952.
152. **Hofmann F, Beavo JA, Bechtel PJ, and Krebs EG**. Comparison of adenosine 3':5'-monophosphate-dependent protein kinases from rabbit skeletal and bovine heart muscle. *J Biol Chem* 250: 7795-7801, 1975.
153. **Honjo H, Boyett MR, Kodama I, and Toyama J**. Correlation between electrical activity and the size of rabbit sino-atrial node cells. *J Physiol* 496 (Pt 3): 795-808, 1996.
154. **Honjo H, Kodama I, Zang WJ, and Boyett MR**. Desensitization to acetylcholine in single sinoatrial node cells isolated from rabbit hearts. *Am J Physiol* 263: H1779-1789, 1992.
155. **Hool LC, and Harvey RD**. Role of beta1- and beta2-adrenergic receptors in regulation of Cl- and Ca2+ channels in guinea pig ventricular myocytes. *Am J Physiol* 273: H1669-1676, 1997.
156. **Hoover DB, Baisden RH, and Xi-Moy SX**. Localization of muscarinic receptor mRNAs in rat heart and intrinsic cardiac ganglia by in situ hybridization. *Circ Res* 75: 813-820, 1994.
157. **Hulme EC, Birdsall NJ, and Buckley NJ**. Muscarinic receptor subtypes. *Annu Rev Pharmacol Toxicol* 30: 633-673, 1990.
158. **Iacono G, and Vassalle M**. Acetylcholine Increases Intracellular Sodium Activity in Sheep Cardiac Purkinje-Fibers. *American Journal of Physiology* 256: H1407-H1416, 1989.
159. **Inc. A**. free-wallpapers and backgrounds 2012 for desktop [website]. http://backgrounds2012.blogspot.com/2011/05/human-heart.html. [07/11/2011, 2011].
160. **Inomata N, Ishihara T, and Akaike N**. Activation kinetics of the acetylcholine-gated potassium current in isolated atrial cells. *Am J Physiol* 257: C646-650, 1989.
161. **Iversen LL**. Role of transmitter uptake mechanisms in synaptic neurotransmission. *Br J Pharmacol* 41: 571-591, 1971.
162. **Iversen LL**. *The uptake and storage of noradrenaline in sympathetic nerves*. London,: Cambridge University Press, 1967, p. xiii, 252 p.
163. **Iversen LL**. The uptake of catechol amines at high perfusion concentrations in the rat isolated heart: A novel catechol amine uptake process. *Br J Pharmacol Chemother* 25: 18-33, 1965.
164. **Iyengar R**. Molecular and Functional Diversity of Mammalian G(S)-Stimulated Adenylyl Cyclases. *Faseb Journal* 7: 768-775, 1993.
165. **Jalink K, and Moolenaar WH**. G protein-coupled receptors: the inside story. *Bioessays* 32: 13-16, 2010.
166. **Johnston C, Siderovski, D.** Resolving G protein-coupled receptor signaling mechanics in vivo using fluorescent biosensors. *CellScience Reviews* 2: 2006.
167. **Jope RS**. High affinity choline transport and acetylCoA production in brain and their roles in the regulation of acetylcholine synthesis. *Brain Res* 180: 313-344, 1979.
168. **Kajimoto K, Hagiwara N, Kasanuki H, and Hosoda S**. Contribution of phosphodiesterase isozymes to the regulation of the L-type calcium current in human cardiac myocytes. *Br J Pharmacol* 121: 1549-1556, 1997.
169. **Kamal MA, Nasim FH, and al-Jafari AA**. In vitro inhibition of human erythrocyte acetylcholinesterase (EC3.1.1.7) by an antineoplastic drug methotrexate. *Mol Cell Biochem* 159: 47-53, 1996.
170. **Kameyama K, Haga K, Haga T, Kontani K, Katada T, and Fukada Y**. Activation by G protein beta gamma subunits of beta-adrenergic and muscarinic receptor kinase. *J Biol Chem* 268: 7753-7758, 1993.
171. **Kamosinska B, Nowicki D, Szulczyk A, and Szulczyk P**. Spinal segmental sympathetic outflow to cervical sympathetic trunk, vertebral nerve, inferior cardiac nerve and sympathetic fibres in the thoracic vagus. *J Auton Nerv Syst* 32: 199-204, 1991.

172. **Karas M, Larochelle P, LeBlanc RA, Dube B, Nadeau R, and Champlain J**. Attenuation of autonomic nervous system functions in hypertensive patients at rest and during orthostatic stimulation. *J Clin Hypertens (Greenwich)* 10: 97-104, 2008.
173. **Karino K, Nabika T, Nishiki M, Iijima K, Nagai A, and Masuda J**. Evaluation of diabetic neuropathy using the tone-entropy analysis, a noninvasive method to estimate the autonomic nervous function. *Biomed Res* 30: 1-6, 2009.
174. **Karliner JS, Simpson PC, Taylor JE, Honbo N, and Woloszyn W**. Adrenergic receptor characteristics of cardiac myocytes cultured in serum-free medium: comparison with serum-supplemented medium. *Biochem Biophys Res Commun* 128: 376-382, 1985.
175. **Karnovsky MJ**. Localization Cholinesterase Activity in Rat Cardiac Muscle by Electron Microscopy. *Journal of Cell Biology* 23: 217-&, 1964.
176. **Kass DA**. Message delivered: how myocytes control cAMP signaling. *Circ Res* 102: 1002-1004, 2008.
177. **Katada T, Bokoch GM, Northup JK, Ui M, and Gilman AG**. The inhibitory guanine nucleotide-binding regulatory component of adenylate cyclase. Properties and function of the purified protein. *J Biol Chem* 259: 3568-3577, 1984.
178. **Katada T, Bokoch GM, Smigel MD, Ui M, and Gilman AG**. The inhibitory guanine nucleotide-binding regulatory component of adenylate cyclase. Subunit dissociation and the inhibition of adenylate cyclase in S49 lymphoma cyc- and wild type membranes. *J Biol Chem* 259: 3586-3595, 1984.
179. **Katada T, Kusakabe K, Oinuma M, and Ui M**. A novel mechanism for the inhibition of adenylate cyclase via inhibitory GTP-binding proteins. Calmodulin-dependent inhibition of the cyclase catalyst by the beta gamma-subunits of GTP-binding proteins. *J Biol Chem* 262: 11897-11900, 1987.
180. **Katada T, Northup JK, Bokoch GM, Ui M, and Gilman AG**. The inhibitory guanine nucleotide-binding regulatory component of adenylate cyclase. Subunit dissociation and guanine nucleotide-dependent hormonal inhibition. *J Biol Chem* 259: 3578-3585, 1984.
181. **Katada T, Oinuma M, and Ui M**. Two guanine nucleotide-binding proteins in rat brain serving as the specific substrate of islet-activating protein, pertussis toxin. Interaction of the alpha-subunits with beta gamma-subunits in development of their biological activities. *J Biol Chem* 261: 8182-8191, 1986.
182. **Katona PG, and Jih F**. Respiratory sinus arrhythmia: noninvasive measure of parasympathetic cardiac control. *J Appl Physiol* 39: 801-805, 1975.
183. **Katona PG, Poitras JW, Barnett GO, and Terry BS**. Cardiac vagal efferent activity and heart period in the carotid sinus reflex. *Am J Physiol* 218: 1030-1037, 1970.
184. **Katz B, and Miledi R**. The binding of acetylcholine to receptors and its removal from the synaptic cleft. *J Physiol* 231: 549-574, 1973.
185. **Kawashima K, Oohata H, Fujimoto K, and Suzuki T**. Plasma concentration of acetylcholine in young women. *Neurosci Lett* 80: 339-342, 1987.
186. **Kies P, Wichter T, Schafers M, Paul M, Schafers KP, Eckardt L, Stegger L, Schulze-Bahr E, Rimoldi O, Breithardt G, Schober O, and Camici PG**. Abnormal myocardial presynaptic norepinephrine recycling in patients with Brugada syndrome. *Circulation* 110: 3017-3022, 2004.
187. **Kirpekar SM, and Lewis JJ**. Some effects of reserpine and hydraliazine upon tissue respiration and the concentration of adenosine nucleotides in certain tissues. *Br J Pharmacol Chemother* 14: 40-45, 1959.
188. **Kithas PA, Artman M, Thompson WJ, and Strada SJ**. Subcellular distribution of high-affinity type IV cyclic AMP phosphodiesterase activity in rabbit ventricular myocardium: relations to the effects of cardiotonic drugs. *Circ Res* 62: 782-789, 1988.
189. **Kleuss C, Raw AS, Lee E, Sprang SR, and Gilman AG**. Mechanism of GTP hydrolysis by G-protein alpha subunits. *Proc Natl Acad Sci U S A* 91: 9828-9831, 1994.

190. **Koch WJ, Inglese J, Stone WC, and Lefkowitz RJ**. The binding site for the beta gamma subunits of heterotrimeric G proteins on the beta-adrenergic receptor kinase. *J Biol Chem* 268: 8256-8260, 1993.
191. **Kochanek K, Xu J, Murphy S, Minino A, and Kung H**. Deaths: Preliminary Data for 2009 HYattsville, MD: 2011.
192. **Kodama I, Boyett MR, Suzuki R, Honjo H, and Toyama J**. Regional differences in the response of the isolated sino-atrial node of the rabbit to vagal stimulation. *J Physiol* 495 (Pt 3): 785-801, 1996.
193. **Koppanyi T, and Macfarlane MD**. The Effect of Atropine on Responses of Normal and Reserpinized Rabbit Atria to Acetylcholine. *Life Sci* 3: 1135-1143, 1964.
194. **Kovyazina IV, Nikolsky EE, and Gaynulov RK**. Dynamics of acetylcholine release the frog neuromuscular junction during rhythmic stimulation and under choline deficiency. *Neurophysiology+* 32: 200-201, 2000.
195. **Krejci E, Martinez-Pena y Valenzuela I, Ameziane R, and Akaaboune M**. Acetylcholinesterase dynamics at the neuromuscular junction of live animals. *J Biol Chem* 281: 10347-10354, 2006.
196. **Krnjevic K, and Mitchell JF**. Diffusion of acetylcholine in agar gels and in the isolated rat diaphragm. *J Physiol* 153: 562-572, 1960.
197. **Kukanova B, and Mravec B**. Complex intracardiac nervous system. *Bratisl Lek Listy* 107: 45-51, 2006.
198. **Kurata Y, Hisatome I, Imanishi S, and Shibamoto T**. Dynamical description of sinoatrial node pacemaking: improved mathematical model for primary pacemaker cell. *Am J Physiol Heart Circ Physiol* 283: H2074-2101, 2002.
199. **Lakatta EG, and DiFrancesco D**. What keeps us ticking: a funny current, a calcium clock, or both? *J Mol Cell Cardiol* 47: 157-170, 2009.
200. **Lakatta EG, Maltsev VA, Bogdanov KY, Stern MD, and Vinogradova TM**. Cyclic variation of intracellular calcium: a critical factor for cardiac pacemaker cell dominance. *Circ Res* 92: e45-50, 2003.
201. **Land BR, Harris WV, Salpeter EE, and Salpeter MM**. Diffusion and binding constants for acetylcholine derived from the falling phase of miniature endplate currents. *Proc Natl Acad Sci U S A* 81: 1594-1598, 1984.
202. **Langeberg LK, and Scott JD**. A-kinase-anchoring proteins. *J Cell Sci* 118: 3217-3220, 2005.
203. **Lazareno S, and Birdsall NJ**. Detection, quantitation, and verification of allosteric interactions of agents with labeled and unlabeled ligands at G protein-coupled receptors: interactions of strychnine and acetylcholine at muscarinic receptors. *Mol Pharmacol* 48: 362-378, 1995.
204. **Lee YC, Wang HP, Lin LY, Chuang KJ, Chiu HM, Wu MS, Chen MF, and Lin JT**. Circadian change of cardiac autonomic function in correlation with intra-esophageal pH. *J Gastroenterol Hepatol* 21: 1302-1308, 2006.
205. **Lefkowitz RJ**. Heterogeneity of adenylate cyclase-coupled beta-adrenergic receptors. *Biochem Pharmacol* 24: 583-590, 1975.
206. **Lefkowitz RJ, and Haber E**. A fraction of the ventricular myocardium that has the specificity of the cardiac beta-adrenergic receptor. *Proc Natl Acad Sci U S A* 68: 1773-1777, 1971.
207. **Lefkowitz RJ, Haber E, and O'Hara D**. Identification of the cardiac beta-adrenergic receptor protein: solubilization and purification by affinity chromatography. *Proc Natl Acad Sci U S A* 69: 2828-2832, 1972.
208. **Lefkowitz RJ, and Levey GS**. Norepinephrine: dissociation of -receptor binding from adenylate cyclase activation in solubilized myocardium. *Life Sci II* 11: 821-828, 1972.
209. **Lei M, Honjo H, Kodama I, and Boyett MR**. Characterisation of the transient outward K+ current in rabbit sinoatrial node cells. *Cardiovascular Research* 46: 433-441, 2000.
210. **Levy MN**. Sympathetic-parasympathetic interactions in the heart. *Circ Res* 29: 437-445, 1971.

211. **Li J, Qu J, and Nathan RD**. Ionic basis of ryanodine's negative chronotropic effect on pacemaker cells isolated from the sinoatrial node. *Am J Physiol* 273: H2481-2489, 1997.
212. **Lindblad DS, Murphey CR, Clark JW, and Giles WR**. A model of the action potential and underlying membrane currents in a rabbit atrial cell. *Am J Physiol* 271: H1666-1696, 1996.
213. **Linder ME, Ewald DA, Miller RJ, and Gilman AG**. Purification and characterization of Go alpha and three types of Gi alpha after expression in Escherichia coli. *J Biol Chem* 265: 8243-8251, 1990.
214. **Lindmar R, Loffelholz K, and Weide W**. Interstitial washout and hydrolysis of acetylcholine in the perfused heart. *Naunyn Schmiedebergs Arch Pharmacol* 318: 295-300, 1982.
215. **Lipsius SL, Huser J, and Blatter LA**. Intracellular Ca2+ release sparks atrial pacemaker activity. *News Physiol Sci* 16: 101-106, 2001.
216. **Lipsius SL, and Vassalle M**. Effects of acetylcholine on potassium movements in the guinea-pig sinus node. *J Pharmacol Exp Ther* 201: 669-677, 1977.
217. **Liu R, Ramani B, Soto D, De Arcangelis V, and Xiang Y**. Agonist dose-dependent phosphorylation by protein kinase A and G protein-coupled receptor kinase regulates beta2 adrenoceptor coupling to G(i) proteins in cardiomyocytes. *J Biol Chem* 284: 32279-32287, 2009.
218. **Loffelholz K**. Release of acetylcholine in the isolated heart. *Am J Physiol* 240: H431-440, 1981.
219. **Loffelholz K, and Pappano AJ**. The parasympathetic neuroeffector junction of the heart. *Pharmacol Rev* 37: 1-24, 1985.
220. **Logothetis DE, Kurachi Y, Galper J, Neer EJ, and Clapham DE**. The beta gamma subunits of GTP-binding proteins activate the muscarinic K+ channel in heart. *Nature* 325: 321-326, 1987.
221. **Lugnier C, Muller B, Le Bec A, Beaudry C, and Rousseau E**. Characterization of indolidan- and rolipram-sensitive cyclic nucleotide phosphodiesterases in canine and human cardiac microsomal fractions. *J Pharmacol Exp Ther* 265: 1142-1151, 1993.
222. **Lyashkov AE, Vinogradova TM, Zahanich I, Li Y, Younes A, Nuss HB, Spurgeon HA, Maltsev VA, and Lakatta EG**. Cholinergic receptor signaling modulates spontaneous firing of sinoatrial nodal cells via integrated effects on PKA-dependent Ca(2+) cycling and I(KACh). *Am J Physiol Heart Circ Physiol* 297: H949-959, 2009.
223. **Maguire ME, Goldmann PH, and Gilman AG**. Reaction of [H-3] Norepinephrine with Particulate Fractions of Cells Responsive to Catecholamines. *Molecular Pharmacology* 10: 563-581, 1974.
224. **Maguire ME, Wiklund RA, Anderson HJ, and Gilman AG**. Binding of (125I)iodohydroxybenzylpindolol to putative beta-adrenergic receptors of rat glioma cells and other cell clones. *J Biol Chem* 251: 1221-1231, 1976.
225. **Mahama PA, and Linderman JJ**. A Monte Carlo study of the dynamics of G-protein activation. *Biophys J* 67: 1345-1357, 1994.
226. **Malpas SC, and Maling TJ**. Heart-rate variability and cardiac autonomic function in diabetes. *Diabetes* 39: 1177-1181, 1990.
227. **Maltsev VA, and Lakatta EG**. A novel quantitative explanation for the autonomic modulation of cardiac pacemaker cell automaticity via a dynamic system of sarcolemmal and intracellular proteins. *Am J Physiol Heart Circ Physiol* 298: H2010-2023, 2010.
228. **Maltsev VA, and Lakatta EG**. Synergism of coupled subsarcolemmal Ca2+ clocks and sarcolemmal voltage clocks confers robust and flexible pacemaker function in a novel pacemaker cell model. *Am J Physiol Heart Circ Physiol* 2009.
229. **Maltsev VA, Vinogradova TM, Bogdanov KY, Lakatta EG, and Stern MD**. Diastolic calcium release controls the beating rate of rabbit sinoatrial node cells: numerical modeling of the coupling process. *Biophys J* 86: 2596-2605, 2004.
230. **Mangoni ME, Couette B, Bourinet E, Platzer J, Reimer D, Striessnig J, and Nargeot J**. Functional role of L-type Ca(v)13Ca(2+) channels in cardiac pacemaker activity. *P Natl Acad Sci USA* 100: 5543-5548, 2003.

231. **Mangoni ME, and Nargeot J**. Genesis and regulation of the heart automaticity. *Physiol Rev* 88: 919-982, 2008.
232. **Matthews-Bellinger J, and Salpeter MM**. Distribution of acetylcholine receptors at frog neuromuscular junctions with a discussion of some physiological implications. *J Physiol* 279: 197-213, 1978.
233. **McConnachie G, Langeberg LK, and Scott JD**. AKAP signaling complexes: getting to the heart of the matter. *Trends Mol Med* 12: 317-323, 2006.
234. **McKean TA**. The density of beta-adrenoreceptors in cardiac muscle membranes of muskrats and guinea pigs. *Gen Pharmacol* 19: 725-727, 1988.
235. **McNeely JD, Windham BG, and Anderson DE**. Dietary sodium effects on heart rate variability in salt sensitivity of blood pressure. *Psychophysiology* 45: 405-411, 2008.
236. **Means AR, and Dedman JR**. Calmodulin--an intracellular calcium receptor. *Nature* 285: 73-77, 1980.
237. **Medugorac I**. Different fractions in the normal and hypertrophied rat ventricular myocardium: an analysis of two models of hypertrophy. *Basic Res Cardiol* 71: 608-623, 1976.
238. **Mendez C, Gruhzit CC, and Moe GK**. Influence of cycle length upon refractory period of auricles, ventricles, and A-V node in the dog. *Am J Physiol* 184: 287-295, 1956.
239. **Mesangeau D, Laude D, and Elghozi JL**. Early detection of cardiovascular autonomic neuropathy in diabetic pigs using blood pressure and heart rate variability. *Cardiovasc Res* 45: 889-899, 2000.
240. **Milligan G, and Klee WA**. The inhibitory guanine nucleotide-binding protein (Ni) purified from bovine brain is a high affinity GTPase. *J Biol Chem* 260: 2057-2063, 1985.
241. **Misu Y, and Kubo T**. A pharmacological evidence for the existence of intracardiac sympathetic ganglia in the rabbit. *Jpn J Pharmacol* 19: 464-465, 1969.
242. **Mitsuiye T, Shinagawa Y, and Noma A**. Sustained inward current during pacemaker depolarization in mammalian sinoatrial node cells. *Circ Res* 87: 88-91, 2000.
243. **Molgaard H, Christensen PD, Sorensen KE, Christensen CK, and Mogensen CE**. Association of 24-h cardiac parasympathetic activity and degree of nephropathy in IDDM patients. *Diabetes* 41: 812-817, 1992.
244. **Mosser VA, Amana IJ, and Schimerlik MI**. Kinetic analysis of M2 muscarinic receptor activation of Gi in Sf9 insect cell membranes. *J Biol Chem* 277: 922-931, 2002.
245. **Mueller H, Motulsky HJ, and Sklar LA**. The potency and kinetics of the beta-adrenergic receptors on human neutrophils. *Mol Pharmacol* 34: 347-353, 1988.
246. **Mukkamala R, and Cohen RJ**. A forward model-based validation of cardiovascular system identification. *Am J Physiol Heart Circ Physiol* 281: H2714-2730, 2001.
247. **Mullershausen F, Zecri F, Cetin C, Billich A, Guerini D, and Seuwen K**. Persistent signaling induced by FTY720-phosphate is mediated by internalized S1P1 receptors. *Nat Chem Biol* 5: 428-434, 2009.
248. **Muntz KH, Calianos TA, Buja LM, Willerson JT, Bernatowicz M, Homcy CJ, and Graham RM**. Electron microscopic localization of the beta-adrenergic receptor using a ferritin-alprenolol probe. *Mol Pharmacol* 34: 444-451, 1988.
249. **Murray KJ**. Cyclic AMP-dependent protein kinase activity ratio assay. *Methods Mol Biol* 41: 113-122, 1995.
250. **Neubig RR, Gantzos RD, and Brasier RS**. Agonist and antagonist binding to alpha 2-adrenergic receptors in purified membranes from human platelets. Implications of receptor-inhibitory nucleotide-binding protein stoichiometry. *Mol Pharmacol* 28: 475-486, 1985.
251. **Nikolaev VO, Bunemann M, Schmitteckert E, Lohse MJ, and Engelhardt S**. Cyclic AMP imaging in adult cardiac myocytes reveals far-reaching beta1-adrenergic but locally confined beta2-adrenergic receptor-mediated signaling. *Circ Res* 99: 1084-1091, 2006.
252. **Nilsson E, and Sporrong B**. Electron microscopic investigation of adrenergic and non-adrenergic axons in the rabbit SA-node. *Z Zellforsch Mikrosk Anat* 111: 404-412, 1970.

253. **Noble D**. Cardiac action and pacemaker potentials based on the Hodgkin-Huxley equations. *Nature* 188: 495-497, 1960.
254. **Noble D, Denyer JC, Brown HF, and DiFrancesco D**. Reciprocal role of the inward currents ib, Na and i(f) in controlling and stabilizing pacemaker frequency of rabbit sino-atrial node cells. *Proc Biol Sci* 250: 199-207, 1992.
255. **Northup JK, Smigel MD, and Gilman AG**. The guanine nucleotide activating site of the regulatory component of adenylate cyclase. Identification by ligand binding. *J Biol Chem* 257: 11416-11423, 1982.
256. **Northup JK, Smigel MD, Sternweis PC, and Gilman AG**. The subunits of the stimulatory regulatory component of adenylate cyclase. Resolution of the activated 45,000-dalton (alpha) subunit. *J Biol Chem* 258: 11369-11376, 1983.
257. **Northup JK, Sternweis PC, and Gilman AG**. The subunits of the stimulatory regulatory component of adenylate cyclase. Resolution, activity, and properties of the 35,000-dalton (beta) subunit. *J Biol Chem* 258: 11361-11368, 1983.
258. **Olufsen MS, Ottesen JT, Tran HT, Ellwein LM, Lipsitz LA, and Novak V**. Blood pressure and blood flow variation during postural change from sitting to standing: model development and validation. *J Appl Physiol* 99: 1523-1537, 2005.
259. **Onaran HO, Costa T, and Rodbard D**. Beta gamma subunits of guanine nucleotide-binding proteins and regulation of spontaneous receptor activity: thermodynamic model for the interaction between receptors and guanine nucleotide-binding protein subunits. *Mol Pharmacol* 43: 245-256, 1993.
260. **Opie LH, Mansford KR, and Owen P**. Effects of increased heart work on glycolysis and adenine nucleotides in the perfused heart of normal and diabetic rats. *Biochem J* 124: 475-490, 1971.
261. **Opthof T**. The mammalian sinoatrial node. *Cardiovasc Drugs Ther* 1: 573-597, 1988.
262. **Opthof T, de Jonge B, Jongsma HJ, and Bouman LN**. Functional morphology of the mammalian sinuatrial node. *Eur Heart J* 8: 1249-1259, 1987.
263. **Osadchii OE**. Myocardial phosphodiesterases and regulation of cardiac contractility in health and cardiac disease. *Cardiovasc Drugs Ther* 21: 171-194, 2007.
264. **Osterrieder W, Noma A, and Trautwein W**. On the kinetics of the potassium channel activated by acetylcholine in the S-A node of the rabbit heart. *Pflugers Arch* 386: 101-109, 1980.
265. **Osterrieder W, Yang QF, and Trautwein W**. The time course of the muscarinic response to ionophoretic acetylcholine application to the S-A node of the rabbit heart. *Pflugers Arch* 389: 283-291, 1981.
266. **Packer M, Carver JR, Rodeheffer RJ, Ivanhoe RJ, DiBianco R, Zeldis SM, Hendrix GH, Bommer WJ, Elkayam U, Kukin ML, and et al.** Effect of oral milrinone on mortality in severe chronic heart failure. The PROMISE Study Research Group. *N Engl J Med* 325: 1468-1475, 1991.
267. **Park DH, Shin CJ, Hong SC, Yu J, Ryu SH, Kim EJ, Shin HB, and Shin BH**. Correlation between the severity of obstructive sleep apnea and heart rate variability indices. *J Korean Med Sci* 23: 226-231, 2008.
268. **Park SB, Lee BC, and Jeong KS**. Standardized tests of heart rate variability for autonomic function tests in healthy Koreans. *Int J Neurosci* 117: 1707-1717, 2007.
269. **Patel TB, Du ZY, Pierre S, Cartin L, and Scholich K**. Molecular biological approaches to unravel adenylyl cyclase signaling and function. *Gene* 269: 13-25, 2001.
270. **Petit-Jacques J, Bois P, Bescond J, and Lenfant J**. Mechanism of muscarinic control of the high-threshold calcium current in rabbit sino-atrial node myocytes. *Pflugers Arch* 423: 21-27, 1993.
271. **Pfeuffer E, Dreher RM, Metzger H, and Pfeuffer T**. Catalytic unit of adenlyate cyclase: purification and identification by affinity crosslinking. *Proc Natl Acad Sci U S A* 82: 3086-3090, 1985.
272. **Pidoux G, and Tasken K**. Specificity and spatial dynamics of protein kinase A signaling organized by A-kinase-anchoring proteins. *J Mol Endocrinol* 44: 271-284, 2010.

273. **Pihel K, Schroeder TJ, and Wightman RM**. Rapid and Selective Cyclic Voltammetric Measurements of Epinephrine and Norepinephrine as a Method to Measure Secretion from Single Bovine Adrenal-Medullary Cells. *Anal Chem* 66: 4532-4537, 1994.
274. **Pott L**. Effects of fast and slowly acting antagonists on the time course of the muscarinic response in guinea-pig atrial muscle. *Pflugers Arch* 399: 35-41, 1983.
275. **Pott L, and Pusch H**. A kinetic model for the muscarinic action of acetylcholine. *Pflugers Arch* 383: 75-77, 1979.
276. **Purves RD**. The time course of cellular responses to iontophoretically applied drugs. *J Theor Biol* 65: 327-344, 1977.
277. **Randall DC**. Towards an understanding of the function of the intrinsic cardiac ganglia. *J Physiol* 528: 406, 2000.
278. **Randall DC, Brown DR, McGuirt AS, Thompson GW, Armour JA, and Ardell JL**. Interactions within the intrinsic cardiac nervous system contribute to chronotropic regulation. *Am J Physiol Regul Integr Comp Physiol* 285: R1066-1075, 2003.
279. **Rangel-Aldao R, and Rosen OM**. Dissociation and reassociation of the phosphorylated and nonphosphorylated forms of adenosine 3':5' -monophosphate-dependent protein kinase from bovine cardiac muscle. *J Biol Chem* 251: 3375-3380, 1976.
280. **Rangel-Aldao R, and Rosen OM**. Effect of cAMP and ATP on the reassociation of phosphorylated and nonphosphorylated subunits of the cAMP-dependent protein kinase from bovine cardiac muscle. *J Biol Chem* 252: 7140-7145, 1977.
281. **Ransnas LA, Jasper JR, Leiber D, and Insel PA**. Beta-adrenergic-receptor-mediated dissociation and membrane release of the Gs protein in S49 lymphoma-cell membranes. Dependence on Mg2+ and GTP. *Biochem J* 283 (Pt 2): 519-524, 1992.
282. **Ransnas LA, Leiber D, and Insel PA**. Inhibition of subunit dissociation and release of the stimulatory G-protein, Gs, by beta gamma-subunits and somatostatin in S49 lymphoma cell membranes. *Biochem J* 280 (Pt 2): 303-307, 1991.
283. **Rice ME, Gerhardt GA, Hierl PM, Nagy G, and Adams RN**. Diffusion coefficients of neurotransmitters and their metabolites in brain extracellular fluid space. *Neuroscience* 15: 891-902, 1985.
284. **Rickenbacher J, and Muller E**. The development of cholinergic ganglia in the chick embryo heart. *Anat Embryol (Berl)* 155: 253-258, 1979.
285. **Robison GA, Butcher RW, Oye I, Morgan HE, and Sutherland EW**. The effect of epinephrine on adenosine 3', 5'-phosphate levels in the isolated perfused rat heart. *Mol Pharmacol* 1: 168-177, 1965.
286. **Rosenberry TL**. Acetylcholinesterase. *Adv Enzymol Relat Areas Mol Biol* 43: 103-218, 1975.
287. **Rosenberry TL, and Bernhard SA**. Studies of catalysis by acetylcholinesterase. Synergistic effects of inhibitors during the hydrolysis of acetic acid esters. *Biochemistry* 11: 4308-4321, 1972.
288. **Ruhparwar A, Kallenbach K, Klein G, Bara C, Ghodsizad A, Sigg DC, Karck M, Haverich A, and Niehaus M**. Adenylate-Cyclase VI transforms ventricular cardiomyocytes into biological pacemaker cells. *Tissue Eng Part A* 16: 1867-1872, 2010.
289. **Sakai R, Hagiwara N, Matsuda N, Kasanuki H, and Hosoda S**. Sodium-potassium pump current in rabbit sino-atrial node cells. *Journal of Physiology-London* 490: 51-62, 1996.
290. **Sattarahmady N, Heli H, and Moosavi-Movahedi AA**. An electrochemical acetylcholine biosensor based on nanoshells of hollow nickel microspheres-carbon microparticles-Nafion nanocomposite. *Biosens Bioelectron*.
291. **Savendahl L, Mar MH, Underwood LE, and Zeisel SH**. Prolonged fasting in humans results in diminished plasma choline concentrations but does not cause liver dysfunction. *Am J Clin Nutr* 66: 622-625, 1997.
292. **Sevilla N, Steer ML, and Levitzki A**. Synergistic activation of adenylate cyclase by guanylyl imidophosphate and epinephrine. *Biochemistry* 15: 3493-3499, 1976.

293. **Shahid M, and Nicholson CD**. Comparison of cyclic nucleotide phosphodiesterase isoenzymes in rat and rabbit ventricular myocardium: positive inotropic and phosphodiesterase inhibitory effects of Org 30029, milrinone and rolipram. *Naunyn Schmiedebergs Arch Pharmacol* 342: 698-705, 1990.
294. **Shannon TR, Wang F, Puglisi J, Weber C, and Bers DM**. A mathematical treatment of integrated Ca dynamics within the ventricular myocyte. *Biophys J* 87: 3351-3371, 2004.
295. **Siegel GJ, Albers RW, Brady ST, and Price DL**. *Basic neurochemistry : molecular, cellular, and medical aspects*. Boston: Elsevier Academic, 2006, p. xxiv, 992 p.
296. **Slenter VA, Salata JJ, and Jalife J**. Vagal control of pacemaker periodicity and intranodal conduction in the rabbit sinoatrial node. *Circ Res* 54: 436-446, 1984.
297. **Smigel MD**. Purification of the catalyst of adenylate cyclase. *J Biol Chem* 261: 1976-1982, 1986.
298. **Smith FD, Langeberg LK, and Scott JD**. The where's and when's of kinase anchoring. *Trends Biochem Sci* 31: 316-323, 2006.
299. **Spiegel AM, Brown EM, Fedak SA, Woodard CJ, and Aurbach GD**. Holocatalytic state of adenylate cyclase in turkey erythrocyte membranes: formation with guanylylimidodiphosphate plus isoproterenol without effect on affinity of beta-receptor. *J Cyclic Nucleotide Res* 2: 47-56, 1976.
300. **Sprang SR**. G protein mechanisms: insights from structural analysis. *Annu Rev Biochem* 66: 639-678, 1997.
301. **Stauffer DA, and Karlin A**. Electrostatic potential of the acetylcholine binding sites in the nicotinic receptor probed by reactions of binding-site cysteines with charged methanethiosulfonates. *Biochemistry* 33: 6840-6849, 1994.
302. **Stein PK, Ehsani AA, Domitrovich PP, Kleiger RE, and Rottman JN**. Effect of exercise training on heart rate variability in healthy older adults. *Am Heart J* 138: 567-576, 1999.
303. **Stein PK, Rottman JN, and Kleiger RE**. Effect of 21 mg transdermal nicotine patches and smoking cessation on heart rate variability. *Am J Cardiol* 77: 701-705, 1996.
304. **Stern MD, Song LS, Cheng H, Sham JS, Yang HT, Boheler KR, and Rios E**. Local control models of cardiac excitation-contraction coupling. A possible role for allosteric interactions between ryanodine receptors. *J Gen Physiol* 113: 469-489, 1999.
305. **Stickle D, and Barber R**. The encounter coupling model for beta-adrenergic receptor/GTP-binding protein interaction in the S49 cell. Calculation of the encounter frequency. *Biochem Pharmacol* 43: 2015-2028, 1992.
306. **Stickle D, and Barber R**. Estimation of the kinetic constants for binding of epinephrine to beta-adrenergic receptors of the S49 cell. *Biochem Pharmacol* 42: 1069-1077, 1991.
307. **Stiles GL, and Lefkowitz RJ**. Thyroid hormone modulation of agonist--beta-adrenergic receptor interactions in the rat heart. *Life Sci* 28: 2529-2536, 1981.
308. **Stiles GL, Taylor S, and Lefkowitz RJ**. Human cardiac beta-adrenergic receptors: subtype heterogeneity delineated by direct radioligand binding. *Life Sci* 33: 467-473, 1983.
309. **Strauss HC, Bigger JT, Jr., and Hoffman BF**. Electrophysiologial and beta-receptor blocking effects of MJ 1999 on dog and rabbit cardiac tissue. *Circ Res* 26: 661-678, 1970.
310. **Sunahara RK, Dessauer CW, and Gilman AG**. Complexity and diversity of mammalian adenylyl cyclases. *Annu Rev Pharmacol Toxicol* 36: 461-480, 1996.
311. **Sunyer T, Codina J, and Birnbaumer L**. GTP hydrolysis by pure Ni, the inhibitory regulatory component of adenylyl cyclases. *J Biol Chem* 259: 15447-15451, 1984.
312. **Szegletes T, Mallender WD, and Rosenberry TL**. Nonequilibrium analysis alters the mechanistic interpretation of inhibition of acetylcholinesterase by peripheral site ligands. *Biochemistry* 37: 4206-4216, 1998.
313. **Tai K, Bond SD, MacMillan HR, Baker NA, Holst MJ, and McCammon JA**. Finite element simulations of acetylcholine diffusion in neuromuscular junctions. *Biophys J* 84: 2234-2241, 2003.
314. **Takai K, Kurashina Y, Suzuki-Hori C, Okamoto H, and Hayaishi O**. Adenylate cyclase from Brevibacterium liquefaciens. I. Purification, crystallization, and some properties. *J Biol Chem* 249: 1965-1972, 1974.

315. **Tang WJ, and Gilman AG**. Type-specific regulation of adenylyl cyclase by G protein beta gamma subunits. *Science* 254: 1500-1503, 1991.
316. **Tang WJ, Krupinski J, and Gilman AG**. Expression and characterization of calmodulin-activated (type I) adenylylcyclase. *J Biol Chem* 266: 8595-8603, 1991.
317. **Taniguchi T, Fujiwara M, Lee JJ, and Hidaka H**. Cyclic 3':5'-nucleotide phosphodiesterase of rabbit sinoatrial node. *Biochim Biophys Acta* 522: 465-476, 1978.
318. **Taniguchi T, Fujiwara M, Lee JJ, and Hidaka H**. Effect of acetylcholine on the norepinephrine-induced positive chronotropy and increase in cyclic nucleotides of isolated rabbit sinoatrial node. *Circ Res* 45: 493-504, 1979.
319. **Taniguchi T, Fujiwara M, Lee JJ, and Hidaka H**. Effect of cholera enterotoxin on pacemaker rate and cyclic adenosine 3':5'-monophosphate in isolated rabbit sinoatrial node. *J Pharmacol Exp Ther* 210: 349-353, 1979.
320. **Taniguchi T, Fujiwara M, and Ohsumi K**. Possible involvement of cyclic adenosine 3':5'-monophosphate in the genesis of catecholamine-induced tachycardia in isolated rabbit sinoatrial node. *J Pharmacol Exp Ther* 201: 678-688, 1977.
321. **Tasken K, and Aandahl EM**. Localized effects of cAMP mediated by distinct routes of protein kinase A. *Physiol Rev* 84: 137-167, 2004.
322. **Taussig R, Quarmby LM, and Gilman AG**. Regulation of purified type I and type II adenylylcyclases by G protein beta gamma subunits. *J Biol Chem* 268: 9-12, 1993.
323. **Taylor CW**. The role of G proteins in transmembrane signalling. *Biochem J* 272: 1-13, 1990.
324. **Taylor EW, Jordan D, and Coote JH**. Central control of the cardiovascular and respiratory systems and their interactions in vertebrates. *Physiol Rev* 79: 855-916, 1999.
325. **Taylor SS, Kim C, Vigil D, Haste NM, Yang J, Wu J, and Anand GS**. Dynamics of signaling by PKA. *Biochim Biophys Acta* 1754: 25-37, 2005.
326. **Taylor SS, Yang J, Wu J, Haste NM, Radzio-Andzelm E, and Anand G**. PKA: a portrait of protein kinase dynamics. *Biochim Biophys Acta* 1697: 259-269, 2004.
327. **Tesmer JJ, Berman DM, Gilman AG, and Sprang SR**. Structure of RGS4 bound to AlF4--activated G(i alpha1): stabilization of the transition state for GTP hydrolysis. *Cell* 89: 251-261, 1997.
328. **Toda N, and Shimamoto K**. The influence of sympathetic stimulation on transmembrane potentials in the S-A node. *J Pharmacol Exp Ther* 159: 298-305, 1968.
329. **Tolkovsky AM, and Levitzki A**. Mode of coupling between the beta-adrenergic receptor and adenylate cyclase in turkey erythrocytes. *Biochemistry* 17: 3795, 1978.
330. **Toyoda F, Ding WG, and Matsuura H**. Responses of the sustained inward current to autonomic agonists in guinea-pig sino-atrial node pacemaker cells. *Br J Pharmacol* 144: 660-668, 2005.
331. **Trautwein W, and Uchizono K**. Electron Microscopic and Electrophysiologic Study of the Pacemaker in the Sino-Atrial Node of the Rabbit Heart. *Z Zellforsch Mikrosk Anat* 61: 96-109, 1963.
332. **Trewhella J**. Protein kinase A targeting and activation as seen by small-angle solution scattering. *Eur J Cell Biol* 85: 655-662, 2006.
333. **Tsuga H, Kameyama K, and Haga T**. Desensitization of human muscarinic acetylcholine receptor m2 subtypes is caused by their sequestration/internalization. *J Biochem* 124: 863-868, 1998.
334. **Tucek S**. *Acetylcholine synthesis in neurons*. London
New York: Chapman and Hall ;
Wiley, 1978, p. xiii, 259 p.
335. **Vallais F, Baselli G, Lucini D, and Pagani M**. Heart rate and vasomotor control during exercise. *Conf Proc IEEE Eng Med Biol Soc* 2007: 578-581, 2007.
336. **van Borren MM, Verkerk AO, Wilders R, Hajji N, Zegers JG, Bourier J, Tan HL, Verheijck EE, Peters SL, Alewijnse AE, and Ravesloot JH**. Effects of muscarinic receptor stimulation on Ca2+ transient, cAMP production and pacemaker frequency of rabbit sinoatrial node cells. *Basic Res Cardiol* 105: 73-87, 2010.
337. **Van Roon AM, Mulder LJ, Althaus M, and Mulder G**. Introducing a baroreflex model for studying cardiovascular effects of mental workload. *Psychophysiology* 41: 961-981, 2004.

338. **Vinogradova TM, Bogdanov KY, and Lakatta EG**. beta-Adrenergic stimulation modulates ryanodine receptor Ca(2+) release during diastolic depolarization to accelerate pacemaker activity in rabbit sinoatrial nodal cells. *Circ Res* 90: 73-79, 2002.
339. **Vinogradova TM, Fedorov VV, Yuzyuk TN, Zaitsev AV, and Rosenshtraukh LV**. Local cholinergic suppression of pacemaker activity in the rabbit sinoatrial node. *J Cardiovasc Pharm* 32: 413-424, 1998.
340. **Vinogradova TM, and Lakatta EG**. Regulation of basal and reserve cardiac pacemaker function by interactions of cAMP-mediated PKA-dependent Ca2+ cycling with surface membrane channels. *J Mol Cell Cardiol* 47: 456-474, 2009.
341. **Vinogradova TM, Lyashkov AE, Zhu W, Ruknudin AM, Sirenko S, Yang D, Deo S, Barlow M, Johnson S, Caffrey JL, Zhou YY, Xiao RP, Cheng H, Stern MD, Maltsev VA, and Lakatta EG**. High basal protein kinase A-dependent phosphorylation drives rhythmic internal Ca2+ store oscillations and spontaneous beating of cardiac pacemaker cells. *Circ Res* 98: 505-514, 2006.
342. **Vinogradova TM, Sirenko S, Lyashkov AE, Younes A, Li Y, Zhu W, Yang D, Ruknudin AM, Spurgeon H, and Lakatta EG**. Constitutive phosphodiesterase activity restricts spontaneous beating rate of cardiac pacemaker cells by suppressing local Ca2+ releases. *Circ Res* 102: 761-769, 2008.
343. **Vinogradova TM, Zhou YY, Bogdanov KY, Yang D, Kuschel M, Cheng H, and Xiao RP**. Sinoatrial node pacemaker activity requires Ca(2+)/calmodulin-dependent protein kinase II activation. *Circ Res* 87: 760-767, 2000.
344. **Vinogradova TM, Zhou YY, Maltsev V, Lyashkov A, Stern M, and Lakatta EG**. Rhythmic ryanodine receptor Ca2+ releases during diastolic depolarization of sinoatrial pacemaker cells do not require membrane depolarization. *Circ Res* 94: 802-809, 2004.
345. **Waelbroeck M, Taton G, Delhaye M, Chatelain P, Camus JC, Pochet R, Leclerc JL, De Smet JM, Robberecht P, and Christophe J**. The human heart beta-adrenergic receptors. II. Coupling of beta 2-adrenergic receptors with the adenylate cyclase system. *Mol Pharmacol* 24: 174-182, 1983.
346. **Wall MA, Coleman DE, Lee E, Iniguez-Lluhi JA, Posner BA, Gilman AG, and Sprang SR**. The structure of the G protein heterotrimer Gi alpha 1 beta 1 gamma 2. *Cell* 83: 1047-1058, 1995.
347. **Walsh KB, Begenisich TB, and Kass RS**. Beta-adrenergic modulation of cardiac ion channels. Differential temperature sensitivity of potassium and calcium currents. *J Gen Physiol* 93: 841-854, 1989.
348. **Walsh KB, and Kass RS**. Regulation of a heart potassium channel by protein kinase A and C. *Science* 242: 67-69, 1988.
349. **Warner HR, and Cox A**. A mathematical model of heart rate control by sympathetic and vagus efferent information. *J Appl Physiol* 17: 349-355, 1962.
350. **Webb JG, Yates PW, Yang Q, Mukhin YV, and Lanier SM**. Adenylyl cyclase isoforms and signal integration in models of vascular smooth muscle cells. *Am J Physiol Heart Circ Physiol* 281: H1545-1552, 2001.
351. **Weldon SL, Mumby MC, and Taylor SS**. The regulatory subunit of neural cAMP-dependent protein kinase II represents a unique gene product. *J Biol Chem* 260: 6440-6448, 1985.
352. **West TC, Falk G, and Cervoni P**. Drug alteration of transmembrane potentials in atrial pacemaker cells. *J Pharmacol Exp Ther* 117: 245-252, 1956.
353. **Whisnant RE, Gilman AG, and Dessauer CW**. Interaction of the two cytosolic domains of mammalian adenylyl cyclase. *P Natl Acad Sci USA* 93: 6621-6625, 1996.
354. **Whittaker VP**. Cholinergic synaptic vesicles are metabolically and biophysically heterogeneous even in resting terminals. *Brain Res* 511: 113-121, 1990.
355. **Whittaker VP**. Some currently neglected aspects of cholinergic function. *J Mol Neurosci* 40: 7-11, 2010.
356. **Whittaker VP**. The storage and release of acetylcholine. *Biochem J* 128: 73P-74P, 1972.

357. **Wichter T, Schafers M, Rhodes CG, Borggrefe M, Lerch H, Lammertsma AA, Hermansen F, Schober O, Breithardt G, and Camici PG**. Abnormalities of cardiac sympathetic innervation in arrhythmogenic right ventricular cardiomyopathy : quantitative assessment of presynaptic norepinephrine reuptake and postsynaptic beta-adrenergic receptor density with positron emission tomography. *Circulation* 101: 1552-1558, 2000.
358. **Wickman KD, Iniguez-Lluhl JA, Davenport PA, Taussig R, Krapivinsky GB, Linder ME, Gilman AG, and Clapham DE**. Recombinant G-protein beta gamma-subunits activate the muscarinic-gated atrial potassium channel. *Nature* 368: 255-257, 1994.
359. **Wilders R**. Computer modelling of the sinoatrial node. *Med Biol Eng Comput* 45: 189-207, 2007.
360. **Wilders R, Jongsma HJ, and van Ginneken AC**. Pacemaker activity of the rabbit sinoatrial node. A comparison of mathematical models. *Biophys J* 60: 1202-1216, 1991.
361. **Wilson IB, and Harrison MA**. Turnover number of acetyl-cholinesterase. *J Biol Chem* 236: 2292-2295, 1961.
362. **Wong W, and Scott JD**. AKAP signalling complexes: focal points in space and time. *Nat Rev Mol Cell Biol* 5: 959-970, 2004.
363. **Yamasaki Y, Fujiwara M, and Toda N**. Effects of intracellularly applied cyclic 3',5'-adenosine monophosphate and dibutyryl cyclic 3',5'-adenosine monophosphate on the electrical activity of sinoatrial nodal cells of the rabbit. *J Pharmacol Exp Ther* 190: 15-20, 1974.
364. **Yan SZ, Hahn D, Huang ZH, and Tang WJ**. Two cytoplasmic domains of mammalian adenylyl cyclase form a Gs alpha- and forskolin-activated enzyme in vitro. *J Biol Chem* 271: 10941-10945, 1996.
365. **Zaccolo M**. Phosphodiesterases and compartmentalized cAMP signalling in the heart. *Eur J Cell Biol* 85: 693-697, 2006.
366. **Zamaklar-Trifunovic D, Seferovic PM, Petrovic M, Zivkovic M, Vukomanovic G, Milic N, Ristic AD, and Zdravkovic M**. [The influence of respiratory pattern on heart rate variability analysis in heart failure]. *Srp Arh Celok Lek* 135: 135-142, 2007.
367. **Zaza A, Robinson RB, and DiFrancesco D**. Basal responses of the L-type Ca2+ and hyperpolarization-activated currents to autonomic agonists in the rabbit sino-atrial node. *J Physiol* 491 (Pt 2): 347-355, 1996.
368. **Zhang H, Holden AV, Kodama I, Honjo H, Lei M, Varghese T, and Boyett MR**. Mathematical models of action potentials in the periphery and center of the rabbit sinoatrial node. *Am J Physiol Heart Circ Physiol* 279: H397-421, 2000.
369. **Zhang H, Holden AV, Noble D, and Boyett MR**. Analysis of the chronotropic effect of acetylcholine on sinoatrial node cells. *J Cardiovasc Electrophysiol* 13: 465-474, 2002.
370. **Zhang H, and Vassalle M**. Mechanisms of adrenergic control of sino-atrial node discharge. *J Biomed Sci* 10: 179-192, 2003.
371. **Zhou J, and Adams JA**. Participation of ADP dissociation in the rate-determining step in cAMP-dependent protein kinase. *Biochemistry* 36: 15733-15738, 1997.
372. **Zhu W, Zeng X, Zheng M, and Xiao RP**. The enigma of beta2-adrenergic receptor Gi signaling in the heart: the good, the bad, and the ugly. *Circ Res* 97: 507-509, 2005.
373. **Zola BE, Miller B, Stiles GL, Rao PS, Sonnenblick EH, and Fein FS**. Heart rate control in diabetic rabbits: blunted response to isoproterenol. *Am J Physiol* 255: E636-641, 1988.